Generation and Analysis of Satellite Laser Ranging Normal Points for Geodetic Parameter Estimation

Inauguraldissertation
der Philosophisch-naturwissenschaftlichen Fakultät
der Universität Bern

vorgelegt von
Linda Geisser
aus Altstätten (SG)

Leiter der Arbeit:
Prof. Dr. Adrian Jäggi
Dr. Ulrich Meyer
Astronomisches Institut der Universität Bern

Generation and Analysis of Satellite Laser Ranging Normal Points for Geodetic Parameter Estimation

Inauguraldissertation
der Philosophisch-naturwissenschaftlichen Fakultät
der Universität Bern

vorgelegt von
Linda Geisser
aus Altstätten (SG)

Leiter der Arbeit:
Prof. Dr. Adrian Jäggi
Dr. Ulrich Meyer
Astronomisches Institut der Universität Bern

Von der Philosophisch-naturwissenschaftlichen Fakultät angenommen.

Bern, 17. August 2023

Der Dekan

Prof. Dr. Marco Herwegh

Year: 2023
Title: Generation and Analysis of Satellite Laser Ranging Normal Points for Geodetic Parameter Estimation
Author: Linda Geisser

Acknowledgements

I would like to thank my supervisors, Prof. Adrian Jäggi and Dr. Ulrich Meyer, for supporting this thesis with their expertise. Further thanks also go to the whole team of the Astronomical Institute of the University of Bern and the Swiss Optical Ground Station in Zimmerwald for their scientific and technical assistance.
Finally, I am thankful for the sophisticated discussions with external experts, e.g., Prof. Krzysztof Sośnica, Dr. Andreja Sušnik or Dr. Daniela Thaller, to name but a few.

Contents

List of Figures

List of Tables

Acronyms

AIUB Astronomical Institute of the University of Bern. 15, 43, 44, 56, 62, 86, 125

ASI Italian Space Agency. 9–12

BKG Federal Agency for Cartography and Geodesy. 15, 43, 44

BSW Bernese GNSS Software. 17, 24, 25, 27, 28, 43, 51, 55, 62, 125, XV

C-SPAD Compensated Single-Photon Avalanche Diode. 6, 65

CA Contribution Analysis. 39, 105

CCR Corner Cube Reflectors. 9–11

CERES Clouds and Earth's Radiant Energy System. 27

CIP Celestial Intermediate Pole. 19

CNES Centre National d'Etudes Spatiales. 10, 12

CODE Center for Orbit Determination in Europe. 15, 40

COST-G Combination Service for Time-variable Gravity Fields. 23, 53, 78–82, 99–101, 113, 115, 121, 126, XIII

CSR Center of Space Research, University of Texas at Austin. 53, 78, 81, 115

DORIS Doppler Orbitography and Radiopositioning Integrated by Satellite. 3, 18

ERP Earth Rotation Parameter. 9, 10, 17–20, 35, 43–45, 50–52, 67, 68, 70, 72–76, 78–80, 82, 87, 89, 91, 98, 99, 101–103, 106–108, 110, 112, 113, 116–118, 126, IX–XI, XV–XVII

ESA European Space Agency. 12

FSM Fitted Signal Model. 78

GFZ German Research Centre for Geosciences. 23, 78

GNSS Global Navigation Satellite Systems. 2, 3, 15, 18, 40

GRACE Gravity Recovery And Climate Experiment. 23, 53, 59, 78, 125

GRACE-FO Gravity Recovery And Climate Experiment Follow-on. 23, 53, 59, 125

GSFC Goddard Space Flight Center. 3

HEO High Earth Orbiter. 7

IAG International Association of Geodesy. 14

IAU International Astronomical Union. 18, 19

ICRF International Celestial Reference Frame. 18, 19

ICRS International Celestial Reference System. 18

IERS International Earth Rotation and Reference Systems Service. 18, 20, 24

ILRS International Laser Ranging Service. 3, 8, 9, 11, 12, 14–16, 23, 43, 50, 55–57, 59, 61, 62, 65, 78–82, 90–95, 97, 99–102, 112, 113, 115, 126, IX, XI–XIII, XV

ITRF International Terrestrial Reference Frame. 11, 14, 18, 19, 22, 90, 95, 97, 125, 127

ITRS International Terrestrial Reference System. 18, 19

JAXA Japan Aerospace Exploration Agency. 10, 12

JPL Jet Propulsion Laboratory. 24

LEO Low Earth Orbiter. 2, 7, 24, 45, 46, 48–50, 115

LOD Length of Day. 32, 50, 51

LRO Lunar Reconnaissance Orbiter. 4

MC Minimum Constraint. 50, 89, 90

MCP Microchannel-plate Multiplier. 13

MEO Medium Earth Orbiter. 7

NASA National Aeronautics and Space Administration. 4, 9, 27, 48, 53

NEQ Normal Equation. 30, 31, 33, 34, 36–40, 43, 50, 78, 83, 87, 89, 97, 102, 108, 109

NNR No-Net-Rotation. 50, 89, 90

NNT No-Net-Translation. 50, 89, 90

NP SLR Normal Points. 1, 3, 4, 55–57, 59–62, 65, 67–72, 86–88, 121, 125, 126, XV

OPR Once-Per-Revolution. 48, 49, 73, 75–83, 99, 104–108, 111, 126, XI, XVI

PMT Photomultiplier Tube. 13

PSD Post-Seismic Deformation. 19

PWC PieceWise-Constant. 51, 52, 73–75, X, XV

PWL PieceWise-Linear. 51, 52, 73–76, 98, 112, X, XV

SH Spherical Harmonic. 1, 2, 10, 35, 43, 48, 49, 53, 73, 76, 78–82, 97–99, 102, 104–109, 111, 112, 115–120, 125, 126, XI–XIV

SLR Satellite Laser Ranging. 1–4, 6–16, 18–20, 27, 28, 35–37, 43–53, 55–57, 59–62, 64–123, 125–127, IX–XVII

SPAD Single-Photon Avalanche Diode. 13, 14

SwissOGS Swiss Optical Ground Station and Geodynamics Observatory Zimmerwald. 4, 6, 7, 13, 15, 47, 56, 58–60, 63, 65–72, 88, 126, IX, X, XV

VCE Variance Component Estimation. 17, 23, 34–38, 74, 83–90, 97, 99, 108–112, 114, 115, 117, 118, 121, 122, 126, IX, XI, XIII, XIV, XVI

VLBI Very Long Baseline Interferometry. 3, 18, 19, 94, 125

WMEAN Weighted Mean. 52

WRMS Weighted Root Mean Square. 52, 75, 77, 80, 83, 88, 92, 93, 100–104, 106, 108, 111, 113, 117, 121, 122

Chapter 1

Introduction

For more than half a century, Satellite Laser Ranging (SLR) has been an essential measuring technique of geodesy, which is defined by Helmert in 1880 as the science of the measurement and mapping of the Earth's surface. Since SLR measures the round-trip time-of-flight of ultra-short laser pulses emitted by a terrestrial ground station and reflected by an artificial Earth orbiter, e.g., a satellite, it can only be performed when the satellite is visible from the ground station. In order to improve the coverage of the satellite orbit with SLR measurements, a global network of ground stations has been formed and is constantly being further developed (Pearlman et al. 2019).
Moreover, geodetic SLR satellites, i.e., spheres covered with retro-reflectors and having a low area-to-mass ratio, were designed to reduce the non-gravitational perturbations and are therefore well suited for long-term studies.
Before the SLR data are processed, the full-rate data may be compressed, which is allowed due to correlations between observations, into a smaller set of so-called SLR Normal Points (NP)s. This compression is today performed on-site at the SLR ground stations. Then, the high accuracy of the NPs allows a reliable determination of, e.g., geocenter coordinate motion, SLR station coordinates and velocities, polar motion or Length-Of-Day (LOD). Even though dedicated gravimetry satellite missions were designed to observe the time-variable Earth's gravity field, the determination of the very low-degree Spherical Harmonic (SH) geopotential coefficients (here: up to degree and order 6) still relies on SLR observations.
However, to describe all the changes of the system Earth, a stable terrestrial reference frame is inevitable. The realization of such a reference frame is based on four different geodetic techniques, where SLR data is essential for the definition of the origin and the scale of the frame, e.g., Altamimi et al. (2016).

In the last years, there has been an on-going development at the ground SLR stations from laser systems with repetition rates of few Hz towards kHz (Pearlman et al. 2019). This results in a large amount of full-rate SLR observations and may lead to different satellite signature effects, such that the compression strategies should be adapted. Moreover, since 2021 most of the SLR stations provide not only NPs but also full-rate data, which allows to homogenize the compression process for all stations.
In this work, on the one hand, data compression processes are analyzed by quantifying the information loss based on simulated SLR data. On the other hand, two different NP generators and their impact on SLR data processing are studied.

It is planned that for further realizations of terrestrial reference frames the SLR contribution should be extended from only using SLR data of LAGEOS-1/2 to also include LARES SLR data. Therefore, in this work an optimized orbit parametrization of LARES and its contribution to a multi-satellite SLR combination of LAGEOS-1/2 is studied. Moreover, the necessary adaption of the orbit parametrizations for a reliable estimation of the low-degree SH geopotential coefficients is discussed.

Finally, to exploit the full potential of SLR, e.g., to reduce correlations between parameters of interest or to extend the parameter space, multi-satellite SLR combinations with geodetic Low Earth Orbiter (LEO), e.g., Stella or Starlette, are generated.

This work was initiated in the framework of the SPACE TIE project, which has the main objective of determining a long-term stable reference frame by unifying all "three pillars" of Geodesy, i.e., the changes in the Earth's shape, rotation and gravity field (Rummel 2000), based on the two satellite geodetic techniques of Global Navigation Satellite Systems (GNSS) and SLR by using co-location sites in space.

This work is arranged by the following chapters:

Chapter 2, *Satellite Laser Ranging*, introduces the observation principle of SLR and the corresponding space and ground segments.

Chapter 3, *Fundamentals of Satellite Geodesy*, gives an overview of the satellite orbit modeling and the underlying mathematical principles, i.e., least-squares adjustment, variance component estimation and the contribution analysis.

Chapter 4, *SLR Data Processing and Validation at AIUB*, presents the SLR data processing and the methodology to validate the quality of the estimated parameters of interest.

Chapter 5, *SLR Normal Point Generation and Analysis*, describes the SLR data compression strategies and validates its quality and impact on the results of SLR data analysis.

Chapter 6, *Optimization of the Geodetic and Orbit Parametrization Based on LAGEOS-1/2 SLR Data*, focuses on optimized geodetic and orbital parametrizations based only on LAGEOS-1/2 SLR data, analyzes the impact of different Earth's gravity field background models.

Chapter 7, *Multi-Satellite SLR Combinations*, deals with combinations of SLR data to several geodetic satellites on NEQ-level, illustrates different weighting methods, e.g., variance component estimation or Helmert's simple estimator, discusses correlations between parameters and the extension of the parameter space.

Chapter 8, *Summary, Conclusions and Outlook*, recapitulates the main results and conclusions of this work and gives an outlook for further studies.

Chapter 2

Satellite Laser Ranging

This chapter introduces the satellite geodetic technique of SLR, which determines the distance between a ground station and a satellite by measuring the round-trip time-of-flight of ultra-short laser pulses (see Sec. 2.1). Beacon Explorer-B, launched in 1964, was the first successful satellite mission, where the satellite was equipped with retro-reflectors and therefore suitable for SLR observations. Actually, the predecessor satellite mission, Beacon Explorer-A, was already designed for SLR observations, however shortly after the launch a malfunction caused a crash and thus no observations were ever taken (Williams 2023). Nevertheless, in 1965, the NASA's Goddard Space Flight Center (GSFC) in Greenbelt, Maryland, was first to successfully detect reflected laser pulses from Beacon Explorer-B (Plotkin et al. 1965). Afterwards, further satellites were equipped with retro-reflectors, e.g., Beacon Explorer-C, GEOS-1 or Diademe-D1C, and new dedicated spacecraft were designed for SLR, e.g., LAGEOS-1/2, Etalon-1/2, Starlette, Stella or LARES/LARES-2 (see Sec. 2.2). This group of spherical satellites are characterized by small area-to-mass ratios, such that the non-gravitational perturbing forces are minimized and therefore the orbit modeling is simplified.

In order to track these satellites on a regular basis and to ensure a good coverage of the orbits, SLR stations were gradually set up all over the world. Since the SLR stations are normally designed and maintained by different national organizations, they differ in the incorporated technology, e.g., laser or timing systems (see Sec. 2.3). At the same time, the International Laser Ranging Service (ILRS, Pearlman et al. 2002) was established to coordinate the SLR network, to collect and provide laser ranging data and to specify guidelines for data handling and processing, e.g., on how to generate NP (see Sec. 5.1). Furthermore, the ILRS does SLR analysis to generate geodetic products (see Sec. 2.4).

Nevertheless, there are also other space geodetic techniques, e.g., Very Long Baseline Interferometry (VLBI), Doppler Orbitography and Radiopositioning Integrated by Satellite (DORIS) and GNSS. Each technique has its advantages and disadvantages and is therefore able to determine different parameters (see Table 2.1). Hence, e.g., for the realization of a stable reference frame (see Sec. 3.1), different geodetic techniques have to be combined (Rothacher 2003).

Table 2.1: Space geodetic techniques and the corresponding parameters, which can be estimated (adapted from Rothacher 2003).

Parameter	SLR	VLBI	DORIS	GNSS
Nutation		x		
Polar motion	x	x	x	x
UT1		x		
Length of day (LOD)	x	x	x	x
Station coordinates	x	x	x	x
Geocenter coordinates	x		x	x
Gravity field	x		x	x

2.1 Observation Principle

SLR is a geodetic technique measuring mainly the two-way time-of-flight Δt of ultra-short laser pulses emitted from a ground station to a satellite, which is ideally equipped with retro-reflectors, and reflected back to the ground station. Nevertheless, SLR can also be used as a one-way measurement technique, where the SLR station measures the emission time of the ultra-short laser pulses and the on-board receiver telescope on the satellite measures the time of reception. The emission and the receiving times are then measured by different clocks, hence, they first have to be synchronized before the time-of-flight and therefore the distance R between the SLR station and the satellite can be determined (Mao et al. 2017). Since the mean signal flux is proportional to R^{-4} (Degnan 1993), the one-way measurement technique enables to perform laser ranging to artificial objects in the interplanetary space. Therefore, e.g., the Lunar Reconnaissance Orbiter (LRO, Chin et al. 2007), a National Aeronautics and Space Administration (NASA) mission with the main goal to produce accurate maps of the Moon to identify future landing sites, was designed to perform one-way laser ranging (Zuber et al. 2010). The NP collected from different SLR stations, e.g., GO1L in Greenbelt, Maryland US, or the Swiss Optical Ground Station and Geodynamics Observatory Zimmerwald (SwissOGS, Schildknecht et al. 2015), over five years from 2009 to 2014 have a precision of 15-30 mm and are used in combination with S-band data for precise orbit determination of the LRO (Mao et al. 2017).

In this work, only the two-way SLR measurements are further used an analyzed. The two-way time-of-flight Δt can also be expressed by the distances between the station and the satellite at different time epochs (see Fig. 2.1). Neglecting atmospheric delays and station biases, this yields

$$\Delta t = \Delta t_1 + \Delta t_2 = \frac{1}{c}\left(|\mathbf{r}_s(t) - \mathbf{r}_{stat}(t - \Delta t_1)| + |\mathbf{r}_s(t) - \mathbf{r}_{stat}(t + \Delta t_2)|\right), \tag{2.1}$$

with

t : reflection time of the laser pulses at the satellite,
Δt_1 : time-of-flight of laser pulses emitted from the ground station to the satellite,
Δt_2 : time-of-flight of laser pulses reflected at the satellite to the ground station,
$\mathbf{r}_s(t)$: position of the satellite at time t,
$\mathbf{r}_{\text{stat}}(t)$: position of the ground station at time t,
c : speed of light.

With a Taylor series expansion and the assumption that $\Delta t_1 \approx \Delta t_2 \approx \frac{1}{2}\Delta t$, the time-of-flight Δt can be approximated when neglecting higher order terms as

$$\Delta t \approx \frac{2}{c}\left(|\mathbf{r}_s(t) - \mathbf{r}_{\text{stat}}(t)|\right). \tag{2.2}$$

Then, the measured distance d between the ground station and the satellite at the reflection time of the laser pulses at the satellite follows from the observation equation (Seeber 2003)

$$d = \frac{\Delta t}{2}c + \Delta d_{\text{sta}} + \Delta d_{\text{sig}} + \Delta d_{\text{sat}} + \Delta d_{\text{rel}} + \eta \tag{2.3}$$

with

Δt : time-of-flight,
c : speed of light,
Δd_{sta} : station related corrections,
Δd_{sig} : signal propagation corrections,
Δd_{sat} : satellite related corrections,
Δd_{rel} : relativistic corrections,
η : unmodeled residual effects.

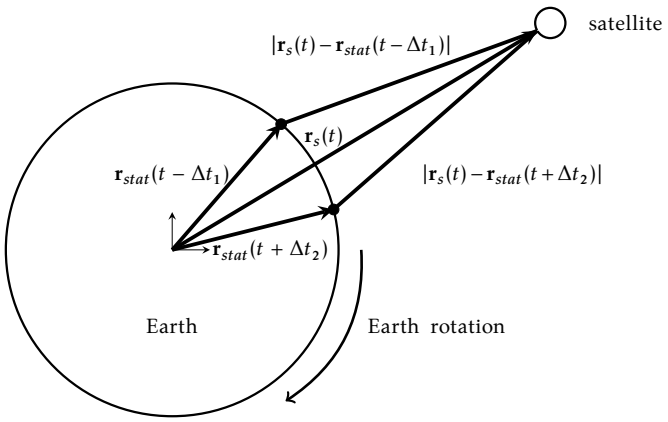

Figure 2.1: Observation principle of SLR.

Station related corrections Δd_{sta} are measurement errors of devices within the measuring system, e.g., timing systems or detectors. In addition, the stations have to take into account the system delays caused by cables, the equipment to direct the laser beam within the internal system and the laser path (Degnan 1985). For this purpose, they measure with the laser system the distance to a calibration target, which is located within the dome or at an external building (Degnan 1985). Hence, the difference to the geometrical light path corresponds to the system delay. Figure 2.2 (left) shows calibration measurements performed at the SwissOGS, where the two-way system delay is −23.72 m. The not normal distribution of the data is characterized by the convolution of the target response function and the system noise (Otsubo et al. 2015), especially from the detector, i.e., the Compensated Single-Photon Avalanche Diode (C-SPAD) (see Sec. 2.3). The large system delay is mainly caused by the length of the laser path in the internal system (Lauber, pers. communication, 2023). Most essential is that this value does not change as long as nothing is modified in the laser system. Otherwise, the laser system is not reliable. All station related corrections should ideally be applied already at the level of data pre-processing at the SLR stations.

The Earth's atmosphere, through which the short laser pulses are propagating from the ground station to the satellite and back to the station, has different properties at different altitudes. Hence, the atmosphere is divided according to the signal propagation velocity (resp. the refractivity) into the troposphere and stratosphere, which cover the layers from the Earth's surface to the altitude of 60 km, consisting of neutral gas and the ionosphere, i.e., the layer from the altitude of 60 km to 1500 km, consisting of gas with charged particles (Torge and Müller 2012). However, the propagation of an optical signal, e.g., laser pulses with a wavelength of 532 nm, is only affected by the troposphere (Seeber 2003). Since the refractivity along the propagation path cannot be directly measured, models describing the gradient of the refractivity at different heights have been developed by, e.g., Marini and Murray (1973) or Mendes and Pavlis (2004). These models analytically describe the correction in zenith direction Δz and provide a mapping function $m(90° - z)$ for the projection at the zenith angle z of the satellite. Therefore, the signal propagation corrections can be expressed as $\Delta d_{\text{sig}} = \Delta z \cdot m(E)$. The functions depend

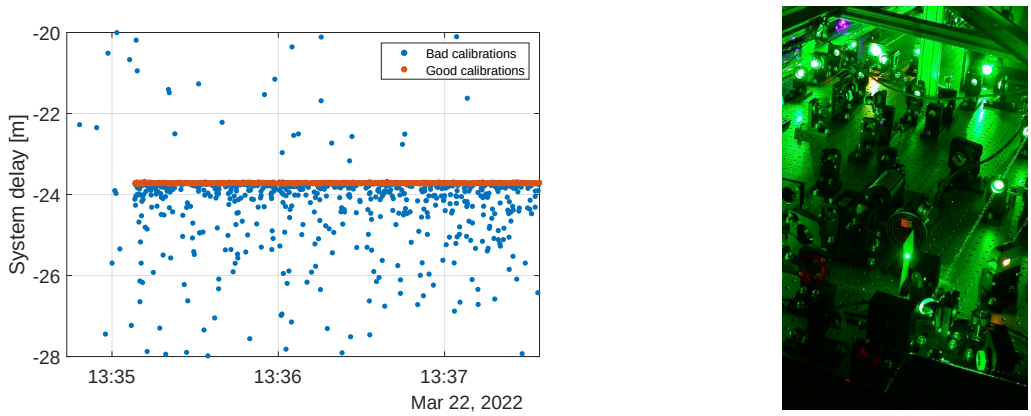

Figure 2.2: Calibration measurements (left) of the laser system (right) at the SwissOGS SLR station to determine the system delay on March 22, 2022.

only on the temperature, the relative humidity and the pressure of the air at the ground station. For the SwissOGS the tropospheric corrections for the given environmental conditions, i.e., 920 mbar pressure, 20 °C and a relative humidity of 80 %, range from about 25 m for an elevation of 4 ° to 2 m in zenith direction (see Fig. 2.3, left). The differences between the tropospheric models Mendes-Pavlis and Marini-Murray are most significant for low elevation angles. In the case of the SwissOGS, satellites are tracked to a minimal elevation angle of 10 ° for LEO, 15 ° for Medium Earth Orbiter (MEO) and 20 ° for High Earth Orbiter (HEO).

The satellite related corrections Δd_{sat} are due to the fact that reflection points of laser pulses do not coincide with the center-of-mass of the satellite, the trajectory of which is modelled in the orbit determination. In the beginning of the SLR era, the correction distance between the reflection point of laser pulses and the actual center-of-mass was empirically determined by pre-launch analyses for each satellite, e.g., 251 mm for LAGEOS-2 (Minott et al. 1993). With increasing ranging accuracy, it became apparent that the distribution of the returned signal and, therefore, the corresponding center-of-mass correction depends on the laser ranging system (Appleby 1993, Kirchner and Koidl 1993), e.g., width of laser pulses, laser ranging regime (single- or multi-photon), screening method and type of detector. For instance, systems ranging on a multi-photon level tend to measure shorter distances than systems ranging in a single-photon regime when using a single-photon detector (Otsubo and Appleby 2003). Consequently, many studies, e.g., Otsubo et al. (1999), Otsubo and Appleby (2003), Otsubo et al. (2015) or Rodríguez et al. (2019) have been carried out to determine system-dependent center-of-mass corrections for spherical geodetic satellite. However, these corrections are not constant in time for SLR stations, because the laser ranging systems are frequently updated and/or improved (see Fig. 2.3, right).

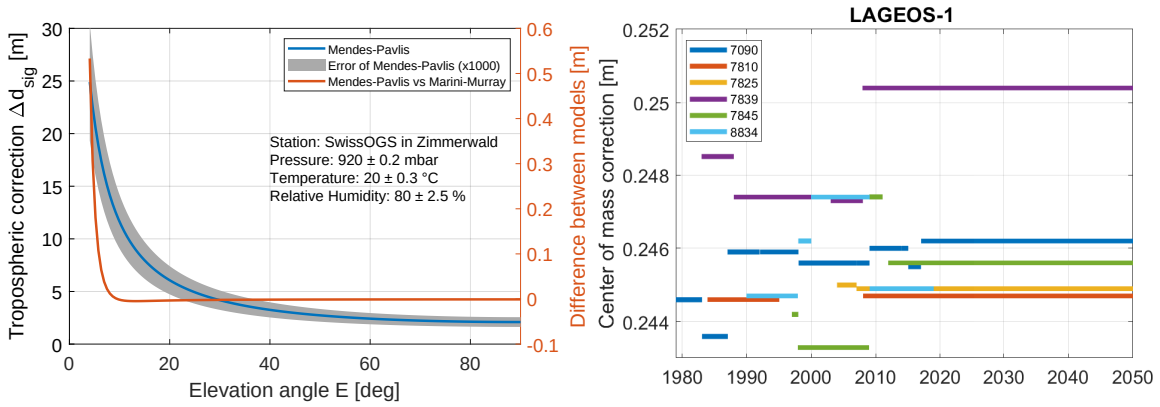

Figure 2.3: Tropospheric correction (left) depending on the elevation of the observations taken at SwissOGS in Zimmerwald. Center-of-mass corrections (right) for LAGEOS-1 for a selected list of stations observing with a wavelength of 532 nm (extracted from the ILRS SLR data handling file[1]).

[1]https://ilrs.dgfi.tum.de/fileadmin/data_handling/ILRS_Data_Handling_File.snx (Accessed: 22/12/2022)

The theory of general relativity implies that the speed of light of laser pulses along their paths changes according to the strength of the gravity field potential. These time delays are also known as the Shapiro effect (Shapiro 1964). Since laser pulses, emitted by a SLR ground station, are travelling within the Earth's gravity field, the Shapiro effect needs to be taken into account as relativistic correction Δd_{rel}.

2.2 Satellites Equipped with Laser Reflectors

Satellite laser ranging can be applied if the satellite is ideally equipped with retro-reflectors. A distinction is made between active and passive satellites. Active satellites are also carrying electronic elements, e.g., sensors, receivers or computers, and therefore have a limited lifetime. In contrary, the passive satellites have no electronic devices on board and can be used as targets for a long time span (Seeber 2003). Geodetic research based on SLR is mainly based on spherical satellites with a small area-to-mass ratio such that the non-gravitational disturbing forces, e.g., air drag or solar radiation pressure, can be minimized and precisely modeled. In the following, a selection of passive spherical satellites, which are used in this work, is presented in more detail. These are: LAGEOS-1/2, Etalon-1/2, Stella, Starlette, Ajisai and LARES/LARES-2. They differ in the composition and the size (see Fig. 2.5) but also in orbital characteristics, e.g., altitude (see Fig. 2.4), inclination and period (see Table 2.2). The technical specifications of the satellites are mainly adopted from the ILRS website[2].

For the SLR processing, the satellites are separated into the following groups

A : LAGEOS-1/2

B : Etalon-1/2

C : LARES

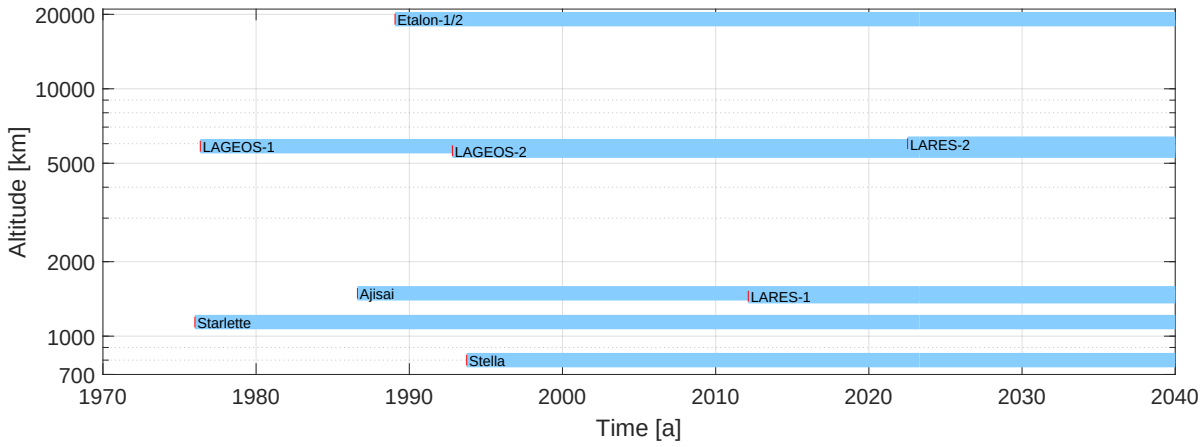

Figure 2.4: Time span of SLR tracking of geodetic SLR satellites at different altitudes (adopted from the ILRS website[2]).

[2]https://ilrs.gsfc.nasa.gov/ (Accessed: 22/12/2022)

D : Starlette

E : Stella

F : LARES-2

2.2.1 LAGEOS-1/2

The space mission of LAGEOS-1 (LAser GEOdynamic Satellite) was elaborated by the NASA. The satellite was launched on May 1976 and at that time it was the first spacecraft dedicated exclusively to SLR. LAGEOS-1 was designed to have a stable orbit with a long lifetime, such that it can serve as a reference point in inertial space. Therefore, the distance measurements between station and satellite can be used to determine the station position with respect to the Earth's center-of-mass (Fitzmaurice et al. 1977). The main purpose was and still is to measure the Earth's tectonic plate motion, the Earth Rotation Parameters (ERP)s and geocenter coordinates (see e.g., Christodoulidis et al. 1985, Smith et al. (1990, 1985) and Pavlis 1999). LAGEOS-1 is a passive spherical satellite with a brass cube core covered with two aluminum alloy caps. The surface is equipped with 426 Corner Cube Reflectors (CCR) to ensure that any incident optical signal is reflected back to the direction of origin (Minott 1974). 422 of the total 426 CCR are made of fused silica to reflect signals in the visible and near infrared spectrum. The other 4 CCR consist of germanium and are therefore well suited for the middle infrared spectrum. This enables research in the non-gravitational thermal thrust effect due to the asymmetric reflectivity of the satellite's hemisphere (Lucchesi 2003b). The thermal thrust of LAGEOS-1/2 is mainly caused by the Yarkovsky effect, the solar Yarkovsky-Schach effect and the asymmetric reflectivity and causes a decay of the semi-major axis of LAGEOS-1/2 (Lucchesi et al. 2020). The Yarkovsky effect is generated by the satellite absorbing infrared radiation of the Earth and re-emitting it in an anisotropic pattern and therefore causing a perturbation force (Rubincam 1987, 1988). Furthermore, the Yarkovsky-Schach effect is related to the anisotropic emission of absorbed solar radiation (Lucchesi et al. 2003).
LAGEOS-1 weighs 407 kg with a diameter of 60 cm. The orbit has a perigee altitude of 5860 km and an inclination of 109.8 °. LAGEOS-2, the successor of LAGEOS-1, is a collaborative mission between NASA and the Italian Space Agency (ASI) launched in October 1992. Its design is very similar to LAGEOS-1, however, the orbital properties are different, i.e., perigee altitude of 5620 km and inclination of 52.6 °. At these high altitudes, the satellite orbits are influenced only marginally by the air drag or the higher-order of the time-variable Earth's gravity field, which simplifies the orbit modeling.

2.2.2 Etalon-1/2

Etalon-1 and Etalon-2 are two Russian space missions launched on January, resp. May, 1989. The main purpose was to support the Russians global navigation system GLONASS by investigating the satellite orbit dynamics and to improve the Earth's gravity field models. These satellites are also used for geodetic research, i.e., to improve station coordinates, ERPs and to determine the gravitational constant GM (Dick et al. 1993). Even the official ILRS products are including Etalon observations. Both satellites were identically manufactured. The spherical satellite is made of metal and the surface is covered

with 2140 fused-quartz and 6 germanium CCR[3]. The orbit specifications of both Etalon satellites are comparable with GLONASS satellites, i.e., a perigee altitude of 19 120 km and an inclination of 64.9 ° resp. 65.5 °.

2.2.3 Starlette, Stella

Starlette (Satellite de Taille Adaptée avec Réflecteurs Laser pour les Etudes de la Terre) and Stella were identically designed and launched in 1975 resp. 1993 by the Centre National d'Etudes Spatiales (CNES). The main purpose of these space missions was the determination and modeling of the solid Earth tides (Williamson and Marsh 1985). Furthermore, several studies, e.g., Sośnica et al. (2014) or Bloßfeld et al. (2018), investigated the contribution of Starlette and Stella to the estimation of geodetic parameters of the global reference frame and the SH geopotential coefficients.
To minimize the area-to-mass ratio, the core of the satellites are made of depleted Uranium 238 alloy and the surfaces are formed as an icosahedron with 20 triangular planes. The planes are made of aluminum and cover three retro-reflectors. Hence, the spherical satellites have a mass of 47 kg with a diameter of 24 cm. Starlette has an eccentric orbit (eccentricity of 0.02) with a perigee altitude of 812 km and 48.8 ° inclination. Stella is a sun-synchronous satellite with a circular orbit and a perigee altitude of 804 km.

2.2.4 Ajisai

Ajisai (also known as Experimental Geodetic Satellite EGS) was launched on August 1986 by todays known Japan Aerospace Exploration Agency (JAXA). The main goal was to test JAXA's two-stage launch vehicle and to determine the precise positioning of isolated Japanese Islands[4]. Despite of this, Sośnica et al. (2014) found that the contribution of Ajisai SLR observations to multi-satellite SLR solutions is significant and improves geodetic parameters, e.g., station coordinates or ERPs. Therefore, Sośnica et al. (2014) claims to use multi-satellite SLR combinations of LAGEOS-1, Starlette and Ajisai for the SLR contribution to realizations of further terrestrial reference frames.
The satellite is spherical with a hollow interior and a shell made of glass-fiber-reinforced plastics. The surface is covered by 1436 uncoated fused silica CCR for laser ranging and 318 mirrors for optical observations to measure Ajisai's spin rate (Sasaki and Hashimoto 1987). With a weight of 685 kg and a diameter of 215 cm the area-to-mass ratio of the satellite is not optimal and the orbit modeling becomes more sophisticated (Sasaki and Hashimoto 1987). The satellite orbit has a perigee altitude of 1490 km and 50 ° inclination.

2.2.5 LARES/LARES-2

LARES (LAser RElativity Satellite), launched on February 2012, is a satellite mission of the ASI. The main goal of this mission is to accurately measure the frame dragging effect, also known as the Lense-Thirring effect (Lense and Thirring 1918), predicted by the theory of General Relativity (Ciufolini et al. 2016). Thereby, the rotation of the Earth

[3] https://space.skyrocket.de/doc_sdat/etalon.htm (Accessed: 08/08/2022)
[4] https://global.jaxa.jp/projects/sat/egs/ (Accessed: 24/02/2023)

drags the axis of a local inertial reference frame, e.g., a satellite, orbiting the Earth (Ciufolini et al. 1996). In analogy, it causes a very small precession of the orbital plane, i.e., a nodal shift, of a satellite in the Earth's gravity field. Consequently, LARES experiences a nodal precession of around 118 mas/a (Ciufolini et al. 2016) due to the Lense-Thirring effect. In comparison, the nodal shift of LARES caused by the oblateness of the Earth is about -2.029 820 73 $\cdot 10^9$ mas/a (Iorio 2010).
LARES can also be used for geodetic research, e.g., to decorrelate low-degree gravity field coefficients or to improve the ITRF. Therefore, it was planned that the ILRS contribution to ITRF2020 and thus the official ILRS products, i.e., the station coordinates and the Earth rotation parameters, should be generated with LAGEOS-1/2, Etalon-1/2 together with LARES (Altamimi et al. 2018). However, this proposal was not realized due to delays at the ILRS analysis centers. Consequently, the contribution of the ILRS to the ITRF2020 is still only based on LAGEOS-1/2 and Etalon-1/2 SLR data.

It is a passive spherical satellite made of very dense tungsten alloy and therefore, with a weight of 387 kg and a diameter of only 36 cm, it is the densest known object in the solar system (Ciufolini et al. 2011a). Additionally, it was formed from a single piece to enable heat exchange, which reduces the thermal thrust perturbation acting on the satellite. The 92 uncoated CCR for performing SLR measurements cover 26 % of the total area (Paolozzi et al. 2015). LARES is placed in an almost circular orbit at 1450 km altitude and 69.5 ° inclination.
LARES-2 was launched on July 2022 by the ASI. However, it was placed in an orbit with a perigee altitude of 5896 km, comparable to the LAGEOS satellites (see Fig. 2.4), and 70.16 ° inclination. It is made of a nickel alloy and is covered with 303 uncoated CCR. With a weight of 297.5 kg and a diameter of 42 cm, LARES-2 has a smaller area-to-mass ratio than the LAGEOS satellites such that the orbit modeling may be simplified. The first analysis of LARES-2 SLR observations are shown in Section 7.3.

Table 2.2: Technical data of spherical SLR satellites (adopted from the ILRS website[2]).

Satellite	launch [yr]	diameter [cm]	weight [kg]	area-to-mass [10^{-4} m^2/kg]	altitude [km]	inclination [°]	period [min]
LAGEOS-1	1976	60.0	407.0	6.9475	5860	109.8	225
LAGEOS-2	1992	60.0	405.4	6.9748	5620	52.6	223
Etalon-1	1989	129.4	1415.0	9.2940	19 120	64.9	676
Etalon-2	1989	129.4	1415.0	9.2940	19 120	65.5	675
Starlette	1975	24.0	47.5	9.5240	812	48.8	104
Stella	1993	24.0	48.0	9.4248	804	98.6	101
Ajisai	1986	215.0	685.0	53.0	1490	50.0	116
LARES	2012	36.4	386.8	2.6903	1450	69.5	115
LARES-2	2022	42.4	297.5	4.7461	5896	70.2	225

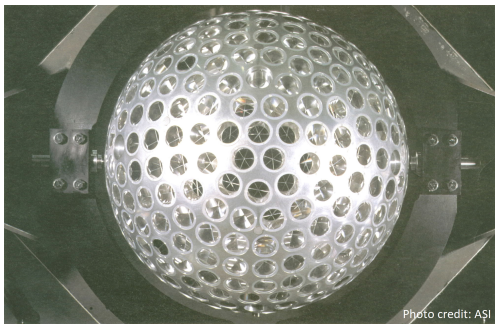

(a) LAGEOS-1/2 (Photo credit: ASI)

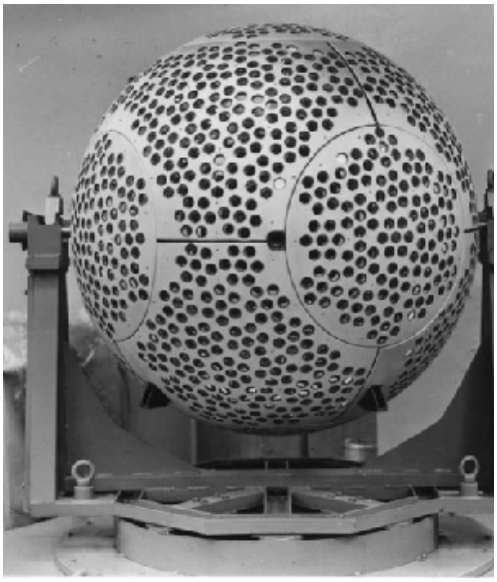

(b) Etalon-1/2 (ILRS website[2])

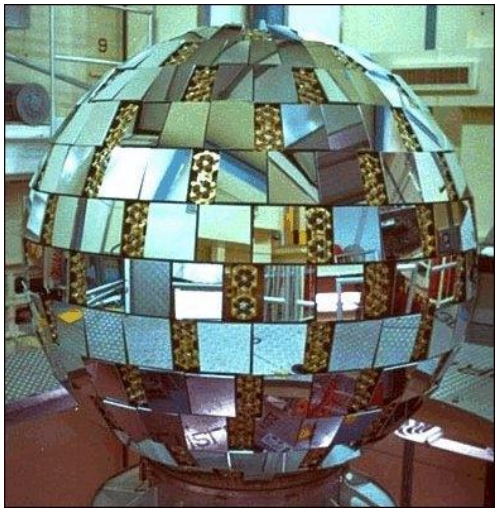

(c) AJISAI (Photo credit: JAXA)

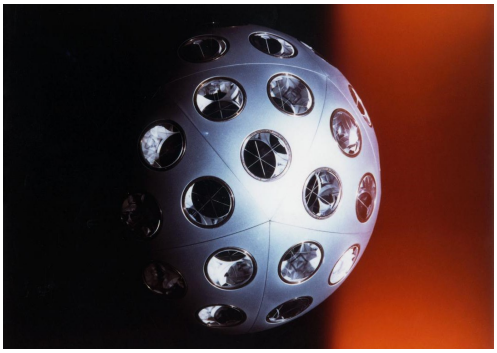

(d) Starlette/Stella (Photo credit: CNES)

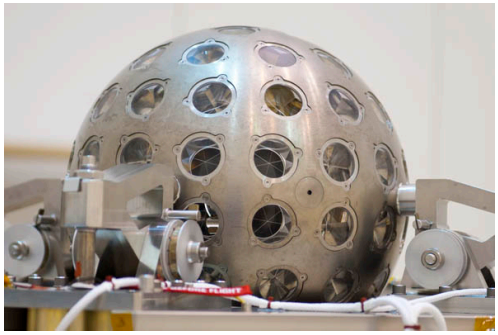

(e) LARES/LARES-2 (Photo credit: ESA)

Figure 2.5: Spherical satellites used for SLR.

2.3 SLR Ground Stations

Figure 2.6 shows the most important components of an SLR ground station, which are a generator of the laser pulses, a signal transmitter, a receiver telescope, a photo-detector of the satellite signal pulses and a time-of-flight measurement device (Seeber 2003). Nevertheless, there are also SLR systems, where the transmitter and the receiver are assembled in the same telescope, e.g., at the SwissOGS in Zimmerwald.

In the beginning of the era of SLR, the stations used a ruby laser with Q-switch to generate laser pulses with a pulse width of 10-40 ns (Degnan 1985). The pulse width is strongly correlated with the accuracy of the range measurement (Seeber 2003), e.g., a pulse width of 10 ns causes a ranging error of 1.5 m. Consequently, other laser systems were developed, e.g., mode-locked Nd:YAG lasers, generating much shorter pulse width of 0.04-0.2 ns at a wavelength of 532 nm and a 10 Hz repetition rate (Degnan 1985, Wilkinson et al. 2019).
Nowadays, however, many SLR stations, e.g., in Graz (Kirchner and Koidl 2004), Herstmonceux or Kunming, are operating with lasers providing high-repetition rates of 1-1000 kHz. This allows to reduce the power pulse energy without decreasing the number of returned photons (Hampf et al. 2019). The high density of data points resulting from a kHz system improves the precision of the Normal Points (Hampf et al. 2019). In addition, it is possible to identify the different retro-reflectors of a satellite by analyzing the full-rate range residuals (Kirchner and Koidl 2004).

After the laser has generated the laser pulses, they are passed through the signal transmitter towards the observed satellite. Further, the backscattered signal from the satellite is received by the telescope and is collected by a photo-detector, which can either be a Photomultiplier Tube (PMT), a Microchannel-plate Multiplier (MCP, Degnan 1985) or a Single-Photon Avalanche Diode (SPAD). Their task is to absorb an incident photon and convert it into an electrical signal, which stops the time-of-flight measurement device. The SPAD detectors are outstanding for their fast rise time of the avalanche to provide good epoch timing. Nevertheless, they are noisier, since different return energies change the detection time and, therefore, causing errors in the range measurements. This is the so-called time-walk effect, which cannot be avoided because it is difficult to perform

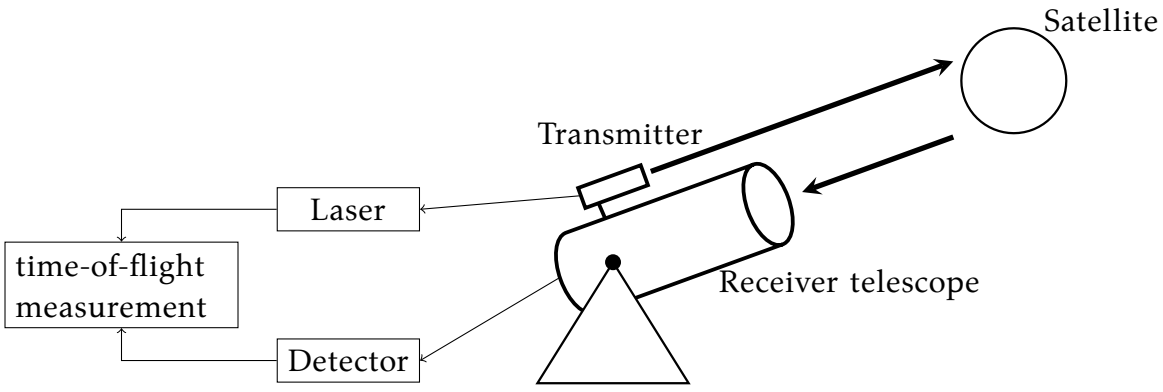

Figure 2.6: General structure of a SLR ground station.

SLR with holding a constant return pulse energy level. However, with the so-called C-SPAD, which is an improved version of the SPAD, the time-walk can be reduced from 200 ps to less than 10 ps (Kirchner and Koidl 1999).

The time-of-flight measurement device is triggered by the signal transmitter when a laser pulse is emitted. The measurement is stopped, if the backscattered signal is recorded by the photo-detector. This time measurement device is either an interval counter or an event timer. The interval counter measures directly the runtime of laser pulses, while the event timer calculates the runtime by measuring the transmitting and the receiving time epoch of the laser pulses. The latter has the advantage that it does not have to wait for the return signal before sending the next one. Therefore, the event timer enables SLR measurements with a high-repetition rate.

2.4 Role of the International Laser Ranging Service

The ILRS was established in 1998 and is an official service of the International Association of Geodesy (IAG) (Pearlman et al. 2002). It collects and provides satellite and lunar laser ranging data and generates own products. In addition, the ILRS sets and develops new standards regarding, e.g., the formation of the normal points (see Sec. 5.1), to ensure a high consistency between the products. The so-called analysis centers are generating on a daily or weekly basis the official ILRS products, e.g., ILRS station coordinates and velocities or Earth Rotation Parameters. Therefore, the ILRS contributes to the maintenance of an accurate ITRF (Altamimi et al. 2011, 2016). At the time of writing, the ILRS network consists of 45 active SLR stations (see Fig. 2.7).
Additionally, Table 2.3 gives further information about the SLR stations. Most of the stations are located on the northern hemisphere, especially in Europe and Southeast Asia.

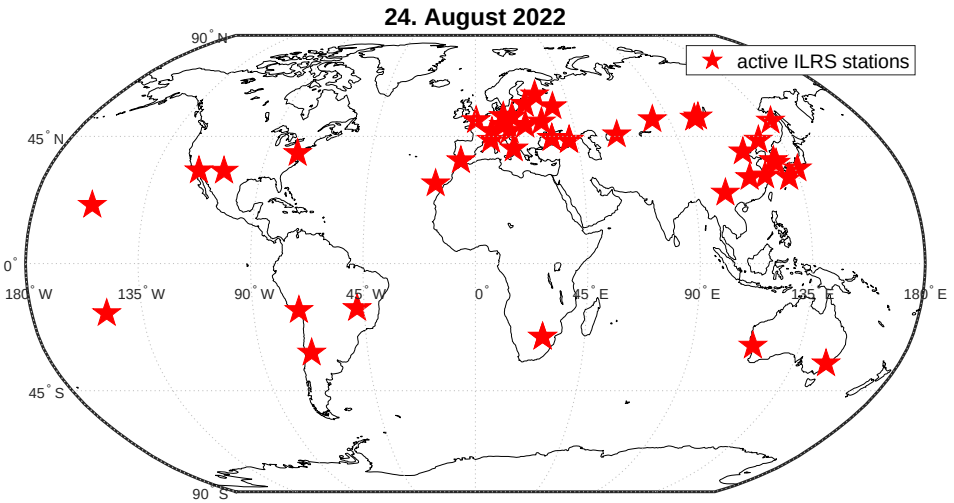

Figure 2.7: ILRS network from August 24, 2022 (adopted from the ILRS website[5]).

[5]https://ilrs.gsfc.nasa.gov/network/stations/index.html (Accessed: 24/08/2022)

Within the ILRS, CODE is a so-called associated analysis center. In this framework, it is validating the quality of the CODE orbit products of GNSS satellites equipped with SLR retro-reflectors. The Astronomical Institute of the University of Bern (AIUB) also generates orbit predictions for GNSS satellites to support their tracking by SLR stations. With the SwissOGS in Zimmerwald, the AIUB also contributes to the ILRS network with one of the most productive stations worldwide. In addition, the AIUB collaborates with the Federal Agency for Cartography and Geodesy (BKG) in Frankfurt, Germany, to generate products for the International Laser Ranging Service (ILRS) and to serve as a backup in the frame of the analysis center activities at BKG.

Table 2.3: Information about SLR stations from the ILRS network (adopted from the ILRS website[2]).

Short station-nr.	Abbreviation	Location
1824	GLSL	Golosiiv, Ukraine
1868	KOML	Komsomolsk-na-Amure, Russia
1873	SIML	Simeiz, Ukraine
1874	MDVS	Mendeleevo 2, Russia
1879	ALTL	Altay, Russia
1884	RIGL	Riga, Latvia
1886	ARKL	Arkhyz, Russia
1887	BAIL	Baikonur, Kazakhstan
1888	SVEL	Svetloe, Russia
1889	ZELL	Zelenchukskya, Russia
1890/1891	BADL/IRKL	Badary/Irkutsk, Russia
1893	KTZL	Katzively, Ukraine
7045	APOL	Apache Point, NM
7090	YARL	Yarragadee, Australia
7105	GODL	Greenbelt, Maryland
7110	MONL	Monument Peak, California
7119	HA4T	Haleakala, Hawaii
7124	THTL	Tahiti, French Polynesia
7237	CHAL	Changchun, China
7249	BEIL	Beijing, China
7358	GMSL	Tanegashima, Japan
7394	SEJL	Sejong City, Republic of Korea
7396	JFNL	Wuhan, China
7403	AREL	Arequipa, Peru
7406	SJUL	San Juan, Argentina
7407	BRAL	Brasilia, Brazil
7501/7503	HARL/HRTL	Hartebeesthoek, South Africa
7701	IZ1L	Izaña (Tenerife), Spain
7810	ZIML	Zimmerwald, Switzerland
7811	BORL	Borowiec, Poland
7819	KUN2	Kunming, China
7821	SHA2	Shanghai, China
7824	SFEL	San Fernando, Spain
7825	STL3	Mt Stromlo, Australia
7827	SOSW	Wettzell, Germany
7838	SISL	Simosato, Japan
7839	GRZL	Graz, Austria
7840	HERL	Herstmonceux, United Kingdom
7841	POT3	Potsdam, Germany
7845	GRSM	Grasse, France
7941	MATM	Matera, Italy
8834	WETL	Wettzell, Germany

Chapter 3

Fundamentals of Satellite Geodesy

This chapter introduces satellite orbit modeling and the underlying mathematical principles. First of all, coordinate reference frames, whether determining a position in space or on Earth, have to be defined (see Sec. 3.1). In addition, ERPs are defined in order to transform one reference frame to the other.
In Section 3.2, the concept of satellite orbit modeling is described. The starting point is a simple two-body problem of the satellite and the Earth. However, in order to better represent the real situation, the problem has to be adjusted by introducing additional perturbations, e.g., the Earth's static and time-variable gravitational field, tides, gravitational effects of other bodies of the solar system, solar radiation pressure or relativistic corrections (see Sec. 3.2.2).

Furthermore, the model parameters can be improved based on a set of observations using least-squares adjustment (see Sec. 3.3). In this process, the parameters can also be constrained, pre-eliminated or stacked. If different sets of observations, e.g., different geodetic techniques or different observed satellites, are to be combined, the method of Variance Component Estimation (VCE) can be used (see Sec. 3.4). In addition, a so-called contribution analysis can be performed to determine the contribution of each set of observations to the improved model parameters (see Sec. 3.5).

In Section 3.6, the method of the long-arc computation, which is regularly used in the Bernese GNSS Software (BSW, Dach et al. 2015), is introduced and modified to also co-estimating Earth's gravity field coefficients. It allows to combine daily satellite arcs into a longer arc, e.g., 7-day arcs, by transforming the initial osculating elements of each day into one set of osculating elements referring to the beginning of the corresponding arc and asking for continuous and differentiable orbits at the day boundaries.
In this thesis, the long-arc computation is applied to study the optimal orbit parametrization of satellites with lower orbital altitudes, e.g., LARES with an altitude of 1400 km (see Sec. 7.1.2).

3.1 Reference Systems and Frames

In order to describe positions of objects in inertial space, e.g., artificial satellites or the Moon, or on the Earth, e.g., SLR stations, reference systems have to be defined. Depending on the need, the systems are fixed in space or rotating, e.g., according to the Earth rotation. The realization of a reference system, called reference frame, is based on measuring coordinates, e.g., of objects (mainly quasars) with a negligible proper motion outside our galaxy or sites on the surface of the Earth, with different geodetic space techniques (Seeber 2003).
The International Earth Rotation and Reference Systems Service (IERS, Petit and Luzum 2010) defines the International Celestial Reference System (ICRS) as well as the International Terrestrial Reference System (ITRS) and realizes the corresponding frames. It also provides and maintains the ERPs to transform coordinates of one reference frame into the other.

3.1.1 International Celestial Reference System and Frame

The International Celestial Reference System (ICRS, Petit and Luzum 2010) is a fixed and non-rotating reference system used for the orientation in space. In 1991, the International Astronomical Union (IAU) recommended to define the ICRS with the following characteristics (Petit and Luzum 2010)

- The origin of the system is located in the barycenter of the solar system.
- The principle plane is located at the mean equator of J2000.0.
- One axis points to the equinox of J2000.0.

The realization of the ICRS is the International Celestial Reference Frame (ICRF) and is based on VLBI estimates of equatorial coordinates of more than 200 extragalactic radio sources (Charlot et al. 2020).

3.1.2 International Terrestrial Reference System and Frame

The International Terrestrial Reference System (ITRS, Petit and Luzum 2010) is an Earth-fixed right-handed orthogonal reference system primarily used to describe station positions. A stable realization of the ITRS, the so-called International Terrestrial Reference Frame (ITRF) is important to understand the dynamics of the Earth and for precise orbit determination of satellites. The construction of the ITRF is based on four space geodetic techniques, i.e., VLBI, DORIS, GNSS and SLR. First, long-term solutions per technique are generated and then they are combined together with local ties at colocation sites and, since ITRF2005, global ties for ERPs (Altamimi and Collilieux 2009, Altamimi et al. (2007, 2016), Seitz et al. 2012).
All SLR analyses in this work are related to the ITRS realization called ITRF2014, which is defined by the following specifications (Altamimi et al. 2016)

- At the epoch 2010.0, the translation and translation rates between the origin of the ITRF2014 and the mean origin received from SLR observations are zero.

- At the epoch 2010.0, the scale factor and scale factor rates between the ITRF2014 and the average of the scale factor and scale factor rates received from VLBI and SLR observations are zero.

- At the epoch 2010.0, the rotation parameters and the rotation rates between the ITRF2014 and the ITRF2008 are zero.

This ITRF is also characterized by the fact that for stations annual and semi-annual terms were estimated and that Post-Seismic Deformation (PSD) models were applied (Altamimi et al. 2016). The latest realization of the ITRS is the ITRF2020 (Altamimi et al. 2018).

3.1.3 Earth Rotation Parameters

Station coordinates are normally represented in the ITRF, whereas the satellite positions are conventionally given in an ICRF. To compute the distance between the station position and the position of the satellite, both positions have to be expressed in the same reference frame. Therefore, coordinates expressed in the ITRF have to be transformed into the ICRF, or vice versa, by using a set of three parameters, the so-called Earth Rotation Parameters, together with a precession-nutation model (see Fig. 3.1). The ERPs are represented by two pole coordinates of the polar motion (x_p and y_p) and the time difference UT1-UTC (also referred as ΔUT). A position vector $\mathbf{r}_\mathrm{ICRF}$ in the ICRF is then transformed into the ITRF according to the following equation (Seeber 2003)

$$\mathbf{r}_\mathrm{ITRF} = \mathbf{R}_2(-x_\mathrm{p})\mathbf{R}_1(-y_\mathrm{p})\mathbf{R}_3(\Theta)\mathbf{N}\mathbf{P}\mathbf{r}_\mathrm{ICRF} \tag{3.1}$$

with

$\mathbf{r}_\mathrm{ICRF}$: position vector expressed in ICRF,
$\mathbf{r}_\mathrm{ITRF}$: position vector expressed in ITRF,
$\mathbf{R}_x(y)$: rotation matrix around the axis x with a rotation angle of y,
$x_\mathrm{p}, y_\mathrm{p}$: polar motion,
Θ : Greenwich apparent sideral time,
$\mathbf{N}$: rotation matrix for nutation,
$\mathbf{P}$: rotation matrix for precession.

The nutation and precession motion of the Earth's rotation axis is caused by the gravitational forces (torques) of the Moon and the Sun acting on the equatorial bulge of the Earth and can be modelled based on a precession-nutation theory, e.g., IAU 2006 (Petit and Luzum 2010, Mathews et al. 2002). Hence, the resulting reference system, i.e., the Celestial Intermediate Pole (CIP), is defined by the true equator and equinox of date (Seeber 2003). The transformation from the CIP to the ITRF is performed by using the ERPs. First, the matrix $\mathbf{R}_3(\Theta)$ translates the non-rotating CIP into an Earth-fixed rotating system, where the rotation angle Θ is the Greenwich apparent sidereal time and is related to the ERP ΔUT (Aoki et al. 1981). Finally, the polar motion which describes the movement of the Earth's rotation axis w.r.t. the Earth's crust is taken into account by

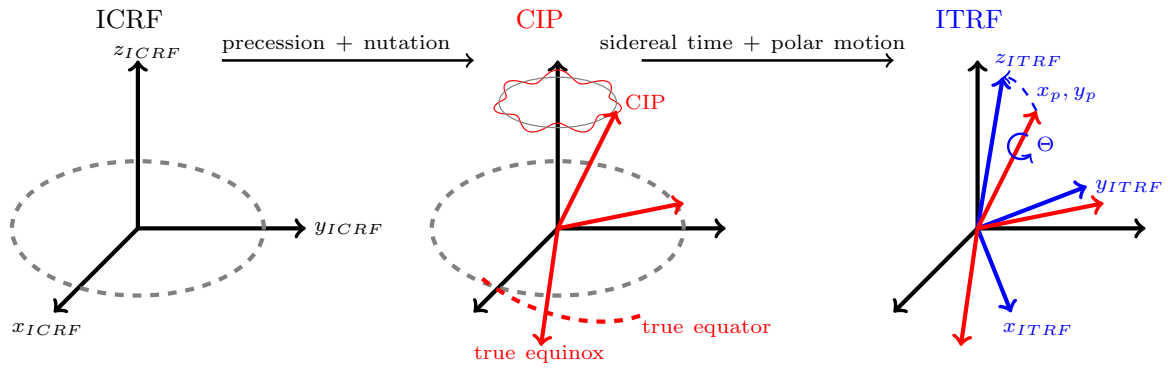

Figure 3.1: Transformation from the ICRF through the CIP to the ITRF.

the rotation matrices $\mathbf{R}_2(-x_\mathrm{p})$ and $\mathbf{R}_1(-y_\mathrm{p})$. The spectral analysis shows that the polar motion is mainly a superposition of an annual and a strong 14-months, i.e., Chandler period/wobble (Chandler 1891), signal (e.g., Beutler et al. 2005).
Figure 3.2 shows the ERP series IERS-14-C04, which is an IERS product based on a multi-technique combination at observation level (Bizouard et al. 2019). The positions of the rotational pole can vary by 0.4″ (resp. 12 m on the Earth's crust). The time difference ΔUT series shows several discontinuities due to the introduction of leap seconds in UTC. They are used to adjust the coordinated universal time UTC to the actual Earth rotation UT1. Therefore, the absolute value of ΔUT has to be smaller than 0.9 s, otherwise, the IERS will add a leap second. In our SLR processing this ERP series is used as a priori information and reference series for comparisons.

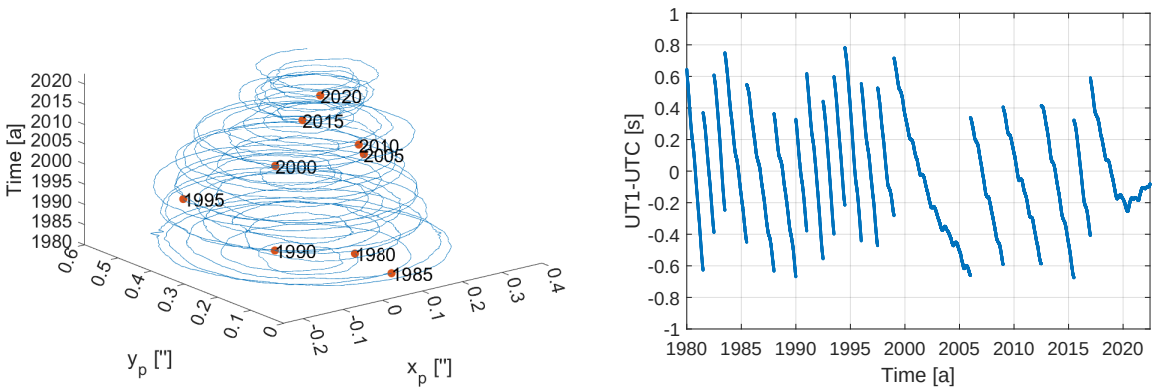

Figure 3.2: Polar motion (left) and time difference ΔUT (right) from the reference series IERS-14-C04 for the years 1982-2021 (Bizouard et al. 2019).

3.2 Satellite Orbit and Background Force Modeling

This section explains how the position, resp., velocity of an Earth orbiting satellite can be determined at any time t. First, a two-body problem between the Earth and the satellite is described by the Keplerian motion. Afterwards, some of the most important orbit perturbations are introduced.

3.2.1 Two-Body Problem

In the simplest case, where only the gravitational force of the Earth is present, the motion of an artificial satellite orbiting the Earth is (Seeber 2003)

$$\ddot{\mathbf{r}}(t) = -\frac{GM}{|\mathbf{r}(t)|^3}\mathbf{r}(t), \tag{3.2}$$

where $\mathbf{r}$ describes the position of the satellite w.r.t. the Earth, which is described as a point mass. Additionally, the relation between the mass of the satellite m and the Earth M is $m << M$, i.e., the mass of the satellite may be neglected, and G is the gravity constant. Eq. 3.2 is a second-order differential equation and has six integration constants, often represented by the six Keplerian orbital elements $(a, e, i, \Omega, \omega, u_0)$ as described in Figure 3.3. The semi-major axis a and the numerical eccentricity e describe the size and shape of the orbit. Whereas, the orbit inclination i and the right ascension of ascending node Ω define the orientation of the orbital plane in space. The orientation of the orbit in the orbital plane is given by the argument of perigee ω. Last, the argument of latitude $u(t_0) = u_0$ may be used to describe the position of the satellite on the orbit at time t_0. Instead of the six Keplerian orbital elements, it is possible to specify the following two solution vectors, i.e., the position resp. velocity vectors at time t_0,

$$\begin{aligned} \mathbf{r}(t_0) &= \mathbf{r}(t_0; a, e, i, \Omega, \omega, u_0), \\ \dot{\mathbf{r}}(t_0) &= \dot{\mathbf{r}}(t_0; a, e, i, \Omega, \omega, u_0). \end{aligned} \tag{3.3}$$

a : semi-major axis
e : numerical eccentricity
i : orbit inclination
Ω : right ascension of ascending node
ω : argument of perigee
$u(t_0)$: argument of latitude at time t_0

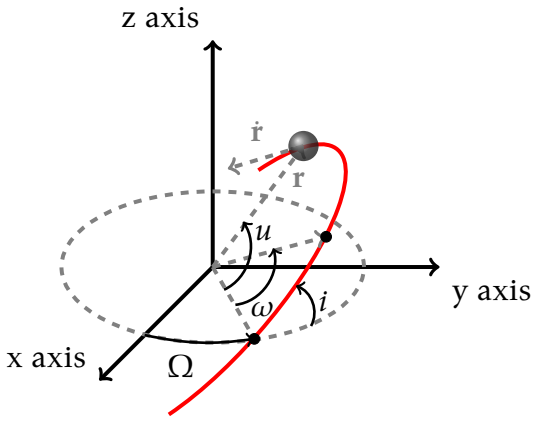

Figure 3.3: Six Keplerian orbital elements of an Earth orbiter in an inertial reference frame, where the x-axis points towards the vernal equinox, the y-axis is perpendicular to the x-axis in the Earth's equatorial plane, z-axis is normal to the equatorial plane and the origin is located in the geocenter.

3.2.2 Orbit Perturbations

In general, however, the orbit of a satellite orbiting the Earth is not only influenced by the gravitational attraction of the Earth, but also by additional forces called perturbation accelerations. They can be gravitational accelerations, e.g., attraction of the Sun or Moon, or non-gravitational accelerations, e.g., atmospheric air drag or solar radiation pressure. In addition, the Earth is no longer considered as a point mass and is instead represented by a volume integral.
Therefore, the equation of motion is the sum of the gravitational attraction of the Earth based on a volume integral and additional perturbing forces (Beutler et al. 2005a)

$$\begin{aligned} \ddot{\mathbf{r}} &= -GM \int_{V_\mathrm{E}} \rho_\mathrm{Er} \frac{\mathbf{r} - \mathbf{r}_\mathrm{E}}{|\mathbf{r} - \mathbf{r}_\mathrm{E}|^3} dV_\mathrm{E} + \mathbf{f}_\mathrm{p} \\ &:= \mathbf{f}_\mathrm{total}(t; \mathbf{r}, \dot{\mathbf{r}}, \mathbf{r}_1, ..., \mathbf{r}_n, p_1, ..., p_d), \end{aligned} \tag{3.4}$$

with the initial conditions given by Eqs. 3.3 and

$\mathbf{f}_\mathrm{p}$: perturbing forces, i.e., gravitational forces of third bodies and non-gravitational forces,
$\mathbf{r}$: geocentric position vector of the satellite,
$\mathbf{r}_\mathrm{E}$: geocentric position vector of a volume element of the Earth,
$\mathbf{r}_i$: geocentric position vector of the third body (with $i \in \{1, ..., n\}$),
ρ_Er : relative density function of the Earth,
V_E : total volume of the Earth,
p_i : dynamic parameters (with $i \in \{1, ..., d\}$).

The perturbing forces can be described in different reference frames, e.g., ITRF or co-rotating orbital frame. The latter system is defined by the three axes in radial direction R (radial), normal to R in the instantaneous orbital plane S (along-track) and normal to the orbital plane W (cross-track) having the origin in the center-of-mass of the satellite (Beutler et al. 2005a).
In the following sections, the acting forces on a satellite orbiting the Earth are explained in more detail.

a) Earth's Gravity Field

The Earth's gravitational acceleration $\ddot{\mathbf{r}}_\mathrm{GR}$ is invariant to rotations, i.e., $\boldsymbol{\nabla} \times \ddot{\mathbf{r}}_\mathrm{GR} = \mathbf{0}$, and can therefore be represented as a gradient of the gravitational potential V

$$\ddot{\mathbf{r}}_\mathrm{GR} = \boldsymbol{\nabla} V. \tag{3.5}$$

Since, the gravitational potential V outside the Earth is a solution of the Laplace's differential equation of second order

$$\Delta V = 0, \tag{3.6}$$

it can be represented by harmonic functions in an Earth-fixed frame using the system of spherical coordinates, i.e., radial distance r, longitude λ and colatitude θ,

$$V(r,\lambda,\theta) = \frac{GM}{r}\sum_{n=0}^{\infty}\left(\frac{a_{\mathrm{E}}}{r}\right)^n \sum_{m=0}^{n}\left[\bar{C}_{nm}\cos(m\lambda) + \bar{S}_{nm}\sin(m\lambda)\right]\bar{P}_{nm}(\cos\theta), \tag{3.7}$$

where $\bar{C}_{nm}$, $\bar{S}_{nm}$ and $\bar{P}_{nm}$ are the fully normalized Earth's spherical harmonic coefficients of degree n and order m, resp., the normalized Legendre functions (Torge and Müller 2012, Petit and Luzum 2010). The relation between the nominal and the normalized values is given by the following factor (Petit and Luzum 2010)

$$N_{nm} := \sqrt{\frac{(n-m)!(2n+1)(2-\delta_{0m})}{(n+m)!}} \qquad \text{where} \qquad \delta_{0m} = \begin{cases} 1 & \text{for} \quad m = 0 \\ 0 & \text{for} \quad m \neq 0 \end{cases} \tag{3.8}$$

such that

$$C_{nm} = N_{nm}\bar{C}_{nm}, \quad S_{nm} = N_{nm}\bar{S}_{nm}, \quad \text{and} \quad \bar{P}_{nm} = N_{nm}P_{nm}. \tag{3.9}$$

The spherical harmonic coefficients $\bar{C}_{nm}$ and $\bar{S}_{nm}$ may represent a subset of the dynamic parameters p_i in Eq. 3.3. Further, a_{E} defines the equatorial radius of the Earth and GM is the gravitational constant multiplied by the mass of the Earth.
The Earth's gravity field models are providing a GM, a_{E} and a set of spherical harmonic coefficients C_{nm} and S_{nm} (often fully normalized) up to a certain maximum degree and order (d/o). If the spherical harmonic coefficients are independent on the time t, it is called a static gravity field model, otherwise, it is a time-variable gravity field model with $C_{nm}(t)$ and $S_{nm}(t)$.

In this thesis, three different gravity field models were used and compared. One is a static gravity field model GGM05S (Ries et al. 2016). The others are time-variable gravity field model, one following the ILRS requirements and is based on GGM05S, where the zonal spherical harmonic coefficients from d/o 2 to d/o 6 and C_{21}/S_{21} of GGM05S are corrected or replaced depending on the time. The second is a product from the Combination Service for Time-variable Gravity Fields (COST-G, Jäggi et al. 2020), where monthly gravity fields of the Gravity Recovery And Climate Experiment Follow-on (GRACE-FO, Landerer et al. 2020) satellite mission of different analysis centers of COST-G are combined using VCE (Meyer et al. 2020). Since the GRACE/GRACE-FO will cover the Earth only after 30 days, the computed global gravity field is impacted by short periodic signals that cannot be resolved. Additionally, the gravimetry satellite missions cannot distinguish between mass changes above, beyond or at the Earth's surface. Therefore, the German Research Centre for Geosciences (GFZ) provides GRACE Atmosphere and Ocean De-Aliasing Level-1B (AOD1B) products for signal separation in the gravity field estimation (Dobslaw et al. 2017).

b) Tides and Pole Tides

The gravitational attraction on the Earth caused by the Sun and the Moon results in a deformation of the solid Earth's crust, the oceans and the atmosphere. These responses are called solid Earth tides, ocean and atmospheric tides. The pole tides describe deformations of the solid Earth and the oceans due to changes in the centrifugal forces induced by the polar motion (see Sec. 3.1.3).
Hence, the Earth's gravitational potential is changed and therefore, the accelerations acting on the satellites have to be adjusted. In the BSW, these tides are modeled as variations in the Earth's gravitational spherical harmonic coefficients according to the IERS 2010 conventions (Petit and Luzum 2010). A detailed description of these implementations in the BSW can be found in Lasser et al. (2020).

c) Gravitational Effects of third bodies (Sun, Moon and Planets)

The solar system consists of multiple celestial bodies besides the Earth, which depending on their mass and distance can perturb the satellite orbits significantly. These are mainly the Sun, the Moon, and three planets, i.e., Jupiter, Venus and Mars. Therefore, these perturbations $\ddot{\mathbf{r}}_{\mathrm{NB}}$ are described by 3-body problems, where the celestial bodies are treated as point masses, and are modelled as (Beutler et al. 2005a)

$$\ddot{\mathbf{r}}_{\mathrm{NB}} = -G \sum_{j=1}^{n} m_j \left(\frac{\mathbf{r} - \mathbf{r}_{\mathrm{E}}}{|\mathbf{r} - \mathbf{r}_{\mathrm{E}}|^3} + \frac{\mathbf{r}_j}{|\mathbf{r}_j|^3} \right). \tag{3.10}$$

Gm_j, i.e., the gravitational constant multiplied by the mass, and the geocenter position vector $\mathbf{r}_j$ of the j-th third body are computed in this work by using the DE405 (Standish 1998) development ephemeris provided by the Jet Propulsion Laboratory (JPL).

d) Atmospheric Drag

For orbit determination of LEOs accelerations caused by the atmospheric drag have to be taken into account. The accelerations due to the atmospheric drag is (Montenbruck et al. 2002)

$$\ddot{\mathbf{r}}_{\mathrm{AD}} = -\frac{1}{2} C_{\mathrm{D}} \frac{A}{m} \rho(t) |\mathbf{v}|^2 \frac{\mathbf{v}}{|\mathbf{v}|} \tag{3.11}$$

with

C_{D} : drag coefficient of the satellite (see Table 3.1),
$\frac{A}{m}$: area-to-mass ratio of the satellite,
$\mathbf{v}$: velocity vector of the satellite expressed in the Earth-fixed system,
$\rho(t)$: time dependent atmospheric density.

The atmospheric density of the Earth $\rho(t)$ is modeled using the NRLMSISE-00 empirical atmospheric model (Picone et al. 2002). It depends on the height, the observation time, the geographic position, the solar (represented by the solar radio flux at 10.7 cm,

Table 3.1: Area-to-mass ratio, drag (C_D) and radiation pressure coefficients (C_R) for different spherical satellites (according to the satellite information file in the BSW).

Satellites	$\frac{A}{m}$ [10^{-4}m^2/kg]	C_D	C_R
LAGEOS-1/2	6.9	0	1.130
Etalon-1/2	9.3	0	1.200
Starlette	9.6	2.37	1.134
Stella	9.4	2.37	1.134
Ajisai	58.0	2.80	1.030
LARES	2.7	2.60	1.070
LARES-2	4.7	2.60	1.070

$F10.7$) and geomagnetic activities (represented by eight 3-hourly planetary equivalent amplitudes A_p). In the BSW, the latter two may either correspond to standard values, i.e., $F10.7 = 120$ and $A_p = 15$, or to actual measured data[6]. In this thesis, the air drag model is only applied to the satellites with an orbital altitude lower than 2000 km.

e) Direct and Indirect Solar Radiation Pressure

The Sun constantly emits photons, where each photon carries an energy of $E = h\nu$, where h is the Planck constant and ν the frequency of the photon. Hence, the total energy coming from the sun flowing through a surface (1 m^2) within a second at a distance of 1 AU is described by the solar constant S.
Then, the radiation pressure is the momentum, which is transferred per time of the photons to an absorbing and/or reflecting surface in a radiation field (Beutler et al. 2005b). The change in momentum of the surface is equivalent to an acceleration.
Consequently, a satellite orbiting the Earth is directly affected by this radiation pressure of the Sun. The acceleration caused by the direct Solar Radiation Pressure (SRP) is (Beutler et al. 2005b)

$$\ddot{\mathbf{r}}_{SRP} = \frac{C_R}{2}\frac{A}{m}\frac{S}{c}\frac{\mathbf{r}-\mathbf{r}_S}{|\mathbf{r}-\mathbf{r}_S|^3}\mathrm{AU}^2 \tag{3.12}$$

with

C_R : radiation pressure coefficient of the satellite,
S : solar constant,
c : speed of light,
$\frac{A}{m}$: area-to-mass ratio of the satellite,
$\mathbf{r}_S$: geocentric position of the Sun,
$\mathbf{r}$: geocentric position of the satellite,
AU : astronomical unit.

[6] http://celestrak.org/SpaceData/SW-Last5Years.txt (Accessed: 05/06/2023)

It is assumed that the satellite is axially symmetrical w.r.t. the Sun (which is true for the spherical satellites) and that the surface of the satellite is normal to the direction of the Sun (Montenbruck et al. 2002). Furthermore, the radiation pressure coefficient C_R depends on the reflectivity of the satellite's surface (see Table 3.1).

Besides the direct solar radiation pressure, also the indirect solar radiation pressure (ERP) caused by the Earth has to be taken into account in the orbit modeling (Seeber 2003). It is differentiated between the optical and the infrared radiation pressure (Montenbruck et al. 2002). The optical radiation pressure is the reflection and scatter of the direct radiation pressure on the Earth. Therefore, it is only emitted on the daylight side of the Earth with a magnitude depending on the Earth's surface or weather conditions, which is described by the albedo factor a. Furthermore, the infrared radiation pressure is the emission of the absorbed direct radiation pressure of the Earth and is characterized by the emissivity factor ϵ. In that case, the perturbing acceleration acting on the satellite (see Fig. 3.4) is a sum of different Earth areas dA (Montenbruck et al. 2002)

$$\ddot{\mathbf{r}}_{\mathrm{ERP}} = \frac{C_R S}{c\pi}\frac{A}{m}\sum_{j=1}^{N}\left(\nu_j a_j \cos\left(\theta_j^{i,S}\right) + \frac{1}{4}\epsilon_j\right) dA_j \cos\left(\theta_j^{i,\mathrm{sat}}\right)\frac{\mathbf{r}-\mathbf{r}_j}{|\mathbf{r}-\mathbf{r}_j|^3} \tag{3.13}$$

where

dA_j : small area of the Earth,
ν_j : shadow function for dA_j $\quad(\nu_j \in [0,1])$,
a_j : albedo reflectivity factor of dA_j,
ϵ_j : albedo emissivity of dA_j,
$\mathbf{r}$: geocentric position of the satellite,
$\mathbf{r}_j$: geocentric position of the area dA_j on the Earth,
$\theta_j^{i,S}$: angle between $\mathbf{r}_j$ and $\mathbf{r}_S$,
$\theta_j^{i,\mathrm{sat}}$: angle between $\mathbf{r}_j$ and $\mathbf{r}$.

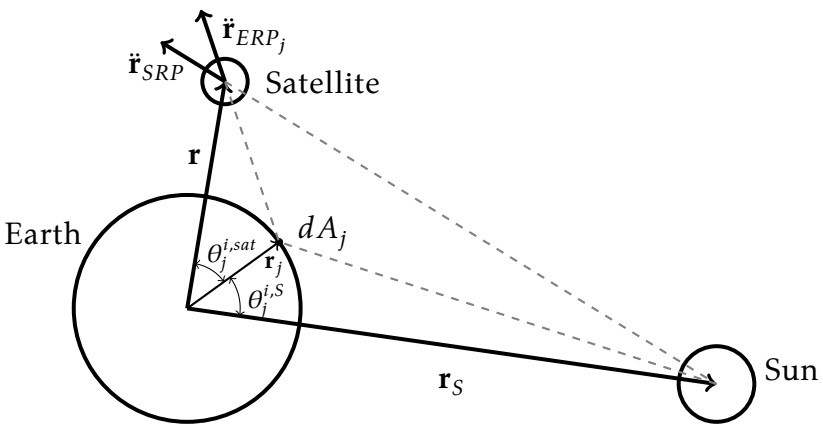

Figure 3.4: Direct (SRP) and indirect radiation pressure (ERP_j from Earth area dA_j) acting on an Earth orbiter.

The shadow function ν_j is used to decide if an Earth area dA_j is on the daylight side of the Earth or in the Earth's shadow. The albedo reflectivity and emissivity factors strongly depend on the month of the year, but they are, however, rather stable over the years (Mao et al. 2021). Therefore, monthly albedo factors generated by averaging several year-specific monthly albedo factors from the Earth given in a 2.5 °×2.5 °-grid, obtained from the Clouds and Earth's Radiant Energy System (CERES, Wielicki et al. 1996) NASA project (ES-4) data set, are used for the orbit determination in the SLR processing using the BSW.

f) Relativistic Corrections

The theory of General Relativity formulated by Einstein (Einstein 1915) implies that gravity causes a curvature of the space-time and that the Newtonian law of gravity is only a first approximation. Therefore, the motion of a satellite orbiting in gravitational fields of the Earth or Sun have to be adapted by relativistic corrections, which are explained in detail in Combrinck (2013).
The main correction of around $10^{-9}\mathrm{m/s}^2$ is due to the motion of a satellite through the curved space-time caused by the gravity of the Earth. Since Schwarzschild was first to find a solution for such a motion, i.e., a motion of a massless point in a gravitational field of a non-rotation, static and spherical symmetric body (Schwarzschild 1916), this effect is known as the Schwarzschild correction.
Furthermore, the Earth's motion through the gravitational field of the Sun causes a precession, also called de Sitter precession (de Sitter 1916), of the orbital pole of a satellite. Then, Lense and Thirring (Lense and Thirring 1918) described an additional perturbation of objects, e.g., satellites, moving within a gravitational field caused by a rotating mass source, e.g., the Earth.
Consequently, the perturbation $\ddot{\mathbf{r}}_{\mathrm{REL}}$ of an Earth orbiter caused by the Schwarzschild, de Sitter and Lense-Thirring corrections predicted by the General Relativity Theory is (Petit and Luzum 2010)

$$\begin{aligned}\ddot{\mathbf{r}}_{\mathrm{REL}} = &\overbrace{\frac{GM_{\mathrm{E}}}{c^2|\mathbf{r}|^3}\left(\left[2(\beta+\gamma)\frac{GM_{\mathrm{E}}}{|\mathbf{r}|}-\gamma\dot{\mathbf{r}}\cdot\dot{\mathbf{r}}\right]\mathbf{r}+2(1+\gamma)(\mathbf{r}\cdot\dot{\mathbf{r}})\dot{\mathbf{r}}\right)}^{Schwarzschild}\\ &+\underbrace{(1+\gamma)\frac{GM_{\mathrm{E}}}{c^2|\mathbf{r}|^3}\left(\frac{3}{|\mathbf{r}|^2}(\mathbf{r}\times\dot{\mathbf{r}})(\mathbf{r}\cdot\mathbf{J})+(\dot{\mathbf{r}}\times\mathbf{J})\right)}_{Lense-Thirring}-\underbrace{\left((1+2\gamma)\frac{GM_{\mathrm{S}}}{c^2|\mathbf{R}|^3}(\dot{\mathbf{R}}\times\mathbf{R})\times\dot{\mathbf{r}}\right)}_{deSitter},\end{aligned} \tag{3.14}$$

with

β, γ : parameterized post-Newtonian parameters, equal to 1 in General Relativity,
$M_{\mathrm{E}}, M_{\mathrm{S}}$: mass of the Earth and Sun, respectively,,
$\mathbf{R}$: position of the satellite w.r.t. the Sun,
$\mathbf{J}$: Earth's angular momentum per unit mass with $|\mathbf{J}| \approx 9.8 \cdot 10^8 \mathrm{m}^2/\mathrm{s}$.

The de Sitter and Lense-Thirring corrections are around $10^{-11}\mathrm{m/s}^2$ and therefore much smaller than the Schwarzschild correction. Nevertheless, the improved accuracy of the

SLR measurements during the last years enables to measure the relativistic corrections, which agree with the postulation of the General Relativity Theory, e.g., Lucchesi (2003), Ciufolini and Pavlis (2004) or Ciufolini et al. (1996,1998, 2011, 2016).

g) Empirical Corrections

Since the background force modeling used in the BSW, for the orbit determination is not perfect, empirical accelerations may be estimated in addition. The empirical acceleration $\ddot{\mathbf{r}}_{\mathrm{EMP}}$ given in the co-rotating orbital frame is characterized by nine unknown dynamic orbit parameters consisting of three constant accelerations (R_0, S_0, W_0), three once-per-revolution cosine accelerations $(R_\mathrm{C}, S_\mathrm{C}, W_\mathrm{C})$ and three once-per-revolution sine accelerations $(R_\mathrm{S}, S_\mathrm{S}, W_\mathrm{S})$ depending on the satellite's argument of latitude u (Beutler et al. 2005b)

$$\ddot{\mathbf{r}}_{\mathrm{EMP}} = \begin{pmatrix} R_0 \\ S_0 \\ W_0 \end{pmatrix} + \begin{pmatrix} R_\mathrm{C} \\ S_\mathrm{C} \\ W_\mathrm{C} \end{pmatrix} \cos(u) + \begin{pmatrix} R_\mathrm{S} \\ S_\mathrm{S} \\ W_\mathrm{S} \end{pmatrix} \sin(u). \tag{3.15}$$

Since the measurements of the SLR geodetic technique are most sensitive in radial direction and have a precision of some millimeters up to few centimeters (Combrinck 2010), the empirical accelerations in this direction $(R_0, R_\mathrm{C}, R_\mathrm{S})$ are not solved for and are therefore set to zero.
To absorb further mis-modelings, especially in the air drag, the BSW allows to apply additional pseudo-stochastic pulses (Beutler et al. 2005a), which are instantaneous velocity changes in radial, along-track or cross-track (given in the co-rotating orbital frame) at specific times (Beutler et al. 1994).

3.3 Parameter Estimation Based on Least-Squares Adjustment

To improve some of the model parameters mentioned in the previous section, a least-squares adjustment based on a set of observations is performed. However, first a functional model has to be defined, which describes the relation between the model parameters and the observations. Occasionally, some of the model parameters should be constrained, pre-eliminated or stacked. This section is mainly based on Dach et al. (2015) and Koch (2007).

3.3.1 Functional and Statistical Model

A functional model $\boldsymbol{\mathcal{F}}$ describes a relation between n observations $\mathbf{l'}$ ($n \times 1$-vector) and u unknown parameters $\mathbf{x}$ ($u \times 1$-vector)

$$\mathbf{l'} = \boldsymbol{\mathcal{F}}(\mathbf{x}). \tag{3.16}$$

If the number of observations n is larger than the number of parameters u, this relation cannot be strictly fulfilled in the presence of observation noise until a residual vector $\mathbf{v}$ ($n \times 1$ -vector) is added. Hence, the observation equation is

$$\mathbf{l'} + \mathbf{v} = \boldsymbol{\mathcal{F}}(\hat{\mathbf{x}}), \tag{3.17}$$

where $\hat{\mathbf{x}}$ ($u \times 1$ -vector) contains the estimated parameters.
The functional model is often not linear and therefore the observation equation has to be linearized by a first-order Taylor series expansion around a priori parameters $\mathbf{x}_0$ ($u \times 1$ -vector)

$$\mathbf{l'} + \mathbf{v} = \boldsymbol{\mathcal{F}}(\mathbf{x}_0) + \mathbf{A} \cdot \Delta\hat{\mathbf{x}} \tag{3.18}$$

with the first-design matrix

$$\mathbf{A} = \begin{pmatrix} \frac{\partial F_1}{\partial x_1} & \cdots & \frac{\partial F_1}{\partial x_u} \\ \vdots & & \vdots \\ \frac{\partial F_n}{\partial x_1} & \cdots & \frac{\partial F_n}{\partial x_u} \end{pmatrix}_{(\mathbf{x}=\mathbf{x}_0)}$$

and the estimated parameter correction $\Delta\hat{\mathbf{x}}$, such that the improved parameters can be eventually expressed as $\hat{\mathbf{x}} = \mathbf{x}_0 + \Delta\hat{\mathbf{x}}$.
Rearranging the observation equation leads to the error equation

$$\mathbf{v} = \mathbf{A} \cdot \Delta\hat{\mathbf{x}} - (\mathbf{l'} - \boldsymbol{\mathcal{F}}(\mathbf{x}_0)) = \mathbf{A} \cdot \Delta\hat{\mathbf{x}} - \mathbf{l}, \tag{3.19}$$

where $\mathbf{l}$ corresponds to the "observed minus computed" (O-C)-term.
The statistical model describes the statistical behaviour of the observations, i.e., it reflects the precision of each observation as well as the correlation between different observations, and is given by the covariance matrix $\mathbf{K}_{ll}$, which allows to compute the weight matrix $\mathbf{P}_{ll}$ according to

$$\mathbf{P}_{ll} = \sigma_0^2 \mathbf{K}_{ll}^{-1}, \tag{3.20}$$

where σ_0 is the a priori variance of the unit weight. If the observations are uncorrelated, the weight matrix is reduced to a diagonal matrix with the diagonal elements $\mathbf{P}_{\mathrm{ll}_{[i,i]}} = \frac{\sigma_0^2}{\sigma_i^2}$, where σ_i^2 is the variance of the i-th observation.

3.3.2 Least-Squares Adjustment

If $n > u$ Eq. 3.19 represent an over determined system. To get one plausible solution out of the infinite number of solutions, the method of least-squares adjustment is used. It requests to minimize the square sum of the weighted residuals, i.e., min. $= \mathbf{v}^T\mathbf{P}_{\mathrm{ll}}\mathbf{v}$. It leads to the Normal Equation (NEQ) system

$$\mathbf{N}\Delta\hat{\mathbf{x}} = \mathbf{b} \tag{3.21}$$

with $\mathbf{N} = \mathbf{A}^T\mathbf{P}_{\mathrm{ll}}\mathbf{A}$ and $\mathbf{b} = \mathbf{A}^T\mathbf{P}_{\mathrm{ll}}\mathbf{l}$. The improvements of the estimated parameters are

$$\Delta\hat{\mathbf{x}} = (\mathbf{A}^T\mathbf{P}_{\mathrm{ll}}\mathbf{A})^{-1}\mathbf{A}^T\mathbf{P}_{\mathrm{ll}}\mathbf{l} = \mathbf{N}^{-1}\mathbf{b} \tag{3.22}$$

and the estimated parameters become $\hat{\hat{\mathbf{x}}} = \mathbf{x}_0 + \Delta\hat{\mathbf{x}}$.
If the degree of freedom $n - u > 0$, the a posteriori variance of the unit weight m_0, i.e., the unbiased estimator of σ_0, is

$$m_0^2 = \frac{\mathbf{v}^T\mathbf{P}_{\mathrm{ll}}\mathbf{v}}{n-u}. \tag{3.23}$$

With a Gaussian error propagation, the covariance matrix of the estimated parameters can be written as

$$\mathbf{K}_{\mathrm{xx}} = [(\mathbf{A}^T\mathbf{P}_{\mathrm{ll}}\mathbf{A})^{-1}\mathbf{A}^T\mathbf{P}_{\mathrm{ll}}]\mathbf{K}_{\mathrm{ll}}[(\mathbf{A}^T\mathbf{P}_{\mathrm{ll}}\mathbf{A})^{-1}\mathbf{A}^T\mathbf{P}_{\mathrm{ll}}]^T = m_0^2(\mathbf{A}^T\mathbf{P}_{\mathrm{ll}}\mathbf{A})^{-1} = m_0^2\mathbf{N}^{-1}, \tag{3.24}$$

where the diagonal element $K_{\mathrm{xx}_{[i,i]}} = \sigma_i^2$ represents the variance of the parameter no. i and the off-diagonal element $K_{\mathrm{xx}_{[i,j]}} = \sigma_{ij}$ represents the covariance between the parameters i and j.
Furthermore, the correlation between two estimated parameter i and j is

$$\rho_{ij} = \frac{\sigma_{ij}}{\sigma_i\sigma_j}. \tag{3.25}$$

3.3.3 Constraining Parameters

Sometimes observations are not sensitive to all of the parameters of the functional model or the parameters are co-linear, such that the NEQ systems become singular. Therefore, additional information about the parameters has to be introduced in the NEQ systems by so called pseudo-observations. This approach is described in detail in Brockmann (1997) and for the sake of completeness, it is briefly summarized here.

The error equation of additional pseudo-observations $\mathbf{c}$ is

$$\mathbf{v}_c = \mathbf{C}\cdot\Delta\hat{\mathbf{x}} - \mathbf{c}, \tag{3.26}$$

where

$\mathbf{v}_c$: residual vector ($r \times 1$-vector),
$\mathbf{C}$: ($r \times u$-matrix),
$\mathbf{c}$: vector with known constants, i.e., pseudo-observations ($r \times 1$-vector).

Hence, the error equations, Eq. 3.19 and 3.26, can be assembled to

$$\begin{pmatrix} \mathbf{v} \\ \mathbf{v}_c \end{pmatrix} = \begin{pmatrix} \mathbf{A} \\ \mathbf{C} \end{pmatrix} \Delta\hat{\mathbf{x}} - \begin{pmatrix} \mathbf{l} \\ \mathbf{c} \end{pmatrix} \tag{3.27}$$

and the corresponding NEQ system is

$$\begin{aligned} (\mathbf{A}^T\mathbf{P}_{ll}\mathbf{A} + \mathbf{C}^T\mathbf{P}_{cc}\mathbf{C})\Delta\hat{\mathbf{x}} &= \mathbf{A}^T\mathbf{P}_{ll}\mathbf{l} + \mathbf{C}^T\mathbf{P}_{cc}\mathbf{c} \\ (\mathbf{N}_{ll} + \mathbf{N}_{cc})\Delta\hat{\mathbf{x}} &= \mathbf{b}_l + \mathbf{b}_c \end{aligned} \tag{3.28}$$

with the weight matrix of the pseudo-observations

$$\mathbf{P}_{cc} = \sigma_0^2\mathbf{K}_{cc}^{-1}. \tag{3.29}$$

These weights, which are also called constraints, determine how good the pseudo- observations have to be fulfilled.

a) Absolute Constraints

If a parameter $\mathbf{x}_i$ is constrained to its a priori value or to any value, e.g., to zero, it is called an absolute constraint.
For the constraining of $\mathbf{x}_i$ to the a priori value $\mathbf{x}_{0_i}$ with an a priori standard deviation σ_{abs}, the following pseudo-observations are used

$$\begin{aligned} \mathbf{C} \text{ with } C_{[i,j]} &= \begin{cases} 1, & \text{if } j = i \\ 0, & \text{otherwise} \end{cases} \\ \mathbf{c} &= \mathbf{0} \\ \mathbf{P}_{cc} \text{ with } P_{cc_{[n,m]}} &= \begin{cases} \frac{\sigma_0^2}{\sigma_{abs}^2}, & \text{if } n = m = i \\ 0, & \text{otherwise} \end{cases} \end{aligned} \tag{3.30}$$

and the NEQ system is

$$(\mathbf{A}^T\mathbf{P}_{ll}\mathbf{A} + \mathbf{C}^T\mathbf{P}_{cc}\mathbf{C})\Delta\hat{\mathbf{x}} = \mathbf{A}^T\mathbf{P}_{ll}\mathbf{l} \tag{3.31}$$

with

$$(\mathbf{A}^T\mathbf{P}_{ll}\mathbf{A} + \mathbf{C}^T\mathbf{P}_{cc}\mathbf{C})_{[n,m]} = \begin{cases} (\mathbf{A}^T\mathbf{P}_{ll}\mathbf{A})_{[i,i]} + \frac{\sigma_0^2}{\sigma_{abs}^2}, & \text{if } n = m = i \\ (\mathbf{A}^T\mathbf{P}_{ll}\mathbf{A})_{[n,m]}, & \text{otherwise.} \end{cases} \tag{3.32}$$

Similarly, the parameter $\mathbf{x}_i$ can be constrained to zero using the Eq. 3.32, in which case only the vector with the constants has to be adapted

$$\mathbf{c} \text{ with } c_j = \begin{cases} -x_{0_i}, & \text{if } j = i \\ 0, & \text{otherwise.} \end{cases} \tag{3.33}$$

In this work, the parameter estimation was performed with applying constraints on

- pseudo-stochastic pulses in along- and cross-track with $\sigma_{\text{abs}} = 10^{-7}$m/s and 10^{-3}m/s, respectively,
- geocenter coordinates with $\sigma_{\text{abs}} = 1$ m,
- range biases with $\sigma_{\text{abs}} = 1$ m,
- X- and Y-pole with $\sigma_{\text{abs}} = 30$ mas,
- LOD with $\sigma_{\text{abs}} = 2$ ms/day.

b) Minimum Constraint Conditions

The Helmert transformation consists of translations (ΔX,ΔY,ΔZ), small rotations (with rotation angles: α, β, γ) and a scaling factor μ (Helmert 1893).

The Helmert transformation of the a priori station coordinates $X_{0,i}$, $Y_{0,i}$ and $Z_{0,i}$ is

$$\underbrace{\begin{pmatrix} \bar{X}_i \\ \bar{Y}_i \\ \bar{Z}_i \end{pmatrix}}_{=:\bar{\mathbf{X}}_i} = \underbrace{\begin{pmatrix} X_{0,i} \\ Y_{0,i} \\ Z_{0,i} \end{pmatrix}}_{=:\mathbf{X}_{0_i}} + \underbrace{\begin{pmatrix} 1 & 0 & 0 & 0 & -Z_i & Y_i & X_i \\ 0 & 1 & 0 & Z_i & 0 & -X_i & Y_i \\ 0 & 0 & 1 & -Y_i & X_i & 0 & Z_i \end{pmatrix}}_{=:\mathbf{C}_i} \underbrace{\begin{pmatrix} \Delta X \\ \Delta Y \\ \Delta Z \\ \alpha \\ \beta \\ \gamma \\ \mu \end{pmatrix}}_{=:\mathbf{p}} \tag{3.34}$$

and in the matrix notation and for all stations simultaneously

$$\bar{\mathbf{X}} = \mathbf{X}_0 + \mathbf{C}\mathbf{p}. \tag{3.35}$$

Then the error equation is

$$\mathbf{v}_c = \mathbf{C}\mathbf{p} - \underbrace{(\bar{\mathbf{X}} - \mathbf{X}_0)}_{=:\mathbf{c}} \tag{3.36}$$

and with the least-squares adjustment the estimation of the Helmert parameters is

$$\hat{\mathbf{p}} = \left(\mathbf{C}^T\mathbf{C}\right)^{-1}\mathbf{C}^T\mathbf{c}. \tag{3.37}$$

Since the improvement of the Helmert transformations is constrained to zero

$$\hat{\mathbf{p}} = \mathbf{0} \tag{3.38}$$

the NEQ system is

$$(\mathbf{A}^T\mathbf{P}_{\mathrm{ll}}\mathbf{A} + \mathbf{C}^T\mathbf{C})\hat{\mathbf{x}} = \mathbf{A}^T\mathbf{P}_{\mathrm{ll}}\mathbf{l}. \tag{3.39}$$

3.3.4 Pre-Elimination of Parameters

The dimension of the NEQ systems can be reduced by pre-eliminating parameters without losing any information (Dach et al. 2015). The unknown parameters $\mathbf{x}$ can be subdivided into two vectors $\mathbf{x}_1$ ($u_1 \times 1$ -vector) and $\mathbf{x}_2$ ($u_2 \times 1$ -vector)

$$\mathbf{x} = \begin{pmatrix}\mathbf{x}_1\\ \mathbf{x}_2\end{pmatrix}, \tag{3.40}$$

where $u_1 + u_2 = u$. Assume that the u_2 parameters in $\mathbf{x}_2$ are to be pre-eliminated. The NEQs can be written as

$$\begin{pmatrix}\mathbf{N}_{11} & \mathbf{N}_{21}^T\\ \mathbf{N}_{21} & \mathbf{N}_{22}\end{pmatrix}\begin{pmatrix}\mathbf{x}_1\\ \mathbf{x}_2\end{pmatrix} = \begin{pmatrix}\mathbf{b}_1\\ \mathbf{b}_2\end{pmatrix} \tag{3.41}$$

and rearranged such that the NEQ is only explicitly depending on the parameters $\mathbf{x}_1$

$$(\mathbf{N}_{11} - \mathbf{N}_{21}^T\mathbf{N}_{22}^{-1}\mathbf{N}_{21})\mathbf{x}_1 = \mathbf{b}_1 - \mathbf{N}_{21}^T\mathbf{N}_{22}^{-1}\mathbf{b}_2. \tag{3.42}$$

Nevertheless, the effect of the pre-eliminated parameters on other parameters is still taken correctly into account.

3.3.5 Stacking of Parameters

Assume that there are two observation equation systems, which are independent of each other

$$\mathbf{l}_1 + \mathbf{v}_1 = \mathbf{A}_1\mathbf{x}_1, \tag{3.43}$$
$$\mathbf{l}_2 + \mathbf{v}_2 = \mathbf{A}_2\mathbf{x}_2. \tag{3.44}$$

The parameters in $\mathbf{x}_1$ and $\mathbf{x}_2$ can be divided into parameters which are common ($\mathbf{x}_{\mathrm{co}} = \mathbf{x}_{\mathrm{co}}^{\mathbf{l}_1} = \mathbf{x}_{\mathrm{co}}^{\mathbf{l}_2}$) and parameters which are specific to the observation $\mathbf{l}_1$ and $\mathbf{l}_2$

$$\mathbf{x}_1 = \begin{pmatrix}\mathbf{x}_1^{\mathbf{l}_1}\\ \mathbf{x}_{\mathrm{co}}^{\mathbf{l}_1}\end{pmatrix} \quad \text{with} \quad \begin{pmatrix}\mathbf{N}_{11}^{\mathbf{l}_1} & \mathbf{N}_{1\mathrm{co}}^{\mathbf{l}_1}\\ \left(\mathbf{N}_{1\mathrm{co}}^{\mathbf{l}_1}\right)^T & \mathbf{N}_{\mathrm{coco}}^{\mathbf{l}_1}\end{pmatrix}\begin{pmatrix}\mathbf{x}_1^{\mathbf{l}_1}\\ \mathbf{x}_{\mathrm{co}}^{\mathbf{l}_1}\end{pmatrix} = \begin{pmatrix}\mathbf{b}_1^{\mathbf{l}_1}\\ \mathbf{b}_{\mathrm{co}}^{\mathbf{l}_1}\end{pmatrix} \tag{3.45}$$

and

$$\mathbf{x}_2 = \begin{pmatrix}\mathbf{x}_2^{\mathbf{l}_2}\\ \mathbf{x}_{\mathrm{co}}^{\mathbf{l}_2}\end{pmatrix} \quad \text{with} \quad \begin{pmatrix}\mathbf{N}_{22}^{\mathbf{l}_2} & \mathbf{N}_{2\mathrm{co}}^{\mathbf{l}_2}\\ \left(\mathbf{N}_{2\mathrm{co}}^{\mathbf{l}_2}\right)^T & \mathbf{N}_{\mathrm{coco}}^{\mathbf{l}_2}\end{pmatrix}\begin{pmatrix}\mathbf{x}_2^{\mathbf{l}_2}\\ \mathbf{x}_{\mathrm{co}}^{\mathbf{l}_2}\end{pmatrix} = \begin{pmatrix}\mathbf{b}_2^{\mathbf{l}_2}\\ \mathbf{b}_{\mathrm{co}}^{\mathbf{l}_2}\end{pmatrix}. \tag{3.46}$$

The superposition of these two NEQs is then

$$\begin{pmatrix} \mathbf{N}_{11}^{l_1} & \mathbf{N}_{1\text{co}}^{l_1} & \mathbf{0} \\ \left(\mathbf{N}_{1\text{co}}^{l_1}\right)^T & \mathbf{N}_{\text{coco}}^{l_1} + \mathbf{N}_{\text{coco}}^{l_2} & \left(\mathbf{N}_{2\text{co}}^{l_2}\right)^T \\ \mathbf{0} & \mathbf{N}_{2\text{co}}^{l_2} & \mathbf{N}_{22}^{l_2} \end{pmatrix} \begin{pmatrix} \mathbf{x}_1^{l_1} \\ \mathbf{x}_{\text{co}} \\ \mathbf{x}_2^{l_2} \end{pmatrix} = \begin{pmatrix} \mathbf{b}_1^{l_1} \\ \mathbf{b}_{\text{co}}^{l_1} + \mathbf{b}_{\text{co}}^{l_2} \\ \mathbf{b}_2^{l_2} \end{pmatrix}. \tag{3.47}$$

3.4 Variance Component Estimation

The parameter estimation is often based on sets of observations provided by different geodetic techniques or to different satellites. They can differ in their size, i.e., number of observations, their sensitivity to a parameter or their stochastic behavior. Therefore, a combination of observation sets allows that a weakness of one observation type may be partially compensated by the strength of another.

In the case of VCE, the individual NEQ systems of each observation set are combined with the incorporation of their stochastic models. In the following, the approach of non-negative block-wise VCE (Förstner 1979) is briefly explained, mainly based on Böckmann et al. (2010).

Consider n individual NEQ systems (see Eq. 3.21)

$$\mathbf{N}_i \Delta\hat{\mathbf{x}}_i = \mathbf{b}_i \qquad i \in \{1, ..., n\} \tag{3.48}$$

which stem from independent sets of observations (with n_i the number of observations). The n individual NEQs can be iteratively combined into one, where all common parameters are stacked (see Sec. 3.3.5)

$$\mathbf{N}_{\text{co}}^{(j)} \Delta\hat{\mathbf{x}}_{\text{co}}^{(j)} = \mathbf{b}_{\text{co}}^{(j)} \tag{3.49}$$

with

$$\mathbf{N}_{\text{co}}^{(j)} = \sum_{i=1}^{n} \frac{\sigma_0^2}{\hat{\sigma}_i^{2(j)}} \mathbf{N}_i \qquad \text{and} \qquad \mathbf{b}_{\text{co}}^{(j)} = \sum_{i=1}^{n} \frac{\sigma_0^2}{\hat{\sigma}_i^{2(j)}} \mathbf{b}_i, \tag{3.50}$$

where j denotes the iteration step. The ratio of $\frac{\sigma_0^2}{\hat{\sigma}_i^{2(j)}}$ defines an appropriate weight for each NEQ system i for iteration j.
The initial value $\hat{\sigma}_i^{2(0)}$ may, e.g., correspond to the a priori variances of unit weight σ_0^2. For all further iteration steps, the variance factor $\hat{\sigma}_i^{2(j+1)}$, computed with the VCE method following (Förstner 1979), reads as

$$\hat{\sigma}_i^{2(j+1)} = \frac{\Omega_i^{(j)}}{r_i^{(j)}} \tag{3.51}$$

with the weighted sum of the residuals squared $\Omega_i^{(j)}$ of each individual NEQ based on

the estimated parameter corrections of the combination $\Delta\hat{\mathbf{x}}_{\text{co}}^{(j)}$

$$\Omega_i^{(j)} = \Delta\hat{\mathbf{x}}_{\text{co}}^{(j)^T}\mathbf{N}_i\Delta\hat{\mathbf{x}}_{\text{co}}^{(j)} - 2\Delta\hat{\mathbf{x}}_{\text{co}}^{(j)^T}\mathbf{b}_i + \mathbf{l}_i^T\mathbf{P}_i\mathbf{l}_i \tag{3.52}$$

and the redundancy factor

$$r_i^{(j)} = n_i - \frac{\sigma_0^2}{\hat{\sigma}_i^{2(j)}}\text{tr}(\mathbf{N}_i\mathbf{N}_{\text{co}}^{(j)^{-1}}). \tag{3.53}$$

Eqs. 3.49 - 3.53 are repeated until convergence is reached.

In this work, VCE is used to combine SLR observations to different geodetic satellites provided by different SLR stations. Moreover, to derive optimal weights of pseudo-observations and consequently to determine whether additional pseudo-stochastic pulses in the LAGEOS-1/2 orbit parametrization may improve the solution. These methods of VCE are following the implementations described in Lasser (2022).

3.4.1 Satellite-Specific VCE

The combination of SLR observations to several geodetic satellites may reduce correlations between parameters of interest or enable an enlargement of the parameter space. While SLR observations to high-orbiting satellites, e.g., LAGEOS-1/2, are essential for the datum definition or the determination of the ERPs and the location of the geocenter, the contribution of satellites orbiting the Earth on a lower altitude allows to reliably estimate low-degree SH gravity field coefficients. However, since their stochastic models differ due to satellite properties, e.g., area-to-mass ratio, diameter or the altitude, a VCE method can be applied to determine a proper weighting of the satellite-specific SLR observations.

Taking into account a combination of SLR observations to three different geodetic satellites (S1, S2 and S3) using VCE (Eqs. 3.51-3.53) yields the following normal equation matrix

$$\mathbf{N}_{\text{co}}^{(j)} = \frac{\sigma_0^2}{\hat{\sigma}_{\text{S1}}^{2(j)}}\mathbf{N}_{\text{S1}} + \frac{\sigma_0^2}{\hat{\sigma}_{\text{S2}}^{2(j)}}\mathbf{N}_{\text{S2}} + \frac{\sigma_0^2}{\hat{\sigma}_{\text{S3}}^{2(j)}}\mathbf{N}_{\text{S3}} \tag{3.54}$$

with the three associated individual normal equation systems

$$\mathbf{N}_i\Delta\hat{\mathbf{x}}_i = \mathbf{b}_i \qquad i \in \{\text{S1}, \text{S2}, \text{S3}\}. \tag{3.55}$$

In this work, the iterative determination of the variance factors is initialized with the following values

$$\hat{\sigma}_{\text{S1}}^{2(0)} = \hat{\sigma}_{\text{S2}}^{2(0)} = \hat{\sigma}_{\text{S3}}^{2(0)} = \sigma_0^2 \tag{3.56}$$

and stops after ten iterations. That this number of iterations is sufficient to ensure convergence of the VCE procedure, can be shown based on LAGEOS-1/2 and LARES SLR

combinations, which are discussed in detail in Section 7.1.4. In this case, the improvement of the weights for LAGEOS-1/2 and LARES are smaller than 1×10^{-3}, which does not significantly affect the estimation of the parameters, after the 7-th, resp., 8-th iteration (see Fig. 3.5). Depending on the weekly SLR combination, however, convergence can be achieved more rapidly.

Since besides the VCE also the so-called Helmert's "simple" estimator (Helmert 1907) is used to determine satellite-specific weights, their relation is briefly shown.
Assume that two satellite groups, i.e., S1 and S2, with the following NEQ systems

$$\mathbf{A}_{\mathrm{S1}}^T \mathbf{P}_{\mathrm{S1}} \mathbf{A}_{\mathrm{S1}} \Delta\hat{\mathbf{x}} = \mathbf{A}_{\mathrm{S1}}^T \mathbf{P}_{\mathrm{S1}} \mathbf{l}_{\mathrm{S1}} \quad \text{and} \quad \mathbf{A}_{\mathrm{S2}}^T \mathbf{P}_{\mathrm{S2}} \mathbf{A}_{\mathrm{S2}} \Delta\hat{\mathbf{x}} = \mathbf{A}_{\mathrm{S2}}^T \mathbf{P}_{\mathrm{S2}} \mathbf{l}_{\mathrm{S2}} \tag{3.57}$$

shall be combined on NEQ-level to a multi-satellite SLR solution by the means of VCE

$$\mathbf{N}_{co} \Delta\hat{\mathbf{x}}_{co} = \mathbf{b}_{co}, \tag{3.58}$$

with the variance factors

$$\begin{aligned} \hat{\sigma}_{\mathrm{S1}}^2 &= \frac{\mathbf{l}_{\mathrm{S1}}^T \mathbf{P}_{\mathrm{S1}} \mathbf{l}_{\mathrm{S1}} + \Delta\hat{\mathbf{x}}_{co}^T \mathbf{A}_{\mathrm{S1}}^T \mathbf{P}_{\mathrm{S1}} (\mathbf{A}_{\mathrm{S1}} \Delta\hat{\mathbf{x}}_{co} - 2\mathbf{l}_{\mathrm{S1}})}{n_{\mathrm{S1}} - \frac{\sigma_0^2}{\sigma_{\mathrm{S1},0}^2} tr(\mathbf{N}_{\mathrm{S1}} \mathbf{N}_{co}^{-1})}, \\ \hat{\sigma}_{\mathrm{S2}}^2 &= \frac{\mathbf{l}_{\mathrm{S2}}^T \mathbf{P}_{\mathrm{S2}} \mathbf{l}_{\mathrm{S2}} + \Delta\hat{\mathbf{x}}_{co}^T \mathbf{A}_{\mathrm{S2}}^T \mathbf{P}_{\mathrm{S2}} (\mathbf{A}_{\mathrm{S2}} \Delta\hat{\mathbf{x}}_{co} - 2\mathbf{l}_{\mathrm{S2}})}{n_{\mathrm{S2}} - \frac{\sigma_0^2}{\sigma_{\mathrm{S2},0}^2} tr(\mathbf{N}_{\mathrm{S2}} \mathbf{N}_{co}^{-1})}. \end{aligned} \tag{3.59}$$

Then, the weighting ratio $\rho_{\mathrm{S1,S2}}^{VCE}$ w.r.t. S1 resulting from the VCE reads as

$$\rho_{\mathrm{S1,S2}}^{VCE} = \frac{\hat{\sigma}_{\mathrm{S1}}^2}{\hat{\sigma}_{\mathrm{S2}}^2}. \tag{3.60}$$

Both variance factors depend on the same solution vector ($\Delta\hat{\mathbf{x}}_{co}$) and the redundancy factors (see Eq. 3.53) account for the correlations between the common parameters in $\Delta\hat{\mathbf{x}}_{\mathrm{S1}}$ and $\Delta\hat{\mathbf{x}}_{\mathrm{S2}}$. If the two satellite groups do not feature any common parameters and

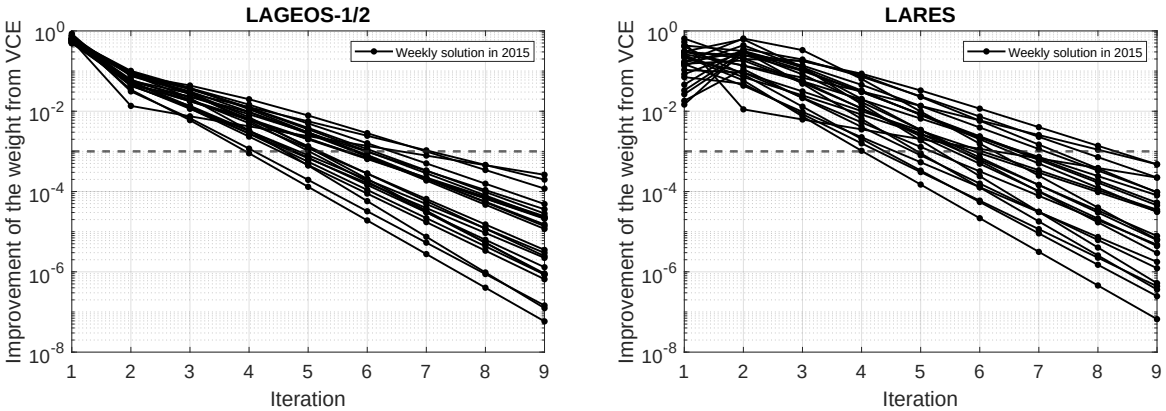

Figure 3.5: Improvement of the estimated weights per iteration step from VCE for LAGEOS-1/2 (left) and LARES (right) resulting from weekly LAGEOS-1/2 and LARES SLR combinations for the year 2015.

$\sigma^2_{S1,0} = \sigma^2_{S2,0} = \sigma^2_0$, the variance factors are identical to the a posteriori variance of unit weight m_0 (see Eq. 3.23) of each single-satellite solution

$$\begin{aligned} m^2_{0,S1} &= \frac{\mathbf{l}^T_{S1}\mathbf{P}_{S1}\mathbf{l}_{S1} + \Delta\hat{\mathbf{x}}^T_{S1}\mathbf{A}^T_{S1}\mathbf{P}_{S1}(\mathbf{A}_{S1}\Delta\hat{\mathbf{x}}_{S1} - 2\mathbf{l}_{S1})}{n_{S1} - u_{S1}} = \frac{\mathbf{l}^T_{S1}\mathbf{P}_{S1}\mathbf{l}_{S1} - \Delta\hat{\mathbf{x}}^T_{S1}\mathbf{A}^T_{S1}\mathbf{P}_{S1}\mathbf{l}_{S1}}{n_{S1} - u_{S1}} \\ m^2_{0,S2} &= \frac{\mathbf{l}^T_{S2}\mathbf{P}_{S2}\mathbf{l}_{S2} + \Delta\hat{\mathbf{x}}^T_{S2}\mathbf{A}^T_{S2}\mathbf{P}_{S2}(\mathbf{A}_{S2}\Delta\hat{\mathbf{x}}_{S2} - 2\mathbf{l}_{S2})}{n_{S2} - u_{S2}} = \frac{\mathbf{l}^T_{S2}\mathbf{P}_{S2}\mathbf{l}_{S2} - \Delta\hat{\mathbf{x}}^T_{S2}\mathbf{A}^T_{S2}\mathbf{P}_{S2}\mathbf{l}_{S2}}{n_{S2} - u_{S2}}. \end{aligned} \tag{3.61}$$

On the contrary, Helmert's simple estimator makes use of the squared RMS of observation residuals from the single-satellite SLR solutions (Bähr et al. 2007)

$$\widehat{RMS}^2_{S1} = \frac{\mathbf{l}^T_{S1}\mathbf{P}_{S1}\mathbf{l}_{S1} - \Delta\hat{\mathbf{x}}^T_{S1}\mathbf{A}^T_{S1}\mathbf{P}_{S1}\mathbf{l}_{S1}}{n_{S1}} \quad \text{and} \quad \widehat{RMS}^2_{S2} = \frac{\mathbf{l}^T_{S2}\mathbf{P}_{S2}\mathbf{l}_{S2} - \Delta\hat{\mathbf{x}}^T_{S2}\mathbf{A}^T_{S2}\mathbf{P}_{S2}\mathbf{l}_{S2}}{n_{S2}}, \tag{3.62}$$

with the weighting ratio w.r.t. S1

$$\rho^{RMS}_{S1,S2} = \frac{\widehat{RMS}^2_{S1}}{\widehat{RMS}^2_{S2}}. \tag{3.63}$$

Note that for $n >> u$, the weighting ratios from VCE and from Helmert's simple estimator coincide if the two satellite groups do not have any common parameters.
Furthermore, the RMS of observation residuals depend on different solution vectors ($\Delta\hat{\mathbf{x}}_{S1}$ and $\Delta\hat{\mathbf{x}}_{S2}$). Moreover, $\widehat{RMS}^2_A$ is a special case of $m^2_{0,S1}$, where the outliers are rejected and the influence of the parameters is not taken into account ($u_{S1} = 0$). This also applies for the satellite group $S2$.
As a result, the VCE with only one solution vector ($\Delta\hat{\mathbf{x}}_{co}$) holds a higher consistency of the weights than the RMS-based approach, where the weights are determined with two different solution vectors ($\Delta\hat{\mathbf{x}}_{S1}$ and $\Delta\hat{\mathbf{x}}_{S2}$). Additionally, Welsch (1978) found that the Helmert's simple estimator is biased and therefore should only be used to get a rough idea of the weighting scheme.

3.4.2 Station-Specific VCE

Since the quality of the SLR observations does not only depend on the satellite but also strongly on the SLR station equipment, e.g., laser system or repetition rate, VCE can be used to perform a station-specific weighting. The underlying assumption is that SLR stations are treated as independent.
For this purpose, NEQs are set up per each station ST_i (for $i \in \{1, ..., n\}$)

$$\mathbf{N}_{ST_i}\Delta\hat{\mathbf{x}}_{ST_i} = \mathbf{b}_{ST_i} \qquad i \in \{1, ..., n\} \tag{3.64}$$

and the combined normal equation matrix based on n stations at the iteration step j follows with

$$\mathbf{N}^{(j)}_{co} = \sum_{i=1}^{n} \frac{\sigma^2_0}{\hat{\sigma}^{2(j)}_{ST_i}}\mathbf{N}_{ST_i}, \tag{3.65}$$

where the initial values $\hat{\sigma}^{2(0)}_{\mathrm{ST}_i}$ are set to σ_0^2 in analogy to Eq. 3.56 and VCE is performed according to Eqs. 3.51 - 3.53.

3.4.3 VCE for the Estimation of Stochastic Model for Stochastic Parameters

The extension of the parameter space by stochastic pulses enables to partially absorb orbit mis-modelings (see Sec. 3.2.2) but may simultaneously exhibit the drawback of intercepting real signal. Therefore, the stochastic pulses have to be constrained reasonably, i.e., the task is to find a proper a priori stochastic model, which can be accomplished with VCE. This approach is thoroughly described in Lasser (2022) and here, for the sake of completeness, only briefly introduced.

The parameter constraints, e.g., of stochastic pulses in R, S and W, can be introduced by additional normal equation systems $\mathbf{N}_{\mathrm{st.pl}}$ (see Eq. 3.28) and the extended (now constrained) NEQ becomes

$$(\mathbf{N} + \mathbf{N}_{\mathrm{st.pl},R} + \mathbf{N}_{\mathrm{st.pl},S} + \mathbf{N}_{\mathrm{st.pl},W})\Delta\hat{\mathbf{x}} = \mathbf{b}. \tag{3.66}$$

Consequently, the interpretation of $\mathbf{N}_{\mathrm{st.pl},i}$ (for $i \in \{R, S, W\}$) as additional individual sets of observations allows to apply VCE. The normal equation matrix then reads as

$$\mathbf{N}^{(j)}_{\mathrm{co}} = \mathbf{N} + \frac{\sigma_0^2}{\hat{\sigma}_R^{2(j)}}\mathbf{N}_{\mathrm{st.pl},R} + \frac{\sigma_0^2}{\hat{\sigma}_S^{2(j)}}\mathbf{N}_{\mathrm{st.pl},S} + \frac{\sigma_0^2}{\hat{\sigma}_W^{2(j)}}\mathbf{N}_{\mathrm{st.pl},W} \tag{3.67}$$

with the unknown variance factors $\hat{\sigma}_R^{2(j)}, \hat{\sigma}_S^{2(j)}$ and $\hat{\sigma}_W^{2(j)}$.
A large variance factor $\hat{\sigma}_i^2$ (for $i \in \{R, S, W\}$) indicates a small weight for the NEQ $\mathbf{N}_{\mathrm{st.pl},i}$, such that the a priori constraints are strongly reduced and the corresponding parameters, i.e., pseudo-stochastic pulses in i, can become large.

3.5 Contribution Analysis

Since in combinations of n individual NEQ systems (see Eq. 3.48) common parameters are stacked, their estimation depend on a subset of n NEQ systems. The contribution of each individual NEQ system to the estimation of a parameter can be measured by the Contribution Analysis (CA).

Assuming that n individual NEQ systems are combined as

$$\mathbf{N} = \sum_{i=1}^{n} \mathbf{N}_i = \sum_{i=1}^{n} \mathbf{A}_i^T \mathbf{P}_{\mathrm{ll},i} \mathbf{A}_i \tag{3.68}$$

where NEQ systems can additionally be weighted.
If $\mathbf{N}$ is invertible, the following must be true

$$\mathbf{N}\mathbf{N}^{-1} = \left(\sum_{i=1}^{n} \mathbf{N}_i \right) \mathbf{N}^{-1} = \mathbf{1}. \tag{3.69}$$

The contribution matrices are defined as (Sneeuw 2000)

$$\mathbf{R}_i := \mathbf{N}_i \mathbf{N}^{-1} \quad \text{for } i \in \{1, ..., n\}, \tag{3.70}$$

where the diagonal elements represent the corresponding contribution numbers. Hence, the contribution of the i-th observation set (with the i-th NEQ) to the j-th parameter is

$$R_{i_{[j,j]}} = \frac{1}{\sigma_0^2} \sum_{k=1}^{u} N_{i_{[j,k]}} K_{\mathrm{xx}_{[k,j]}}, \tag{3.71}$$

with the covariance matrix $\mathbf{K}_{\mathrm{xx}}$ (see Eq. 3.24).
If $\mathbf{N}_i$ is a diagonal matrix which is the case for pseudo-observations, i.e., constraints on pseudo-stochastic pulses, the above expression simplifies to

$$R_{i_{[j,j]}} = \frac{\sigma_j^2}{\sigma_{i,j}^2}, \tag{3.72}$$

with the variances σ_j and $\sigma_{i,j}$ related to $\mathbf{N}$ and the individual NEQ system $\mathbf{N}_i$, respectively. It follows that $0 \leq R_{i_{[j,j]}} \leq 1$ for all $i \in \{1, ..., n\}$ and $j \in \{1, ..., u\}$.

Furthermore, the CA can also be performed on combinations of differently weighted NEQ systems.

3.6 Long-Arc Computation

In this section, the formalism of long-arcs based on NEQ systems of short arcs introduced by Beutler et al. (1996) is explained. This computation method is operationally used in the GNSS processing (e.g., Lutz et al. 2016) at the Center for Orbit Determination in Europe (CODE, Dach et al. 2009).

Assume that for each day $i \in \{1, 2, ..., n\}$ the following normal equation system (see Sec. 3.3) can be set up

$$\mathbf{N}_i \Delta\hat{\mathbf{x}}_i = \mathbf{b}_i \tag{3.73}$$

The estimated parameters $\hat{\mathbf{x}}_i$ for day i, are the sum of the a priori values $\mathbf{x}_{0,i}$ and the corrections $\Delta\hat{\mathbf{x}}_i$, may consist of, e.g., osculating orbital elements $E_{k,i}$ (with $k \in \{1, ..., 6\}$) referring to t_i, the beginning of day i, and dynamic parameters $p_{k,i}$ (with $k \in \{1, ..., d\}$) (see Eq. 3.4). The dynamic orbit parameters $q_{k,i}$ (with $k \in \{1, ..., m_q\}$, where $m_q < d$) and the gravity field parameters $g_{k,i}$ (with $k \in \{1, ..., m_g\}$, where $m_g \leq d - m_q$) each are subsets of the dynamic parameters $p_{k,i}$.
The long-arc approach requests continuity and differentiability at the day boundaries (for day i and $i + 1$)

$$\begin{aligned} \mathbf{r}_i(t_{i+1}) &= \mathbf{r}_{i+1}(t_{i+1}), \\ \dot{\mathbf{r}}_i(t_{i+1}) &= \dot{\mathbf{r}}_{i+1}(t_{i+1}), \end{aligned} \tag{3.74}$$

where t_{i+1} represents the end of day i and the beginning of day $i + 1$, respectively.
If only one set of gravity field parameters shall be computed for the entire long-arc, the following equation holds

$$\begin{aligned} g_{k,i} = g_{k,i+1} \qquad & \text{for} \quad k \in \{1, 2, 3, ..., m_g\} \\ & \text{and} \quad i \in \{1, ..., n-1\}. \end{aligned} \tag{3.75}$$

Based on this parametrization, the orbit can be developed into a Taylor series around the a priori orbit $(\mathbf{r}_{0,i}, \dot{\mathbf{r}}_{0,i})$ and linearized by only using a first-order Taylor expansion

$$\begin{aligned} &\mathbf{r}_{0,i} + \sum_{k=1}^{6} \frac{\partial \mathbf{r}_{0,i}}{\partial E_{k,i}} \Delta E_{k,i} + \sum_{k=1}^{m_q} \frac{\partial \mathbf{r}_{0,i}}{\partial q_{k,i}} \Delta q_{k,i} + \sum_{k=1}^{m_g} \frac{\partial \mathbf{r}_{0,i}}{\partial g_{k,i}} \Delta g_{k,i} = \\ &\quad \mathbf{r}_{0,i+1} + \sum_{k=1}^{6} \frac{\partial \mathbf{r}_{0,i+1}}{\partial E_{k,i+1}} \Delta E_{k,i+1} + \sum_{k=1}^{m_q} \frac{\partial \mathbf{r}_{0,i+1}}{\partial q_{k,i+1}} \Delta q_{k,i+1} + \sum_{k=1}^{m_g} \frac{\partial \mathbf{r}_{0,i+1}}{\partial g_{k,i+1}} \Delta g_{k,i+1} \\ &\dot{\mathbf{r}}_{0,i} + \sum_{k=1}^{6} \frac{\partial \dot{\mathbf{r}}_{0,i}}{\partial E_{k,i}} \Delta E_{k,i} + \sum_{k=1}^{m_q} \frac{\partial \dot{\mathbf{r}}_{0,i}}{\partial q_{k,i}} \Delta q_{k,i} + \sum_{k=1}^{m_g} \frac{\partial \dot{\mathbf{r}}_{0,i}}{\partial g_{k,i}} \Delta g_{k,i} = \\ &\quad \dot{\mathbf{r}}_{0,i+1} + \sum_{k=1}^{6} \frac{\partial \dot{\mathbf{r}}_{0,i+1}}{\partial E_{k,i+1}} \Delta E_{k,i+1} + \sum_{k=1}^{m_q} \frac{\partial \dot{\mathbf{r}}_{0,i+1}}{\partial q_{k,i+1}} \Delta q_{k,i+1} + \sum_{k=1}^{m_g} \frac{\partial \dot{\mathbf{r}}_{0,i+1}}{\partial g_{k,i+1}} \Delta g_{k,i+1} \end{aligned} \tag{3.76}$$

and

$$g_{0,k,i} + \Delta g_{k,i} = g_{0,k,i+1} + \Delta g_{k,i+1}, \tag{3.77}$$

where $g_{0,k,i}$ are the a priori gravity field coefficients for day i.
Then, Eqs. 3.76 can be written as

$$\mathbf{x}_{0,i} + \mathbf{H}_i \Delta\mathbf{E}_i + \mathbf{Q}_i \Delta\mathbf{q}_i + \mathbf{G}_i \Delta\mathbf{g}_i = \mathbf{x}_{0,i+1} + \mathbf{H}_{i+1} \Delta\mathbf{E}_{i+1} + \mathbf{Q}_{i+1} \Delta\mathbf{q}_{i+1} + \mathbf{G}_{i+1} \Delta\mathbf{g}_{i+1} \tag{3.78}$$

with

$$\begin{aligned} \mathbf{x}_{0,i} &= \begin{pmatrix} \mathbf{r}_{0,i} \\ \dot{\mathbf{r}}_{0,i} \end{pmatrix}, \\ \mathbf{H}_i &= \begin{pmatrix} \frac{\partial \mathbf{x}_{0,i}}{\partial E_{1,i}} & \cdots & \frac{\partial \mathbf{x}_{0,i}}{\partial E_{6,i}} \end{pmatrix}, \\ \mathbf{Q}_i &= \begin{pmatrix} \frac{\partial \mathbf{x}_{0,i}}{\partial q_{1,i}} & \cdots & \frac{\partial \mathbf{x}_{0,i}}{\partial q_{m_q,i}} \end{pmatrix}, \\ \mathbf{G}_i &= \begin{pmatrix} \frac{\partial \mathbf{x}_{0,i}}{\partial g_{1,i}} & \cdots & \frac{\partial \mathbf{x}_{0,i}}{\partial g_{m_g,i}} \end{pmatrix}. \end{aligned} \tag{3.79}$$

The transformation of the osculating orbital parameters from day $i+1$ to day i is

$$\begin{aligned} \Delta\mathbf{E}_{i+1} =& \mathbf{H}_{i+1}^{-1}(\mathbf{x}_{0,i} - \mathbf{x}_{0,i+1}) + \mathbf{H}_{i+1}^{-1}\mathbf{H}_i \Delta\mathbf{E}_i \\ &+ \mathbf{H}_{i+1}^{-1}(\mathbf{Q}_i \Delta\mathbf{q}_i - \mathbf{Q}_{i+1}\Delta\mathbf{q}_{i+1}) \\ &+ \mathbf{H}_{i+1}^{-1}(\mathbf{G}_i - \mathbf{G}_{i+1})\Delta\mathbf{g}_i + \mathbf{H}_{i+1}^{-1}\mathbf{G}_{i+1}(\mathbf{g}_{0,i+1} - \mathbf{g}_{0,i}) \end{aligned} \tag{3.80}$$

and the recursive transformation is (see Appendix A)

$$\begin{aligned} \Delta\mathbf{E}_{i+1} =& \mathbf{H}_{i+1}^{-1}\mathbf{H}_1 \Delta\mathbf{E}_1 + \mathbf{H}_{i+1}^{-1}(\mathbf{G}_1 - \mathbf{G}_{i+1})\Delta\mathbf{g}_1 + \mathbf{H}_{i+1}^{-1}\left(\mathbf{Q}_1\Delta\mathbf{q}_1 - \mathbf{Q}_{i+1}\Delta\mathbf{q}_{i+1}\right) \\ &+ \mathbf{H}_{i+1}^{-1}\left[\mathbf{x}_{0,1} - \mathbf{x}_{0,i+1} + \mathbf{G}_{i+1}\left(\mathbf{g}_{0,i+1} - \mathbf{g}_{0,1}\right)\right]. \end{aligned} \tag{3.81}$$

In addition, the corresponding recursive transformation of the gravity field parameters is

$$\Delta\mathbf{g}_{i+1} = \Delta\mathbf{g}_1 + (\mathbf{g}_{0,1} - \mathbf{g}_{0,i+1}). \tag{3.82}$$

Hence, with the transformations in Eq. 3.81 and 3.82 the parameters $\Delta\hat{\mathbf{x}}_i$ for days $i \in \{2, 3, ..., n\}$ can be expressed in the form

$$\Delta\hat{\mathbf{x}}_i = \mathbf{B}_i \cdot \Delta\hat{\mathbf{x}}_1 + \mathbf{C}_i. \tag{3.83}$$

Chapter 4

SLR Data Processing and Validation at AIUB

In this work, SLR data (Noll 2010) provided by the ILRS are processed with the BSW. The SLR data analysis in the BSW was developed in collaboration with the BKG (Thaller et al. 2008) and are maintained by the AIUB.

The SLR data processing is separated in two steps. First, the SLR data are screened to eliminate large outliers (see Sec. 4.1). Afterwards, satellite-specific NEQs are set-up on the basis of the remaining SLR data.
Satellite orbits are characterized within the BSW by six initial osculating orbital elements (see Sec. 3.2) referring to the beginning of the arc and up to nine dynamic orbit parameters (Beutler et al. 2005a). A satellite arc over several days is either determined by one set of those orbit parameters (in this work named *true-arc*), or by stacking daily arcs with continuity and differentiability conditions at the day boundaries (called *long-arc*, Beutler et al. 1996). However, the orbit modeling with empirical parameters must be adapted depending on the satellite and the set of parameters. This is detailed in Section 4.2.
The satellite orbits together with station coordinates, range biases for selected stations as recommended by the ILRS, and the global geodetic parameters of interest, i.e., ERPs, geocenter coordinates and SH geopotential coefficients, are estimated in a least-squares adjustment, either using a single NEQ system or by combining several NEQ systems (see Sec. 4.3).
The quality of the different SLR combinations are validated by comparing all estimated parameters with internal and external quality metrics (see Sec. 4.4).

4.1 SLR Data Screening

The outlier detection is performed in the BSW on the level of observation residuals using the following two rejection criteria:

Criterion 1: All observation residuals of a station per satellite are rejected, if the RMS of the residuals w.r.t. the mean offset of the residual time series per satellite exceeds the pre-defined maximum overall value $\sigma_{\max}$.

Criterion 2: An observation residual is rejected if it exceeds the pre-defined absolute maximum $res_{\max}$.

In this work, the SLR data screening is realized in two steps, similar to the operational SLR processing at AIUB and BKG.
The first step (see Fig. 4.1) is a rough screening, where the residual statistics of given SLR data for each satellite group are generated by using a priori satellite orbits (see Sec. 4.2) and applying all background models without estimating any parameters, e.g., ERPs are fixed to IERS-14-C04 reference series and the station coordinates to the positions given by the SLRF2014. Then, the station with the largest RMS of the residual time series per satellite is selected and checked for the rejection criteria with $\sigma_{\max} = 125$ mm for LAGEOS-1/2, 200 mm for LARES/LARES-2/Ajisai and 250 mm for Stella/Starlette/Etalon-1/Etalon-2 and ranging iteratively from $res_{\max} = 10$ m to 1 m. Furthermore, only stations with more than $o_{\min} = 9$ observations per 7-day arc for LAGEOS-1/2 (resp. $o_{\min} = 2$ for

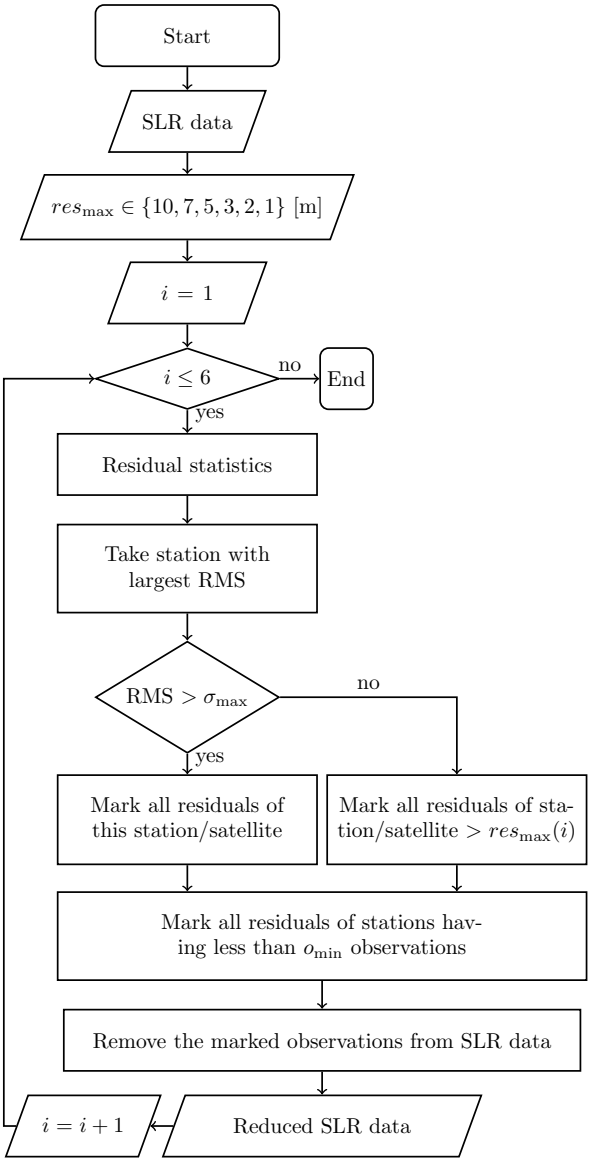

Figure 4.1: Schematic illustration of the first SLR data screening step.

LEOs) are considered.
With the remaining SLR data, the second screening step is performed (see Fig. 4.2). Now, the observation residuals result from a first solution where orbit parameters, i.e., six osculating and five empirical orbit parameters, station coordinates and ERPs are co-estimated in a least-squares adjustment. Then, again the station with the largest RMS of the residual time series per satellite is selected and checked for the rejection criteria

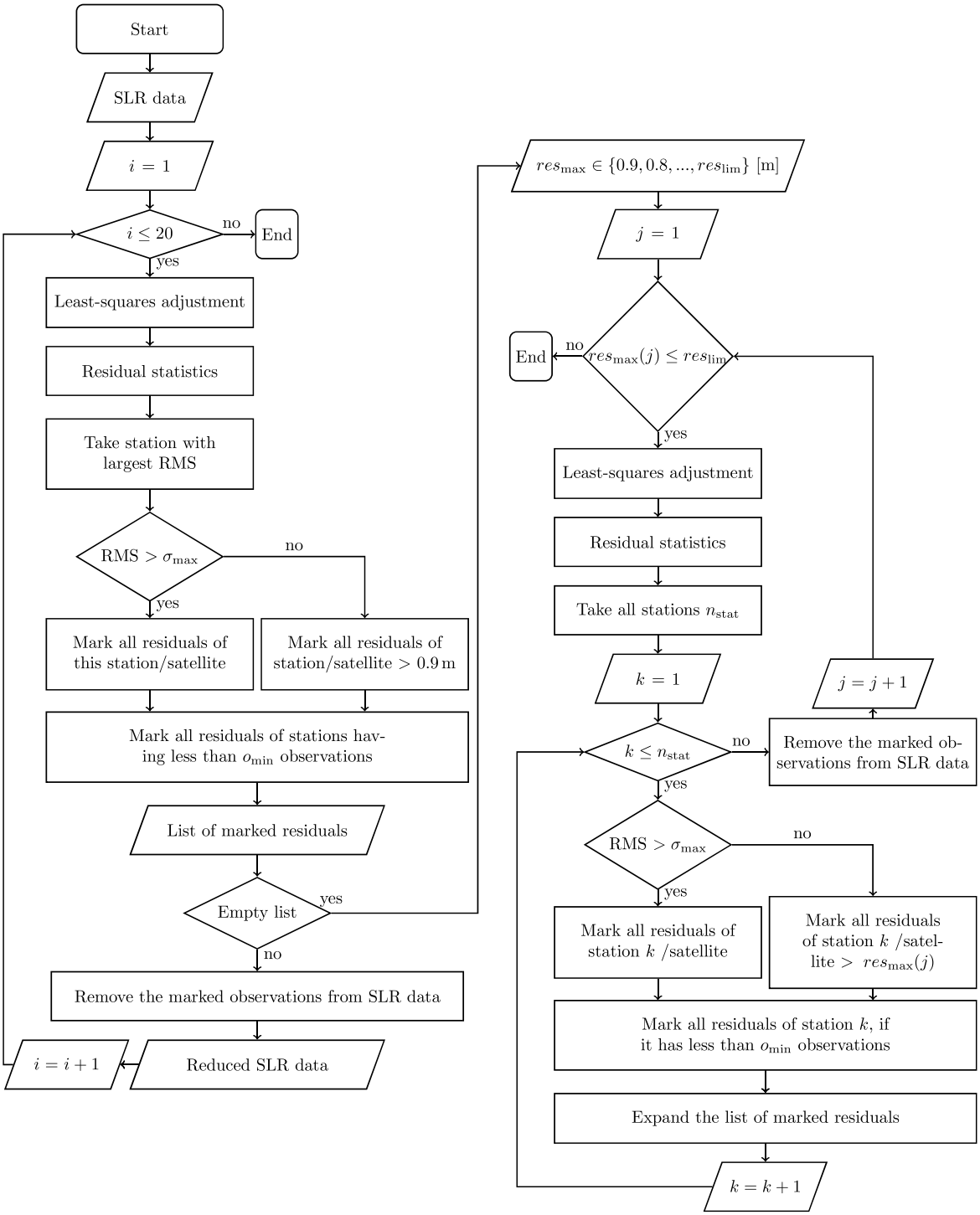

Figure 4.2: Schematic illustration of the second SLR data screening step.

Table 4.1: Maximum overall value $\sigma_{\max}$, absolute maximum $res_{\max}$ and the minimum number of observations $o_{\min}$ used for the data screening of different satellite groups.

Satellite	Screening Step 1			Screening Step 2		
	$\sigma_{\max}$ [mm]	$res_{\max}$ [m]	$o_{\min}$	$\sigma_{\max}$ [mm]	$res_{\lim}$ [m]	$o_{\min}$
LAGEOS-1/2	125	{10, 7, 5, 3, 2, 1}	10	62.5	0.05	10
Etalon-1/2	250	{10, 7, 5, 3, 2, 1}	1	62.5	0.1	1
LARES/LARES-2	200	{10, 7, 5, 3, 2, 1}	1	62.5	0.07	3
Stella/Starlette	250	{10, 7, 5, 3, 2, 1}	5	62.5	0.07	3
Ajisai	200	{10, 7, 5, 3, 2, 1}	1	62.5	0.07	3

with $\sigma_{\max} = 62.5$ mm and $res_{\max} = 0.9$ m. Furthermore, only stations providing $o_{\min} = 9$ of LAGEOS-1/2 (resp. $o_{\min} = 2$ of LEO) observations per arc are further used. This is repeated until no further rejections are requested. Afterwards, if not more than 20 iterations were performed, the editing mode is changed such that the rejection criteria are applied on all observation residuals, where $res_{\max}$ ranging iteratively from 0.9 m to 0.05 m for LAGEOS-1/2 (resp. to 0.07 m for LEOs and to 0.1 m for Etalon-1/2). Table 4.1 summarizes the parameter settings of $\sigma_{\max}$, $res_{\max}$ and $o_{\min}$ for the two screening steps for each satellite group.

Applying the SLR data screening, an average of 2 % of the data are rejected for LAGEOS-1/2 and LARES for the years 2015-2020. For the geodetic SLR satellites with the highest altitudes, i.e., Etalon-1/2, an average of 7 % (resp. 8 % for Etalon-2) of the data are removed. While for the SLR LEOs Starlette, Stella and Ajisai 12 %, 30 %, resp., 40 % of the data are rejected by the screening.
Although the percentage of rejected data varies depending on the satellite, the mean number of used observations per weekly SLR combination for LAGEOS-1/2, Starlette and even Ajisai are comparable with around 1400 observations (see Fig. 4.3). Except for Etalon-1/2 and Stella, the mean numbers of observations are always between 1100-1500. The small observation numbers of Etalon-1/2, i.e., more than ten times lower than, e.g., for LAGEOS-1, can be explained, on one hand, by the small number of SLR stations providing Etalon-1/2 observations. On average only ten different SLR stations deliver data to Etalon-1/2 per week, while in case of LAGEOS-1 or LAGEOS-2 on average more than 20 different SLR stations contribute. On the other hand, Etalon-1/2 have a revolution time of almost twelve hours (see Table 2.2) and are, therefore, at most twice a day in the field of view of a SLR ground station. Instead of observing the same pass over a long time span, the observation priority is given to the low-flying satellites[7].
The mean satellite observation number of Stella with 530 is also significantly lower than for the comparable Starlette satellite with 1480, even though they have almost the same orbit altitude and the same tracking priority. Furthermore, the mean number of SLR stations observing Stella or Starlette differs only by three stations. The visibility of LEOs

[7]https://ilrs.gsfc.nasa.gov/missions/mission_operations/priorities/index.html (Accessed: 23/02/2023)

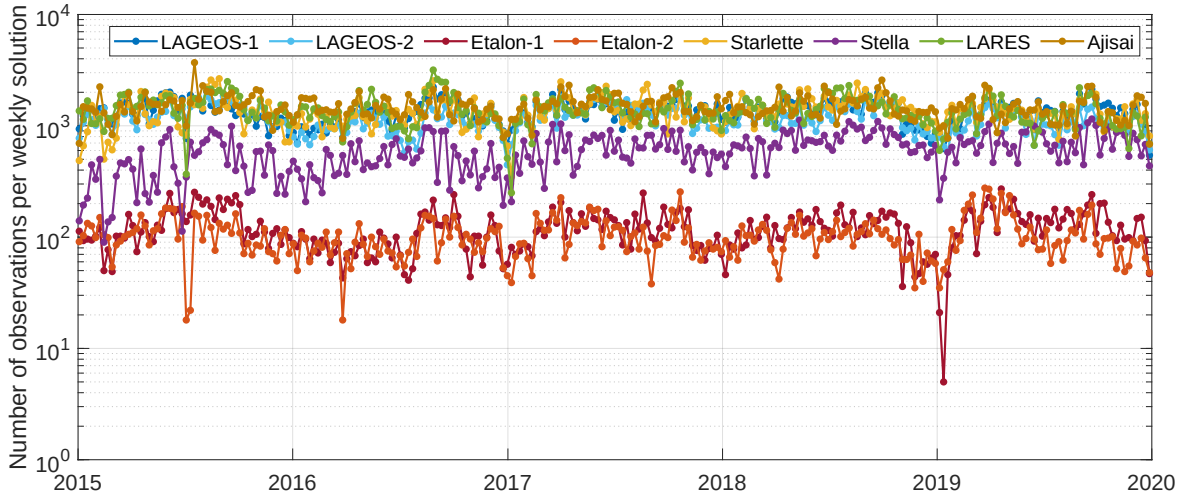

Figure 4.3: Number of SLR observations to eight geodetic satellites used for the weekly SLR processing for the years 2015-2020.

strongly depends on the orbit inclination (Otsubo et al. 2016). Starlette with an inclination of around 50 ° cannot be observed from the polar regions. In contrary to Stella, whose inclination is about 98 ° and is therefore more often observable from the polar regions than from the lower latitudes. Since most of the SLR stations are located in the lower latitudes between 50 °N/S, the small observation number of Stella may be explained with the bad satellite visibility (Otsubo et al. 2016).

Having a closer look on the data contribution of each individual station to SLR solutions during the time period 2015-2020 reveals that the most productive station is Yarragadee (7090) located in Australia (see Fig. 4.4). The 15 most productive stations deliver 80 % of the used data volume, of which the first four stations (Yarragadee, SwissOGS, Mt.

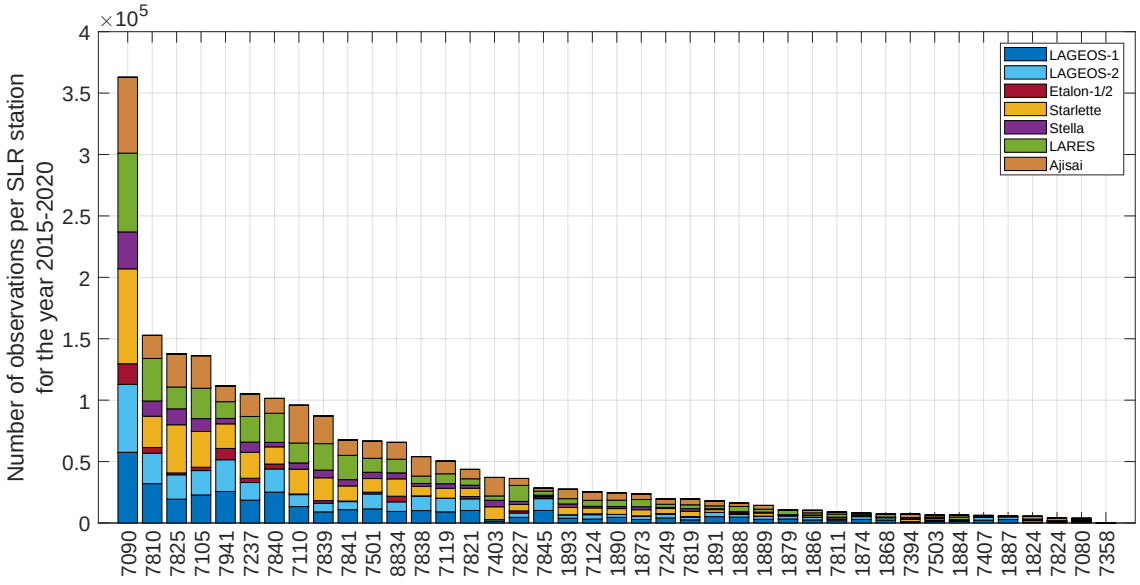

Figure 4.4: SLR data contribution of each individual station to the weekly SLR processing for the years 2015-2020.

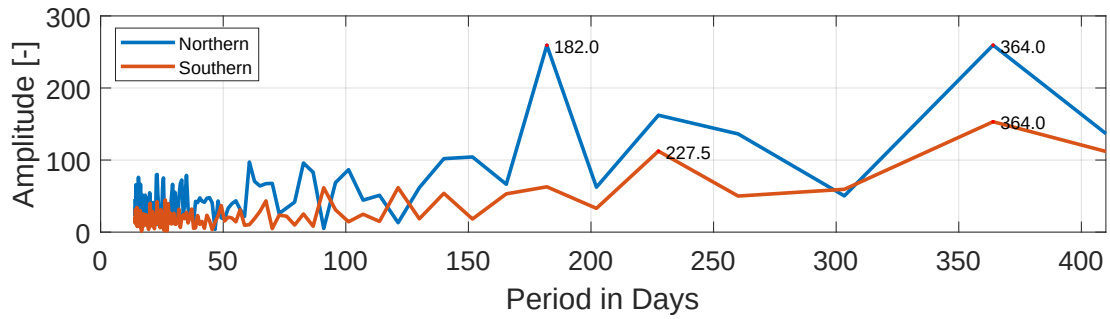

Figure 4.5: Spectral analysis of weekly LAGEOS-1/2 SLR observation numbers taken by stations on the northern, resp., southern hemisphere for the years 2015-2020.

Stromlo, Greenbelt) account for already 40 %.
Furthermore, almost 70 % of the satellite observations are taken by SLR stations located on the northern hemisphere. However, this is to be expected because of the geographical distribution of the SLR stations (see Sec. 2.4). A spectral analysis of the observation numbers to LAGEOS-1/2 by hemisphere (see Fig. 4.5) exhibits that the northern hemisphere shows a strong semi-annual and annual signal. It is reasonable to assume that the stations on the northern hemisphere observe less during their winter and summer months, while the number of observations provided by the southern hemisphere has a higher stability over time.

4.2 Orbit Parametrization and Modeling

In general, 7-day true-arcs are represented by the six initial osculating orbital elements and five dynamical orbit parameters, i.e., a constant acceleration S_0 in along-track (S) and Once-Per-Revolution (OPR) sine and cosine accelerations (S_S resp. S_C) in along-track and in cross-track (W_S resp. W_C). Dynamic orbit parameters in radial direction (R) are not set-up since SLR measurements are most sensitive in R and the information should be preserved to the extend possible. In the BSW, the dynamic orbit parameters are introduced to mainly absorb the mis-modeling of the solar radiation pressure (Dach et al. 2015).
Since LEOs experience a more variable orbit environment, e.g., a higher density of the atmosphere and feature an increased sensitivity to the SH geopotential coefficients, an improved or extended background force modeling and a more sophisticated orbit parametrization are needed than for the higher Earth orbiting satellites, e.g., LAGEOS-1/2 and Etalon-1/2. Therefore, the air drag is additionally modeled with NRLMSISE-00 (Picone et al. 2002) and different a priori gravity field models are validated (see Sec. 7.2.1). Table 4.2 lists all the background models used for the SLR data processing.
The a priori orbits are generated by fitting a set of predicted satellite positions, distributed by the NASA's Archive of Space Geodesy Data (Noll 2010), in an orbit determination process, where the six osculating and five dynamic orbit parameters are estimated.

Table 4.2: A priori background models used for the SLR data processing.

Models	Description	
Reference frame	SLRF2014[8]	
Earth rotation parameters	IERS-14-C04[9]	(Bizouard et al. 2019)
Nutation model	IAU2000	(Mathews et al. 2002)
Subdaily pole model	DESAI	(Desai and Sibois 2016)
Earth's gravity field	GGM05S: d/o 90	(Ries et al. 2016)
Tides	Solid Earth tides	(Petit and Luzum 2010)
	Ocean tides: FES2014b: d/o 30 + admittances	(Lyard et al. 2021)
	Atmospheric tides	(Dobslaw et al. 2017)
Pole tides	Solid Earth pole tides	(Petit and Luzum 2010)
	Ocean pole tides	
Loading corrections	Ocean tidal loading	(Lyard et al. 2021)
	Atmospheric tidal loading	(Ray and Ponte 2003)
De-aliasing products	Atmosphere + Ocean RL06: d/o 30	(Dobslaw et al. 2017)
Third body attractions	DE405	(Standish 1998)
Air drag	NRLMSISE-00	(Picone et al. 2002)
Direct solar radiation pressure	with radiation pressure coefficient C_R= 1.13	
Earth radiation pressure	albedo reflectivity and emissivity	(see Sec. 3.2e))
Relativistic corrections	Schwarzschild	(Petit and Luzum 2010)
	Lense-Thirring	
	deSitter	

Furthermore, orbits can be computed as 7-day long-arcs with daily dynamic orbit parameters (see Sec. 3.6) or by additionally introducing pseudo-stochastic pulses, which may partially absorb possible air drag mis-modeling. Analyses indicated that an orbit parametrization with 2 pseudo-stochastic pulses in S per day are sufficient for LARES (see Sec. 7.1.1), while the other LEOs require twelve pseudo-stochastic pulses per day (see Sec. 7.2.1).

Nevertheless, these orbit parametrizations have to be further adapted, if the estimated parameter space contains low-degree SH geopotential coefficients because OPR-W accelerations are strongly correlated with C_{20} (Jäggi et al. 2012, Bloßfeld et al. 2014) and OPR-S with C_{30} (see Sec. 7.1.3). Consequently, SH geopotential coefficients can only be estimated reliably if the OPR-W and OPR-S accelerations are not set-up for specific

[8]https://cddis.nasa.gov/archive/slr/products/resource/SLRF2014_POS+VEL_2030.0_200325.snx (Accessed: 22/12/2022)
[9]https://hpiers.obspm.fr/eoppc/eop/eopc04/ (Accessed: 22/12/2022)

satellites, in particular for the geodetic LEOs.

4.3 Geodetic Parametrization

Depending on the definition of the set of parameters, a single geodetic technique may not be able to estimate all parameters and the corresponding NEQ system becomes singular. Therefore, particular parameters must be be constrained or even fixed (see Sec. 3.3.3). In the case of a standard SLR combination, the following set of parameters is estimated:

- orbit parameters (osculating and dynamic orbital parameters, pseudo-stochastic pulses),
- station coordinates,
- geocenter coordinates,
- range biases and
- ERPs.

In the standard processing, constraints have to be applied to the station coordinates (see Sec. 4.3.1) and ERPs (see Sec. 4.3.2) to provide a non-degenerate NEQ system.

4.3.1 Datum Definition

Instead of fixing particular stations to their a priori coordinates, it is more physical to use Minimum Constraint (MC) conditions on a subset of stations (see Sec. 3.3.3). To be able to co-estimate ERPs and geocenter coordinates, No-Net-Rotation (NNR) and No-Net-Translation (NNT) conditions have to be applied. For this, the three rotation angles and the three translations of the Helmert transformation are constrained to zero and the mean rotation and translation of the subset of core stations are kept to zero.
The stations in the subset are characterized by featuring stable station coordinates. The ILRS provides a list of such core stations[10], but the list can be verified by using a Helmert transformation approach (see Sec. 6.6) as well.

4.3.2 Earth Rotation Parameters

The ERPs consist of the polar motion (x_p,y_p) and the universal time $UT1$. The offset of $UT1$ w.r.t. UTC at time t is

$$\Delta UT(t) = UT1(t) - UTC(t) \tag{4.1}$$

and Length of Day (LOD) reads as

$$\mathrm{LOD}(t) = -\Big(\Delta UT(t + 1day) - \Delta UT(t)\Big)/day. \tag{4.2}$$

[10] https://ilrs.dgfi.tum.de/fileadmin/data_handling/ILRS_Data_Handling_File.snx (Accessed: 22/12/2022)

In the BSW, the ERPs can be parametrized using a PieceWise-Constant (PWC) or a PieceWise-Linear (PWL) model (see Fig. 4.6). For the PWC parametrization, constant offsets at noon w.r.t. the a priori values are estimated on a daily basis for the polar motion. The daily drift is, however, taken over from the a priori models. ΔUT (see Eq. 4.1) are fixed to the a priori model, e.g., IERS-14-C04 reference series, at the beginning of each day and only LOD is estimated on a daily basis. The PWL parametrization is based on polygons, i.e., piecewise-linear functions between the vertices at the beginning of each day. Therefore, the estimated polar motion as well as ΔUT are referring to the vertices of the polygon. However, SLR as well as the other satellite geodetic techniques are only able to estimate LOD but not the offset ΔUT due to correlations with the satellite's ascending node (Rothacher et al. 1999). Hence, one per 7-day arc of the daily ΔUT values has to be fixed to the a priori model to remove this singularity.

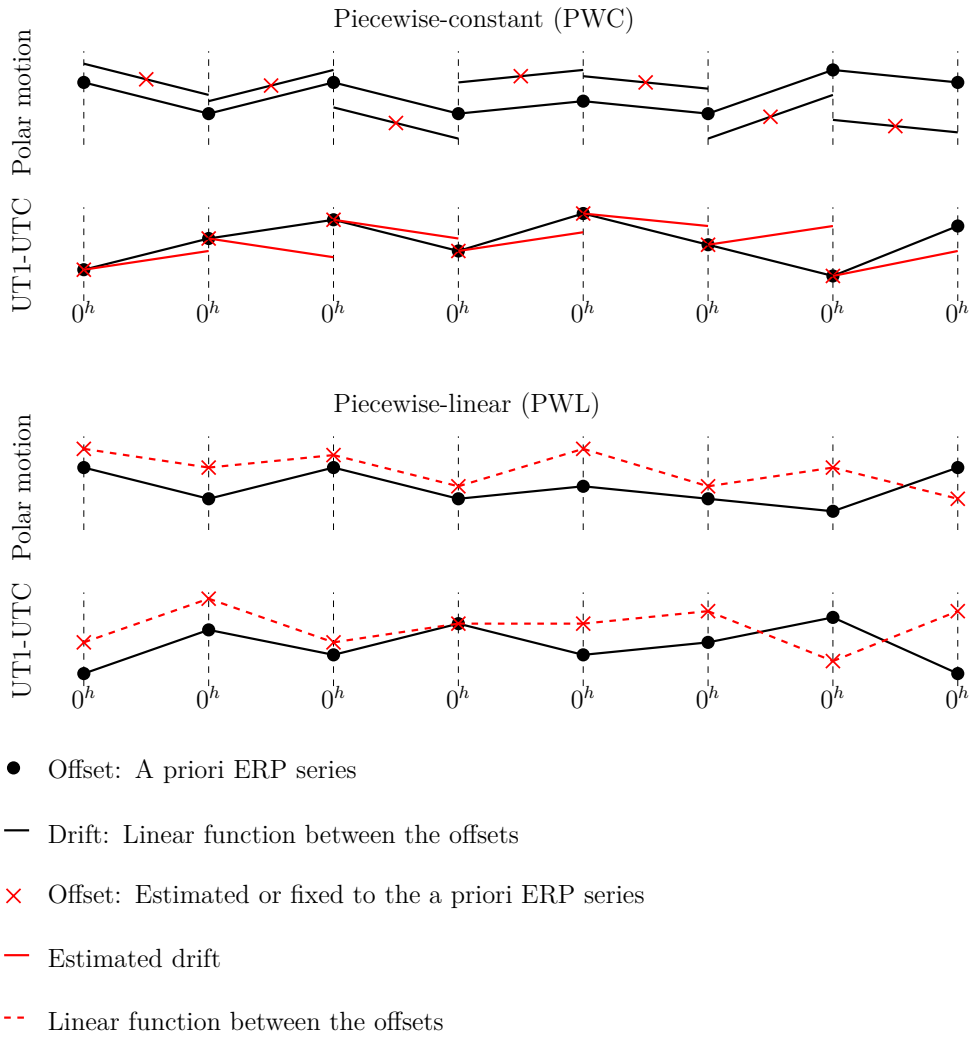

Figure 4.6: Piecewise-constant (top) or piecewise-linear (bottom) parametrization of the ERPs (adapted from Thaller 2008).

4.4 Methodology of SLR Solution Analysis

In this section, the general approach to validate the quality of the weekly SLR solutions is presented. For this purpose, the time series of estimated parameters from several SLR solutions are compared with internal and external quality metrics. Additionally, an outlier detection on the time series of the comparison ensures that the statistical conclusions are reliable.

4.4.1 Earth Rotation Parameters

In this work, the daily estimated ERPs of weekly SLR solutions are compared to the reference series IERS-14-C04 (see Sec. 3.1.3). For the PWC parametrization of the ERPs, ΔUT is fixed for each day and for the PWL parametrization only the 4^{th} offset of ΔUT is fixed to the a priori value at 0^{h} epoch. To incorporate also the estimated drift of ΔUT in the validation, the parameter estimates are linearly interpolated between the nearest two 0^{h} epochs to the 12^{h} epoch. Additionally, a linear interpolation of ΔUT is performed on the reduced UT1R-UTC values, which take short periodic corrections (up to 35 days) due to tidal deformation to the Earth's rotation into account (Petit and Luzum 2010). Furthermore, an outlier detection with a rejection level of 2.5σ, where σ is the expected standard deviation, is applied on the time series of the variations of the daily estimated ERPs of several weekly SLR solutions w.r.t. the reference series. Hence, the quality of the estimated time series of the ERPs c, i.e., X-Pole, Y-Pole and ΔUT, can be determined by the mean of the time series and the Weighted Root Mean Square (WRMS)

$$\text{WRMS}_c = \sqrt{\frac{1}{\sum_{i=1}^{n} \frac{1}{\sigma_{c,i}^2}} \sum_{i=1}^{n} \frac{1}{\sigma_{c,i}^2} \cdot x_{c,i}^2}, \quad \text{for } c \in \{\text{X-Pole, Y-Pole, } \Delta UT\} \tag{4.3}$$

with

n : total number of daily estimates from several weekly solutions,
$x_{c,i}$: variation of the i-th estimate w.r.t. the reference series for parameter c with $i \in \{1, ..., n\}$,
$\sigma_{c,i}$: formal error of the parameter c for the i-th estimated value.

4.4.2 Station Coordinates

The weekly estimated station coordinates of the core stations are compared to the corresponding reference station coordinates from SLRF2014 after estimating seven parameters of a Helmert transformation (see Eq. 3.34). Further, the RMS of the residuals in each component $c \in \{\text{X, Y, Z}\}$ is calculated. The time series of the RMS, composed of several weekly solutions, is reduced by an outlier detection with a rejection level of 2.5σ in each component. Afterwards, the Weighted Mean (WMEAN) of RMS for the component c is

$$\text{WMEAN}(RMS_c) = \frac{1}{\sum_{i=1}^{n} n_{\text{sta},i}} \sum_{i=1}^{n} n_{\text{sta},i} \cdot RMS_{c,i} \quad \text{for } c \in \{\text{X, Y, Z}\} \tag{4.4}$$

with

n : number of weekly solutions,
$RMS_{c,i}$: RMS of the component c for the i-th weekly solution with $i \in \{1, ..., n\}$,
$n_{\text{sta},i}$: number of core stations used to form $RMS_{c,i}$.

4.4.3 Spherical Harmonic Geopotential Coefficients

The weekly estimated SH geopotential coefficients are compared with external reference series provided by the Center of Space Research, University of Texas at Austin (CSR, Cheng et al. 2011) and COST-G (Jäggi et al. 2020).
The Center of Space Research, University of Texas at Austin (CSR) reference series consists of monthly estimates up to degree/order 5 and C_{61}/S_{61} determined with SLR observations to five geodetic satellites. It is preferred over the well-known reference series TN-14 having a data gap in 2018 (Loomis et al. 2020) of NASA GSFC, since this reference series covers all years from 2002 to 2021. For the matching time spans, the two series are nearly identical.
On the contrary, the COST-G products are based on observations collected by the dedicated GRACE/GRACE-FO satellite gravity missions.

The Earth's gravity field models depend on geophysical constants GM and Earth radius $a_{\mathbf{E}}$. The SH geopotential coefficients $C_{nm,i}/S_{nm,i}$ of the system i using the constants GM_i and $a_{\text{E},i}$ can be transformed into a system j with GM_j and $a_{\text{E},j}$ by

$$C_{nm,j} = \frac{GM_i}{GM_j}\left(\frac{a_{\text{E},i}}{a_{\text{E},j}}\right)^n C_{nm,i} \quad \text{and} \quad S_{nm,j} = \frac{GM_i}{GM_j}\left(\frac{a_{\text{E},i}}{a_{\text{E},j}}\right)^n S_{nm,i}. \tag{4.5}$$

The geopotential is a sum of the time-dependent and time-independent tidal potentials of external bodies, e.g., Moon or Sun, and the Earth. If, however, the time-dependent tidal potentials are neglected, such that only a permanent deformation of the Earth remains, it is called a mean-tide model (Petit and Luzum 2010). If the time-independent potentials of the external bodies are deducted from the mean-tide, the resulting tide system is called zero-tide. On the contrary, the tide-free geopotential describes the mean-tide reduced by the time-independent tidal potentials. Hence, the SH geopotential coefficient C_{20} can be formulated in different tide systems, i.e., in the zero-tide system C_{20}^{zt} or in the tide-free system C_{20}^{tf}. According to Petit and Luzum (2010) the transformation between the zero-tide and tide-free system is given by

$$C_{20}^{\text{zt}} = C_{20}^{\text{tf}} - 4.1736 \cdot 10^{-9}. \tag{4.6}$$

In this work, all SH geopotential coefficients are given in the zero-tide system with the geophysical constants $GM = 3.986\,004\,415 \cdot 10^{14}\,\text{m}^3/\text{s}^2$ and $a_{\text{E}} = 6.378\,136\,3 \cdot 10^6\,\text{m}$.

In addition to the comparison of the time series, the corresponding amplitude spectra, computed by a Fourier-Transformation, are analyzed as well.

Chapter 5

SLR Normal Point Generation and Analysis

SLR stations collect a large amount of SLR full-rate data, especially due to the trend towards laser systems with high repetition rates, i.e., ≥1 kHz. At the time of writing, ten SLR stations, mainly located in Asian countries and Central Europe, have already installed a kHz laser system[11].
SLR full-rate data are strongly correlated, and thus, contain redundant information (Seeber 2003), they can be reasonably compressed into a much smaller number of representative observations, so-called *Normal Points* (NPs). However, it must be ensured that after the data reduction, the essential information of the full-rate data still remains.
The ILRS provided in 1997 the *Herstmonceux NP algorithm*, which contains a method of SLR full-rate data screening and the generation of NPs (see Sec. 5.1).
In Section 5.2, a simulation study is performed to investigate whether signal information and stochastic properties are lost through the NP generation process or if there are possible optimizations of the procedure (see Sec. 5.2).

At the time of writing, it is common that SLR stations generate their NPs on-site and provide them through the ILRS data centers to the analysis centers. Most of the SLR stations adapted the general approach, i.e., the Herstmonceux NP algorithm of the ILRS, to improve the quality of their NPs. Consequently, slightly different NP generation procedures may introduce systematic errors in the SLR analysis.
In 2018, the ILRS has requested all SLR stations to also provide SLR full-rate data (Noll and Pearlman 2018), to enable the analysis centers to generate the NPs of each SLR station in a consistent way. Therefore, a SLR NP generator, named *NORMPT*, is implemented in a development version of the BSW (see Sec. 5.3). This program allows to use different trend functions, e.g., polynomial functions or adjusted orbit trajectories (see Sec. 5.3.2), and screening methods, e.g., RMS-based or leading-edge filters (see Sec. 5.3.3), to form NPs.

Most of the full-rate data files provided by the ILRS are already reduced such that only data are included, which were used by the station to form their NPs. This prevents a correct screening with the program NORMPT. Therefore, only the full-rate data from

[11] https://ilrs.gsfc.nasa.gov/network/index.html (Accessed: 24/08/2022)

the SwissOGS are used at the moment in this work to generate NPs. Since the ILRS has requested the SLR stations that their submitted full-rate data should also contain data outside the screening level, e.g., $\pm 5\sigma$ (Carabajal, pers. communication, 2023), it will be possible to generate NPs from other SLR stations in the future.
The impact and the quality of these newly derived NPs can be immediately verified in subsequent space geodetic analyses (see Sec. 5.4). To this end, no further station information, e.g., the number of SLR full-rate data compressed into a NP or their RMS, is yet used in the SLR processing at AIUB.

5.1 Herstmonceux Normal Point Algorithm of the ILRS

The Herstmonceux NP algorithm provided by the ILRS consists of two parts, namely the SLR data screening and the NP generation[12].

Part 1: SLR data screening

1.a) Generate *Prediction Residuals* $PR = O - C$ (Observed-Computed).

1.b) Find a trend function f (fitted to signal data) to minimize the remaining trends in PR.

1.c) Compute *Fit Residuals* $FR = PR - f(PR)$ of signal data.

1.d) Calculate the RMS of the FRs (RMS_{FR}) and find signal data, where the corresponding FRs are larger than the rejection level of n·RMS with $n = 3.0$ for multi-photon and $n = 2.5$ for single-photon systems, respectively.

1.e) Reject the data found in 1.d) and go back to 1.b).

The SLR data screening (see Part 1) is performed to classify the full-rate data in noise, i.e., falsely induced signals in the detector due to background radiations (Degnan 1993), and the actual signal of the observed satellite. For this purpose, prediction residuals PRs, which are the differences between observed and computed distances between the ground station and the satellite, are generated (see Fig. 5.2, top). The observed distances are calculated according to Eq. 2.3. The computed distances are the differences between the a priori station coordinates and satellite positions given by the SLRF2014 reference frame and the a priori orbit (see Sec. 4.2), respectively.
Since PRs may still feature a trend, a function f is fitted to the signal (see Fig. 5.2, middle) and the fit residuals FRs are formed. If the FRs are fully detrended, they are supposed to represent the random error of the observations. Consequently, all data within a certain rejection level of n·RMS_{FR}, with a pre-defined scaling factor n and the RMS of FRs, are considered as signal (see Fig. 5.2, bottom). They are then again used to build the trend function in 1.b). These steps are repeated until no further full-rate data are recognized as signal (see Fig. 5.1).

[12] https://ilrs.gsfc.nasa.gov/data_and_products/data/npt/npt_algorithm.html (Accessed: 24/08/2022)

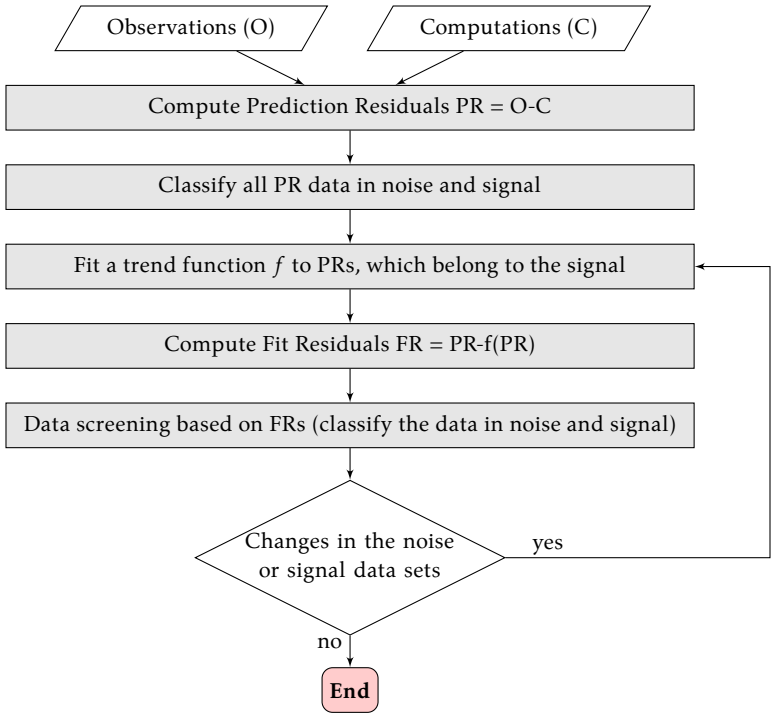

Figure 5.1: Schematic illustration of the SLR data screening (Part 1).

Part 2: SLR NP generation

2.a) Subdivide the day containing FRs of signal data into fixed bins (called bins) starting at 0^h UTC. The interval length depends on the altitude of the satellite (see Table 5.1).

2.b) Compute the mean value $\overline{FR}_i$ and the mean epoch $\bar{t}_i$ of all FRs in the bin i.

2.c) Find the observation O_i with its fit residual FR_i, whose observation epoch t_i is nearest to the mean epoch $\bar{t}_i$ in the bin i.

2.d) The NP for bin i is then $NP_i = O_i - FR_i + \overline{FR}_i$.

The remaining signal data are further compressed into the NP data. For the NP generation process of the ILRS (see Part 2), each satellite pass is divided into fixed bins. The mean of the fit residuals FR_i within each bin i $\overline{FR}_i$ is calculated, which ideally represents the random error of the bin. Consequently, the NP_i of the bin i corresponds to the observation O_i, with the observation epoch t_i closest to the mean epoch of the bin i, which is reduced to the mean of the random error of the bin i (see Fig 5.3)

$$NP_i = O_i - FR_i + \overline{FR}_i. \tag{5.1}$$

This ILRS NP algorithm has standardized the procedures of SLR data screening and NP generation. However, NPs are individually generated by each SLR station, where the data processing is adapted to perform it in a best possible way. Consequently, a consistent NP generation cannot be guaranteed.

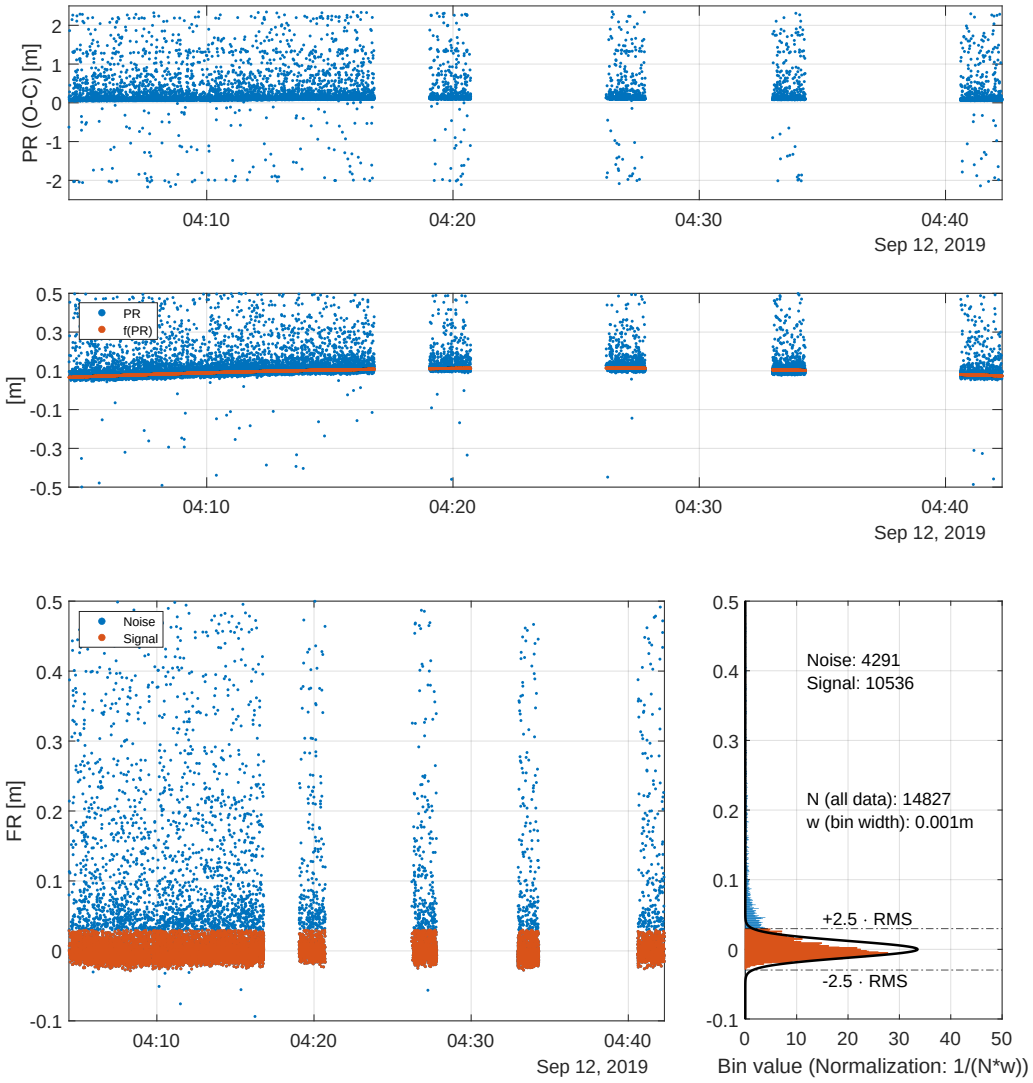

Figure 5.2: Prediction residuals PRs (top), i.e., observed-computed, fitted trend function $f(PR)$ (middle) and the corresponding fit residuals FRs (bottom) with a 2.5·RMS rejection criteria to separate signal from noise of a LAGEOS-1 pass observed by SwissOGS on September 12, 2019.

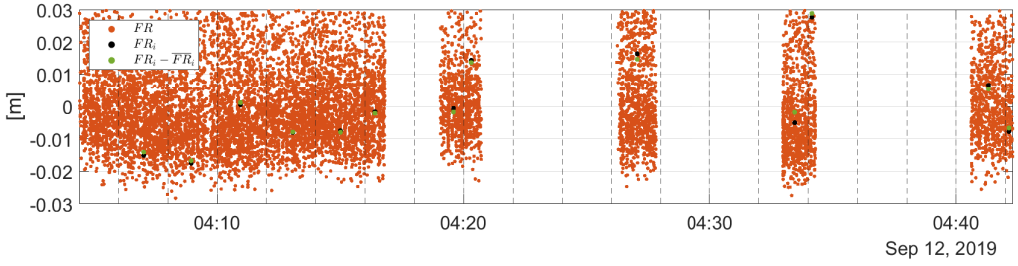

Figure 5.3: FRs corresponding to the signal with FR_i and $FR_i - \overline{FR_i}$ for each bin i of a LAGEOS-1 pass observed by SwissOGS on September 12, 2019.

Table 5.1: NP bin size recommendations from the ILRS website[13].

Altitude [km]	Bin size [s]	Satellites
<550	5	GRACE, GRACE-FO
550-800	15	Sentinel-3
800-2000	30	Starlette, Stella, Ajisai, LARES
2000-5000	60	
5000-8000	120	LAGEOS-1/2, LARES-2
8000-15000	180	
>15000	300	Etalon-1/2, GNSS

5.2 Simulation Study on SLR Data Compression

This simulation study aims to give further insights into the full-rate data compression and its justification. For this purpose, SLR full-rate data are simulated by noisy fit residuals along a known polynomial function of degree 2, representing a satellite pass observed from the Earth. These data are compressed into a few NPs according to the NP algorithm described in Section 5.1. The reduced data set of NPs is then used to determine a polynomial function of degree 2 based on a least-squares adjustment. A comparison with the known polynomial function then indicates the quality of the performed data reduction. The better the two functions coincide, the less information is lost during the data compression.
Moreover, this simulation study enables to compare different trend functions and NP bin sizes as a function of the observation time span.
However, due to the strong simplification of the problem it cannot be expected that conclusions may directly be transferred to the real SLR data compression at different SLR stations without further investigations.

5.2.1 Simulation Approach

For the sake of simplicity, a SLR full-rate data set of a typical LAGEOS-1 pass observed by the SwissOGS over 40 minutes is simulated. The SLR full-rate data $o(t)$ are represented by a superposition of a known polynomial function of degree 2, $P_2(t)$, and a measurement- and background-noise function $n(t)$. The computed orbit $c(t)$ is represented by the same known polynomial $P_2(t)$ but superposed with a trend function $tr(t)$ accounting for orbit mis-modelings. To summarize, the simulated observations and computations can be expressed as

$$\begin{aligned} o(t) &= P_2(t) + n(t) \text{ and} \\ c(t) &= P_2(t) + tr(t). \end{aligned} \tag{5.2}$$

The measurement- and background-noise and the trend functions are empirically determined based on a typical observation of a LAGEOS-1 pass observed by the SwissOGS

[13]https://ilrs.gsfc.nasa.gov/data_and_products/data/npt/index.html (Accessed: 22/12/2022)

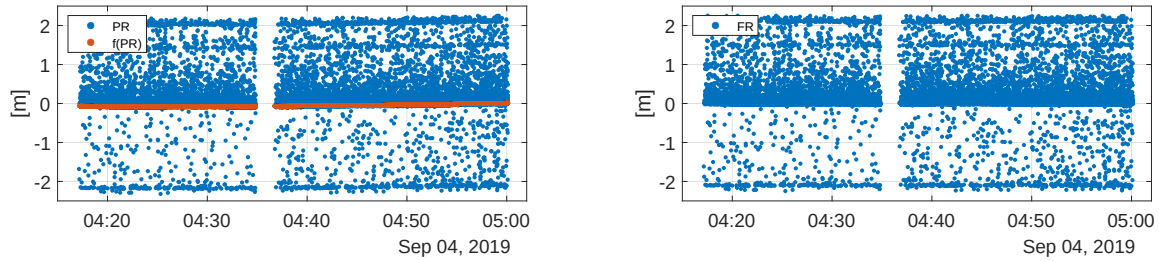

Figure 5.4: Prediction residuals PRs, a trend function $f(PR)$ (left) and the corresponding fit residuals $FR = PR - f(PR)$ (right) of a LAGEOS-1 pass as observed by the SwissOGS on September 12, 2019.

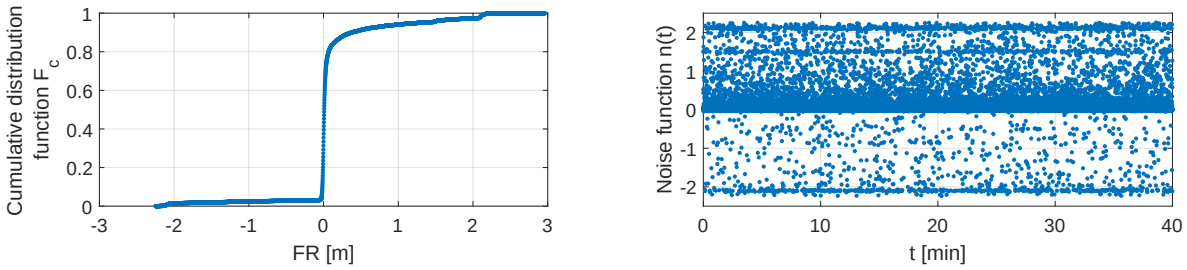

Figure 5.5: Cumulative distribution function F_c (left) of the FRs (shown in the Fig. 5.4, right) and the simulation of the measurement- and background noise function $n(t)$ (right).

during night. The trend function $tr(t)$ is set to $f(PR)$ (see Fig. 5.4, left) and the noise $n(t)$ is modeled according to the probability density function of the FRs (see Fig. 5.4, right). The latter is realized by evaluating the inverse cumulative distribution function F_c^{-1} of the FRs (see Fig. 5.5, left) for random uniform variables $r_u(t) \in [0, 1]$ (see Fig. 5.5, right)

$$n(t) = F_c^{-1}(r_u(t)). \tag{5.3}$$

Using the generated PR as $o(t) - c(t)$, the NP algorithm (see Sec. 5.1) can be applied on the simulated observed $o(t)$ and computed $c(t)$ values. The resulting NPs are used to estimate a polynomial $\hat{P}_2(t)$ of degree 2, which is supposed to represent $P_2(t)$ based on least-squares adjustment. The quality of the NPs is validated by comparing the RMS of the differences between the polynomials $\hat{P}_2(t)$ and $P_2(t)$.

5.2.2 Observation Time Span

SLR measurements can only be performed to one satellite at the time. SLR station operators will switch between several satellites based on the visibility and the priority list. Therefore, the assumption of observing an entire satellite pass would be unrealistic. Consequently, to better reflect the reality, the simulated full-rate data are reduced by inserting several data gaps with different time spans, such that the actual observation time span t_{obs} w.r.t. the total time span of 40 minutes is between 10 % and 100 %.
A consistency test first analyzes whether the true parabola $P_2(t)$ can be reconstructed by the newly generated NPs for different observation time spans t_{obs}. First, full-rate data

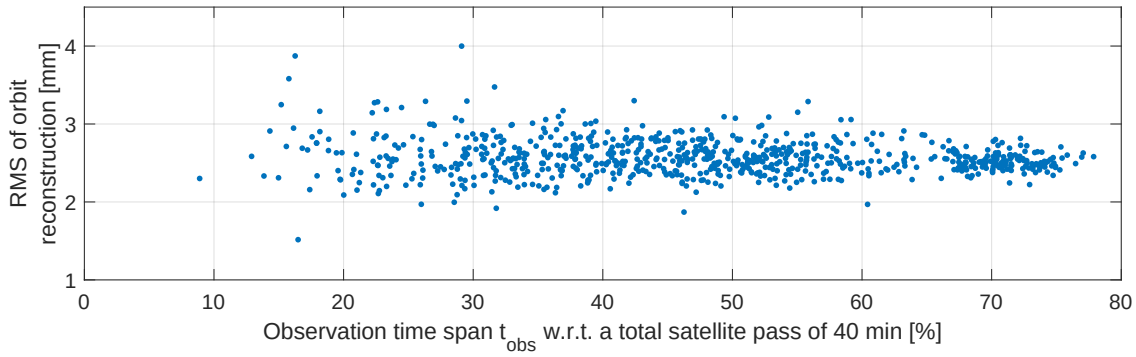

Figure 5.6: RMS of the orbit differences for a trend function as a polynomial of degree 3 for different observation time spans with a bin length of 2 minutes.

over 40 minutes are simulated. Afterwards, 1000 samples of prediction residuals using different observation time spans are generated. The bin size of the NP generation is set to 120 seconds, which is the current ILRS standard for LAGEOS-1.
In this setup, the mean RMS of the orbit differences becomes 2.6 mm, where the scatter increases with the reduction of the observation time span (see Fig. 5.6). The fact that a shorter observation time span may have either a positive or negative impact on the orbit reconstruction is related to the distribution of the introduced data gaps.

5.2.3 Bin Size of the Normal Points

The NP bin sizes shown in Table 5.1 were specified in 1997, when the SLR stations were operating laser systems with repetition rates between 5-10 Hz. Nowadays, the SLR stations move towards laser systems with higher repetition rate, e.g., 1-2 kHz. Consequently, the amount of data becomes larger and the same NP precision can be already achieved within smaller observation time span. Therefore, the tracking time of a satellite can be reduced without loss of precision and in addition, the SLR stations are able to track more satellites during the same time span.
This simulation compares the RMS of orbit differences from solutions with different lengths of the NP bin sizes, e.g., 120s, 90s, 60s or 30s. Fig. 5.7 shows the differences in

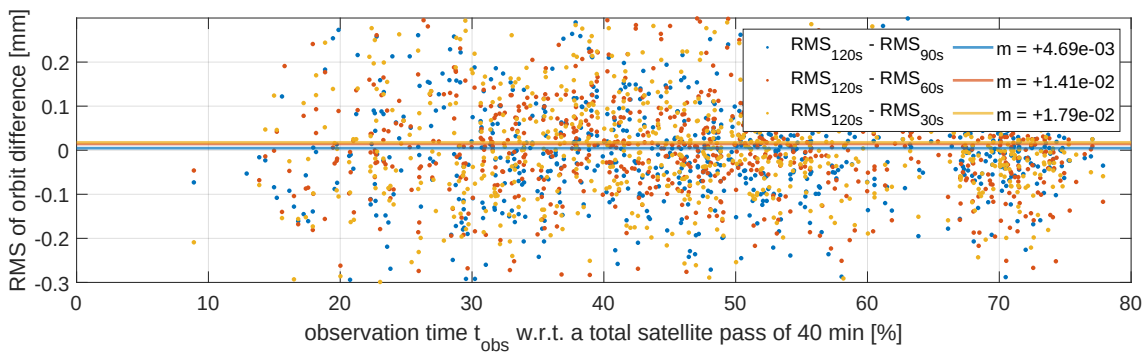

Figure 5.7: RMS of the orbit differences for different observation time spans using several bin sizes.

the RMS of orbit differences for several NP bin sizes w.r.t. the basic bin size of 120s. A NP bin size of 90s reduces the RMS of orbit differences only by about 4.7×10^{-3} mm compared to a NP bin size of 120s. Smaller NP bin sizes reduce the RMS slightly more by 1.4×10^{-2} mm to 1.8×10^{-2} mm. This analysis would suggest to use a shorter NP bin size than 120s for LAGEOS observations. However, in this simulation shorter bin sizes will directly lead to more NP data, which will not generally be the case for real SLR observations. Since the additional gained time will be used to track other satellites.

This simulation study may be a motivation for further investigations, e.g., about the distribution over the satellite orbit of the collected NP data and its impact on the parameter estimation.

5.3 SLR Data Screening and Normal Point Generation at AIUB

In order to perform the SLR full-rate to NP data compression in addition to their processing at AIUB, a new program called NORMPT was developed and incorporated into a development version of the BSW. It mainly follows the ILRS NP algorithm with few adjustments and extensions in the steps 1.b) and 1.d). In the first iteration step of the SLR data screening it is already essential to roughly discriminate between signal and noise, to generate a meaningful trend function f (see Sec. 5.3.1). The detrending of the *PR*s is either based on a polynomial or an adjusted orbit trajectory (see Sec. 5.3.2). Finally, a RMS-based filter or the leading edge method can be used to obtain the signal (see Sec. 5.3.3).

5.3.1 Initialization of the Signal

To reduce the remaining trend in *PR*s, the trend function in step 1.b) has to be fitted to the signal. However, the location of the signal is not known in the first iteration and is therefore roughly determined by a histogram analysis.
The *PR*s of a satellite pass are divided into pre-defined time intervals δt and bins δb (see Fig. 5.8). This lattice structure forms the basis for the histogram analysis, where per time interval a histogram with the bin size δb is validated. The size of these two parameters mainly depends on the repetition rate of the laser system of the ground station and the quality of the computed orbit. A smaller repetition rate has the consequence of less data collected per time, and therefore, a longer time interval δt is needed for the histogram analysis. However, the *PR*s within a δt should not feature a trend.
In the next step, the mean values (called *grid points*), i.e., the mean observation time span and the mean of the *PR*s, are calculated for each histogram for the bin with the most data points (see Fig. 5.8). Finally, a polynomial function of degree 2 is fitted to the grid points and only the data within a fixed pre-defined distance δd to the fit function are interpreted as signal.

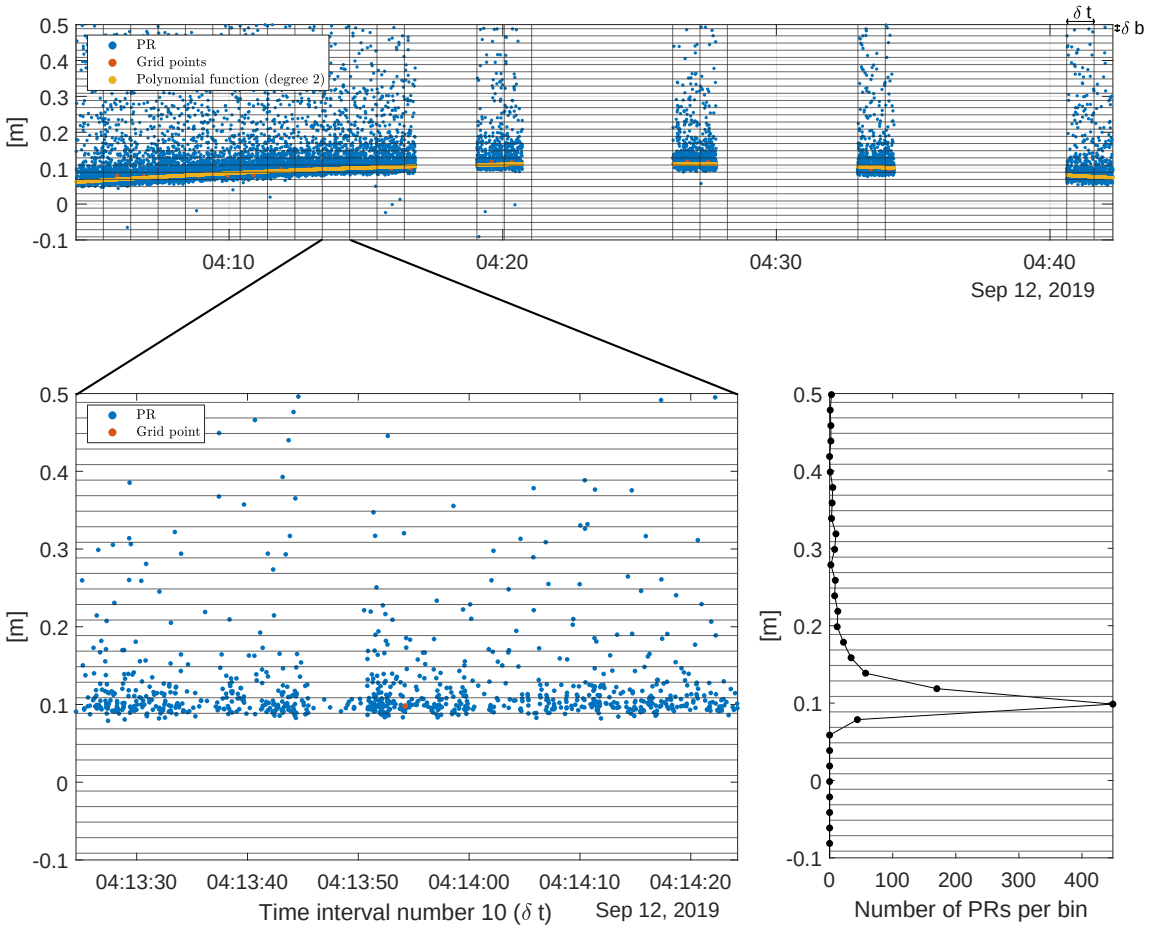

Figure 5.8: Initialization of the signal by fitting a polynomial through the densest bins determined by histogram analysis per time interval $\delta t = 1min$ and bin $\delta b = 0.02m$ of a LAGEOS-1 pass observed by the SwissOGS on September 12, 2019.

5.3.2 Detrending of Systematics in the Prediction Residuals

Before the screening is finally applied, the remaining systematic errors in the PRs have to be reduced. Therefore, a so-called trend function is generated and the corresponding fit residuals $FR = PR - f(PR)$ are calculated. The trend function can either be an empirically determined polynomial or an adjusted orbit trajectory.

a) Polynomial Function

A least-squares adjustment of polynomials to PRs is characterized by its mathematical simplicity. However, such a trend function does not contain any physical modeling of the underlying orbit problem.
The degree of polynomials should be kept as low as possible, otherwise, high frequency oscillations are introduced when fitting the residuals (see Fig. 5.9). In addition, polynomials have the disadvantage that the data boundaries are more affected by errors of the parameter estimation process.

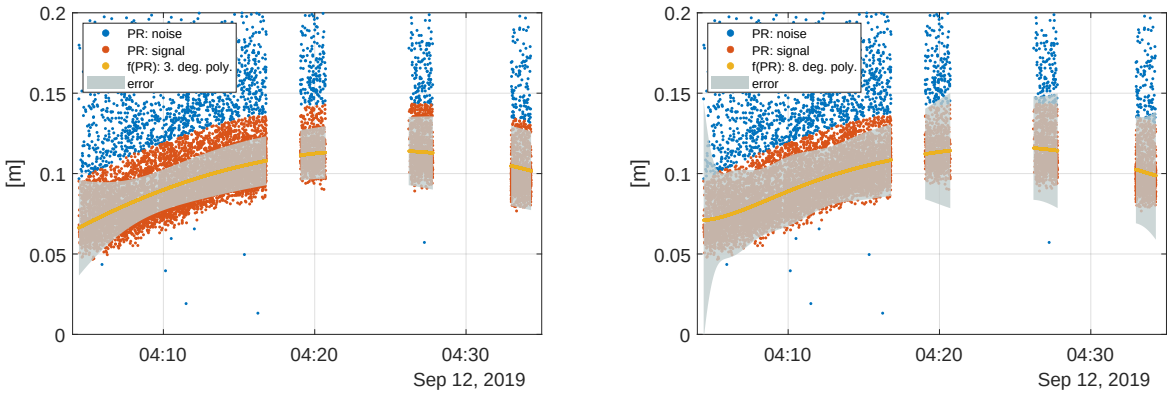

Figure 5.9: Detrending of PRs, of a LAGEOS-1 pass observed by the SwissOGS, by fitting polynomials of degree 3 (left) and 8 (right) to the corresponding signal.

b) Adjusted Orbit Trajectory

In contrary to the detrending with polynomial functions, the adjusted orbit trajectory relies on physical principles, e.g., the use of physical models for satellite motion. The prediction residuals are minimized by estimating the a priori orbit parameters, i.e., six Keplerian orbit parameters, based on least-squares adjustment.

A distance d between a SLR station (stat) and a satellite (sat) at time t can be expressed either as $d_o(t)$ with the range equation (see Eq. 2.3) based on the measured time-of-flight Δt, or as $d_c(t) = |\mathbf{r}_{\text{stat}}(t) - \mathbf{r}_{\text{sat}}(t)|$, the computed difference of the geocentric station and satellite position. In the latter case, the error equation (see Eq. 3.19) reads as

$$\mathbf{v} = \mathbf{A}\Delta\hat{\mathbf{x}} - \bar{\mathbf{l}} = \begin{pmatrix} \frac{\partial d_c(t_1)}{\partial a} & \frac{\partial d_c(t_1)}{\partial e} & \frac{\partial d_c(t_1)}{\partial i} & \frac{\partial d_c(t_1)}{\partial \Omega} & \frac{\partial d_c(t_1)}{\partial \omega} & \frac{\partial d_c(t_1)}{\partial u_0} \\ \cdot & & & & & \cdot \\ \cdot & & & & & \cdot \\ \cdot & & & & & \cdot \\ \frac{\partial d_c(t_n)}{\partial a} & \frac{\partial d_c(t_n)}{\partial e} & \frac{\partial d_c(t_n)}{\partial i} & \frac{\partial d_c(t_n)}{\partial \Omega} & \frac{\partial d_c(t_n)}{\partial \omega} & \frac{\partial d_c(t_n)}{\partial u_0} \end{pmatrix} \begin{pmatrix} \Delta a \\ \Delta e \\ \Delta i \\ \Delta \Omega \\ \Delta \omega \\ \Delta u_0 \end{pmatrix} - \begin{pmatrix} d_o(t_1) - d_c(t_1) \\ \cdot \\ \cdot \\ \cdot \\ d_o(t_n) - d_c(t_n) \end{pmatrix},$$

where the design matrix becomes

$$\mathbf{A} = \begin{pmatrix} \sum_{i=1}^{3} \frac{\partial d_c}{\partial r_{\text{sat}}(i)} \frac{r_{\text{sat}}(i)}{\partial a}\Big|_{t_1} & \cdots & \sum_{i=1}^{3} \frac{\partial d_c}{\partial r_{\text{sat}}(i)} \frac{r_{\text{sat}}(i)}{\partial u_0}\Big|_{t_1} \\ \cdot & & \cdot \\ \cdot & & \cdot \\ \cdot & & \cdot \\ \sum_{i=1}^{3} \frac{\partial d_c}{\partial r_{\text{sat}}(i)} \frac{r_{\text{sat}}(i)}{\partial a}\Big|_{t_n} & \cdots & \sum_{i=1}^{3} \frac{\partial d_c}{\partial r_{\text{sat}}(i)} \frac{r_{\text{sat}}(i)}{\partial u_0}\Big|_{t_n} \end{pmatrix}$$

$$= \begin{pmatrix} \sum_{i=1}^{3} \frac{r_{sat}(i)-r_{stat}(i)}{d_c} \frac{r_{sat}(i)}{\partial a}\Big|_{t_1} & \cdots & \sum_{i=1}^{3} \frac{r_{sat}(i)-r_{stat}(i)}{d_c} \frac{r_{sat}(i)}{\partial u_0}\Big|_{t_1} \\ \vdots & & \vdots \\ \sum_{i=1}^{3} \frac{r_{sat}(i)-r_{stat}(i)}{d_c} \frac{r_{sat}(i)}{\partial a}\Big|_{t_n} & \cdots & \sum_{i=1}^{3} \frac{r_{sat}(i)-r_{stat}(i)}{d_c} \frac{r_{sat}(i)}{\partial u_0}\Big|_{t_n} \end{pmatrix}.$$

Since the six osculating orbital parameters cannot be determined by SLR data from only one satellite pass, they are constrained with an a priori sigma of 20 m for semi-major axis a, 10^{-6} for eccentricity e, $0.1''$ for inclination i, $1.0''$ for the right ascension of the ascending node Ω, $10''$ for the argument of perigee ω and $5''$ for the argument of latitude u_0.

5.3.3 Screening Techniques for SLR Normal Point Generation

The profile of the FRs histogram is a convolution of the target response function $TR(x)$ and the system noise $SN(x)$ (Otsubo et al. 2015). Since the laser pulses are reflected at the satellite on different retro-reflectors, which have slightly different distances to the ground station, the received laser pulses become broader. This specific signature of the received laser pulse depends on the properties of the satellite and corresponds to the target response function (Otsubo et al. 2015). The main source of the system noise at the SwissOGS is the C-SPAD detector, which is causing an asymmetric distribution of the signal with a long tail, which can be clearly seen in the FRs of the LAGEOS-1 pass observed by the SwissOGS shown in Figure 5.10.

Consequently, the distribution of the FRs strongly depends on the laser system, e.g., the detector, and the ranging scheme, i.e., single- or multi-photon. If the distribution is near-Gaussian, the RMS-based filter can be used as the screening method. However, if the assumption is no longer valid, the Leading-Edge screening method (Kirchner and Koidl 2004) may be a good alternative. There, the focus is placed only on the front of the distribution, which is less affected by the system noise, e.g., the long tail.

a) RMS-Based Filter

The RMS-based filter is in accordance with the data screening defined in the NP algorithm of the ILRS (see Sec. 5.1). First, a polynomial $f_n(PR)$ of degree n is fitted using least-squares adjustment to the flagged input data PRs from the first initialization (see Sec. 5.3.1). For near-Gaussian distributed data sets, the RMS of the fit residuals $FR = PR - f_n(PR)$ multiplied by a factor i is used as a clipping criterion. Therefore, all observations, where the corresponding fit residual is within the interval $[-i \cdot RMS, +i \cdot RMS]$, are flagged. With the new set of flagged data, the same procedure is repeated until no data are marked or the 20^{th} iteration step is reached. Finally, the flagged data are used to generate the NPs. Figure 5.10 shows the flagged fit residuals from the last iteration step of a LAGEOS-1 pass observed from the SwissOGS.

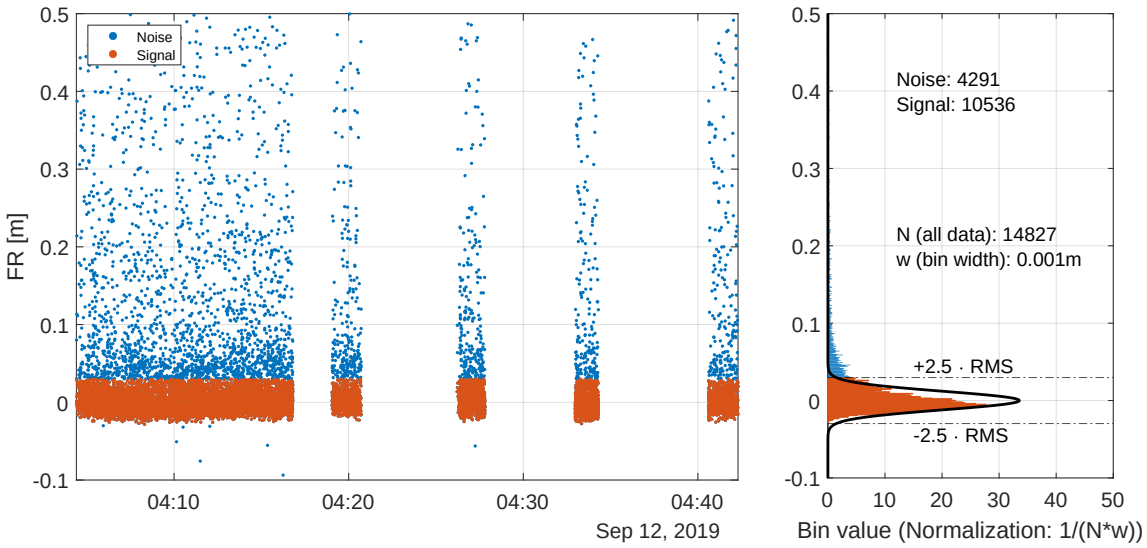

Figure 5.10: SLR data screening based on the fit residuals FRs with a 2.5·RMS rejection criteria to separate signal from noise of a LAGEOS-1 pass observed by the SwissOGS on September 12, 2019.

b) Leading-Edge Filter

The Leading-Edge (LE) filter method does not require the distribution of the data to be Gaussian. To obtain a histogram, the data are smoothed using a polynomial fit function. Then, each data point res_i is represented by a Gaussian function

$$K_i(x) = \frac{1}{\sqrt{2\pi}} e^{-\frac{1}{2}\left(\frac{x-res_i}{h}\right)^2} \tag{5.4}$$

where h is the bandwidth. The sum of all n Gaussian functions forms the Kernel Density Estimator (KDE)

$$\hat{p}(x) := \frac{1}{nh} \sum_{i=1}^{n} K_i(x) = \frac{1}{\sqrt{2\pi} nh} \sum_{i=1}^{n} e^{-\frac{1}{2}\left(\frac{x-res_i}{h}\right)^2}. \tag{5.5}$$

Since only the front of the histogram if of interest, the maximum of the KDE is determined and the front part is mirrored to the other side. With the Nelder-Mead algorithm (Nelder and Mead 1965, O'Neill 1971) a best Gaussian fit to the remaining histogram is performed. The LEHM (Leading-Edge of Half Maximum) is defined as the front point with the half maximum. From the LEHM, a fixed clipping is applied such that all the observations within this range are marked as signal (see Fig. 5.11). The process is iterated until no new observation is marked.

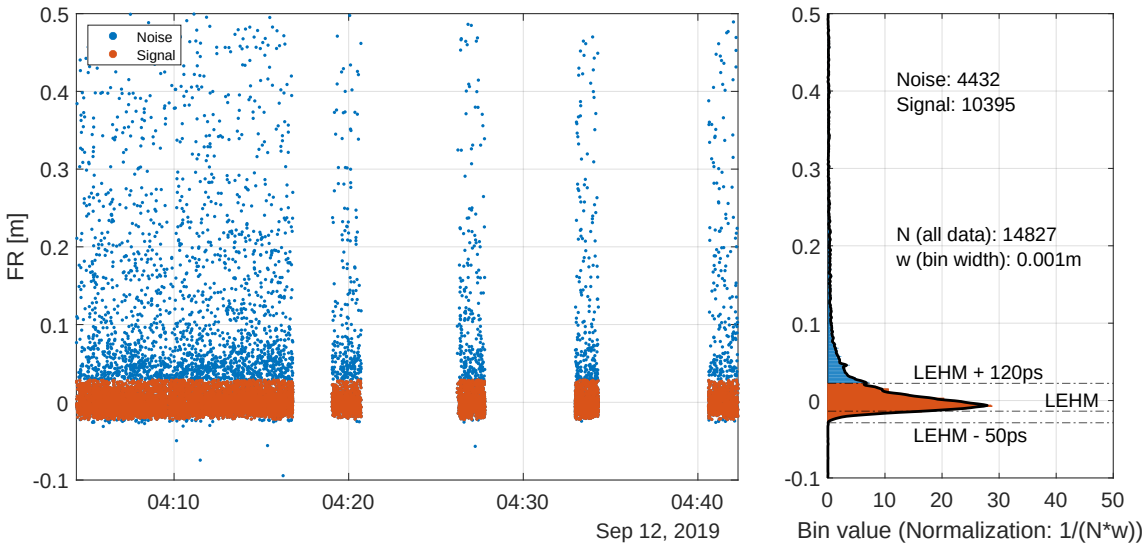

Figure 5.11: SLR data screening based on the fit residuals FRs with a Leading-Edge filter using a lower and upper clipping level of −50 ps and 120 ps of a LAGEOS-1 pass observed by the SwissOGS on September 12, 2019.

5.4 Analysis of Normal Points from the SwissOGS

In this section, LAGEOS-1/2 SLR full-rate data provided by the SwissOGS for four months, from July to October 2019, are used to form the corresponding NPs with the new generator NORMPT. To study the impact of different screening methods, number of observations or bin sizes, the newly formed NPs of the SwissOGS are processed together with LAGEOS-1/2 NPs provided by other SLR stations. The LAGEOS-1/2 satellite orbits are determined in 7-day arcs, where geodetic parameters, i.e., ERPs, station and geocenter coordinates, and range biases for selected stations are co-estimated (see Table 6.1). Since the a priori range biases and center-of-mass corrections of SwissOGS in the data-handling file referring to the standard NPs of SwissOGS, they have to be re-estimated for the investigations with NORMPT.

5.4.1 Comparison of Different Trend Functions and Screening Methods

The LAGEOS-1/2 NPs of SwissOGS are generated using the trend function

- adjusted orbit trajectories (AO),

and two screening methods

- RMS-based filter with a rejection level of $\pm 2.5 \cdot \mathrm{RMS}$ (RMS),
- Leading-Edge filter with a rejection level of $[-50\mathrm{ps}, +120\mathrm{ps}]$ (LEHM).

This leads to the following two NP generations: AO-RMS and AO-LEHM, where the solution AO-RMS is most comparable with the NP generation method used at the SwissOGS.

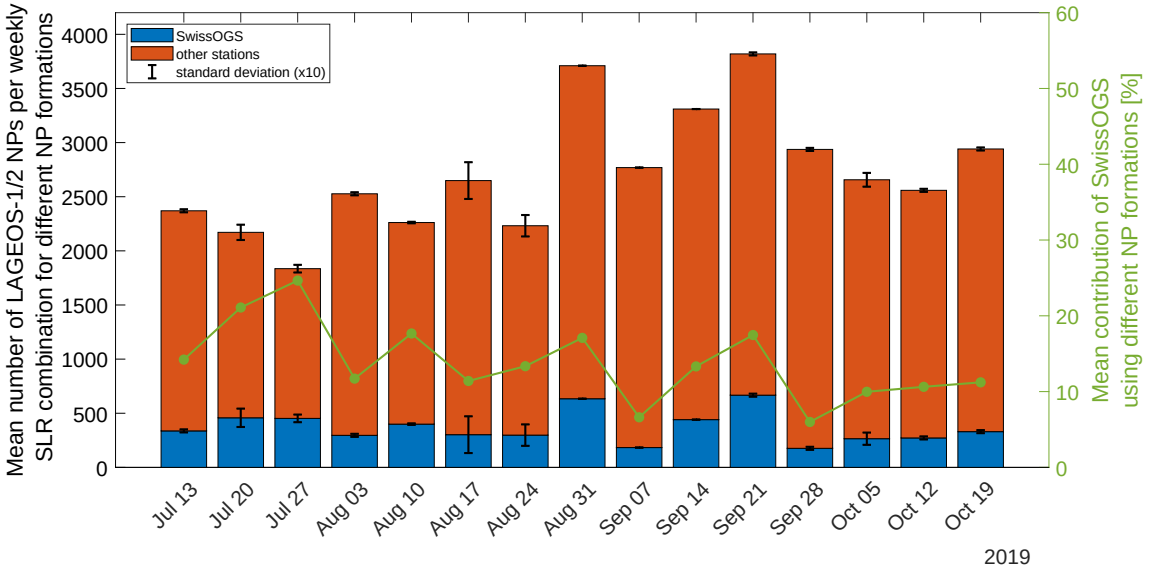

Figure 5.12: Mean number of NPs used for weekly LAGEOS-1/2 SLR combinations and the mean contribution of the SwissOGS.

The SwissOGS contributes on average with 367 and at least with 176 LAGEOS-1/2 SLR data to the weekly solution. Therefore, the percentage of LAGEOS-1/2 SLR NP data of SwissOGS only ranges from 6.0 % to 24.7 % of the total data volume (see Fig. 5.12) such that the impact of the SwissOGS SLR data to the parameter estimation is per se limited. Furthermore, it should also be noted that the number of SLR NP data from the SwissOGS varies for a weekly solution by up to 24 data points, depending on the NP generation algorithm. Consequently, the number of used NPs from SwissOGS differ between the two solutions AO-RMS and AO-LEHM only by 1.2 % on average and by a maximum of 7.6 %.

Although the percentage of newly generated SLR NP data is small, notable differences in some of the estimated geodetic parameters occur when using different NP versions. When comparing the estimated ERP corrections w.r.t. the IERS-14-C04 series, it is noticeable that the polar motion is more sensitive to the used screening method in x-direction than in y-direction (see Table 5.2). The bias of the X-pole changes by almost 5 µas and only by 0.3 µas for the Y-pole. While for the solution AO-LEHM the bias of the polar motion slightly increases, the bias of UT1-UTC decreases to 4 µs. However, the WRMS of the estimated ERP corrections are comparable between the two different solutions.
The weighted mean RMS of the Helmert transformation of the station coordinates does not noticeably change for different screening methods (see Table 5.2).

In Figure 5.13 the additionally estimated range biases of LAGEOS-1/2 for SwissOGS are compared. Regardless of the NP generation, it is consistently found that range biases between 1.2 cm to 1.4 cm must be applied for the SwissOGS. Even for the NP generation AO-RMS, which is comparable to the original NP generation at the SwissOGS, on which the computation of the applied a priori center-of-mass corrections (0.2447 m for LAGEOS-1 and 0.2439 m for LAGEOS-2, extracted from data handling file) was based. This may indicate a revision of the center-of-mass corrections for the SwissOGS. How-

Table 5.2: Estimated ERP corrections w.r.t. the IERS-14-C04 reference series and the weighted mean RMS of the Helmert transformation of the station coordinates w.r.t. SLRF2014 resulting from LAGEOS-1/2 SLR combinations, where the NPs of the SwissOGS are differently generated, from mid-July to mid-October in 2019.

Sol-ID	X-pole [μas]		Y-pole[μas]		UT1-UTC [μs]		Weighted mean RMS of Helmert transf. [mm]		
	Bias	WRMS	Bias	WRMS	Bias	WRMS	North	East	Up
AO-RMS	82.1	152.4	50.4	106.1	7.2	68.0	6.8	4.1	14.4
AO-LEHM	87.0	153.9	50.7	107.7	4.0	68.9	6.8	4.1	14.4
Differences [%]									
RMS vs LEHM	6.0	1.0	0.6	1.5	−44.4	1.3			

ever, a final conclusion would require a comprehensive analysis of longer time series. The observation residuals of LAGEOS-1/2 NPs from SwissOGS are comparable with an RMS of 7.37 mm and 7.49 mm for the two different screening methods are comparable (see Fig. 5.14). Nevertheless, the scatter of NPs from individual satellite passes, e.g., begin of July or mid-August, can vary noticeably between AO-RMS and AO-LEHM.

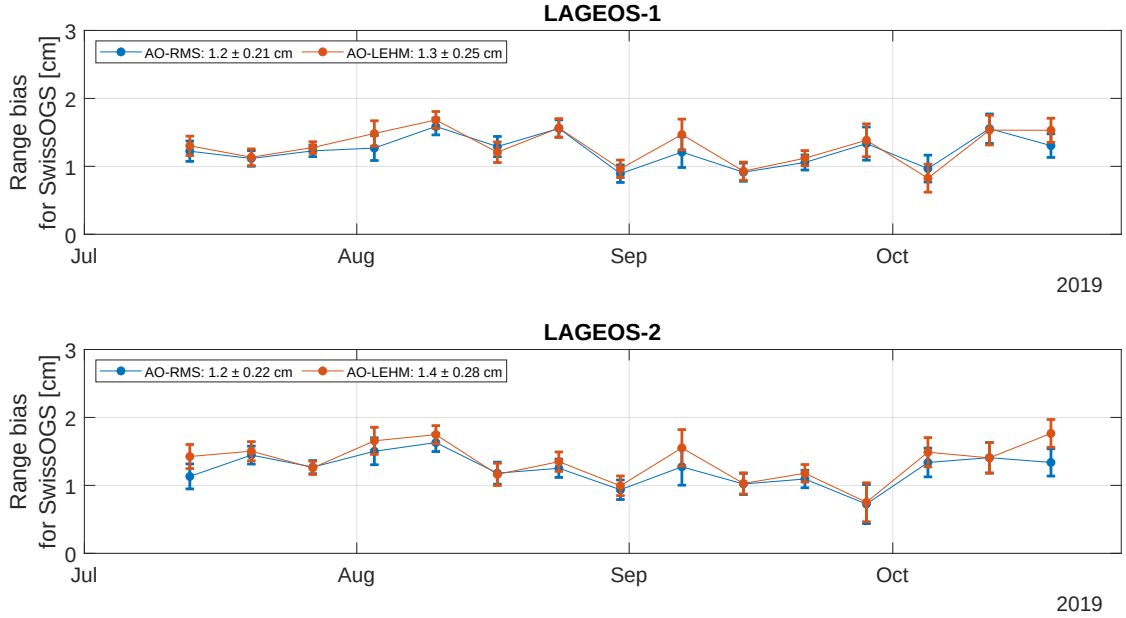

Figure 5.13: Range biases for LAGEOS-1 (top) and LAGEOS-2 (bottom) for the SLR station SwissOGS resulting from LAGEOS-1/2 SLR combinations, where the NPs of the SwissOGS are differently generated, from mid-July to mid-October in 2019.

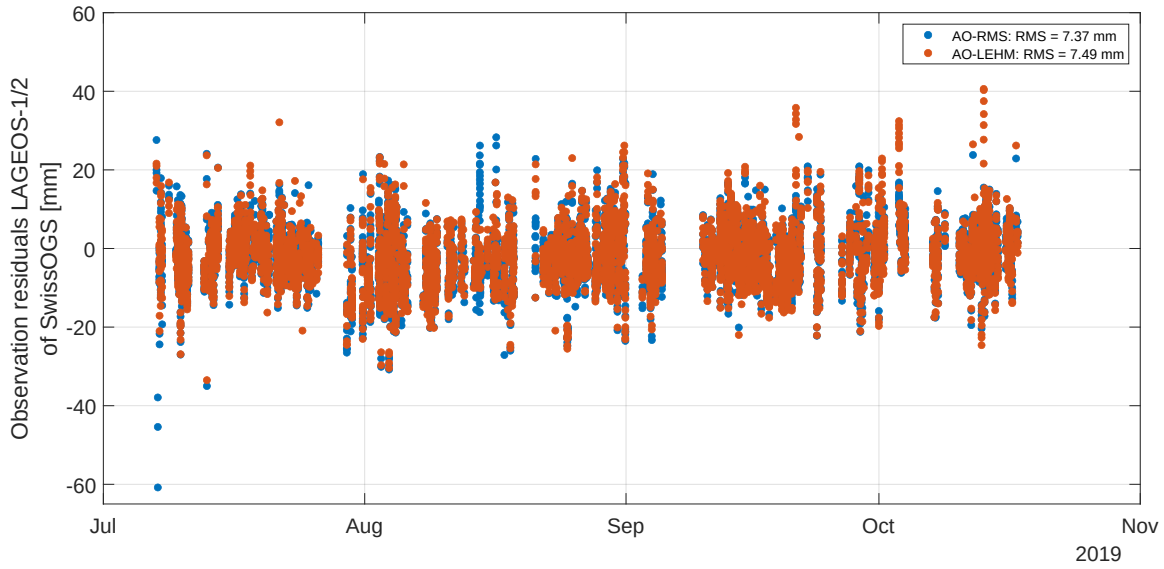

Figure 5.14: Observation residuals of LAGEOS-1/2 of the SwissOGS resulting from LAGEOS-1/2 SLR combinations, where the NPs of the SwissOGS are differently generated, from mid-July to mid-October in 2019.

5.4.2 Number of Observations

A weekly LAGEOS-1/2 SLR combination between July and October 2019 is based on an average of 2711 SLR observations and 134 parameters of interest. Due to this limited number of SLR observations and the low degree of freedom (see Sec. 3.3.2), the estimation and the statistical statements of the SLR processing can become less reliable.
The possible reduction of the NP bin size will allow to track more satellites during the same time span but may lead to fewer NP data per satellite.
In order to study the influence of the SLR observation number on the estimated parameters, the data volume of SLR NPs of SwissOGS are reduced by 10 % and 50 % while using an adjusted orbit trajectory and RMS-based screening method.

Except for UT1-UTC, all estimated ERPs differ only by less than 1.7 % when the data volume of SwissOGS is reduced by 10 % (see Table 5.3). If only half of the SwissOGS NPs are used for the weekly SLR processing, the polar motion is degraded in x-direction and slightly improved in y-direction, respectively. In all cases, the offset of UT1-UTC is reduced by almost more than 4 µs, when the data volume is reduced.

The RMS of the observation residuals of LAGEOS-1/2 only from SwissOGS are within 0.2 mm, regardless of whether 100 % or only 50 % of the SwissOGS NP data are used (see Table 5.3).

Finally, it should be noted that random SLR observations of SwissOGS were deleted over the whole observed time span, i.e., from July to October 2019, for the data reduction. There are no restrictions on the deleted number of observations per satellite pass nor per day. Hence to make sure that a data reduction of 10 % can really be represented by the generated solution (AO-RMS 90), further studies need to be conducted. The main

Table 5.3: Estimated ERP corrections w.r.t. the IERS-14-C04 reference series resulting from LAGEOS-1/2 SLR combinations, where the NP data volume of the SwissOGS is reduced, from mid-July to mid-October in 2019.

Sol-ID and data vol. of SwissOGS [%]		X-pole [μas] Bias	X-pole [μas] WRMS	Y-pole[μas] Bias	Y-pole[μas] WRMS	UT1-UTC [μs] Bias	UT1-UTC [μs] WRMS	RMS of obs. res. SwissOGS [mm]
AO-RMS	100	82.1	152.4	50.4	106.1	7.2	68.0	7.37
AO-RMS	90	83.5	152.7	50.6	106.9	3.4	68.4	7.38
AO-RMS	50	85.8	154.2	49.0	105.3	2.0	69.1	7.57
Differences [%]								
AO-RMS	100 vs 90	1.7	0.2	0.4	0.8	−52.8	0.6	
AO-RMS	100 vs 50	4.5	1.2	−2.8	−0.8	−72.2	1.6	

objective would be to analyze the impact of NPs taken at different times at a day, e.g., midnight or noon, or during the satellite pass or high/low elevation angle. Furthermore, it could be studied if it is more useful to provide several NPs of one satellite pass or less NPs per pass but for several satellite fly-bys per day.

5.4.3 Bin Size for NP Generation

Since the SwissOGS is using a 100 Hz laser system, a reduction of the length of the bin size can be considered. Therefore, additional NPs are generated by using an adjusted orbit trajectory with a RMS-based screening method and NP bin sizes of 90 s and 30 s. Consequently, with shorter bin sizes but the same full-rate data, the number of NPs increases automatically (see Fig. 5.15).

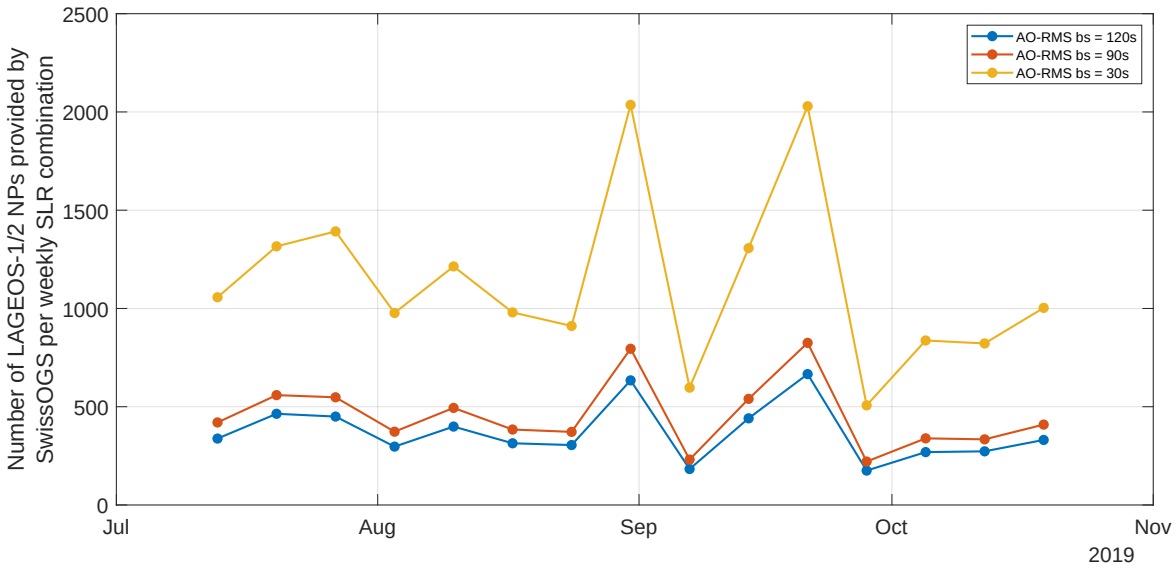

Figure 5.15: Number of LAGEOS-1/2 NPs provided by the SwissOGS per weekly SLR combination when using NP bin sizes of 120s, 90s and 30s.

Table 5.4: Estimated ERP corrections w.r.t. the IERS-14-C04 series resulting from LAGEOS-1/2 SLR combinations, where the bin size of the NP generation of the SwissOGS full-rate data is reduced, from mid-July to mid-October in 2019.

Sol-ID and bin size [s]		X-pole [μas]		Y-pole[μas]		UT1-UTC [μs]		RMS of obs. res. SwissOGS [mm]
		Bias	WRMS	Bias	WRMS	Bias	WRMS	
AO-RMS	120	82.1	152.4	50.4	106.1	7.2	68.0	7.37
AO-RMS	90	81.5	151.4	53.2	107.9	7.8	67.9	7.22
AO-RMS	30	76.7	151.9	51.4	118.1	11.2	68.7	6.93
Differences [%]								
AO-RMS	120 vs 90	−0.7	−0.7	5.6	1.7	8.3	−0.1	
AO-RMS	120 vs 30	−6.6	−0.3	2.0	11.3	55.6	1.0	

Therefore, it is again quite challenging to decide whether observed changes in the estimated parameters are due to the different number of observations or the applied NP bin size. Nevertheless, the comparison of the ERPs shows that the X-pole slightly improves, while the bias and WRMS of Y-pole and UT1-UTC degrade (see Table 5.4). This is in contrast to the RMS of LAGEOS-1/2 observation residuals of the SwissOGS, which can be improved by reducing the length of the bin size (see Table 5.4).

Although the differences in the estimated parameters are not significant, these results indicate that a homogeneous NP generation of all SLR stations may have an impact on the estimates of SLR processing.

Chapter 6

Optimization of Geodetic and Orbit Parametrization Based on LAGEOS-1/2 SLR Data

This chapter focuses on the analysis and optimization of the orbit and geodetic parametrization based on LAGEOS-1/2 (satellite group A) SLR combinations. The basic parameters characterizing the LAGEOS-1/2 SLR combinations are listed in Table 6.1. If the parametrization is adapted, it is explicitly mentioned in the corresponding section.

In Section 6.1 the impact of the ERP parametrization, i.e., as PWC or PWL functions, is studied. The correlations between the ERPs, especially UT1-UTC, and the OPR-W accelerations are discussed in Section 6.2. Since the OPR-W accelerations and the low-degree SH geopotential coefficient C_{20} are strongly correlated (see Sec. 6.3), the impact of different a priori gravity field models is analyzed as well.

Table 6.1: Basic parametrization for LAGEOS-1/2 SLR combinations.

Parameters	LAGEOS-1/2 (A)	
Osculating elements	$a, e, i, \Omega, \omega, u_0$ 1 set per 7 days	
Dynamic orbit parameters	S_0, S_S, S_C, W_S, W_C 1 set per 7 days	**(Sec. 6.2)**
Pseudo-stochastic pulses	none	**(Sec. 6.4)**
Station coordinates	1 set per 7 days NNR/NNT minimal constraints	**(Sec. 6.6)**
Geocenter coordinates	1 set per 7 days	
Range biases	1 set per 7 days selected stations	
ERPs	daily piecewise linear (PWL)	**(Sec. 6.1)**

Afterwards, in Section 6.4, VCE is used to determine whether pseudo-stochastic pulses in along-track and cross-track are required for the satellite orbit modeling of LAGEOS-1/2. Finally, the realization of a proper datum definition is studied (see Sec. 6.6). The latter is essential to perform reliable parameter estimations but challenging, since the geographical distribution of the SLR station network is inhomogeneous.

This chapter forms the foundation for further multi-satellite SLR combinations, which are discussed in detail in Chapter 7.

6.1 ERP Parametrization

The estimated ERP corrections w.r.t. the IERS-14-C04 reference series can be represented by PWC or PWL functions (see Sec. 4.3.2). The main difference is that the PWL parametrization ensures continuity at day boundaries, which is therefore more physical, in contrary to the PWC function.
To study the impact of these two ERP parametrizations, weekly LAGEOS-1/2 SLR combinations based on 7-day true-arcs (see Sec. 4.2) are performed for the year 2015. The quality of SLR combinations is determined by comparing the estimated ERP corrections w.r.t. the IERS-14-C04 reference series and by the mean RMS of observation residuals.

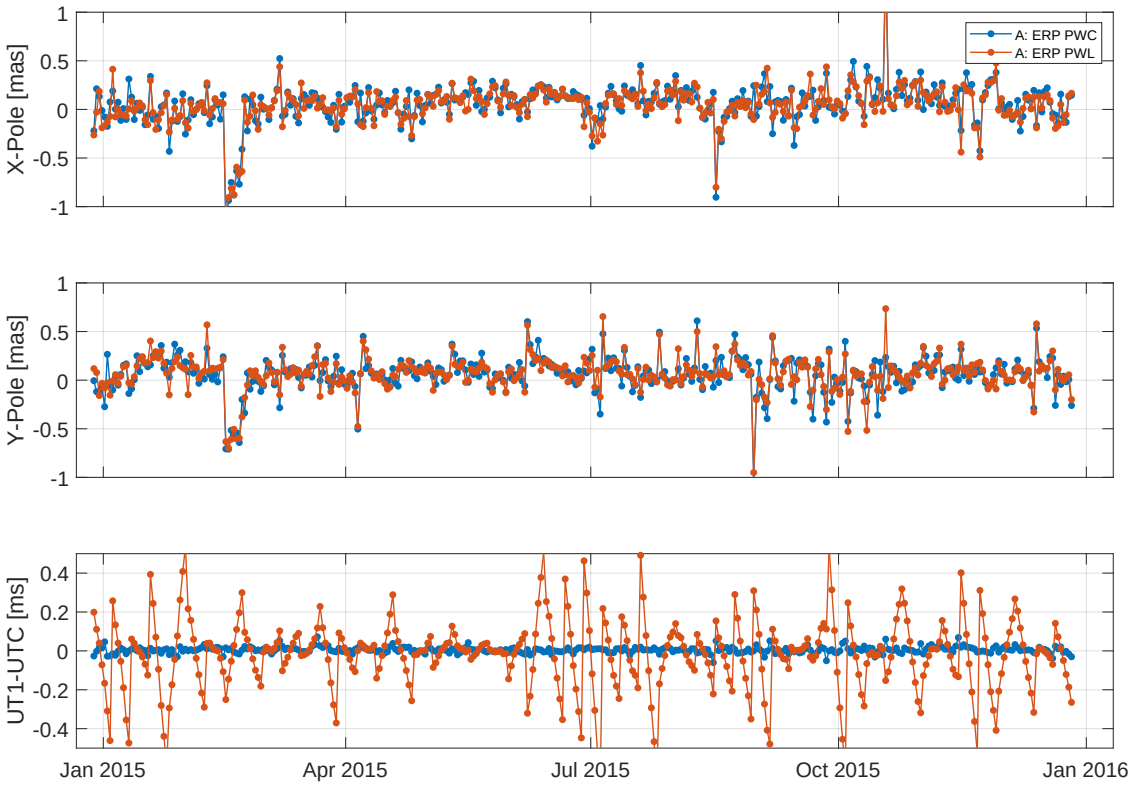

Figure 6.1: Time series of estimated ERP corrections w.r.t. the IERS-14-C04 reference series of SLR combinations of LAGEOS-1/2 data for the year 2015. The ERPs are either represented by PWC or PWL functions.

Table 6.2: Estimated ERP corrections w.r.t. the IERS-14-C04 reference series of SLR combinations of LAGEOS-1/2 data for the year 2015. The ERPs are either represented by PWC or PWL functions.

Model for ERPs	Mean RMS obs. res. [mm]	X-pole [μas]		Y-pole [μas]		UT1-UTC [μs]	
		Bias	WRMS	Bias	WRMS	Bias	WRMS
PWC	9.64±1.82	73.7	142.3	75.9	126.2	4.5	11.7
PWL	9.28±1.51	60.3	127.9	69.6	114.0	−0.1	61.8

The PWL model for the ERPs improves the WRMS of the polar motion w.r.t. the reference series by 10 % (see Table 6.2). The biases of the polar motion in x- and y-direction are also reduced by 13 µas and 6 µas, respectively. In contrast, the WRMS of UT1-UTC increases significantly by 81 % compared with the estimates, where the PWC model is applied. This is to be expected, since for the PWC parametrization all daily UT1-UTC values are fixed to the a priori values, while in the PWL case only one UT1-UTC value at the 4-th day of a weekly SLR combination is fixed (see Sec. 4.3.2). Therefore, UT1-UTC is more loosely constrained and follows a sawtooth function (see Fig. 6.1). These large variations in UT1-UTC result from the high correlations with the ascending node Ω and the OPR-W accelerations (Rothacher et al. 1999), which are further described in Section 6.2.
The mean RMS of observation residuals of the PWL model can be reduced on the submillimeter level.

Since the PWL parametrization of ERPs is more physical due to the enforced continuity at day boundaries, and moreover, improves the polar motion and slightly reduces the mean RMS of observation residuals, it is used as the standard parametrization of ERPs for all further SLR combinations. The sawtooth behaviour of UT1-UTC is mitigated by neglecting OPR-W accelerations in the orbit modeling (see Sec. 6.2).

6.2 Correlations Between UT1-UTC, Longitude of the Ascending Node and OPR-W Sine Accelerations

The mean correlation matrix of LAGEOS-1/2 SLR combinations (see Fig. 6.2), characterized by the parameters listed in Table 6.1, where ERPs are parametrized as PWL for the year 2015, features strong correlations, especially between UT1-UTC, a, Ω and OPR-W sine acceleration (W_S), which were already discussed in Rothacher et al. (1999) and Bloßfeld et al. (2014).

Rothacher et al. (1999) explained the correlation between the first derivative of UT1-UTC, i.e., the drift of UT1-UTC, and the Keplerian elements as

$$\frac{\partial}{\partial t}(UT1 - UTC) = -\frac{\dot{\Omega} + \cos(i) \cdot \dot{u}_0}{\rho} \tag{6.1}$$

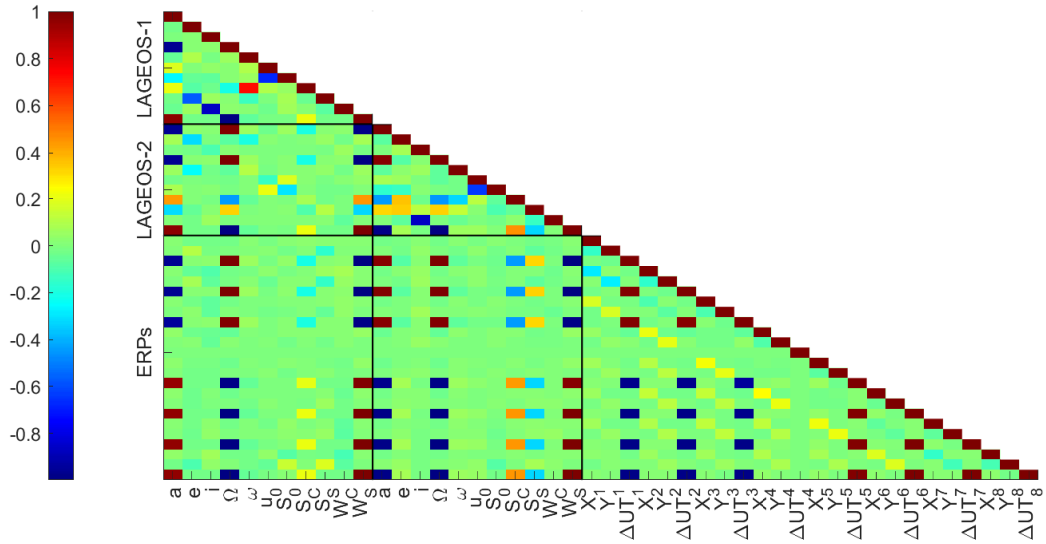

Figure 6.2: Mean correlation matrix of the six osculating orbital parameters, the dynamic orbit parameters and the ERPs of LAGEOS-1/2 SLR combinations for the year 2015.

with the ratio of universal time to sidereal time $\rho \approx 1.0027379$.
The main effects causing a secular perturbation in the Keplerian elements, especially in Ω, are the empirical accelerations estimated in cross-track direction, the SH geopotential coefficient C_{20} (see Sec. 6.3), and relativistic effects (Bloßfeld et al. 2014). The changes in the argument of latitude $\dot{u}_0$ is mainly affected by changes in the semi-major axis a (Bloßfeld et al. 2014).

In the following, the impact of the OPR-W accelerations on the estimates of UT1-UTC is analyzed. The perturbation of Ω caused by the cross-track terms (W) follows from the Gaussian perturbation equations (Beutler et al. 2005a) and reads as

$$\dot{\Omega} = \frac{r \cdot \sin(u)}{na^2\sqrt{1-e^2}\sin(i)} \left(W_0 + W_S \sin(u) + W_C \cos(u)\right) \tag{6.2}$$

Table 6.3: Estimated ERP corrections w.r.t. the IERS-14-C04 reference series and the mean RMS of the observation residuals of LAGEOS-1/2 resulting from SLR combinations based on LAGEOS-1/2 data, when the ERPs are PWL parametrized with (w/) and without (w/o) estimating OPR-W accelerations for the year 2015.

OPR-W acc.	Mean RMS obs. res. [mm]	X-pole [μas]		Y-pole [μas]		UT1-UTC [μs]	
		Bias	WRMS	Bias	WRMS	Bias	WRMS
w/	9.28±1.51	60.3	127.9	69.6	114.0	−0.1	61.8
w/o	14.20±2.73	48.7	191.5	80.1	175.8	−7.4	23.8

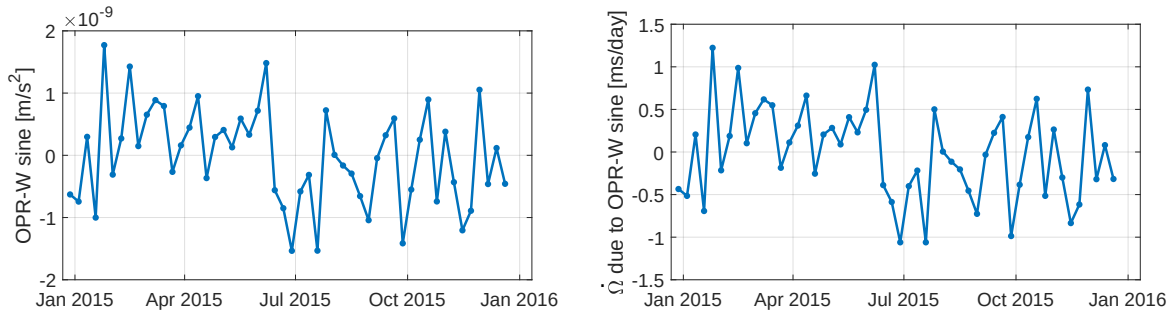

Figure 6.3: Estimated OPR-W sine accelerations (left) of LAGEOS-1 and the induced perturbations of the ascending node Ω (right) of LAGEOS-1 (see Eq. 6.4) from LAGEOS-1/2 SLR combinations for the year 2015.

with the satellite's mean motion

$$n = \sqrt{\frac{GM}{a^3}}. \tag{6.3}$$

Since only the periodic dynamic orbit parameters OPR-W sine (W_S) and cosine (W_C) accelerations are estimated, Eq. 6.2 can be rearranged to

$$\dot{\Omega} = \frac{r \cdot W_S}{2na^2\sqrt{1-e^2}\sin(i)} + \frac{r\,(W_C \sin(2u) - W_S \cos(2u))}{2na^2\sqrt{1-e^2}\sin(i)}, \tag{6.4}$$

where the first term describes a drift in the ascending node and the second term induces periodic variations when integrating Eq. 6.4. For the simultaneous estimation of the mean ascending node only the first term is relevant. For instance, estimated OPR-W sine accelerations of LAGEOS-1 (see Fig. 6.3, left) induce perturbations in the ascending node up to 1 ms/day (see Fig. 6.3, right).
If OPR-W accelerations are not set up, the WRMS w.r.t. the IERS-14-C04 reference series of UT1-UTC can be reduced by more than 50 % (see Table 6.3). On the contrary, the polar motion is significantly degraded by about 60 µas in each direction. The mean RMS of observation residuals increases significantly by 5 mm (see Fig. 6.4).
In conclusion, if the orbit parametrization of LAGEOS-1/2 is realized without OPR-W accelerations, all estimated parameters, except for UT1-UTC, are harmed. Therefore, to

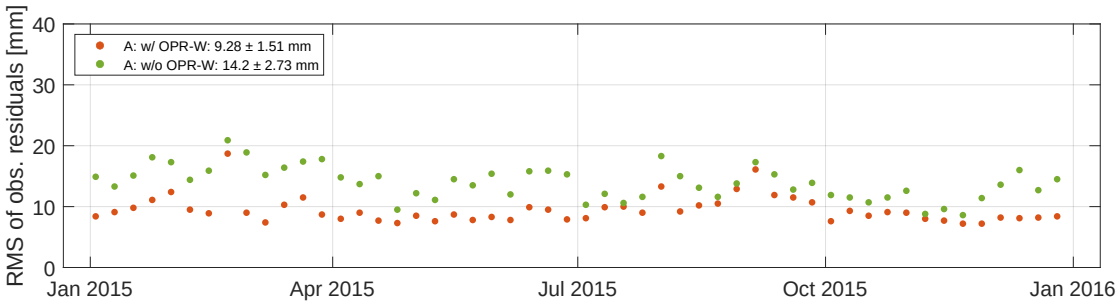

Figure 6.4: Mean RMS of the observation residuals of LAGEOS-1/2 with (w/) or without (w/o) estimating OPR-W accelerations for the year 2015.

reduce the mis-modeling in cross-track, either the background model, e.g., time-variable a priori gravity field model, needs to be replaced by a better model or the set of parameters may be extended, e.g., with the SH geopotential coefficient C_{20} (see Sec. 6.3). Furthermore, pseudo-stochastic pulses in cross-track can partially replace the OPR-W accelerations without causing correlations with SH geopotential coefficients and improving the other geodetic parameters, e.g., ERPs or station coordinates. This is discussed in Section 7.1.3.

6.3 A Priori Gravity Field Models and Co-Estimation of SH Geopotential Coefficient C_{20}

If the SH geopotential coefficients are not estimated in the SLR processing, they are kept fixed to the a priori values given by the pre-defined background model. Hence, any error in the a priori background model leads to systematic errors in the estimates of the parameters. In the following, three different a priori gravity field models and their impact on SLR combinations are analyzed

- GGM05S the standard product provided by the CSR (Tapley et al. 2013): A static gravity field model with SH geopotential coefficients up to degree 180 based on 10 years of Gravity Recovery And Climate Experiment (GRACE) data. The coefficient C_{20} is replaced by an analysis of SLR measurements. Furthermore, C_{21} and S_{21} are computed according to Eq. 6.5.

- Time-variable ILRS: A time-variable gravity field based on the static gravity field model GGM05S, where C_{20} is corrected, while the tesseral coefficients C_{21}/S_{21} and the zonal SH geopotential coefficients from degree 3 up to 6 are replaced by values determined and provided by the ILRS (Pavlis, pers. communication, 2021). The temporal resolution of the corrections and replacements is one week.

- Combination Service for Time-variable Gravity Fields (COST-G): A Fitted Signal Model (FSM) derived from monthly gravity field models, combined from monthly solutions of various analysis centers of COST-G, where the solutions are based on the data of the GRACE and GRACE Follow-On (GRACE-FO) satellite missions (Meyer et al. 2020). The coefficients of the COST-G FSM are modeled by an offset, a drift, as well as by annual and bi-annual periodic functions.
  The low-degree gravity field coefficients, especially the zonal harmonic coefficient C_{20} and C_{30} in case of GRACE-FO, are better determined by SLR (Cheng and Ries 2017, Loomis et al. 2020). Therefore, C_{20} is replaced by a SLR and GRACE/GRACE-FO combination on NEQ level provided by the GFZ (König et al. 2019). In addition, as long as nothing else is mentioned, C_{21} and S_{21} are computed according to Eq. 6.5.

Since C_{21} and S_{21} describe by definition the position of the Earth's figure axis, they can be expressed as (Lambeck 1971)

$$\begin{aligned} C_{21}(t) &= \sqrt{3}\bar{x}_{\mathrm{p}}(t)C_{20} - \bar{x}_{\mathrm{p}}(t)C_{22} + \bar{y}_{\mathrm{p}}(t)S_{22}, \\ S_{21}(t) &= -\sqrt{3}\bar{y}_{\mathrm{p}}(t)C_{20} - \bar{y}_{\mathrm{p}}(t)C_{22} - \bar{x}_{\mathrm{p}}(t)S_{22}, \end{aligned} \tag{6.5}$$

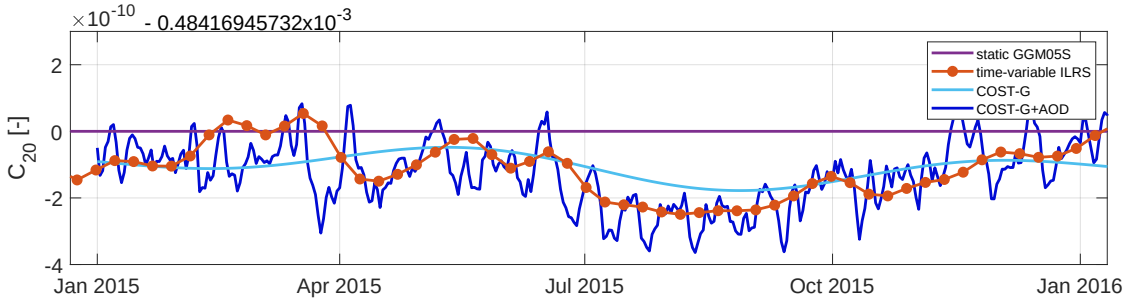

Figure 6.5: Time series of the SH geopotential coefficient C_{20} (zero-tide) given by the three analyzed a priori gravity field models for the year 2015.

with the mean pole coordinates $\bar{x}_p(t)$ and $\bar{y}_p(t)$ according to Petit and Luzum (2010). All SLR combinations presented in this work use a priori gravity field models up to d/o 90 for the orbit determination of the satellites.

The comparison of the time series of the SH geopotential coefficients C_{20}, shown in Figure 6.5, leads to the assumption that in the gravity field estimation procedure of the ILRS the background model for the atmosphere and ocean de-aliasing (AOD) was neglected. Hence, C_{20} provided by the ILRS will additionally contain the mass variability due to the atmosphere and oceans. In contrary to the SH geopotential coefficients of the COST-G, where in the gravity field estimation the AOD products were used.
Since in the SLR processing performed in this work AOD corrections are introduced separately, they are applied twice for the corrected and replaced SH geopotential coefficients of the time-variable gravity field model from the ILRS. Nevertheless, it is better to add AOD corrections than to ignore them altogether.

The SH geopotential coefficient C_{20} represents the oblateness of the Earth. The equatorial bulge induces a rotation of the angular momentum vector of a satellite Earth orbiter (Seeber 2003). Therefore, the orbital plane of the satellite rotates and the ascending node is precessing. Furthermore, a non-polar satellite orbit is perturbed in cross-track by the gravitational force of the equatorial bulge. Hence, C_{20} is strongly correlated with the OPR-W sine accelerations (Jäggi et al. 2012). Perturbing accelerations acting on a satellite caused by variations of C_{20} (ΔC_{20}) read as

$$\begin{pmatrix} R' \\ S' \\ W' \end{pmatrix}_{C_{20}} = GMa^2 \Delta C_{20} \frac{3}{2} \frac{1}{r^4} \begin{pmatrix} 1 - \frac{3}{2}\sin^2(i) + \frac{3}{2}\sin^2(i)\cos(2u) \\ \sin^2(i)\sin(2u) \\ \sin(2i)\sin(u) \end{pmatrix}. \tag{6.6}$$

The impact of different a priori gravity field models and of different parametrizations, e.g., with or without OPR-W accelerations or C_{20}, on weekly SLR combinations of LAGEOS-1/2 are studied for the year 2015. The quality of the SLR combinations are analyzed by comparing the estimates of parameters, e.g., ERPs, station coordinates, C_{20} and observation residuals.

When OPR-W accelerations are estimated and SH geopotential coefficients are fixed to

the corresponding a priori values, the COST-G model improves the polar motion w.r.t. the time-variable ILRS model by more than 5 % (see Table 6.4). On the contrary, the WRMS and the bias of UT1-UTC are degraded by 28 % and 83 %, respectively.

The absence of the OPR-W accelerations causes the geodetic parameters to partially absorb mis-modelings. Hence, the WRMS of the polar motion increases by more than 60 µas. Nevertheless, for this parametrization, the COST-G model shows the smallest biases in all ERPs. In addition, it also reduces the WRMS of all ERPs, except for the polar motion in x-direction. Since, however, the correlation between OPR-W sine accelerations and UT1-UTC are significantly reduced, UT1-UTC can be better determined. Hence, the WRMS of UT1-UTC is reduced by more than 50 %.
If OPR-W accelerations are neglected, the estimation of C_{20} improves all ERPs, except for the bias of the polar motion in y-direction, independent of the a priori gravity field model. Moreover, the estimated ERPs are comparable, such that the bias and WRMS of the polar motion are within 15 µas and 7 µas, respectively. However, the level of the WRMS of the polar motion, where the OPR-W accelerations are estimated, cannot be achieved as long as no additional pseudo-stochastic pulses in cross-track are applied (see Sec. 7.1.3).

The comparison of the weighted mean RMS of the Helmert transformation of the estimated station coordinates w.r.t. the SLRF2014 reference is not an independent quality control and has to be interpreted carefully. The station positions and velocities in SLRF2014 are computed based on LAGEOS-1/2 SLR data, where the orbits are parametrized by the six osculating and five dynamic orbit parameters. Therefore, it is to be expected that changing the parametrization and/or the SLR data set, i.e., include SLR data to other geodetic satellites than LAGEOS-1/2, may increase the mean RMS of the Helmert transformations. However, the SLRF2014 is the only reliable reference for SLR station coordinates and is therefore used for the station coordinate validation.

Table 6.4: Estimated ERP corrections w.r.t. the IERS-14-C04 reference series using only LAGEOS-1/2 data with different a priori gravity field models and with or without estimating OPR-W accelerations for the year 2015.

Grav. model	OPR-W acc.	SH geop. coeff.	X-pole [μas] Bias	X-pole [μas] WRMS	Y-pole [μas] Bias	Y-pole [μas] WRMS	UT1-UTC [μs] Bias	UT1-UTC [μs] WRMS
Static	w/	w/o	83.3	135.2	66.6	107.6	−3.8	70.6
ILRS	w/	w/o	60.3	127.9	69.6	114.0	−0.1	61.8
COST-G	w/	w/o	59.7	119.7	65.6	108.0	−8.4	79.0
Static	w/o	w/o	76.7	237.6	63.6	228.5	−10.0	30.2
ILRS	w/o	w/o	48.7	191.5	80.1	175.8	−7.4	23.8
COST-G	w/o	w/o	48.7	194.2	60.7	165.2	−6.7	23.3
Static	w/o	w/ C_{20}	55.8	159.8	72.2	138.5	−5.2	24.3
ILRS	w/o	w/ C_{20}	42.2	155.2	81.9	139.7	−4.5	24.7
COST-G	w/o	w/ C_{20}	41.3	153.0	72.8	140.0	−3.9	22.2

In this case, the comparison of the weighted mean RMS of the Helmert transformation of the estimated station coordinates shows that when OPR-W accelerations are estimated the values are almost identical for each a priori gravity field model (see Table 6.5). In general, the omission of the OPR-W accelerations increases the weighted mean RMS in each component (see Fig. 6.6, left). SLR combinations using a static gravity field model suffer most, such that the North and East components are degraded by more than 85 % and the Up component by 35 %, respectively. However, the estimation of C_{20} is again able to reduce the RMS of the Helmert transformation of station coordinates in all directions to the same level, independent of the applied a priori gravity field model (see Fig. 6.6, right).

Without estimating OPR-W accelerations, the RMS of the observation residuals of both LAGEOS satellites becomes larger (see Table 6.5). Already, the estimation of C_{20} reduces the RMS by more than 3 mm. Independent of the a priori gravity field model, the RMS of observation residuals is around 10.8 mm, while the COST-G model induces the smallest scattering.

Finally, Figure 6.7 shows the time series of estimated SH geopotential coefficient C_{20}. As already mentioned, the estimates of C_{20}, where the OPR-W accelerations are estimated, are not reliable. All other solutions show a small offset w.r.t. the CSR reference series. Nevertheless, they follow the same trend and feature only small variations. The time series of C_{20} estimated based on the static and the time-variable ILRS a priori gravity field models are almost identical. Only the solution with the COST-G model has a slightly different behaviour at some time periods, where it is shifted towards the CSR reference series. This is probably caused by strong correlations with the higher zonal SH geopotential coefficients, i.e., C_{40} and C_{60}, which are fixed to the a priori gravity field coefficients.

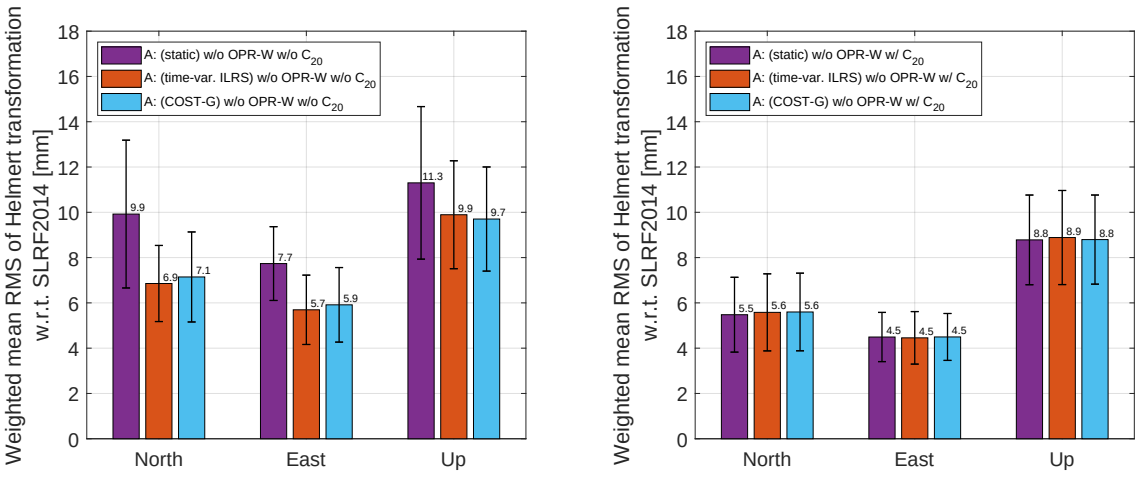

Figure 6.6: Weighted mean RMS of Helmert transformations of station coordinates w.r.t. SLRF2014 of SLR combinations based on LAGEOS-1/2 data, without using OPR-W accelerations for the orbit parametrization and fixing the SH geopotential coefficients to a priori values from different gravity field models (left) or when instead of the OPR-W accelerations C_{20} is estimated using different a priori gravity field models (right) for the year 2015.

Table 6.5: Mean RMS of observation residuals of LAGEOS-1/2 and the weighted mean RMS of Helmert transformations of station coordinates w.r.t. SLRF2014 in North, East and Up resulting from SLR combinations based on LAGEOS-1/2 data using different a priori gravity field models and when neglecting or estimating OPR-W accelerations for the year 2015.

Grav. model	OPR-W acc.	SH geop. coeff.	Mean RMS obs. res. [mm]	Weighted mean RMS of Helmert transformation [mm]		
				North	East	Up
Static	w/	w/o	9.44±1.90	4.9	4.1	8.3
ILRS	w/	w/o	9.28±1.51	4.9	4.2	8.3
COST-G	w/	w/o	9.39±1.93	4.9	4.1	8.3
Static	w/o	w/o	18.4 ±3.64	9.9	7.7	11.3
ILRS	w/o	w/o	14.2 ±2.73	6.9	5.7	9.9
COST-G	w/o	w/o	14.2 ±3.66	7.1	5.9	9.7
Static	w/o	w/ C_{20}	10.8 ±2.32	5.5	4.5	8.8
ILRS	w/o	w/ C_{20}	10.8 ±2.24	5.6	4.5	8.9
COST-G	w/o	w/ C_{20}	10.6 ±2.06	5.6	4.5	8.8

Therefore, the estimates of C_{20} also absorb signals which are related to the other zonal SH geopotential coefficients. Since these higher degree coefficients are different for the COST-G model compared with the static and the time-variable ILRS gravity field, it can only be seen in the estimates of C_{20} where the COST-G model is applied.

In summary, when the a priori gravity field coefficients are fixed, the estimated parameters, e.g., ERPs or station coordinates, change depending on the a priori gravity field model. In this case, the performance of the COST-G model is comparable with the time-variable ILRS model. If C_{20} is estimated instead of OPR-W accelerations , the estimates of the ERPs and station coordinates are almost independent of the used a priori gravity field model. However, since only a limited number of gravity field coefficients, i.e., only C_{20}, are estimated, the correlations between the zonal SH geopotential coefficients can induce a bias in the estimates of C_{20}.

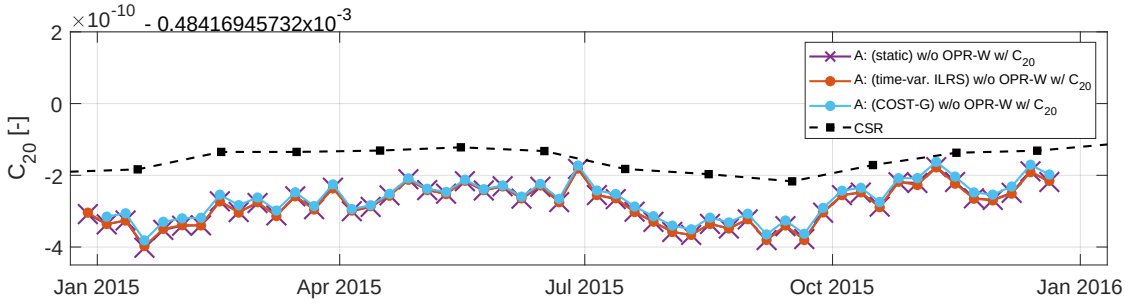

Figure 6.7: Time series of estimated SH geopotential coefficient C_{20} for SLR combinations of LAGEOS-1/2 without estimating OPR-W accelerations and using different a priori gravity field models for the year 2015.

6.4 Orbit Parametrization With Pseudo-Stochastic Pulses

Both LAGEOS-1/2 satellites are orbiting the Earth at relatively high altitudes (see Table 2.2) and, therefore, have very stable orbits, e.g., the mean semi-major axis of LAGEOS-1 and LAGEOS-2 feature a decay of only 20.3 cm/a, resp., 23.9 cm/a during the time period from 1994 to 2011 (Sośnica 2015). The decay can mainly be explained by the Yarkovsky and Yarkovsky-Schach effect (Rubincam 1988, Lucchesi et al. 2003).
Due to this high stability of the LAGEOS-1/2 orbits, it is so far assumed that no additional pseudo-stochastic pulses in *S* or *W* directions are needed in the orbit parametrization (see Table 6.1) to significantly improve the estimation of the parameters. However, the technique of VCE enables the determination of appropriate constraints of pseudo-stochastic pulses (see Sec. 3.4.3). Therefore, weekly SLR NEQs based on LAGEOS-1/2 observations with twice per day pseudo-stochastic pulses in *S* and *W* are generated. Moreover, for each week two NEQs containing only the parameter constraints for the pseudo-stochastic pulses in *S* and *W* are formed. Hence, the following three SLR solutions are validated:

- LAGEOS-1/2 without estimating any pseudo-stochastic pulses.
- LAGEOS-1/2 with estimating twice per day pseudo-stochastic pulses in *S* and *W* without applying any constraints.
- LAGEOS-1/2 with estimating twice per day pseudo-stochastic pulses in *S* and *W*, where the applied constraints on the pseudo-stochastic pulses are estimated with VCE.

The comparison of the estimated pseudo-stochastic pulses for LAGEOS-1 and LAGEOS-2 with or without applying constraints in S, resp., W shows that VCE assigns constraints on the pseudo-stochastic pulses (see Fig. 6.8). Consequently, outliers are mitigated and the pseudo-stochastic pulses in *S* are significantly smaller than in *W* with 0.39 µm/s and 7.34 µm/s, respectively, for LAGEOS-1. The strength of the constraints can also be characterized by the estimated weights of NEQs containing only the parameter constraints of pseudo-stochastic pulses (see Fig. 6.9). The weights for the constraints in *S* are larger than in *W* by a mean factor of 10^2. This implies that the previous orbit parametrization with six osculating orbit parameters and five dynamic orbit parameters, i.e., constant acceleration in *S*, OPR sine and cosine accelerations in *S* and *W*, features more modeling deficiencies in *W* than in *S*. However, this may be a result of missing constant accelerations in *W*.

If pseudo-stochastic pulses for LAGEOS-1/2 are estimated without applying any constraints, the WRMS of the polar motion increases by more than 5 % in x-direction and 24 % in y-direction, respectively (see Table 6.6). If, however, constraints according to VCE are applied, the WRMS of the polar motion can be reduced by more than 9 µas. On the contrary, the bias of the X-pole increases by 15 %, while UT1-UTC does not change significantly for different orbit parametrizations.
The weighted mean RMS of Helmert transformations of station coordinates are improved most by estimating pseudo-stochastic pulses and applying constraints according

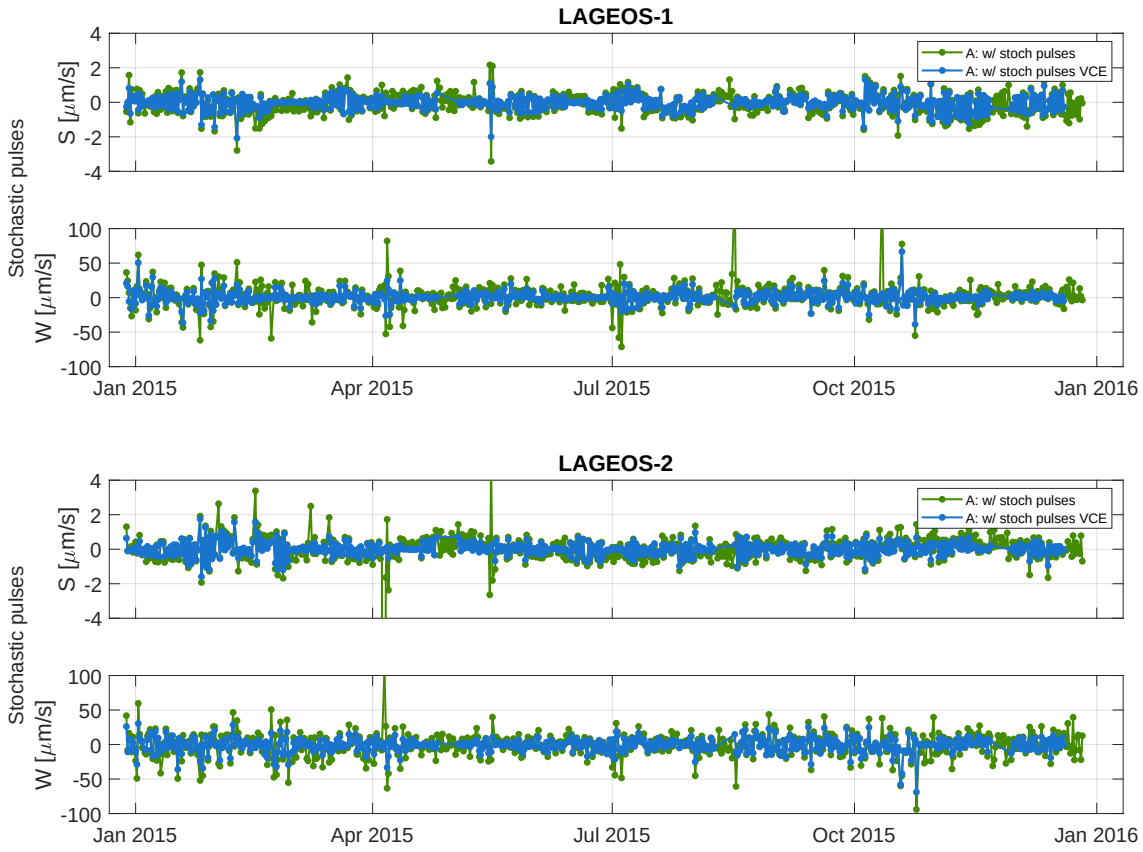

Figure 6.8: Estimated pseudo-stochastic pulses twice per day in *S* and *W* for LAGEOS-1 (top) and LAGEOS-2 (bottom) with or without applying constraints derived by VCE of LAGEOS-1/2 SLR combinations in the year 2015.

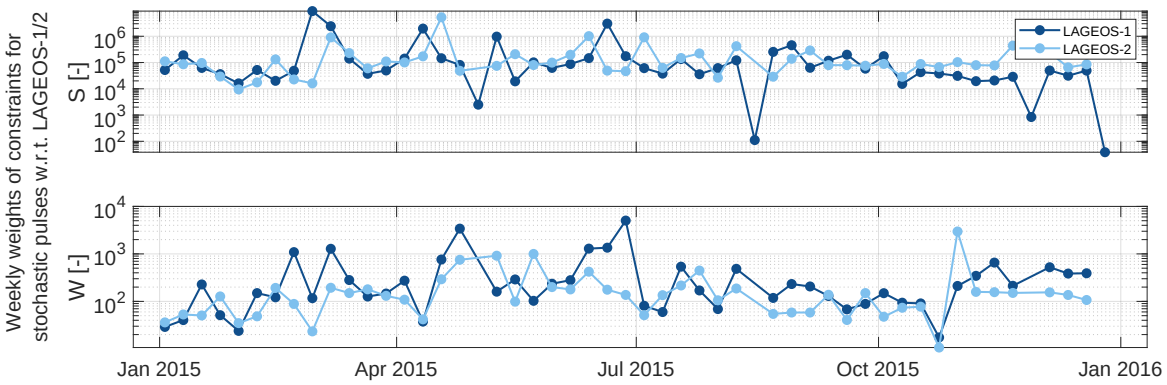

Figure 6.9: Weekly weights derived by VCE of the constraints for pseudo-stochastic pulses in *S* and *W* w.r.t. the weights of LAGEOS-1/2 for the year 2015.

Table 6.6: Estimated ERP corrections w.r.t. the IERS-14-C04 reference series and the mean RMS of the observation residuals of LAGEOS-1/2 when pseudo-stochastic pulses twice per day in *S* and *W* for LAGEOS-1/2 are set up and the constraints are derived by VCE of LAGEOS-1/2 SLR combinations for the year 2015.

Stoch. pulses in *S*/*W* applied	constr.	X-pole [μas] Bias	WRMS	Y-pole[μas] Bias	WRMS	UT1-UTC [μs] Bias	WRMS	Mean RMS of obs. residuals [mm] LAGEOS-1	LAGEOS-2
w/o		60.4	128.0	69.6	114.0	1.1	60.4	9.29 ±1.62	9.09 ±1.57
w/	none	59.9	135.0	79.0	141.8	−1.4	57.1	8.43 ±1.62	8.27 ±1.63
w/	VCE	69.0	125.9	80.3	128.9	1.2	59.0	8.37 ±1.58	8.26 ±1.66

to VCE (see Fig. 6.10). The RMS is reduced by 0.4 mm in the horizontal plane and 0.2 mm in Up.
With the estimation of the pseudo-stochastic pulses, the mean RMS of the observation residuals can be reduced by 9 % (see Table 6.6). However, this is to be expected because the additionally estimated parameters, i.e., pseudo-stochastic pulses, enable to compensate for mis-modelings.

The orbits are analyzed by comparing the improved 7-day true-arc solutions with the predicted orbit from the previous weekly SLR combination (see Fig. 6.11).
If pseudo-stochastic pulses are omitted, the orbit position differences in *S* are in most cases the smallest. Furthermore, constraints on pseudo-stochastic pulses estimated by VCE can to a certain extent prevent the orbit position differences from diverging in time. Nevertheless, the long-term orbit stability is impaired when pseudo-stochastic pulses for LAGEOS-1/2 are set-up.
Furthermore, the additional number of parameters increases by 26 per satellite. Con-

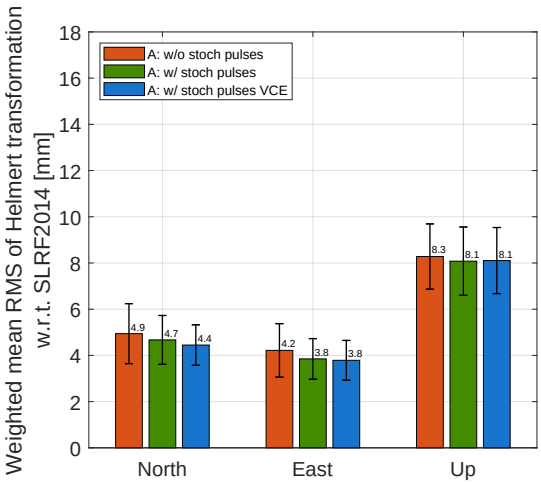

Figure 6.10: Weighted mean RMS of Helmert transformation of station coordinates w.r.t. SLRF2014 resulting from LAGEOS-1/2 SLR combinations when pseudo-stochastic pulses twice per day in *S* and *W* for LAGEOS-1/2 are set up and their constraints are derived by VCE for the year 2015.

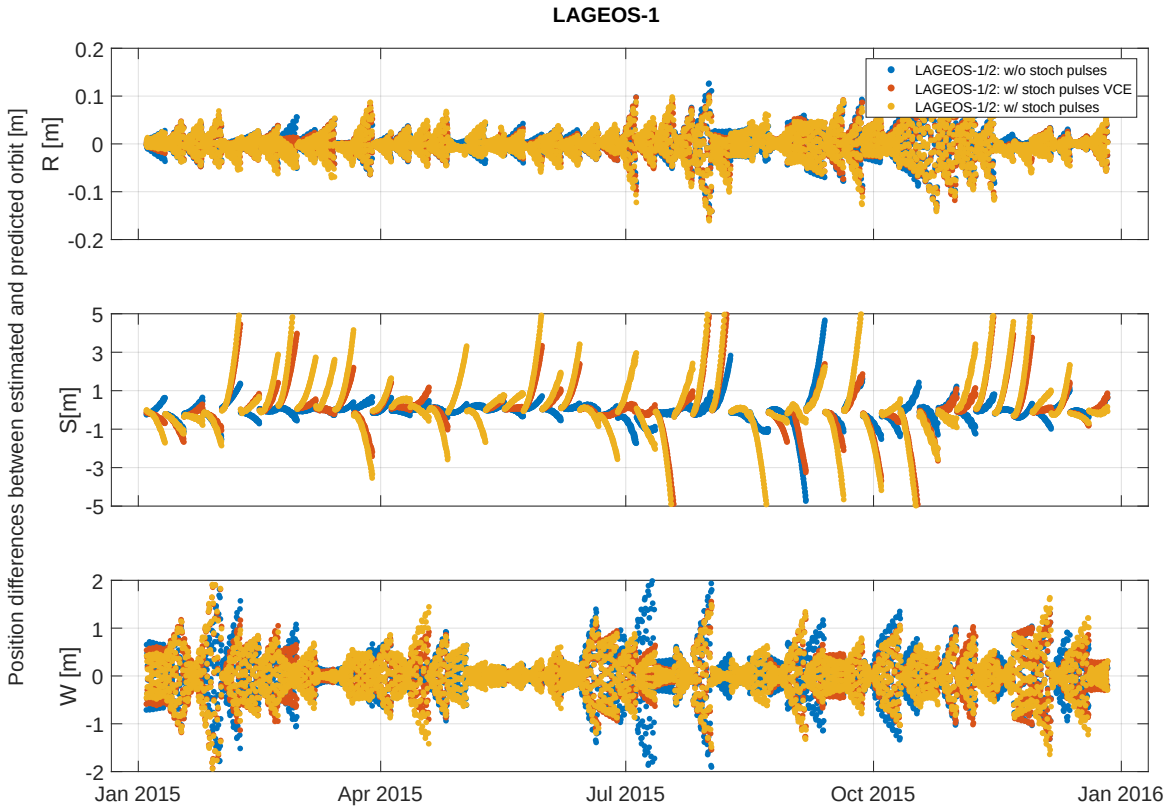

Figure 6.11: Position differences in the $\mathcal{R}$-system between estimated and predicted 7-day orbits of LAGEOS-1 resulting from LAGEOS-1/2 SLR combinations when no additional pseudo-stochastic pulses are estimated (blue) or when pseudo-stochastic pulses twice per day for LAGEOS-1/2 are set up free (red) or with constraints derived by VCE (yellow) for the year 2015.

sequently, the degree of freedom used in a least-squares adjustment is reduced and the accuracy and reliability of the statistical analysis is reduced. In all further SLR combinations, as a consequence, the orbits of LAGEOS-1/2 are parametrized without applying any pseudo-stochastic pulses.

6.5 VCE Weights per SLR Station

In the SLR processing at AIUB each NP is equally weighted. Hence, no further station information, e.g., number of SLR full-rate data compressed into a NP or the bin RMS of these full-rate data, is used. As mentioned in Section 4, only the outliers of the NP data are eliminated.
Due to the diversity of SLR stations, e.g., laser systems or photo-detectors (see Sec. 2.1), the measurement performance of each station can be different. Consequently, each NP or at least the contribution of each SLR station should ideally be weighted according to their quality.

In the following, the influence of a station- and satellite-specific weighting derived by VCE (see Sec. 3.4.2) in SLR combinations based on LAGEOS-1/2 data, is studied. For

this purpose, NEQ systems based on weekly observations provided by one individual SLR station to one specific satellite, i.e., LAGEOS-1 and LAGEOS-2, are generated. The number of NEQ systems of a weekly LAGEOS-1/2 SLR solution is then the sum of the number of stations providing NP data to LAGEOS-1 and the number of stations providing NP data to LAGEOS-2. Since not every SLR station observes both satellites, it might contribute with only one NEQ system.

The quality of a station- and satellite-specific weighting scheme is validated by analyzing the determined weights and by comparing the estimated geodetic parameters, i.e., ERPs and station coordinates, for the year 2015.
The (unnormalized) mean weights per station and satellite, i.e., LAGEOS-1 and LAGEOS-2, over the year 2015 are summarized in Figure 6.12. The highest mean weights get LAGEOS-1 data provided by the SLR stations in Graz, Austria (7839) with 5.57 and in Tahiti, French Polynesia (7124) with 5.52, respectively. However, their weights for the LAGEOS-2 observations are at least 40 % smaller with 2.66 and 3.19. With a mean of 4.14 receives the SLR station in Grasse, France (7845) the highest weight over all stations observing LAGEOS-2. However, the received mean weights cannot be related to the mean number of provided observations.
Furthermore, 15 different SLR stations get a mean weight below 1. Three of them are located in China (7821, 7249, 7237), seven are located in Russia (1891, 1890, 1889, 1888, 1886, 1874, 1868), four in Eastern Europe (1893, 1887, 1873, 1824) and only one station in Western Europe (7824). Consequently, these stations have only a marginal impact on SLR combinations.

To get a better understanding of station- and satellite-specific VCE, the derived weights are compared with the corresponding observation residuals for LAGEOS-1 data pro-

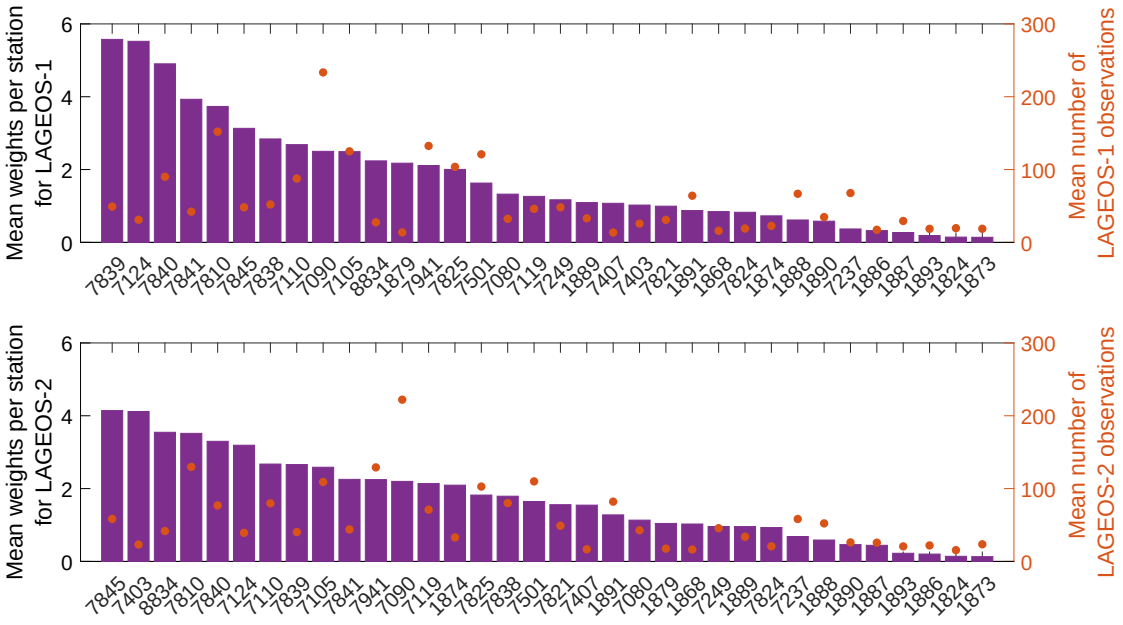

Figure 6.12: Mean weights per stations for LAGEOS-1 and LAGEOS-2 from the VCE of LAGEOS-1/2 SLR combinations for the year 2015.

vided by SwissOGS for the year 2015 (see Fig. 6.13). For some of the weekly SLR combinations, e.g., at the begin or end of September, the RMS of the observation residuals is larger, but also the inverse of the corresponding weight increases. Hence, VCE ensures that the influence of observations with large residuals is reduced. However, if a station has a temporary performance problem during the week, such that some of the observation residuals become larger, the whole weekly contribution of this station is down weighted, even if it also provides good observations. Consequently, it might be beneficial in the future to weight the contribution of SLR stations per day or even per each individual observed pass of a satellite.
However, not all weights can be explained by the RMS of the observation residuals. There are also other factors, e.g., the temporal distribution over the satellite passes, or the simultaneous performance of the other SLR stations.

The comparison of the estimated geodetic parameters reveals that the station- and satellite specific VCE reduces the bias of the X-pole by 14 %, while the WRMS of the Y-pole is decreased by 6.6 µas (see Table 6.7). Only the bias and WRMS of UT1-UTC are increased by 14 % and 1.4 µs, respectively.
The weighted mean RMS of the Helmert transformation of station coordinates are comparable, except for the up component, which is slightly increased by 2 % when the station and satellites are weighted individually (see Table 6.7).

In conclusion, station-specific weighting derived by VCE can be used for SLR combinations, although their impact on the estimated geodetic parameters is limited. Since the weights reflect the quality of the NPs provided by each station, this method could possibly be used in the procedure of the SLR NP data screening.

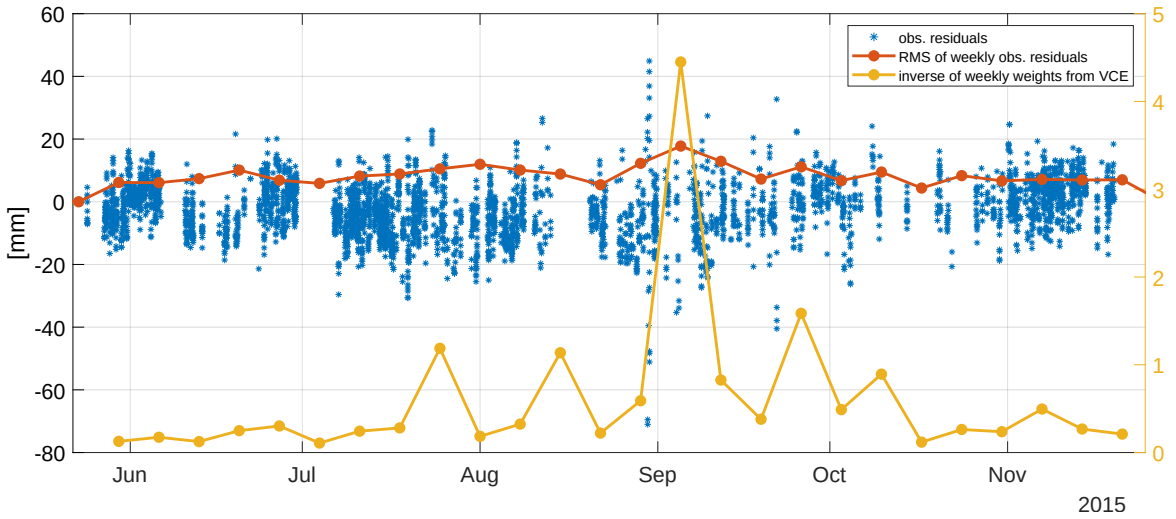

Figure 6.13: Comparison of the observation residuals (blue) and the weekly RMS (red) of LAGEOS-1/2 data provided by SwissOGS with the estimated station-specific weights derived by VCE (yellow) for the SwissOGS.

Table 6.7: Estimated ERP corrections w.r.t. the IERS-14-C04 reference series and the weighted mean RMS of the Helmert transformation of station coordinates w.r.t. SLRF2014 resulting from LAGEOS-1/2 SLR combinations with or without using the station- and satellite-specific VCE for the year 2015.

Stat./Sat.-specific VCE	X-pole [μas]		Y-pole[μas]		UT1-UTC [μs]		Weighted mean RMS of Helmert transf. [mm]		
	Bias	WRMS	Bias	WRMS	Bias	WRMS	North	East	Up
w/o	61.4	129.5	69.6	114.1	−0.1	61.8	4.9	4.2	8.3
w/	52.8	129.5	69.6	107.7	−1.5	59.7	4.9	4.2	8.5

6.6 Datum Definition

As discussed in Section 4.3.1, depending on the set of parameters, the application of constraints on particular parameters, e.g., station coordinates, is essential to prevent NEQ systems from becoming singular. For this reason, the datum definition is realized by applying MC conditions, i.e., NNR and NNT, on a subset of SLR stations (here also called *core stations*).
Coulot et al. (2010) and Zajdel et al. (2019) showed that the choice of core stations used for the datum definition has an impact on the stability of ERP time series. Further studies, e.g., Otsubo et al. (2016), illustrated that also the geographical distribution of SLR stations influences the estimation of geodetic parameters. It is therefore important to perform a stable datum definition in the SLR processing.

In order to study the influence of the datum realization on the co-estimated geodetic parameters, weekly LAGEOS-1/2 SLR combinations using different sets of core stations are analyzed for the years 2015-2020. Since, however, only an average of 24 and at least 13 SLR stations provided LAGEOS-1/2 data, the number of possible core stations and

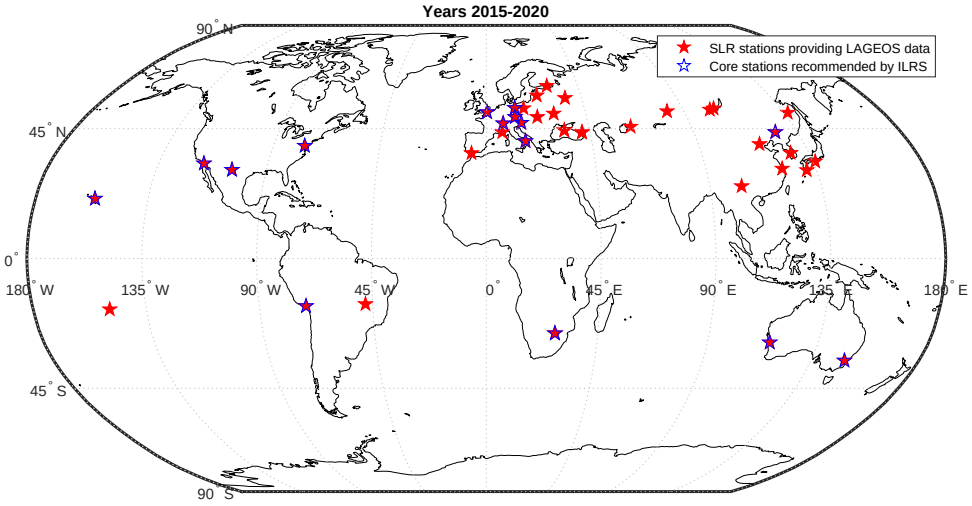

Figure 6.14: Geographical distribution of SLR stations providing LAGEOS-1/2 data during the time span 2015-2020.

their geographical distribution is inhomogeneous and may change on a weekly basis. The list of core stations can either be pre-defined and fixed or iteratively determined with the use of Helmert transformations. The latter method is very similar to the approach used in Zajdel et al. (2019) and is illustrated in Figure 6.15. First, an a priori list of core stations is defined containing either

- core stations recommended by the ILRS (ILRS) (see Fig. 6.14),
- SLR stations with a station number higher than 7000 (7000) (motivated by the weights derived by VCE, see Fig. 6.12) or
- all SLR stations (ALL).

Then, the weekly SLR combinations are processed, whereas NNR/NNT MC conditions are applied on the core stations of the pre-defined list. The estimated station coordinates are then compared with the corresponding station coordinates given by the ITRF using a Helmert transformation. If the largest residual in North, East or Up exceeds a predefined threshold, e.g., 25 mm, the corresponding SLR station is rejected from the list. Afterwards, the adjusted list of core stations is used again for the parameter estimation. This process is repeated until all residuals of the core station coordinates are lower than the threshold. It ensures that only stations with a high station coordinate stability are used for the datum definition.

In the following, the datum definition within the parameter estimation is realized by using three different pre-defined lists of core stations, i.e., ILRS, 7000 or ALL, and

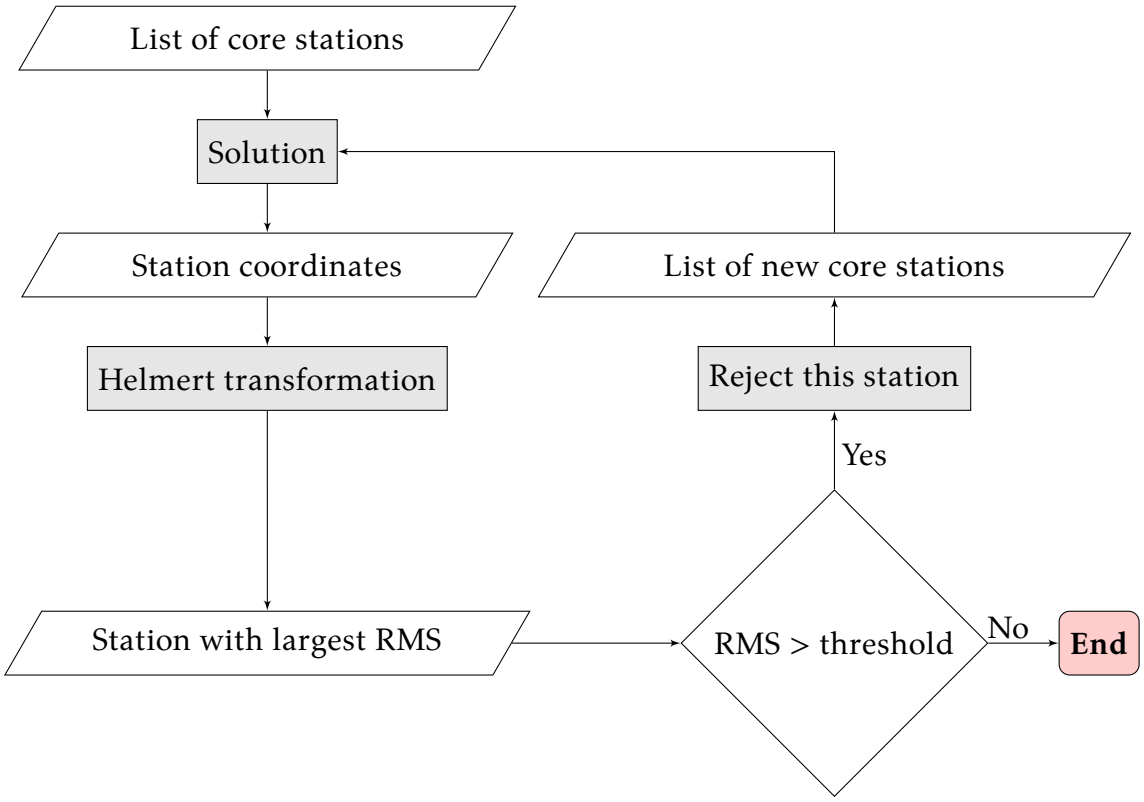

Figure 6.15: Schematic illustration of the Helmert approach to determine the list of core stations, which should be used for the datum definition.

by applying the Helmert transformation approach with three different thresholds, i.e., 10 mm, 25 mm and 50 mm. For simplicity, the SLR combinations are abbreviated by the name of the used pre-defined list of core stations and if the Helmert transformation approach is used (-T) and the corresponding threshold, e.g., ILRS-T25.
The quality of the SLR combinations are analyzed by comparing the list of used core stations and the geodetic parameters, i.e., ERPs, station and geocenter coordinates.
The percentage occurrence of SLR stations as core stations reveals that except for the stations 7237 (Changchun, China) and 7403 (Arequipa, Peru), the Helmert transformation approach using a threshold of 25 mm rejects almost no core stations recommended by the ILRS (see Fig. 6.16). The time series of the Helmert transformations of the SLR stations 7237 and 7403, shown in Figure 6.17, confirms the weak stability of the station coordinates, especially in comparison with the very stable station 7090 in Yarragadee, Australia. While station 7403 has a large scatter in all three directions and contributes on an irregular basis, station 7237 features an annual signal in the Up component.
Consequently, as a precautionary measure, these two stations may not be considered as core stations.
Furthermore, the solution ALL-T25 makes use of 25 other stations for the datum definition, which are not recommended by the ILRS. However, only eleven of them are used in more than 20 % of all weekly SLR combinations.

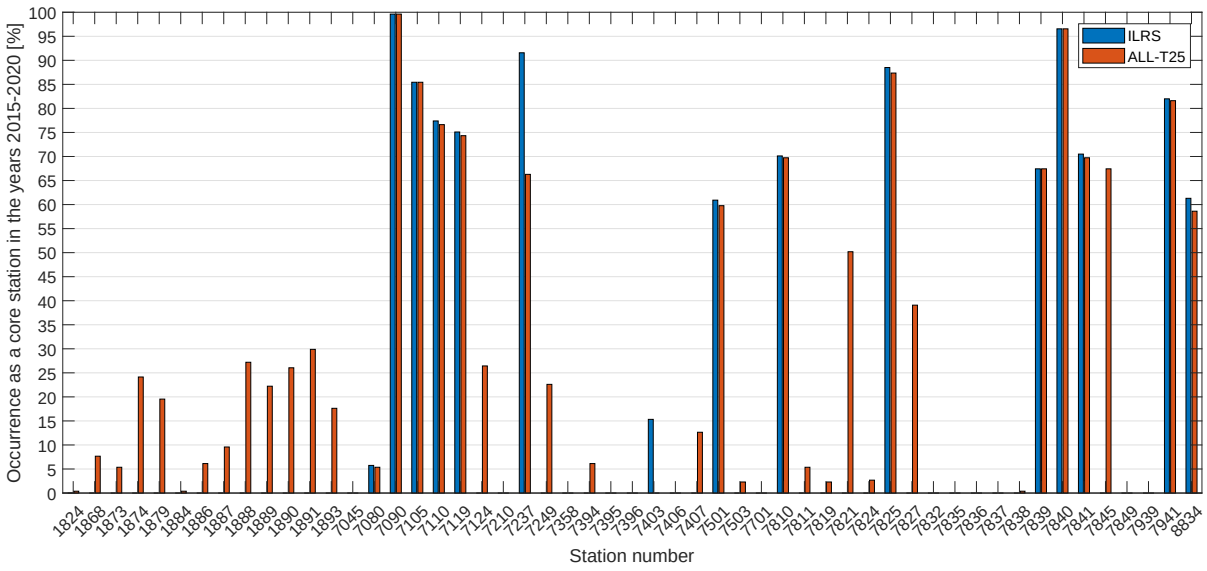

Figure 6.16: Occurrence as SLR core station in the years 2015-2020 for the solutions ILRS (blue) and ALL-T25 (orange).

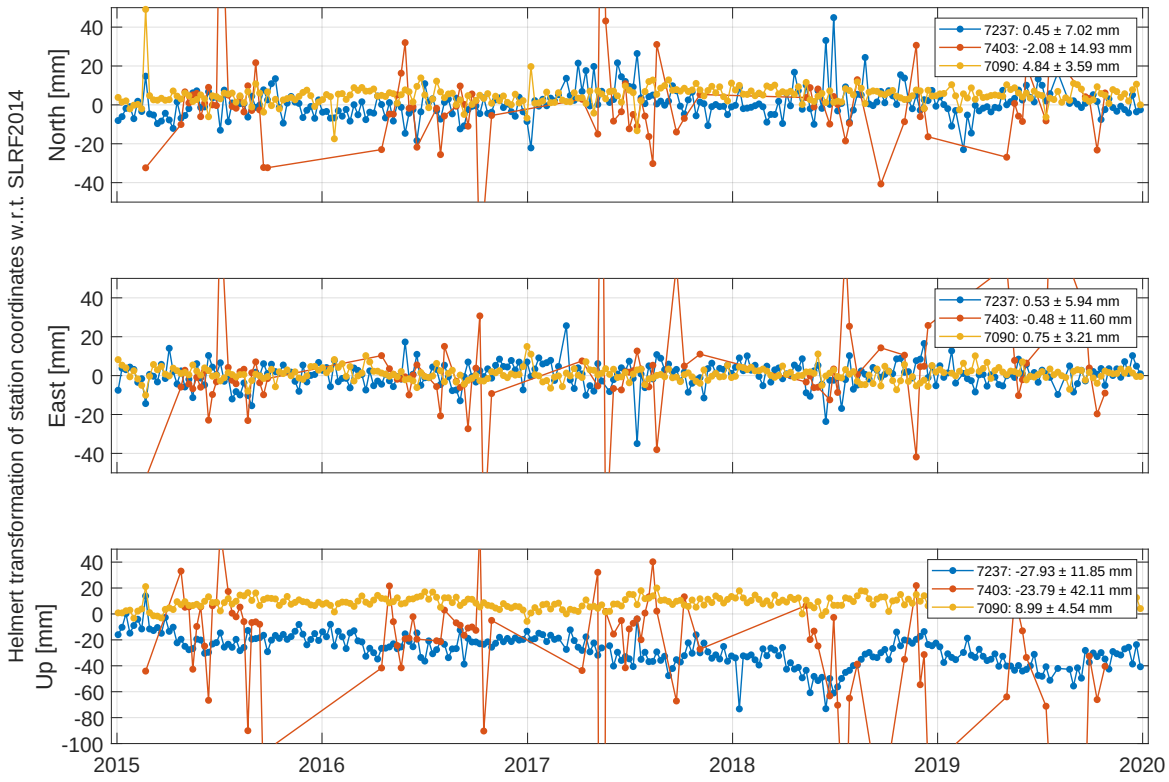

Figure 6.17: Time series of the Helmert transformation from the estimated station coordinates w.r.t. SLRF2014 in North, East and Up for the SLR stations 7237 (blue), 7403 (orange) and 7090 (yellow) for the years 2015-2020. The datum definition is realized by using the ILRS core station list without the Helmert approach.

The comparison of estimated polar motion corrections w.r.t. the IERS-14-C04 reference series shows that the bias and WRMS in x-direction are significantly larger than in the corresponding y-direction regardless of the datum realization (see Table 6.8). E.g., for the ILRS solution, the bias and WRMS between the X- and Y-pole differ by 63 % and 17 %. This is a consequence of the inhomogeneous geographical distribution of the SLR core stations. The SLR station clustering in Europe enhances a better determination of the meridian plane passing through Greenwich and improves the estimation of polar motions in y-direction, which coincide with the 90 °W meridian.
The systematic shift of the polar motion w.r.t. the reference series can be reduced when the geographical distribution is improved by using more stations for the datum definition (compare solutions ILRS, 7000 and ALL in Table 6.8). If, in contrast to the pre-defined core stations of the ILRS, all stations are used for the realization of the datum definition, the bias of polar motions in x- and y-direction is reduced by 42 % and 92 %, respectively.

Since the rejection level of the iterative Helmert transformation with a threshold of 10 mm is smaller than the observation accuracy of station coordinates, the quality of the estimated polar motion is degraded. The bias of the polar motion in x- and y-direction is significantly increased by 43 µas and 69 µas when the pre-defined core station list ALL is used and the threshold is reduced from 25 mm to 10 mm. The low threshold leads to

Table 6.8: Mean estimated scale of the Helmert transformation w.r.t. the SLRF2014 and the estimated ERP corrections w.r.t. IERS-14-C04 series from LAGEOS-1/2 SLR combinations using different datum definitions for the years 2015-2020.

Sol-ID	List of core stations	Apply Helmert	Threshold [mm]	Scale [ppb]	X-pole [μas] Bias	X-pole [μas] WRMS	Y-pole [μas] Bias	Y-pole [μas] WRMS
ILRS	ILRS	No	-	−0.091	85.6	142.1	31.9	118.1
ILRS-T50	ILRS	Yes	50	−0.067	84.1	140.9	28.9	116.2
ILRS-T25	ILRS	Yes	25	0.098	101.6	151.4	38.3	115.9
ILRS-T10	ILRS	Yes	10	0.325	114.6	159.9	80.7	135.1
7000	7000	No	-	−0.385	50.2	141.6	11.0	135.4
7000-T50	7000	Yes	50	−0.297	47.3	140.3	22.1	133.3
7000-T25	7000	Yes	25	−0.140	56.8	133.7	24.4	120.7
7000-T10	7000	Yes	10	0.276	106.4	152.5	77.6	138.1
ALL	ALL	No	-	−0.164	49.7	153.1	2.4	138.3
ALL-T50	ALL	Yes	50	−0.148	53.6	146.2	13.1	133.2
ALL-T25	ALL	Yes	25	−0.034	69.7	141.9	2.6	121.1
ALL-T10	ALL	Yes	10	0.292	113.0	157.1	71.8	134.3

a significant reduction of the number of core stations used for the datum definition. For this reason, only the SLR combinations using Helmert transformations with a threshold of 25 mm or 50 mm are further discussed.
In the case of the pre-defined ILRS core station list, the bias and WRMS of polar motions can be slightly improved by using the Helmert transformations with a threshold of 50 mm (see Table 6.8). Although this threshold is very loose, it prevents that especially the station 7403 is rejected for the datum definition. The contribution of this station to the datum definition is small because it rarely tracked LAGEOS-1/2 during the time period of 2015-2020, such that it occurs only in 15 % of the SLR combinations. If the threshold is set to 25 mm, also the station 7237 is rejected in many cases. Since this station provides LAGEOS-1/2 data for 92 % of the weekly SLR combinations, the bias and the WRMS of the polar motion increase by at least 34 % and 13 %, respectively. It is the only station located in the Northeast that is present in the pre-defined ILRS core station list.
Since the a priori list of ILRS core stations is already strongly reduced, i.e., on average 10 stations are used for datum definition, a small threshold reduces the number of core stations even more, such that the realization of a proper datum definition is not possible anymore.
Using the list of core stations 7000 or ALL without the Helmert transformation increases the WRMS of the polar motion, where the bias simultaneously decreases w.r.t. the ILRS based solution. A medium threshold of 25 mm improves the WRMS of the polar motion the most. A looser threshold may cause also unstable stations to be used for the datum definition, which reduces the quality of the polar motion estimation.

The scale of the frame corresponds to the estimated scaling factor of the Helmert transformation w.r.t. the a priori reference frame SLRF2014 and is a measure of consistency

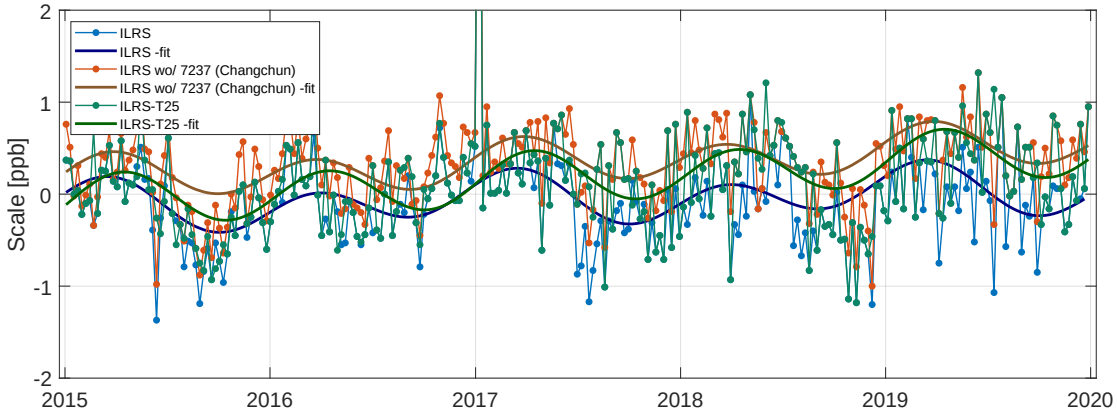

Figure 6.18: Time series of the estimated scales from the Helmert transformation w.r.t. the a priori reference frame SLRF2014.

with the reference. Already earlier studies, e.g. Angermann and Müller (2009) or Zajdel et al. (2019), showed an impact of the SLR station network, which is used to realize the datum definition, on the estimation of the scale. This can be confirmed by the results given in Table 6.8.
The difference between the mean scales derived by using different datum definitions, where the Helmert transformation with a threshold of 10 mm is excluded, is 0.48 ppb. Moreover, the range of the estimated scales is almost three times smaller than the scale offset between SLR and VLBI solutions in the ITRF2014 reference frame (Altamimi et al. 2016).
The time series of the estimated scales show in general an increasing variation with time (see Fig. 6.18). However, this is to be expected, since the quality of the reference frame SLRF2014 decreases after 2015. Furthermore, if the datum definition is realized without station 7237 in Changchun, China, the offset of the scale differs by 0.30 ppb.

Station 7237 is very productive and therefore strongly contributes to LAGEOS-1/2 SLR combinations. To further study the impact of this station also the geocenter coordinates are analyzed (see Fig. 6.19). The comparison is made between LAGEOS-1/2 SLR combinations when the datum is realized based on the ILRS core stations with or without station 7237. Therefore, an offset, a drift, annual and bi-annual amplitudes are estimated by least-squares fit to the time series of the geocenter coordinates. The offset in x- and y-direction differ by at least 1 mm and even changes the sign (see Table 6.9), while the offset in z-direction is −2.18 mm and therefore almost 2 mm larger than without the use of station 7237. The drift of the geocenter coordinates are in each direction minor and comparable between the two solutions. The annual signals are not strongly affected by the use of station 7237 as a core station. In contrast, the bi-annual amplitude increases in Y and reduces in Z by more than 0.4 mm.

In conclusion, the Helmert transformation approach can stabilize the estimates of SLR combinations, especially the ERPs. The inhomogeneous geographical distribution of the core stations has a noticeable influence on the scale and the geocenter coordinates. Since

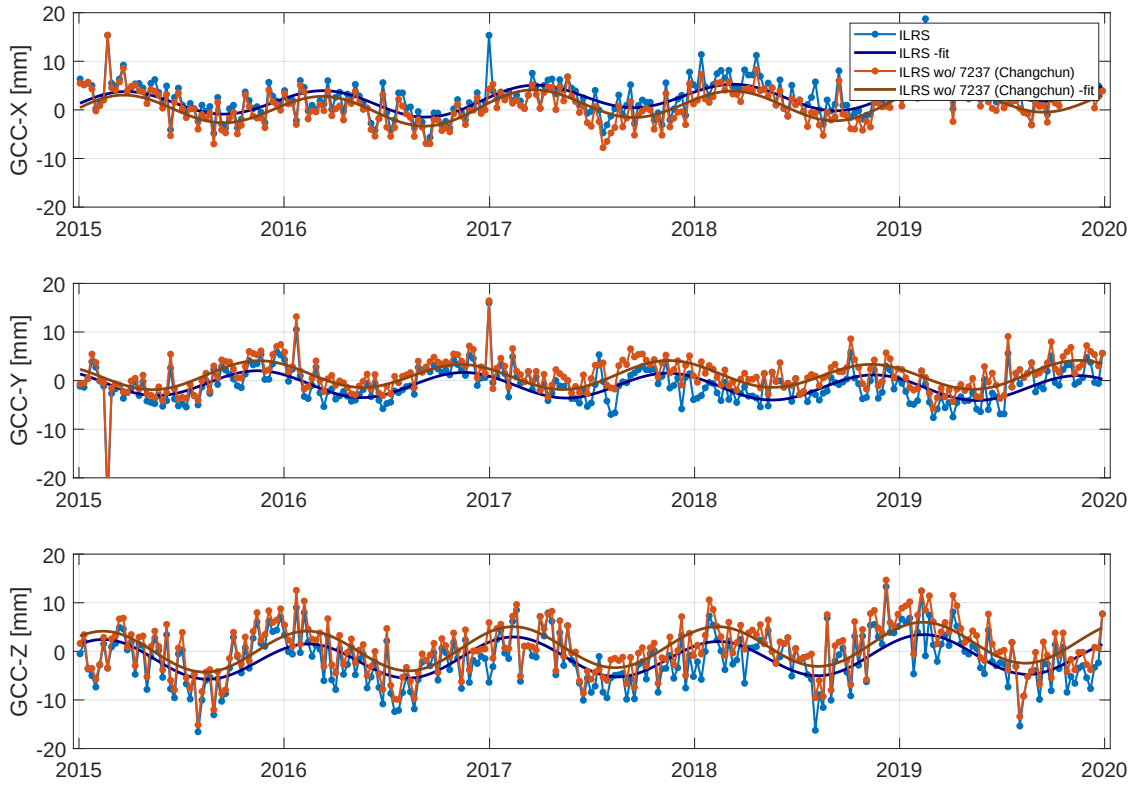

Figure 6.19: Estimated geocenter coordinates with and without the station Changchun in China (7237) used as a core station for the years 2015-2020.

SLR is the only technique to determine the geocenter coordinates, which are further used to realize the origin of ITRFs, further investigations on the impact of core station on the geocenter determination should be conducted.
The study of a proper realization of a datum definition was performed towards the end of the thesis, all further SLR combinations use a datum definition based on the ILRS core station list without using the Helmert transformations. However, for future SLR analyses, it is recommended to use the Helmert transformation approach for a proper datum definition.

Table 6.9: Offset, drift, annual and bi-annual amplitudes of the fitting functions to the estimated geocenter coordinates in X, Y and Z during the years 2015-2020. The estimates of the geocenter coordinates are from LAGEOS-1/2 SLR combinations with or without using the station in Changchun, China (7237) for the datum definition.

Fit of geocenter coordinates	w/ 7237	w/o 7237
Offset in X [mm]	0.528 ± 0.363	-0.453 ± 0.338
Drift in X [mm/day]	0.002 ± 0.011	0.001 ± 0.010
Annual ampl. in X [mm]	3.050 ± 0.436	3.162 ± 0.406
Bi-annual ampl. in X [mm]	0.794 ± 0.439	0.739 ± 0.409
Offset in Y [mm]	-0.594 ± 0.363	0.833 ± 0.327
Drift in Y [mm/day]	-0.001 ± 0.011	0.000 ± 0.001
Annual ampl. in Y [mm]	2.631 ± 0.428	2.671 ± 0.386
Bi-annual ampl. in Y [mm]	0.111 ± 0.430	0.531 ± 0.388
Offset in Z [mm]	-2.180 ± 0.416	-0.479 ± 0.395
Drift in Z [mm/day]	0.001 ± 0.013	0.001 ± 0.012
Annual ampl. in Z [mm]	4.215 ± 0.494	4.444 ± 0.469
Bi-annual ampl. in Z [mm]	0.720 ± 0.497	0.292 ± 0.472

Chapter 7

Multi-Satellite SLR Combinations

Combinations of SLR observations to different geodetic satellites have advantages, e.g., to better determine geodetic parameters, to extend the parameter space or to mitigate correlations between sought-after parameters. With the assumption that satellite-specific observations are uncorrelated, combinations can be performed on NEQ-level, where each NEQ can be weighted individually.

Initially, it was planned that the ILRS contribution to the realization of a stable ITRF2020 (Altamimi et al. 2018) is extended, so that not only SLR observations to LAGEOS-1/2 and Etalon-1/2 but also to LARES are used. This was, however, delayed but will probably be an objective for realizations of further ITRFs.
Therefore, Section 7.1 focuses only on the optimization of the orbit parametrization and background force modeling of LARES in order to improve the estimation of sought-after parameters in LAGEOS-1/2 and LARES SLR combinations. Etalon-1/2 data are intentionally excluded, since VCE provides an average weight of 0.04 for Etalon-1/2 data in SLR combinations with LAGEOS-1/2 data (weighted with 1). Hence, the contribution of Etalon-1/2 SLR data is minor.
Furthermore, the full strength of SLR LARES data, i.e., the stronger sensitivity to the Earth's gravity field, is revealed by extending the parametrization with co-estimating low-degree SH geopotential coefficients.
Since the quality of SLR observations to different geodetic satellites can vary, e.g., due to satellite size and material properties or orbit altitude, the weighting scheme of satellite-specific NEQs is essential. Therefore, different weighting methods, i.e., VCE (Förstner 1979) and Helmert's simple estimator (Helmert 1907), based on LAGEOS-1/2 and LARES SLR combinations are compared.

In Section 7.2, multi-satellite SLR combinations based on LAGEOS-1/2, LARES and Stella/Starlette are analyzed. With an altitude of around 800 km, Stella and Starlette are currently among the lowest-flying geodetic satellites. The more variable environment requests a more detailed background force modeling, e.g., a priori gravity field and air drag model, and an extended orbit parametrization.
Afterwards, the contribution of additional Stella and Starlette SLR data to estimated geodetic parameters, especially to SH geopotential coefficients, is validated.

Finally, in Section 7.3, the first collected SLR data to LARES-2, which was launched in mid of 2022, are analyzed in multi-satellite SLR combinations with LAGEOS-1/2 and LARES. Since the altitude of LARES-2 is comparable with the one of the LAGEOS-1/2 satellites, their orbit parametrization is also used for LARES-2. Since there are no studies on the center-of-mass corrections for LARES-2 at this early stage of the mission, range biases of LARES-2 are estimated for all SLR stations.

7.1 Impact of LARES SLR Data to Multi-Satellite SLR Combinations

First, the orbit of LARES is parametrized in analogy to the orbit parametrization used for LAGEOS-1/2 (see Table 7.1), but with estimating additional pseudo-stochastic pulses in along-track to partially absorb mis-modelings that may occur due to the more variable environment (see Sec. 7.1.1). Furthermore, the impact of the redefined background models, e.g., air drag and a priori gravity field, are validated. Apart from the pseudo-stochastic pulses, the mis-modelings may also be absorbed by daily dynamic orbit parameters provided by the long-arc computation (see Sec. 7.1.2).
Section 7.1.3 shows how the additional SLR data to LARES enables an extension of

Table 7.1: Basic parametrization of LAGEOS-1/2 and LARES SLR combinations.

Parameters	LAGEOS (A)	LARES (C)	
Osculating elements	$a, e, i, \Omega, \omega, u_0$ 1 set per 7 days		
Dynamic orbit parameters	S_0, S_S, S_C, W_S, W_C 1 set per 7 days	1 set per 7 days (7d true-arc) 1 set per day (7d long-arc)	**(Sec. 7.1.2)**
Pseudo-stochastic pulses	none	twice per day along-track (S) cross-track (W)	**(Sec. 7.1.1)**
Station coordinates	1 set per 7 days NNR/NNT minimal constraints		
Geocenter coordinates	1 set per 7 days		
Range biases	1 set per 7 days selected stations	all stations	
ERPs	daily piecewise linear (PWL)		
SH geopotential coeff.	1 set per 7 days up to d/o 4		**(sec. 7.1.3)**

the parameter space with low-degree SH geopotential coefficients, but only if the orbit parametrization is adapted accordingly.
Hence, the orbit parametrizations are adapted by reducing the five empirical orbit parameters

a: by neglecting OPR-W accelerations for satellite groups A/C/D/E,

b: by neglecting OPR-S accelerations for satellite groups C/D/E,

c: by neglecting OPR-S accelerations for satellite group A,

or introducing additional pseudo-stochastic pulses

d: 2 per day in S/W for satellite group C and 12 per day in S/W for satellite groups D/E.

All LAGEOS-1/2 and LARES SLR combinations are generated by using fixed weights of 1 for LAGEOS-1/2 and 0.45 for LARES data, respectively. They are determined by comparing the squared RMS of observation residuals from single-satellite solutions according to Helmert's simple estimator (see Sec. 7.1.4). Nevertheless, there are also other weighting methods, e.g., VCE, providing a high consistency, so their impact on combined LAGEOS-1/2 and LARES SLR solutions will be analyzed as well (see Sec. 7.1.4).

7.1.1 Orbit Modeling and Parametrization of LARES

Compared to LAGEOS-1/2 satellites, LARES is orbiting the Earth at a much lower altitude, i.e., 1400 km, where the background force modeling of the time-variable upper atmosphere density and the Earth's gravity field may have to be taken into account and the orbit parametrization may become more demanding.

The total mass density of the atmosphere at that height is still very low and therefore the air drag modeling with NRLMSISE-00 (Picone et al. 2002) based on the standard values or the actually measured data for $F10.7$ and A_p (see Sec. 3.2.2) does not significantly influence the determination of the a priori orbit (see Sec. 4.2). The comparison (without estimating Helmert transformation parameters) of orbit positions determined with or without applying an air drag model shows an RMS difference in S of only 9 mm (see Fig. 7.1). In R and W directions, position differences are on sub-millimeter level or even zero.
Consequently, the differences in the estimates of the geodetic parameters, e.g., station coordinates, ERPs and geocenter coordinates, of LAGEOS-1/2 and LARES SLR combinations with different air drag models, are neglectable and not further discussed.
Nonetheless, for all further SLR combinations the air drag is modeled with the actually measured data for the orbit determination of LARES.

In contrast to the air drag modeling, the background force modeling of the Earth's gravity field strongly affects the orbit determination of LARES. When using the ILRS or the COST-G time-variable gravity field model (see Sec. 6.3), the RMS of orbit position differences in R, S and W are 9 mm, 46 mm and 7 mm, respectively (see Fig. 7.1).

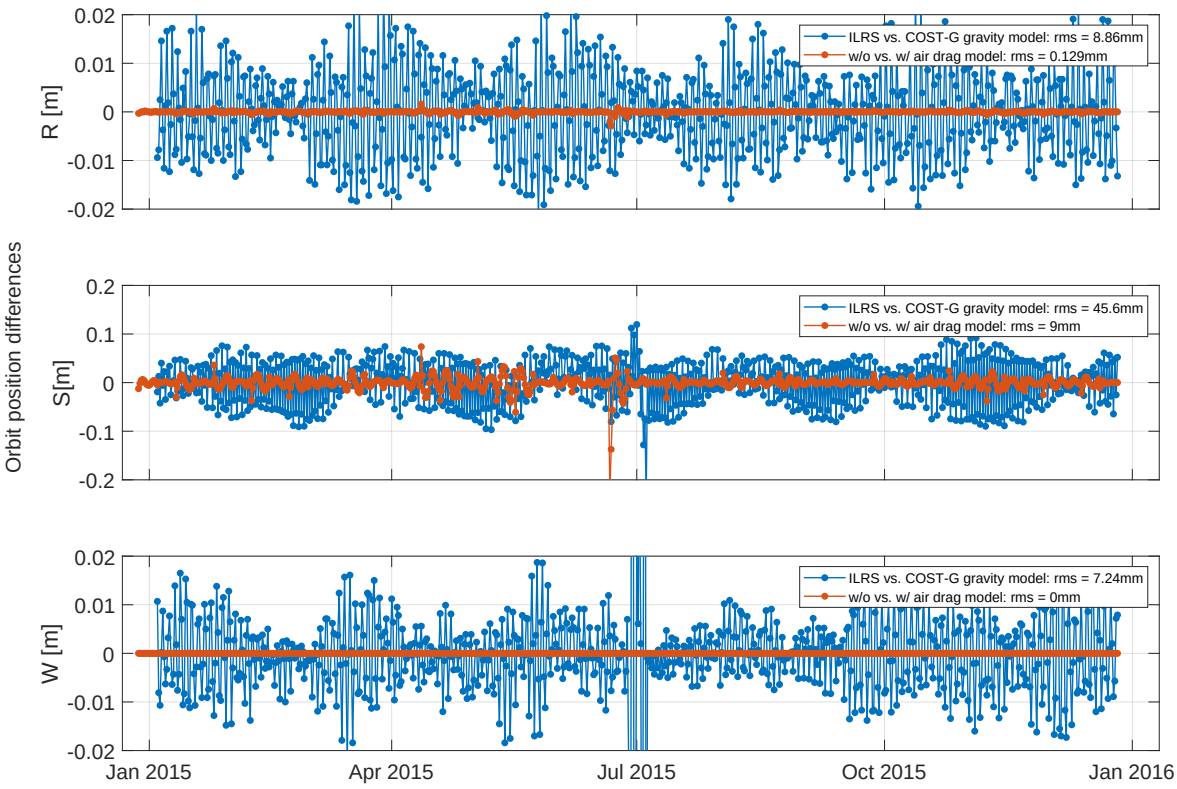

Figure 7.1: Orbit position differences of LARES satellite in the $\mathcal{R}$-system with or without applying an air drag model (red) and when two different gravity field models (blue), i.e., time-variable models provided by the ILRS or COST-G, are applied for the year 2015.

Consequently, the choice of the a priori gravity field model, e.g., ILRS or COST-G time-variable gravity field product and replacing C_{21}/S_{21}, has a major impact on the estimated geodetic parameters and the observation residuals of LAGEOS-1/2 and LARES SLR combinations performed for the years 2015-2020.
While in LAGEOS-1/2 SLR combinations, discussed in Section 6.3, the bias of the polar motion is reduced by less than 6 % (see Table 6.5), with LARES it is changed by more than 140 % with a sign change when using the COST-G a priori gravity field model and replacing C_{21}/S_{21} (see Table 7.2). The WRMS of the X-pole increases by 6 %, while the WRMS of the Y-pole is reduced by 19 % w.r.t. the use of the time-variable ILRS gravity field. In addition, the estimates of UT1-UTC are also improved, such that the bias is reduced by 37 % and the WRMS by 14 %, respectively. The majority of the changes can be explained by the replacement of the SH geopotential coefficients C_{21}/S_{21}.
Figure 7.2 shows that the weighted mean RMS of the Helmert transformation of station coordinates for SLR combinations using the COST-G product can be reduced especially in the horizontal direction, i.e., 1.1 mm in North and 0.6 mm in East. While the impact of the a priori gravity field model on the Helmert transformation of station coordinates from LAGEOS-1/2 combinations is neglectable (see Table 6.5).
Furthermore, if the a priori gravity field is modeled according to the COST-G product, the mean RMS of the observation residuals are reduced by 2.0 mm to 15.7 mm and when C_{21}/S_{21} are replaced to 14.9 mm (see Fig. 7.3).
Consequently, when using the COST-G gravity field model as a priori, C_{21}/S_{21} should

Table 7.2: Estimated ERP corrections w.r.t. the IERS-14-C04 reference series of LAGEOS-1/2 and LARES SLR combinations using different a priori gravity field models and applying pseudo-stochastic pulses two or twelve per day in *S* for LARES for the years 2015-2020.

Sat.	Stoch.pl. in S for C	Grav. model	Replace C_{21}/S_{21}	X-pole [μas] Bias	X-pole [μas] WRMS	Y-pole [μas] Bias	Y-pole [μas] WRMS	UT1-UTC [μs] Bias	UT1-UTC [μs] WRMS
A+C	2/day	ILRS	no	−86.8	166.5	38.3	146.1	−16.3	87.0
A+C	2/day	COST-G	no	−74.8	148.7	60.4	136.8	−8.9	79.1
A+C	2/day	COST-G	yes	126.6	177.3	−16.0	117.6	−10.2	75.2
A+C	12/day	ILRS	no	−31.0	134.7	34.1	131.0	−11.6	78.9

be replaced according to Eq. 6.5.

Finally, when using the time-variable ILRS gravity field and setting up twelve (approx. one per orbit revolution) instead of two pseudo-stochastic pulses in along-track on a daily basis for LARES, ERPs and the RMS of the Helmert transformation of station coordinates are improved (see Table 7.2 and Fig. 7.2).
More detailed, the WRMS of the polar motion can be improved by 19 % in x-direction and 10 % in y-direction, respectively. The bias is reduced mainly in x-direction by 55.8 µas. In addition, the bias and the WRMS of UT1-UTC is improved by 29 % and 10 %, respectively. The RMS of the Helmert transformation of station coordinates is improved only marginally in the horizontal plane by 0.4 mm in North and 0.2 mm in East, respectively. The mean RMS of the observation residuals can be reduced by 1.4 mm.
However, most of the estimated geodetic parameters are still inferior to the estimates of SLR combinations using the COST-G gravity field with only two pseudo-stochastic pulses per day in along-track for LARES. Therefore, a reliable a priori gravity field model

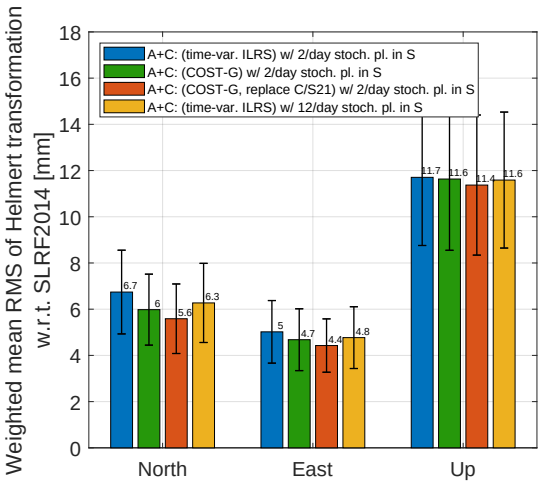

Figure 7.2: Weighted mean RMS of the Helmert transformation of station coordinates w.r.t. SLRF2014 of LAGEOS-1/2 and LARES SLR combinations using different a priori gravity field models and applying two or twelve pseudo-stochastic pulses in *S* for LARES for the years 2015-2020.

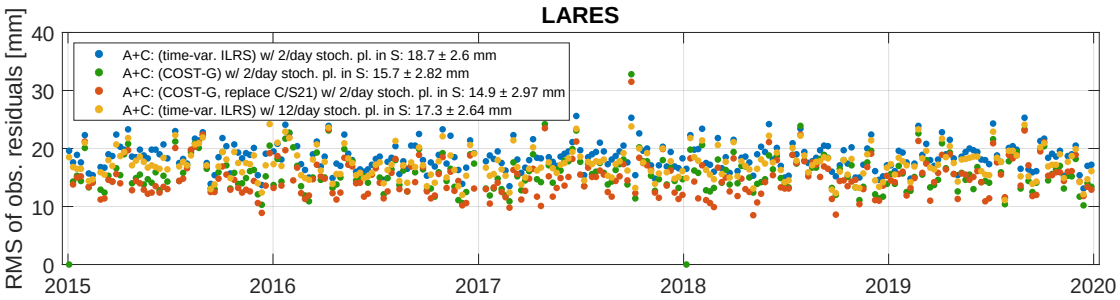

Figure 7.3: RMS of LARES observation residuals resulting from LAGEOS-1/2 and LARES SLR combinations using different a priori gravity field models and applying pseudo-stochastic pulses two or twelve per day in *S* for LARES for the years 2015-2020.

can diminish the necessity of more than two additional pseudo-stochastic pulses. This is also preferable, since the physical interpretation of the pseudo-stochastic pulses is very difficult or even impossible.

7.1.2 Orbit Parametrization of LARES Using Long-arc Approach

The long-arc computation allows combining daily arcs into a 7-day arc by transforming the initial osculating elements of the daily NEQs into one set of osculating elements referring to the beginning of a 7-day arc (see Sec. 3.6). In contrary, the dynamic orbit parameters can be kept on a daily basis and may account for modeling deficiencies.
In the following, 7-day arcs of LARES are realized for the years 2015-2020 by using two different orbit modeling approaches:

- **7d true-arc**: one set of initial osculating orbital elements and one set of dynamic orbit parameters are estimated for 7 days (in analogy to the orbit parametrization of LAGEOS).
- **7d long-arc**: one set of initial osculating orbital elements and daily dynamic orbit parameters are estimated for 7 days.

The air drag is modeled using the empirical atmospheric model NRLMSISE-00 (Picone et al. 2002) based on actually observed data and the a priori gravity field model is based on the time-variable ILRS product.

The quality of the long-arc approach is validated by comparing ERPs and the Helmert transformation of station coordinates, to the results of the true-arc approach. At the time of writing, the reconstruction of the orbit with the daily estimated dynamic orbit parameters, especially when SH geopotential coefficients are co-estimated, was not yet feasible, and therefore, it was not possible to compute observation residuals.
The comparison of the estimated ERPs (see Table 7.3) shows that including LARES and using the true-arc parametrization increases the WRMS of the X-pole and Y-pole w.r.t. the LAGEOS-1/2 solution by 17 %, resp., 23 %. The bias of the X-pole differs by 172 µas and even the sign changes. In contrast to the Y-pole, which is only shifted by 6 µas. This displacement of the X- and Y-pole can be partially explained by the unbalanced inclinations of the satellite orbits, i.e., retrograde (LAGEOS-1) or prograde (LAGEOS-2, LARES)

Table 7.3: Estimated ERP corrections w.r.t. the IERS-14-C04 reference series resulting from LAGEOS-1/2 and LARES SLR combinations when using the 7d true- or long-arc orbit modeling approaches for LARES for the years 2015-2020.

Sat.	Arc for C	X-pole [μas]		Y-pole [μas]		UT1-UTC [μs]	
		Bias	WRMS	Bias	WRMS	Bias	WRMS
A		85.6	142.1	31.9	118.1	−1.7	64.3
A+C	true	−86.8	166.5	38.3	146.1	−16.3	87.0
A+C	long	−55.1	136.1	39.0	133.6	−9.7	84.5

motion, which introduce a systematic bias. This phenomenon can be confirmed by an experiment of LAGEOS-1/2 SLR solutions, where different weights were assigned to LAGEOS-1 and -2 to enforce an imbalance. Table 7.4 shows that the higher weighting of LAGEOS-2, which corresponds to the inclusion of LARES, reduces the X-pole by 197 % and the Y-pole only by 16 %. In contrary, if the impact of LAGEOS-1 is increased by setting a weight of ten, the X- and Y-pole are shifted, as expected, in the other direction than before.

Furthermore, with the long-arc orbit parametrization for LARES, the WRMS of the polar motion decreases w.r.t. the true-arc parametrization. The X-pole can be estimated most precisely, while the Y-pole can only be improved compared with the true-arc LARES parametrization, but not with the LAGEOS-1/2 SLR combination.

Table 7.4: Estimated ERP corrections w.r.t. the IERS-14-C04 reference series resulting from LAGEOS-1/2 SLR combinations, where LAGEOS-1 and LAGEOS-2 are differently weighted, for the year 2015.

Sat.	Weights for LAGEOS-1/2	X-pole [μas]		Y-pole[μas]		UT1-UTC [μs]	
		Bias	WRMS	Bias	WRMS	Bias	WRMS
A	1/10	0.3	136.5	58.2	147.8	−4.3	87.4
A	1/1	60.4	128.0	69.9	114.0	1.1	60.4
A	10/1	115.5	175.5	83.4	134.9	−7.0	73.8

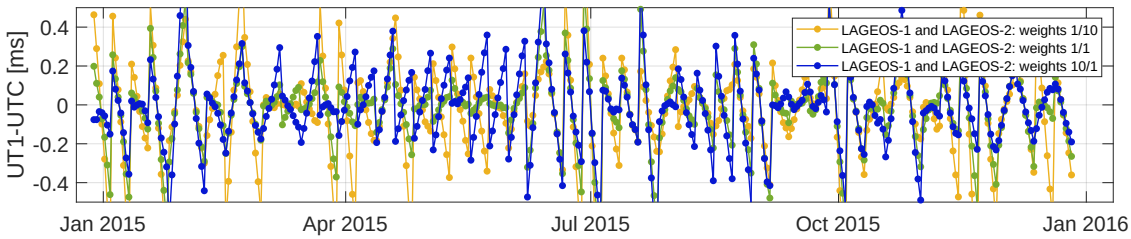

Figure 7.4: Estimated UT1-UTC corrections w.r.t. the IERS-14-C04 series resulting from LAGEOS-1/2 SLR combinations, where LAGEOS-1 and LAGEOS-2 are differently weighted, for the year 2015.

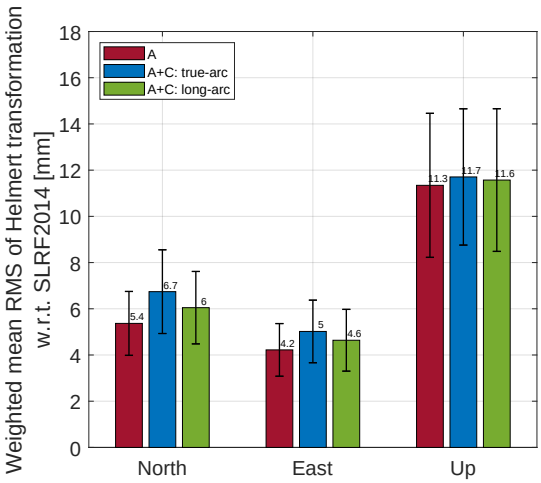

Figure 7.5: Weighted mean RMS of the Helmert transformation of station coordinates w.r.t. SLRF2014 resulting from LAGEOS-1/2 and LARES SLR combinations when using the 7d true- or long-arc orbit modeling approaches for LARES for the years 2015-2020.

The increased bias and WRMS of UT1-UTC, when LARES is included, can again be explained by the unbalanced inclinations of the orbits, which enlarges the saw tooth behaviour of the time series of UT1-UTC (see Fig. 7.4).

In general, if LARES contributes to SLR combinations, the RMS of the Helmert transformation of station coordinates w.r.t. SLRF2014 increases (see Fig. 7.5). This is to be expected, since the SLRF2014 is only based on LAGEOS-1/2 SLR data. Nevertheless, if daily dynamic orbit parameters are used for LARES, the RMS is reduced in North by 0.6 mm, in East by 0.4 mm and in Up by 0.1 mm w.r.t. the true-arc orbit parametrization of LARES.

The analysis of the estimated geodetic parameters implies that the orbit of LARES should be represented by a long-arc. This is, however, not surprising, since the 7d long-arc approach makes use of 30 more parameters, i.e., daily dynamic orbit parameters, which are then able to account for further mis-modelings.

7.1.3 Contribution of LARES SLR Data to Co-Estimated SH Geopotential Coefficients

The lower orbital altitude of LARES and therefore its increased sensitivity to the Earth's gravity field improves the estimates of the low-degree SH geopotential coefficients in multi-satellite SLR combinations (Bloßfeld et al. 2018). However, the extension of the parametrization, e.g., with low-degree SH geopotential coefficients, leads to new correlations between parameters and may thus prevent reliable estimations of parameters.
The analysis of the mean correlation matrix of the year 2015 confirms the results of Bloßfeld et al. (2018), that SH geopotential coefficients, especially the even zonal SH coefficients C_{20} and C_{40}, as well as the OPR-S cosine accelerations S_C and C_{30} are strongly correlated (see Fig. 7.6).
The correlation between the SH geopotential coefficients and the gained sensitivity to

C_{40} lead to the fact that instead of only C_{20} also higher SH geopotential coefficients have to be co-estimated. Otherwise, C_{20} cannot be reliably estimated (see Fig. 7.7, top), since it will also partially absorb the signal of C_{40}. Therefore, the SH geopotential coefficients need to be co-estimated up to d/o 4.

As already pointed out in Section 6.3, a reliable co-estimation of C_{20} is only feasible if the OPR-W accelerations are neglected. Analogously, this applies for the estimation of C_{30}, which is only reasonable if the strong correlations with OPR-S accelerations are diminished.
Similar to the perturbing accelerations acting on a satellite caused by the variation of C_{20} (see Eq. 6.6), they can also be derived for variations of C_{30} (ΔC_{30}) (see Appendix B)

$$\begin{pmatrix} R' \\ S' \\ W' \end{pmatrix}_{C_{30}} = GMa^3 \Delta C_{30} \frac{5}{2} \frac{1}{r^5} \begin{pmatrix} \frac{12}{5} \sin(i) \sin(u) - 4 \sin^3(i) \sin^3(u) \\ \frac{3}{4} \sin^3(i) \cos(u) - \frac{3}{4} \sin^3(i) \cos(2u) - \frac{3}{5} \sin(i) \cos(u) \\ \frac{3}{2} \sin^2(i) \cos(i)(1 - \cos(2u)) - \frac{3}{5} \cos(i) \end{pmatrix}. \quad (7.1)$$

Although the correlations between C_{30} and the OPR-S cosine accelerations of LAGEOS-1/2 and LARES are almost equally strong (see Fig. 7.6), it is sufficient to not set up only the OPR-S accelerations of LARES for estimating a reliable C_{30} (see Fig. 7.8). This can be explained by performing a CA, where the contribution of LAGEOS-1/2 to determine C_{30} is on average 2.5 times smaller than for LARES, such that the impact of the correlations with OPR-S accelerations of LAGEOS-1/2 is limited.

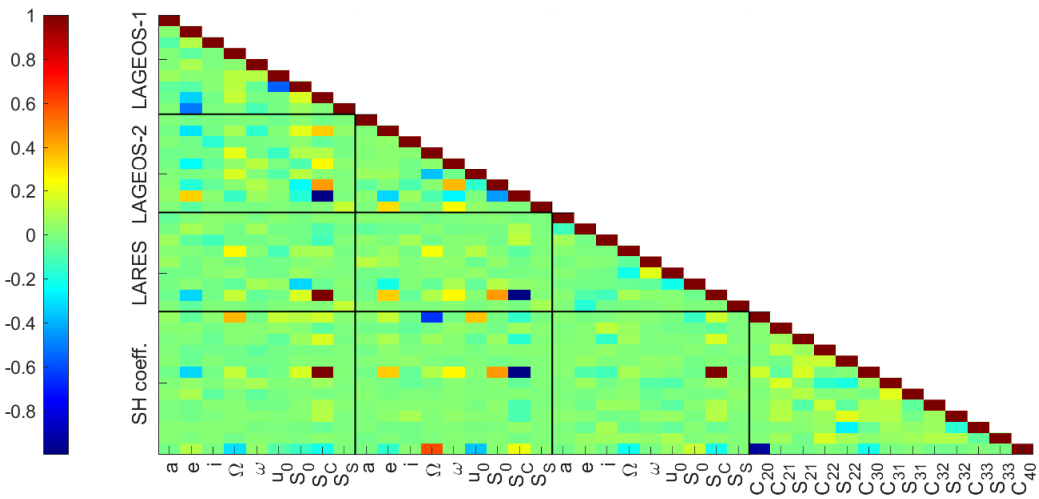

Figure 7.6: Mean correlation matrix of LAGEOS-1/2 and LARES SLR combinations when co-estimating SH geopotential coefficients for the year 2015.

The importance of the OPR-S accelerations of LAGEOS-1/2 becomes obvious when analyzing other geodetic parameters, e.g., ERPs, station coordinates and C_{20}.
Without the use of OPR-S accelerations for LARES, the WRMS of the polar motion increases by 5 % (see Table 7.5). If additionally the OPR-S accelerations of LAGEOS-1/2 are canceled, the WRMS of the polar motion increases by more than 50 % and 80 % in

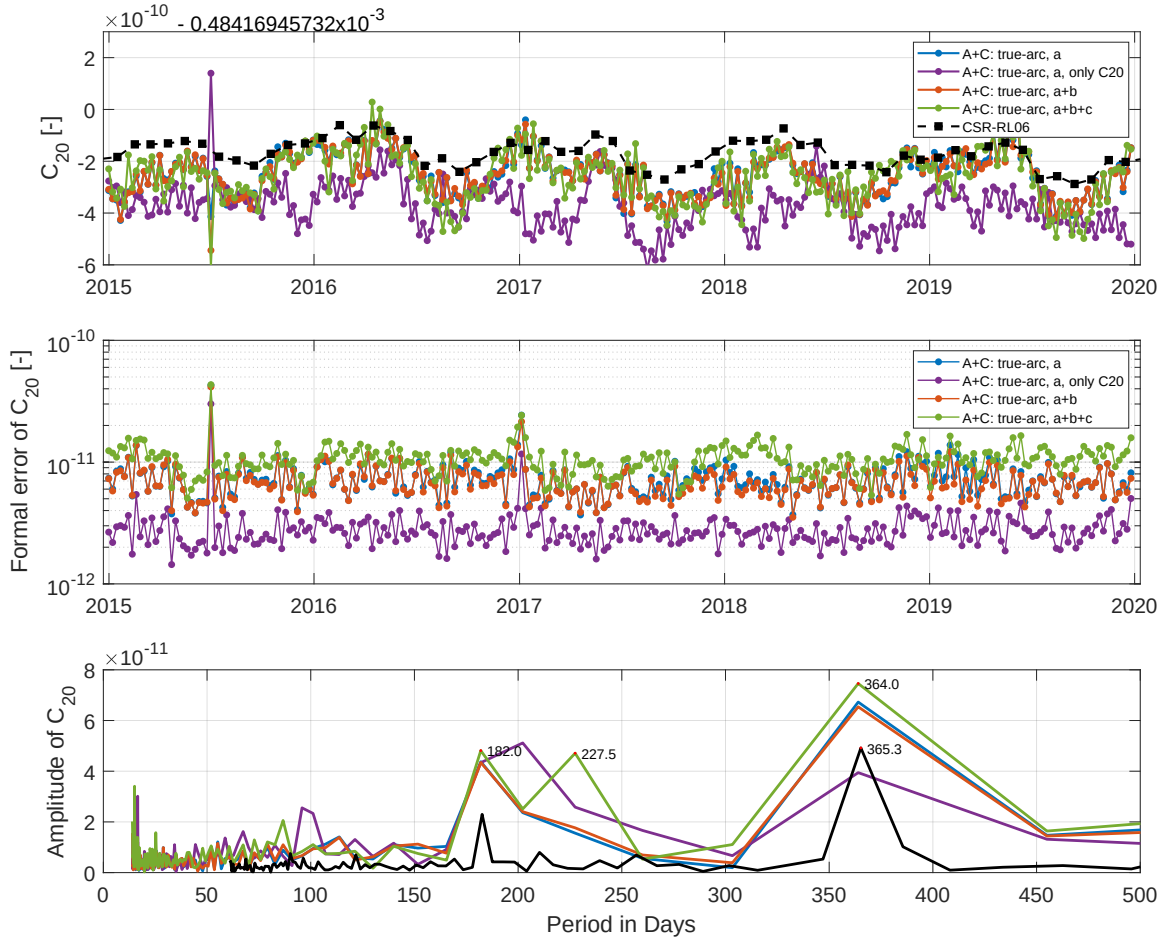

Figure 7.7: Time series of the estimated SH geopotential C_{20} (top), its formal error (middle) and the amplitude spectrum (bottom) of LAGEOS-1/2 and LARES SLR combinations using different orbit parametrizations and estimating C_{20} or SH geopotential coefficients up to d/o 4 for the years 2015-2020.

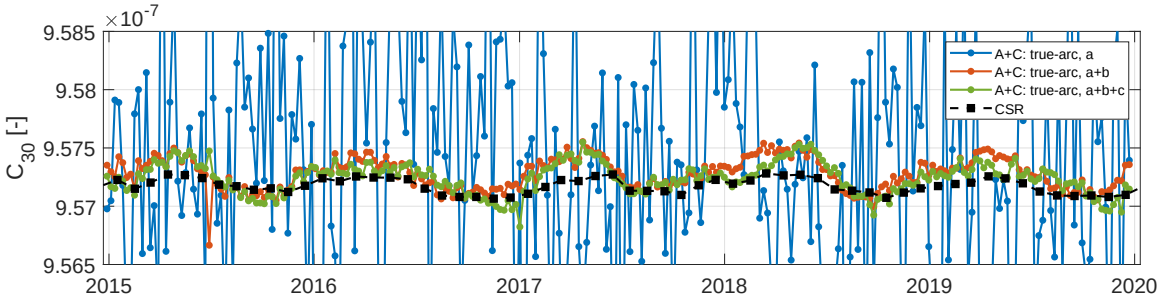

Figure 7.8: Time series of the estimated SH geopotential C_{30} of LAGEOS-1/2 and LARES SLR combinations using different orbit parametrizations for the years 2015-2020.

Table 7.5: Estimated ERP corrections w.r.t. the IERS-14-C04 reference series of LAGEOS-1/2 and LARES SLR combinations using different orbit parametrizations for the years 2015-2020.

Sat.	Est. SH geo. coeff.	Arc for C	X-pole [μas] Bias	WRMS	Y-pole[μas] Bias	WRMS	UT1-UTC [μs] Bias	WRMS
A	-	7d true	85.6	142.1	31.9	118.1	−1.7	64.3
A+C: a	4/4	7d true	76.0	200.6	10.2	160.3	1.0	25.5
A+C: $a+b$	4/4	7d true	73.1	209.8	14.0	167.2	0.3	25.2
A+C: $a+b+c$	4/4	7d true	64.5	304.5	−1.2	292.0	2.9	28.9
A+C: $a+b+d$	4/4	7d true	60.0	136.9	19.9	125.2	0.4	22.6
A+C: $a+b$	4/4	7d long	73.7	203.1	14.0	160.6	0.5	23.1

x- and y-direction, respectively. However, the corresponding bias can be reduced by at least 10 µas.
The weighted mean RMS of the Helmert transformation of station coordinates also increases without the use of OPR-S accelerations for LAGEOS-1/2 to 10.4 mm in the horizontal plane and to 14.8 mm for the Up component, respectively (see Fig. 7.9).
The time series of C_{20} are almost identical, independent of using OPR-S accelerations for LAGEOS-1/2 (see Fig. 7.7, top). However, the formal error of C_{20} increases (see Fig. 7.7, middle) and the spectra features a new strong signal at 227.5 days (see Fig. 7.7, bottom), which may correspond to the draconitic year of LAGEOS-2, i.e., 222 days (Sośnica 2015), if OPR-S accelerations for LAGEOS-1/2 are neglected.

The reduction of the orbit parameters for LARES to six initial Keplerian elements and only one dynamic orbit parameter in along-track (S_0) diminishes the usefulness of the long-arc approach tremendously. The difference between the true- and long-arc orbit

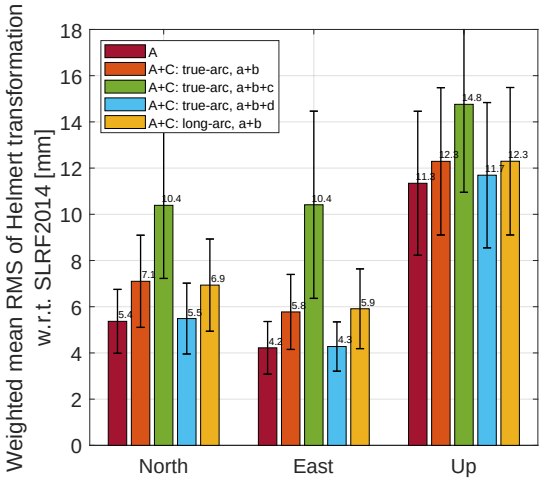

Figure 7.9: Weighted mean RMS of the Helmert transformation of station coordinates w.r.t. SLRF2014 of LAGEOS-1/2 and LARES SLR combinations using different orbit parametrizations for the years 2015-2020.

parametrization remains only in weekly, resp., daily constant accelerations in along-track. Consequently, the WRMS of the polar motion and UT1-UTC improve only slightly by around 4 % and 8 %, respectively (see Table 7.5). The RMS of the Helmert transformation of station coordinates differ only by 0.2 mm w.r.t. the true-arc orbit parametrization (see Fig. 7.9).

The redefinition of the orbit parametrization of LARES, i.e., the exclusion of the OPR-S and OPR-W accelerations, and the additional estimation of the SH geopotential coefficients up to d/o 4 cause a general degradation of the polar motion and the station coordinates when comparing to LAGEOS-1/2 SLR combinations, where no SH geopotential coefficients are estimated. Only if pseudo-stochastic pulses two per day in S and especially in W are set-up for the orbit parametrization of LARES, the quality of the estimated geodetic parameters is improving again. Then, a comparison with LAGEOS-1/2 SLR combination, which is capable of properly estimating the polar motion and the station coordinates, reveals only minor discrepancies. While the WRMS of the polar motion is only slightly changed by 3.7 % and −6 %, the bias of the polar motion is improved by 25.6 µas and 12 µas in x- and y-direction, respectively (see Table 7.5).
The RMS of the Helmert transformation of station coordinates are slightly higher with 0.1 mm in each direction of the horizontal plane and 0.4 mm in Up, for the LAGEOS-1/2 and LARES SLR combination, when additional pseudo-stochastic pulses are applied, than for the LAGEOS-1/2 SLR combination (see Fig. 7.9).

In conclusion, the orbit parameterization of LAGEOS-1/2 and LARES must be adjusted, i.e., by only applying three dynamic orbit parameters (S_0,S_S and S_C) for LAGEOS-1/2 and only one dynamic orbit parameter S_0 for LARES, to estimate reliable low-degree SH geopotential coefficients. In order to still partially absorb background force modeling deficiencies, pseudo-stochastic pulses, which are not strongly correlated with SH geopotential coefficients, in along- and cross-track can be applied. This allows to estimate reliable SH geopotential coefficients together with ERPs and station coordinates.

7.1.4 Satellite Specific Weights and Their Impact on Combined LAGEOS-1/2 and LARES SLR Combinations

Multi-satellite SLR combinations are generated by combining single satellite-specific NEQs, where a proper weighting for each different satellite group according to their data quality is essential. It can be derived, e.g., by using VCE or Helmert's "simple" estimator (see Sec. 3.4.1).

As it can be seen in Figure 7.10 (left), the mean RMS of observation residuals for LARES-only solutions are significantly larger than for a LAGEOS-only solution and the weights are more scattered, if the station and geocenter coordinates are estimated (compare Fig. 7.10 left and right). This indicates that LARES-only solutions cannot provide reliable station and geocenter coordinates. In this case, the ratio of the mean squared RMS of observation residuals $\rho_{A,C}^{RMS}$ over the years 2015-2020 becomes 0.11. Hence, in a multi-satellite SLR combination, the impact of the LAGEOS-1/2 data would be weighted al-

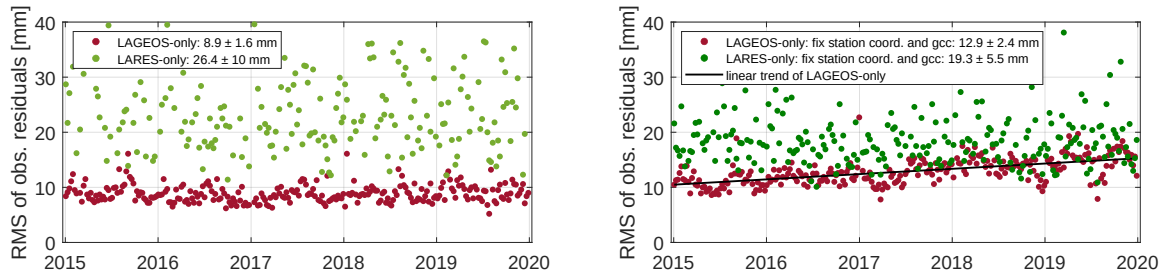

Figure 7.10: RMS of observation residuals for LAGEOS- and LARES-only solutions when estimating station and geocenter coordinates (left) or when fixing the station and the geocenter coordinates (right) for the years 2015-2020.

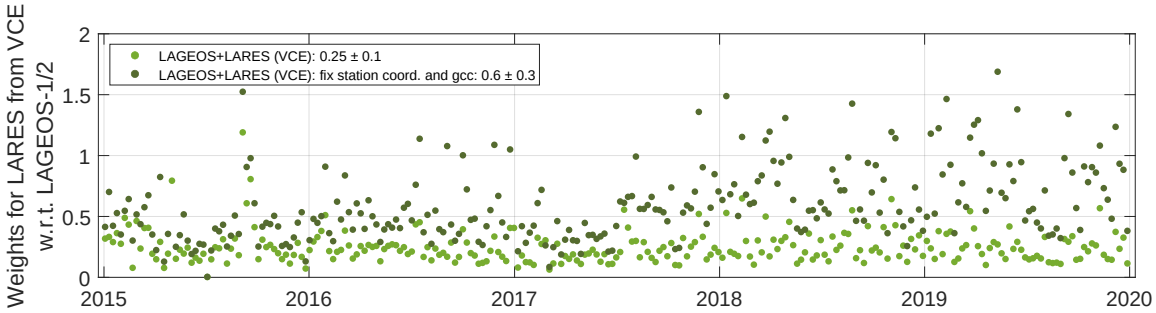

Figure 7.11: Weekly weights for LARES derived by VCE of combined LAGEOS-1/2 and LARES SLR combinations when estimating (light green) or fixing (dark green) the station and geocenter coordinates for the years 2015-2020.

most 10 times higher than of the LARES data.
Furthermore, the parametrization is adapted by fixing the station and geocenter coordinates to the a priori station coordinates of the SLRF2014 and to the origin, respectively. However, since the quality of the reference frame ITRF2014 decreases after 2015, the RMS of observation residuals, especially for the LAGEOS-only solution, are continuously increasing in time (see Fig. 7.10, right). The mean RMS of LAGEOS-1/2 observation residuals increases by 3 mm, while for the LARES-only solution it is improved by 7 mm. Consequently, the ratio of the mean squared RMS of observation residuals $\rho_{A,C}^{RMS}$ over the years 2015-2020 is therefore more balanced with 0.45.

After determining the satellite specific weights, they are introduced as fixed a priori weights for the LAGEOS-1/2 and LARES combination on NEQ-level. Such a satellite combination often enables an extension of the parameter space, e.g., by additionally estimating SH Earth's gravity field coefficients up to d/o 4 (see Sec. 7.1.3). In this case, the parametrization used for the determination of the weights differs from the parametrization used in the multi-satellite solution.
On the contrary, the weighting and satellite combination on NEQ-level performed by VCE are always based on the same parametrization and therefore ensures a consistency between observations and estimated parameters. In addition, the weights from the VCE are not constant, since they are estimated on a weekly basis (see Fig. 7.11). Compared to the RMS-based weighting ratio, the VCE obtains larger ratio by a factor of 2.3 when co-estimating station and geocenter coordinates, resp., 1.3 when the station and geocenter

Table 7.6: Estimated ERP corrections w.r.t. the IERS-14-C04 reference series resulting from LAGEOS-1/2 and LARES SLR combinations when using fixed weights per satellite group or VCE for the years 2015-2020.

Sat.	Weights (A/C)	X-pole [μas]		Y-pole[μas]		UT1-UTC [μs]	
		Bias	WRMS	Bias	WRMS	Bias	WRMS
A	1/-	85.6	142.1	31.9	118.1	−1.7	64.3
A+C	1/0.11	23.2	114.2	34.6	117.9	−5.2	69.3
A+C	1/0.45	−86.8	166.5	38.3	146.1	−16.3	87.0
A+C	VCE	−12.2	125.0	33.6	122.2	−9.2	76.1

coordinates are fixed.

The impact of the satellite specific weighting methods is studied by comparing the results in terms of ERPs, the RMS of the Helmert transformation of station coordinates and the RMS of the observation residuals, of LAGEOS-1/2 and LARES SLR combinations using the parametrization of Table 7.1, where the station and geocenter coordinates are estimated. Therefore, the following three weighting methods are compared:

- constant weights of 1 for LAGEOS-1/2 and 0.11 for LARES (derived by the RMS-based weighting method, when the station and geocenter coordinates are estimated),
- constant weights of 1 for LAGEOS-1/2 and 0.45 for LARES (derived by the RMS-based weighting method, when the station and geocenter coordinates are fixed),
- weekly weights for LAGEOS-1/2 and LARES derived by the VCE.

The additional SLR data from LARES improves the polar motion in x-direction, but only if LARES is weighted with 0.11 or based on the VCE. The bias is reduced by more

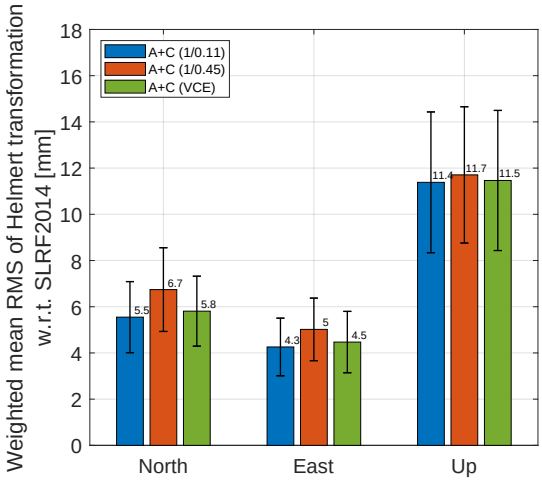

Figure 7.12: Weighted mean RMS of Helmert transformation of station coordinates w.r.t. SLRF2014 resulting from LAGEOS-1/2 and LARES SLR combinations when using fixed weights per satellite group or VCE for the years 2015-2020.

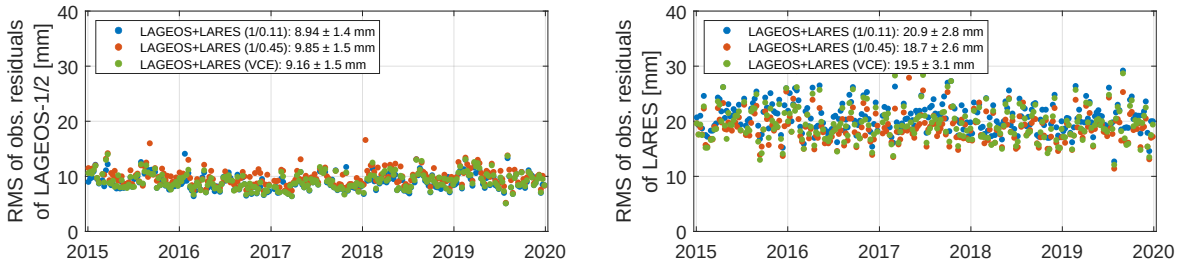

Figure 7.13: RMS of LAGEOS-1/2 (left) and LARES (right) observation residuals resulting from LAGEOS-1/2 and LARES SLR combinations when using fixed weights per satellite group or VCE for the years 2015-2020.

than 62 µas and the WRMS by at least 12 %. On the contrary, the Y-pole shows much smaller changes in the bias and WRMS. Furthermore, the worse UT1-UTC value can be explained by a strong correlation with the estimated OPR-W acceleration of LARES (see Sec. 6.2). In general, it can be observed that the results from the SLR combinations derived with the VCE are always between the SLR combinations, where a fixed weight of 0.11 or 0.45, respectively, for LARES is used. This is to be expected, since the mean weight for LARES from the VCE is 0.25. Consequently, this behavior can also be seen on the RMS of the Helmert transformation of station coordinates in North, East and Up. The higher LARES is weighted, the worse the RMS becomes (see Fig. 7.12).
Moreover, a higher weight for LARES observations implies that the least-squares adjustment follows the LARES observations closer, and therefore, observation residuals of LARES are improved. Figure 7.13 shows the RMS of observation residuals of LAGEOS-1/2 and LARES. The higher the weights of LARES, the better its RMS of observation residuals, while this value becomes larger for LAGEOS-1/2.

7.2 Multi-Satellite SLR Combinations With Geodetic LEO Satellites

After the detailed study of LAGEOS-1/2 and LARES SLR combinations, SLR observations to geodetic LEO satellites, i.e., Starlette (D) and Stella (E), are now included. These additional satellites are orbiting the Earth on an even lower altitude than LARES (see Table 2.2) and therefore the background force modeling, e.g., air drag and the a priori gravity field, have to be refined (see Sec. 7.2.1).

The lower altitudes of the additional SLR satellites further enlarge the sensitivity to SH geopotential coefficients (see Sec. 7.2.2). It will increase the degree and order of reliably estimated SH geopotential coefficients and will improve their quality.
The multi-satellite SLR combinations are based on the parametrization listed in Table 7.7, unless otherwise mentioned in the text.

Table 7.7: Basic parametrization of multi-satellite SLR combinations based on LAGEOS-1/2, LARES and Starlette/Stella data.

Parameters	LAGEOS-1/2 (A)	LARES (C)	Starlette/Stella (D/E)
Osculating elements	$a, e, i, \Omega, \omega, u_0$		
	1 set per 7 days		
Dynamic orbit parameters	1 set per 7 days		
	S_0, S_S, S_C	S_0	
Pseudo-Stochastic pulses	none	twice per day	twelve per day
		along-track (S)	along-track (S)
		cross-track (W)	cross-track (W)
Station coordinates	1 set per 7 days		
	NNR/NNT minimal constraints		
Geocenter coordinates	1 set per 7 days		
Range biases	1 set per 7 days		
	selected stations	all stations	
ERPs	daily		
	piecewise linear (PWL)		
SH geopotential coeff.	1 set per 7 days		
	up to d/o 5 + C_{61} + S_{61}		

7.2.1 Orbit Parametrization and Modeling of Geodetic SLR LEO Satellites

The differences of the satellite position of Starlette when the air drag is neglected or when it is taken into account by applying the air drag background model NRLMSISE-00 (Picone et al. 2002) based on actually measured data are much more pronounced than for LARES. While the orbit position differences for LARES are on the sub-millimeter level in R, less than 2 cm in S and even zero in W (see Fig. 7.1), they are significantly larger for Starlette (see Fig. 7.14) with an RMS of 6 mm in R, 27 cm in S and on the sub-millimeter level in W, respectively. The fact that the orbit positions in S show the largest impact can be readily explained by the fact that the air drag acts anti-parallel to the (Earth-fixed) velocity direction of the satellite (see Eq. 3.11).

The impact of the air drag modeling and the extension of the orbit parametrization with pseudo-stochastic pulses in S for Starlette is studied by comparing the estimated parameters of SLR multi-satellite combinations with LAGEOS-1/2 and LARES using VCE. In a first approach, the SH geopotential coefficients are fixed to the a priori values of the time-variable ILRS gravity field model, while five dynamic orbit parameters are set-up for each satellite.
The estimates of the geodetic paramters, i.e., ERPs and Helmert transformation of sta-

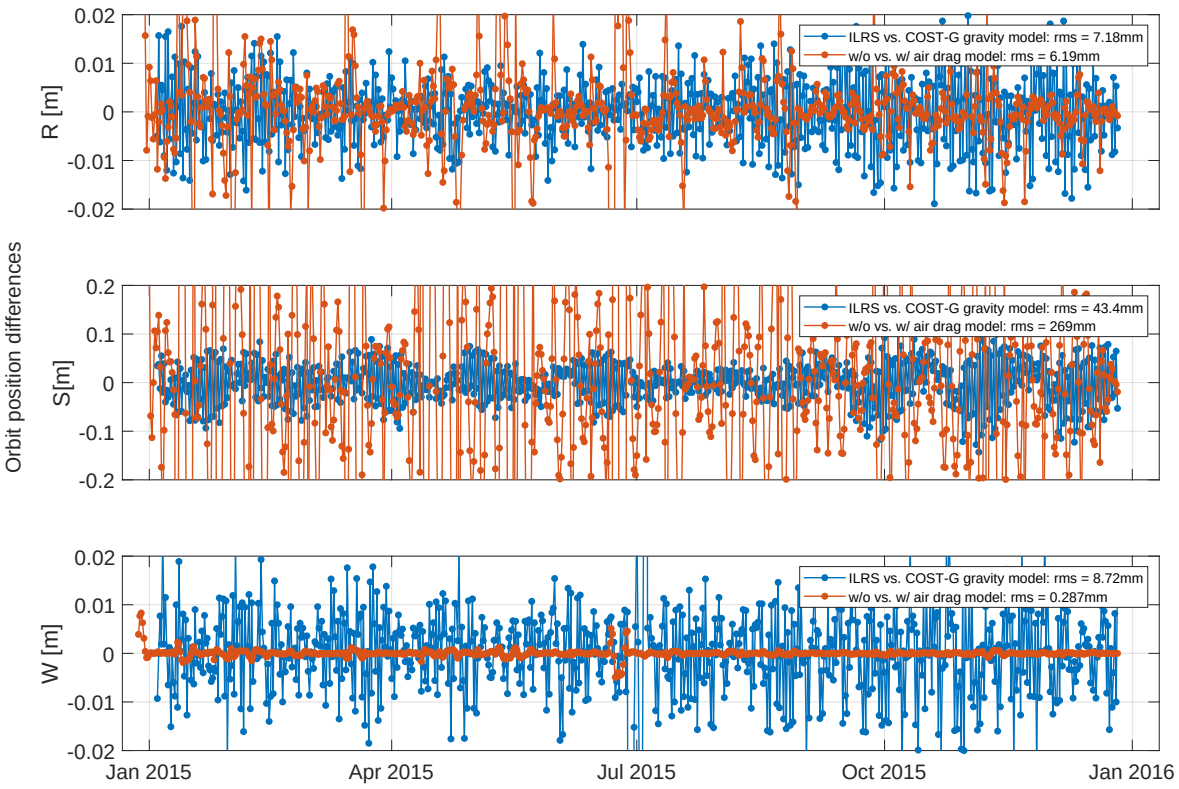

Figure 7.14: Orbit position differences for Starlette in the $\mathcal{R}$-system with or without using the air drag model (red) and when two different gravity field models (blue), i.e., time-variable model provided by the ILRS or COST-G, are applied for the year 2015.

tion coordinates, are almost independent of the air drag modeling of Starlette. The discrepancies in the bias and WRMS of the ERPs are smaller or equal to 1 µas for the polar motion and 1 µs for UT1-UTC, respectively (see Table 7.8). If additional pseudo-stochastic pulses are applied for Starlette, the WRMS of the polar motion increases by 7.0 % and 2.7 % in x- and y-direction, respectively. In contrary to UT1-UTC, where the WRMS is reduced by 8.4 %. While the bias of the X-pole is more than doubled, the bias of the Y-pole is slightly reduced by 8 µas.
The weighted RMS of the Helmert transformation of station coordinates w.r.t. SLRF2014

Table 7.8: Estimated ERP corrections w.r.t. the IERS-14-C04 reference series for SLR multi-satellite combinations of LAGEOS-1/2, LARES and Starlette data, when the air drag is neglected or modeled for Starlette for the year 2015-2020.

Sat.	Air drag	St. pl. in S for D	X-pole [μas]		Y-pole[μas]		UT1-UTC [μs]	
			Bias	WRMS	Bias	WRMS	Bias	WRMS
A+C+D	w/o	-	11.9	124.5	39.1	127.9	−9.6	77.6
A+C+D	w/	-	11.3	125.4	40.0	126.9	−8.6	76.7
A+C+D	w/o	12/day	24.6	133.2	31.2	131.4	−8.2	71.1
A+C+D	w/	12/day	24.6	133.2	30.9	131.2	−8.5	71.1

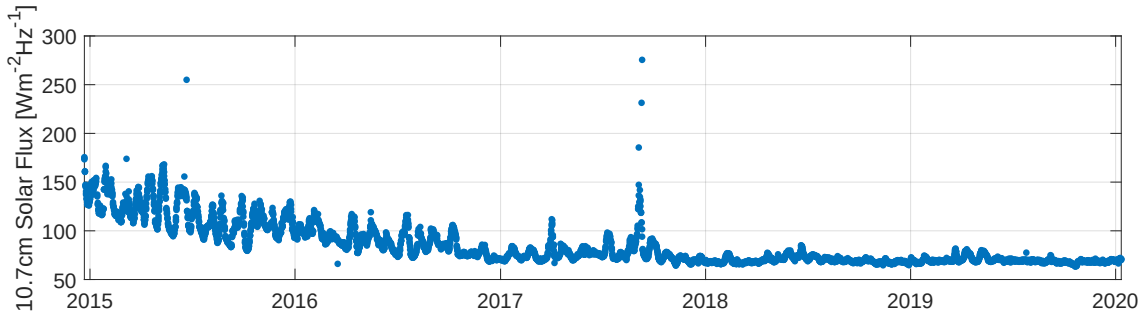

Figure 7.15: The observed 10.7 cm Solar Flux corrected for variations in the Earth-Sun distance for the years 2015-2020[14].

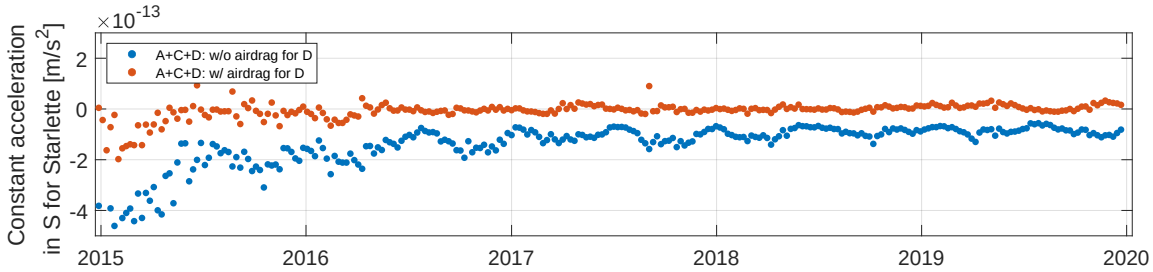

Figure 7.16: Estimated constant accelerations in S for Starlette, when the air drag is neglected (blue) or modeled (orange), in case of SLR combinations of LAGEOS-1/2, LARES and Starlette for the years 2015-2020.

agree also within 0.1 mm for each direction and are therefore not shown here.

The contribution of SLR observations to Starlette is limited, which is a consequence of the small weights that are assigned by VCE to Starlette (see Fig. 7.17). Although the mean weight of Starlette slightly increases when an air drag model is applied, it is almost 3 and 20 times smaller than for LARES and LAGEOS-1/2, respectively. Only the use of pseudo-stochastic pulses for Starlette can increase the weights by almost a factor of ten.
Furthermore, the time series of the weights from VCE of Starlette, when no pseudo-stochastic pulses are used, feature a linear trend (see Fig. 7.17). In 2015, the mean weights are 0.022 and 0.024 without and with an air drag modeling. In contrary to the year 2019, where the mean weights are 0.11 and 0.097, respectively. The temporal variations of the solar flux (see Fig. 7.15), which has a strong effect on the air density and therefore on the strength of the air drag, reveal that the weights from VCE for Starlette are smaller when the solar activity is high and vice versa. This is an indication that there are still problems in the air drag modeling or a priori gravity model.
Nevertheless, the benefit of air drag modeling with NRLMSISE-00 for Starlette is clearly visible in the estimated constant acceleration in S (see Fig. 7.16), which can be strongly reduced.
The additional use of pseudo-stochastic pulses in along-track, which are constrained

[14]https://spaceweather.gc.ca/forecast-prevision/solar-solaire/solarflux/sx-en.php (Accessed: 28/03/2023)

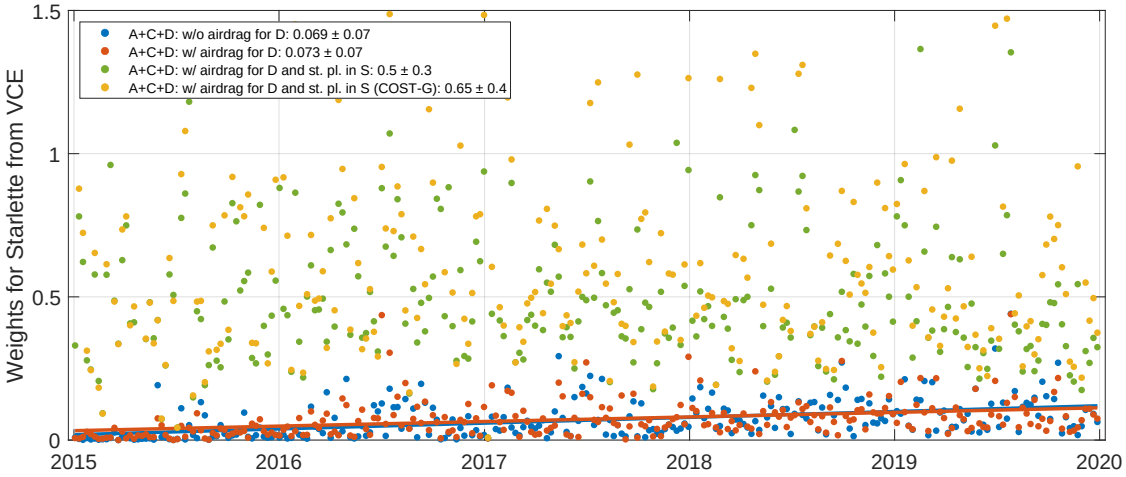

Figure 7.17: Weekly weights for Starlette derived by VCE resulting from LAGEOS-1/2, LARES and Starlette SLR combinations when the air drag is neglected or modeled for Starlette for the years 2015-2020.

with $\sigma = 10^{-6}$m/s, for the orbit parametrization of Starlette increases the mean weight from VCE to 0.5 (see Fig. 7.17). This indicates that the air drag modeling for Starlette is not sufficient and, therefore, causes modeling deficiencies in along-track, which can be partially absorbed by pseudo-stochastic pulses. Hence, Starlette can only contribute reasonably to the estimation of the geodetic parameters if pseudo-stochastic pulses in along-track are set-up (see Table 7.8).

Furthermore, the weights derived by VCE (see Fig. 7.17) reveal that the SLR observations of Starlette better fit to the background modeling, when the time-variable gravity field model of COST-G with replacing C_{21}/S_{21} is used instead of the gravity field model provided by the ILRS.

7.2.2 Contribution of LEO SLR Data to Co-Estimated SH Geopotential Coefficients

As shown in Section 7.1.3, combinations of LAGEOS-1/2 and LARES SLR observations already enable to co-estimate low-degree SH geopotential coefficients. The inclusion of further SLR data to LEOs, i.e., Starlette and Stella, may strengthen the sensitivity to SH geopotential coefficients and may reduce correlations between sought-after parameters. Hence, the parametrization is further extended to co-estimate SH geopotential coefficients up to d/o 5 and C_{61}/S_{61} and is therefore more comparable to the reference series of CSR.

The time series of estimated zonal SH geopotential coefficients (see Fig. 7.18) show that the extension to also co-estimate d/o 5 and C_{61}/S_{61} is only reasonable if Starlette and Stella SLR data are used in the SLR processing. Furthermore, the annual signal of C_{20} and especially C_{30} is damped (see Fig. 7.19) and their time series better coincide with the reference series of CSR. The gained sensitivity to C_{50} allows a reliable estimation of this

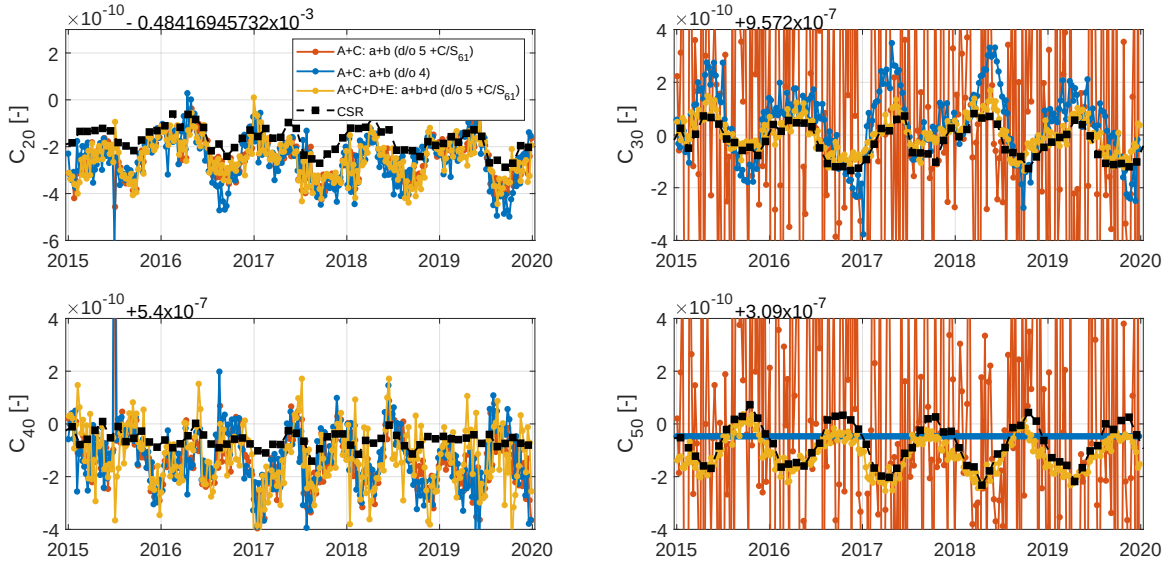

Figure 7.18: Time series of estimated zonal SH geopotential coefficients C_{20}, C_{30}, C_{40} and C_{50} resulting from LAGEOS-1/2, LARES, Starlette and Stella SLR combinations when using different parametrizations for the years 2015-2020.

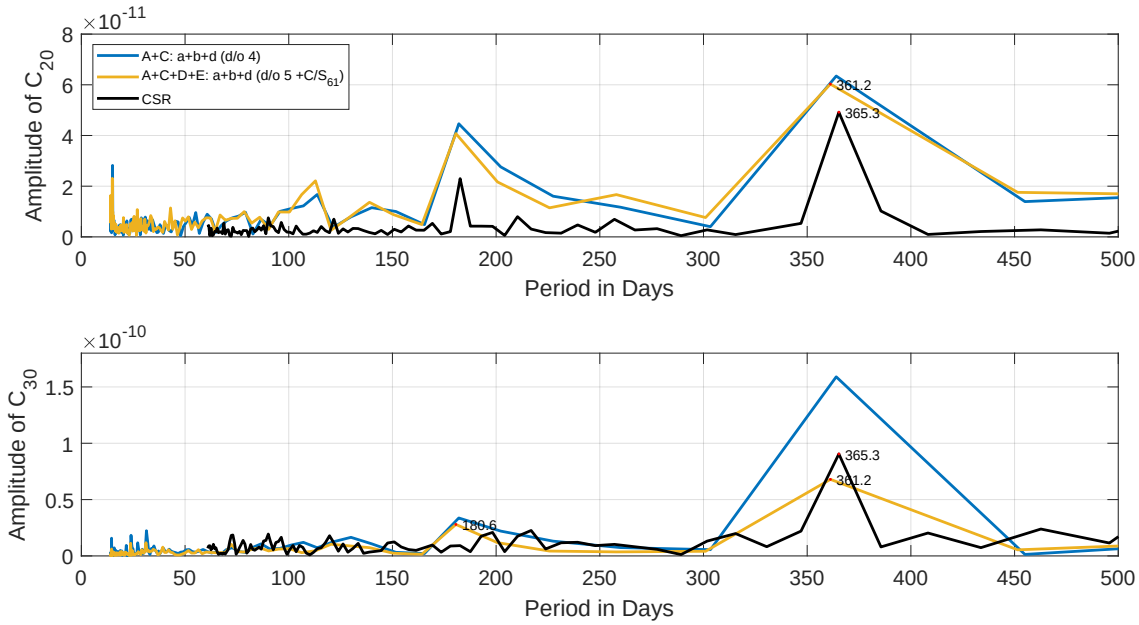

Figure 7.19: Amplitudes from the spectral analysis for C_{20} (top) and C_{30} (bottom) resulting from LAGEOS-1/2, LARES, Starlette and Stella SLR combinations when using different parametrizations for the years 2015-2020.

parameter and may therefore attenuate the signal in the strongly correlated coefficient C_{30}.
In conclusion, the estimation of SH geopotential coefficients is further improved with the inclusion of Starlette and Stella.

The comparison of the ERPs shows much smaller differences between the LAGEOS-1/2 and LARES SLR combinations when SH geopotential coefficients of d/o 5 and C_{61}/S_{61}

Table 7.9: Estimated ERP corrections w.r.t. the IERS-14-C04 reference series resulting from LAGEOS-1/2, LARES, Starlette and Stella SLR combinations when using different parametrizations for the years 2015-2020.

Sat.	Est. SH geo. coeff.	X-pole [μas] Bias	X-pole [μas] WRMS	Y-pole[μas] Bias	Y-pole[μas] WRMS	UT1-UTC [μs] Bias	UT1-UTC [μs] WRMS
A	-	85.6	142.1	31.9	118.1	−1.7	64.3
A+C: $a+b+d$	4/4	61.2	140.1	16.3	128.8	0.1	22.8
A+C: $a+b+d$	$5/5+C/S_{61}$	67.8	142.9	21.7	129.1	0.1	22.5
A+C+D+E: $a+b$	$5/5+C/S_{61}$	69.9	158.1	20.7	140.7	1.8	25.0
A+C+D+E: $a+b+d$	$5/5+C/S_{61}$	76.0	147.5	15.0	128.6	0.9	22.3

are co-estimated instead of fixing them to the a priori values (see Table 7.9). The WRMS of the ERPs increases by less than 2 %, while the bias of the polar motion enlarges by 6.6 µas and 5.4 µas in x- and y-direction, respectively.
The benefit of additional pseudo-stochastic pulses of low-flying satellites, i.e., LARES, Starlette and Stella, in along- and cross-track for LAGEOS-1/2, LARES, Starlette and Stella SLR combinations is reflected in the reduction of the WRMS of the ERPs about 7 % to 11 %. While the bias of the X-pole increases by 6.1 µas, the bias of the Y-pole and UT1-UTC is reduced by 5.7 µas and 0.9 µs, respectively.
The weighted mean of the Helmert transformation of station coordinates agrees within 0.1 mm in North, 0.6 mm in East and 0.4 mm in Up (see Fig. 7.20).

Figure 7.21 shows the weights for each satellite group derived by VCE for LAGEOS-1/2, LARES, Starlette and Stella combinations, i.e., A+C+D+E: a+b+d solutions. The mean weights for the years 2015-2020 are 1.2 for LAGEOS-1/2, 1.1 for LARES, 1.8 for Starlette and 0.5 for Stella. In contrary to the weights in Fig. 7.17, where Starlette is weighted more than three times less. Hence, the additional estimation of the SH geopotential coef-

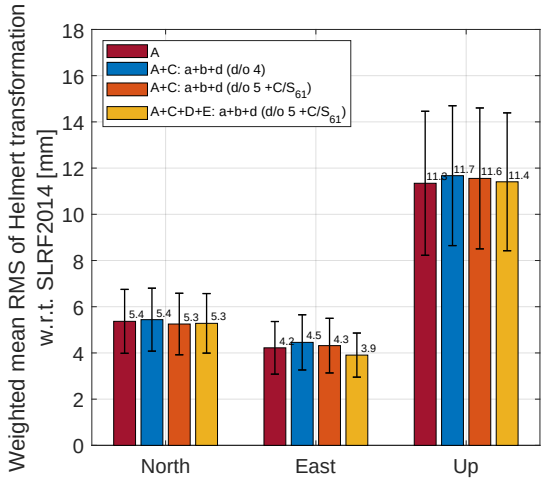

Figure 7.20: Weighted mean RMS of Helmert transformation of station coordinates w.r.t. SLRF2014 resulting from LAGEOS-1/2, LARES, Starlette and Stella SLR combinations using different parametrizations for the years 2015-2020.

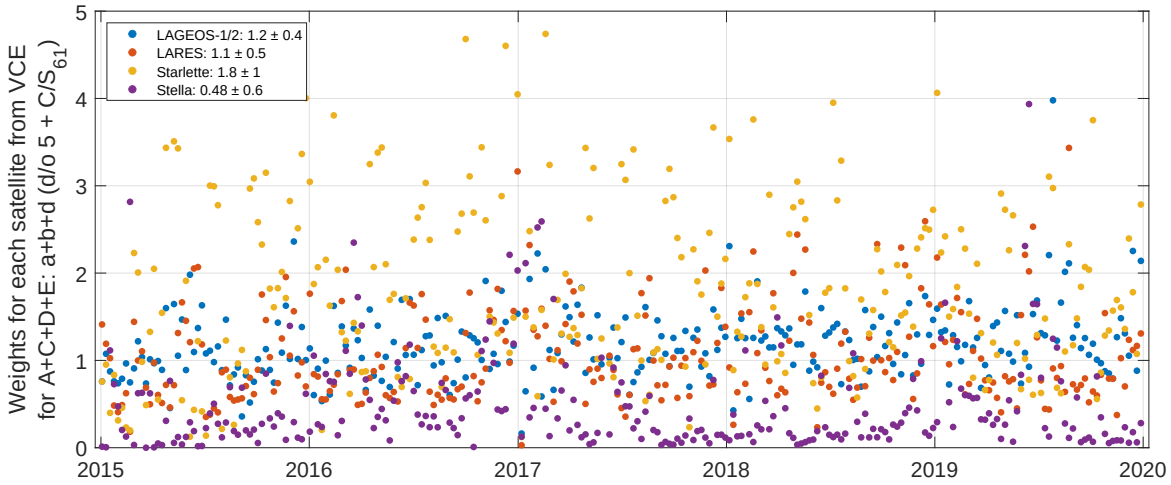

Figure 7.21: Weekly weights for LAGEOS-1/2 (blue), LARES (orange), Starlette (yellow) and Stella (violet) derived by VCE resulting from LAGEOS-1/2, LARES, Starlette and Stella SLR combinations when SH geopotential coefficients up to d/o 5 and C_{61}/S_{61} are co-estimated for the years 2015-2020.

ficients leads to a better agreement between the Starlette observations and the estimated modeling parameters.

Further insights into the use of each satellite group for the parameter estimation may be provided by the contribution analysis on ERPs, geocenter coordinates and SH geopotential coefficients.
The estimation of the polar motion is mainly based on LAGEOS-1/2 and LARES SLR data, which have contributions of 0.7 and 0.2, respectively (see Fig. 7.22). In contrary to UT1-UTC, which is almost only determined by LAGEOS-1/2. While the contribution of Starlette is at least 0.05 on the polar motion, the contribution of Stella is insignificant and can therefore be neglectable for all ERPs.
The estimation of the geocenter coordinates in x- and y-directions is again mainly based on LAGEOS-1/2 and LARES with contributions of 0.75 and 0.14, respectively (see Fig. 7.23). In z-direction, the contribution of Starlette is increased to 0.3 at the expense of the LAGEOS-1/2 contribution part.
The satellite specific contribution to the estimation of the SH geopotential coefficients are averaged over the years 2015-2020 and shown in Figure 7.24. It can be clearly seen that the estimation of C_{20}, C_{21} and S_{21} almost only rely on LAGEOS-1/2.
LARES contributes noticeably to all sectorial and zonal SH geopotential coefficients C_{30}, C_{40} and C_{50}. It has the largest contribution to a subset of degree 4 terms, which are C_{40}, C_{41} and S_{41}. Starlette, however, essentially contributes to the tesseral SH geopotential coefficients. Stella is again almost neglectable for the estimation of the low-degree SH geopotential coefficients. It only starts to slightly contribute to the highest estimated terms C_{61} and S_{61}.

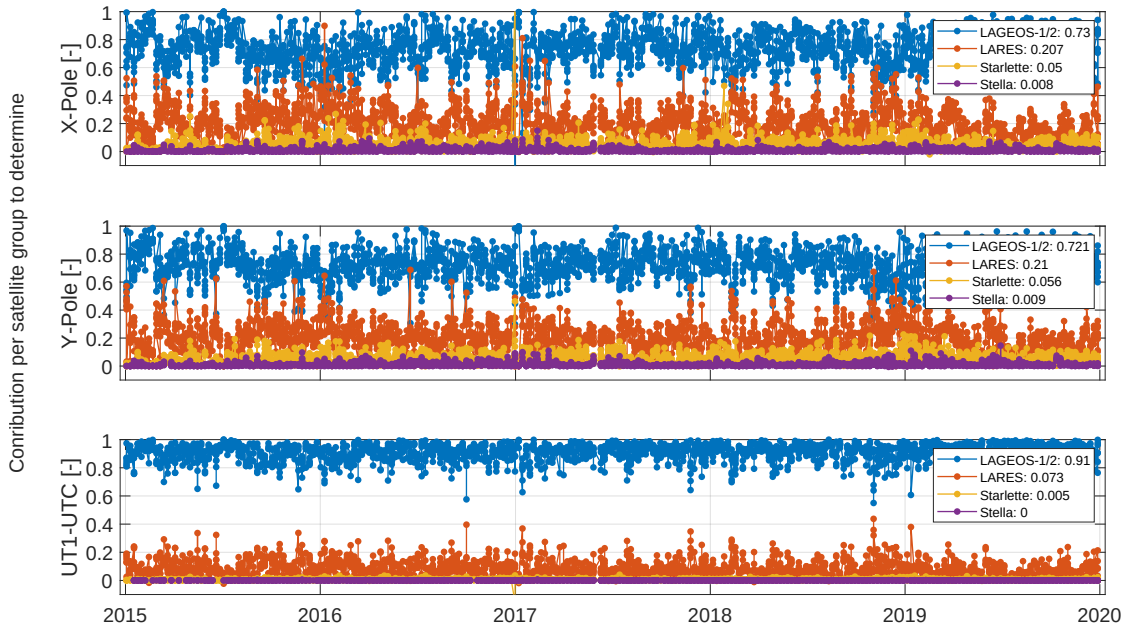

Figure 7.22: Contribution of each satellite group to the estimation of ERPs from LAGEOS-1/2, LARES, Starlette and Stella SLR combinations when estimating SH geopotential coefficients up to d/o 5 and C_{61}/S_{61}, i.e., solution A+C+D+E: a+b+d (d/o 5 + C/S_{61}).

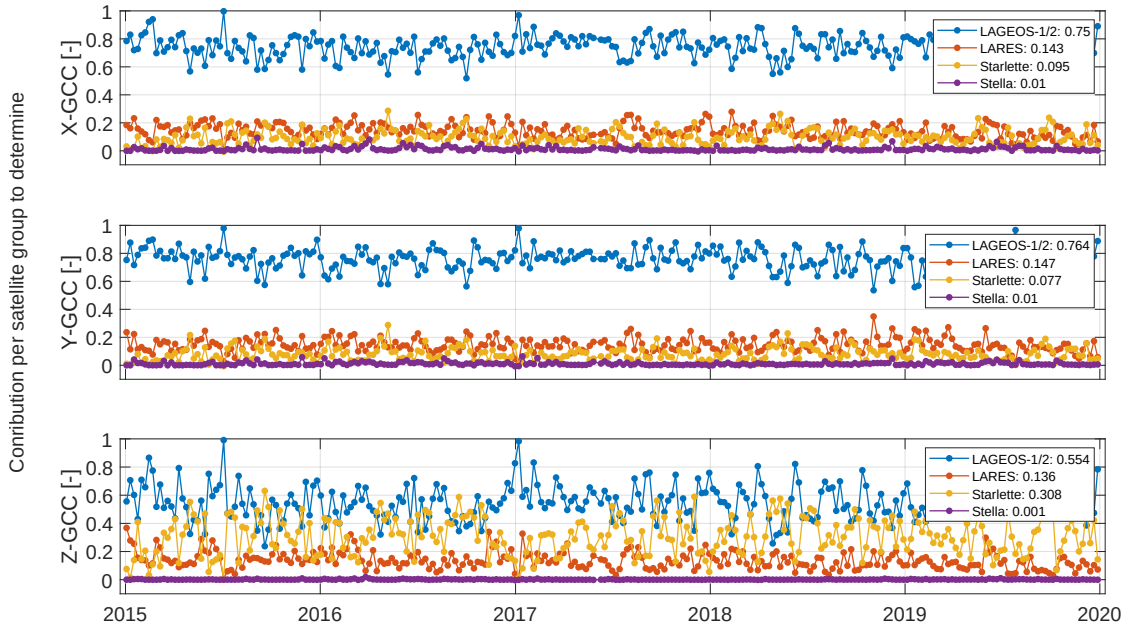

Figure 7.23: Contribution of each satellite group to the estimation of geocenter coordinates from LAGEOS-1/2, LARES, Starlette and Stella SLR combinations when estimating SH geopotential coefficients up to d/o 5 and C_{61}/S_{61}, i.e., solution A+C+D+E: a+b+d (d/o 5 + C/S_{61}).

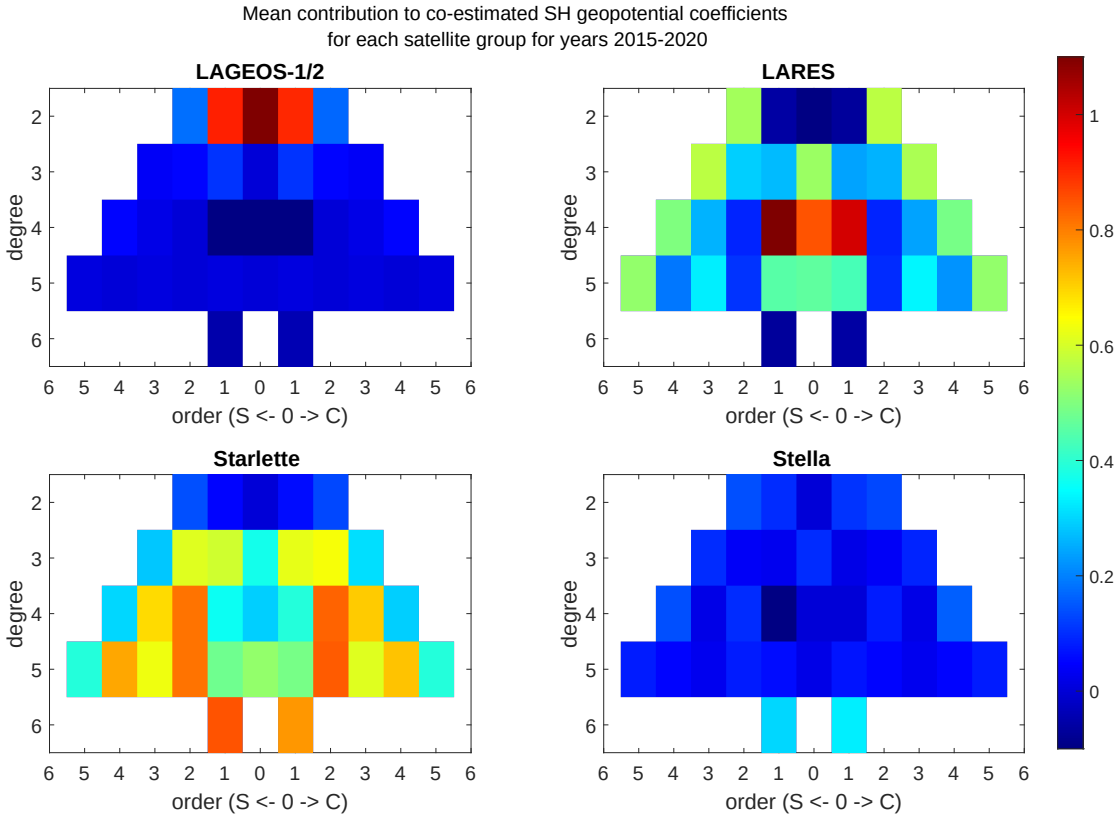

Figure 7.24: Mean contribution of each satellite group to the estimation of SH geopotential coefficients from LAGEOS-1/2, LARES, Starlette and Stella SLR combinations when estimating SH geopotential coefficients up to d/o 5 and C_{61}/S_{61}, i.e., solution A+C+D+E: a+b+d (d/o 5 + C/S_{61}), for the years 2015-2020.

7.3 First Analysis of LARES-2 SLR Data

The LARES-2 satellite mission was launched on July 13, 2022, and the SLR station in Graz, Austria, received the first signals nine days later (see Sec. 2.2). Afterwards, an increasing number of SLR stations started to track LARES-2, such that the SLR LARES-2 NP data used for weekly SLR processing from mid-July to mid-November, 2022, are provided by 19 different SLR stations (see Fig. 7.25, left). The amount of processed LARES-2

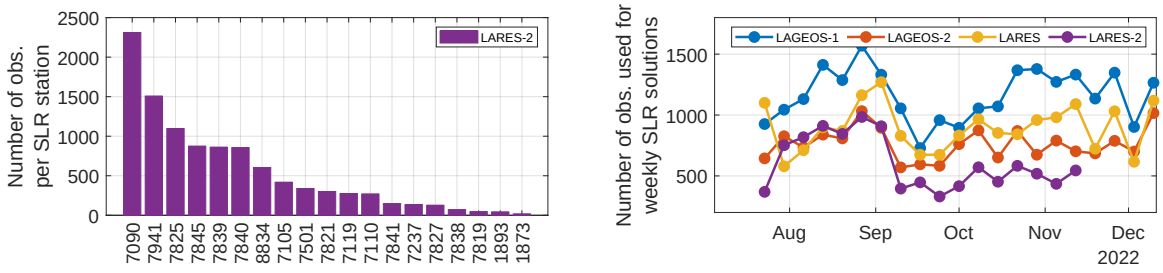

Figure 7.25: Number of NP SLR data to LARES-2 per SLR station (left) and per weekly SLR combination (right) with LAGEOS-1/2 and LARES used for the SLR analysis between mid-July until mid-November, 2022.

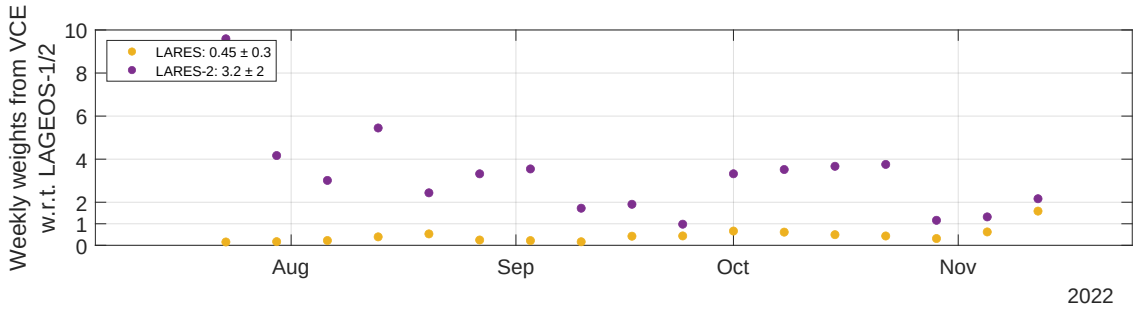

Figure 7.26: Weekly weights for LARES (yellow) and LARES-2 (violet) derived by VCE w.r.t. the LAGEOS-1/2 weights resulting from LAGEOS-1/2, LARES and LARES-2 SLR combinations from mid-July to mid-November, 2022.

NPs almost reaches the level of LAGEOS-2 observations (see Fig. 7.25, right).

LARES-2 has a comparable orbit altitude as the LAGEOS-1/2 satellites (see Table 2.2), and consequently, in a first step, the same orbit parametrization can be adopted (see Table 7.1). Since, at the time of writing, the system-dependent center-of-mass correction and range bias of LARES-2 for each individual SLR station are not yet determined as for LAGEOS-1/2 (Otsubo and Appleby 2003), range biases are additionally estimated for all SLR stations.
Furthermore, the static a priori Earth's gravity field model GGM05S (see Table 4.2) is replaced by the time-variable gravity field model provided by the COST-G (Peter et al. 2022) in order to reduce the mis-modeling especially for LARES.

The contribution of LARES-2 SLR data is studied by validating SLR combinations based on LAGEOS-1/2 and LARES/LARES-2 using VCE.
The weekly estimated weights for LARES-2 are on average 3.24 times higher than for the well performing LAGEOS-1/2 satellites, while LARES is only weighted less than 50 % of LAGEOS-1/2 (see Fig. 7.26). Therefore, the VCE indicates that LARES-2 SLR observations fit even better to the estimated model parameters than LAGEOS-1/2 observations. This can be expected, due to the small area-to-mass ratio of LARES-2 (see Table 2.2) and the rather high orbit altitude.
Nevertheless, the inclusion of LARES-2 data does not significantly change the bias and the WRMS of the polar motion in x-direction (see Table 7.10). However, the bias of the

Table 7.10: Estimated ERP corrections w.r.t. the IERS-14-C04 reference series and the weighted mean RMS of the Helmert transformation of station coordinates w.r.t. SLRF2014 resulting from LAGEOS-1/2, LARES and LARES-2 SLR combinations from mid-July to mid-November, 2022.

Sat.	X-pole [μas]		Y-pole[μas]		UT1-UTC [μs]		RMS of Helmert [mm]		
	Bias	WRMS	Bias	WRMS	Bias	WRMS	North	East	Up
A+D	152.2	198.5	11.7	154.6	−9.5	69.4	7.3	4.8	17.3
A+D+F	158.2	198.5	32.0	140.6	−5.1	76.0	7.4	4.9	17.1

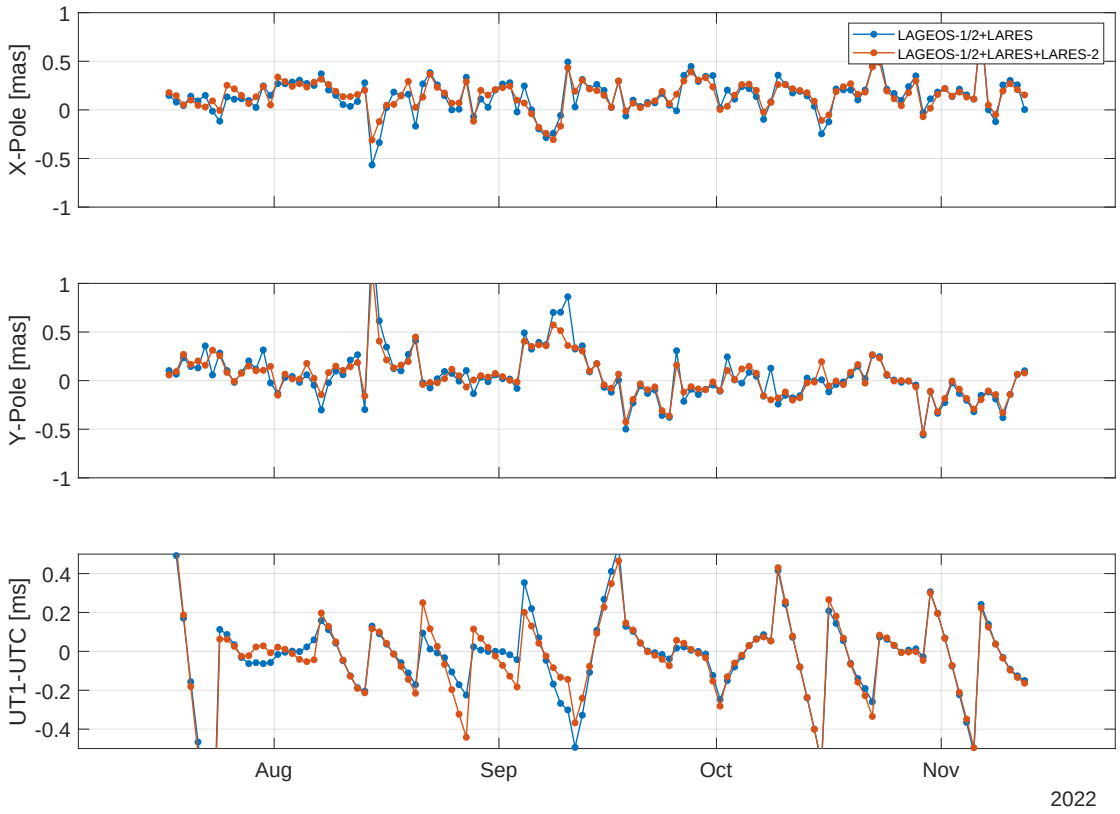

Figure 7.27: Estimated ERP corrections w.r.t. the IERS-14-C04 reference series resulting from LAGEOS-1/2, LARES and/or LARES-2 SLR combinations from mid-July to mid-November, 2022.

Y-pole is more than doubled, while the WRMS can be reduced by 14 µas. The slightly increased WRMS in UT1-UTC can be explained by the unbalanced inclinations of the satellite orbits, i.e., retrograde (LAGEOS-1) or prograde (LAGEOS-2, LARES, LARES-2) motion. Since LARES-2 receives a high weight from the VCE, the ascending nodes are systematically shifted to the benefit of the satellites with a retrograde motion. Hence, through the correlation between the ascending nodes and UT1-UTC (see Eq. 6.1) also the estimation of UT1-UTC is affected and, therefore, the saw tooth behaviour of the time series of UT1-UTC becomes slightly more distinctive (see Fig. 7.27). This can be confirmed by the experiment of LAGEOS-1/2 SLR combinations (see Sec. 7.1.2), where an imbalance with different weights for LAGEOS-1, resp. LAGEOS-2 is enforced (see Fig. 7.4).
The weighted mean RMS of the Helmert transformation of station coordinates w.r.t. SLRF2014 increases only by 0.1 mm in the horizontal plane and 0.2 mm in up direction, if LARES-2 data are included (see Table 7.10).

The estimated range biases for LARES-2 for each individual SLR station are mainly between −18 cm and −17 cm (see Fig. 7.28). These large range biases are caused by the center-of-mass corrections, which are so far not applied. Except for the SLR stations 7819, 7821, 7838 and 7841, the standard deviations of the range biases are smaller than 5 mm.
Furthermore, in Figure 7.29 the RMS of the observation residuals per satellite group,

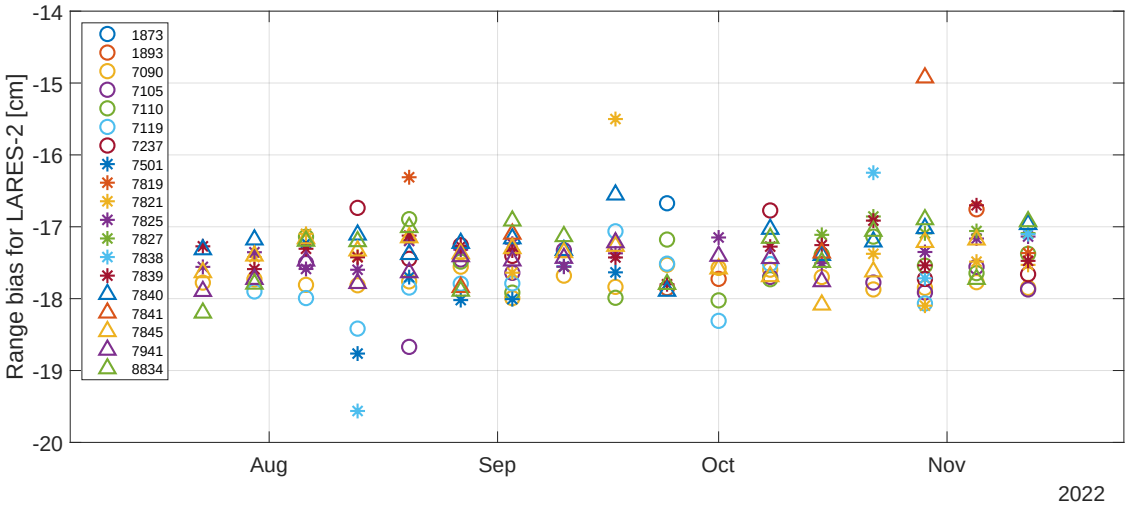

Figure 7.28: Weekly estimated range biases (including the center-of-mass corrections) for LARES-2 of each SLR station resulting from LAGEOS-1/2, LARES and LARES-2 SLR combinations from mid-July to mid-November, 2022.

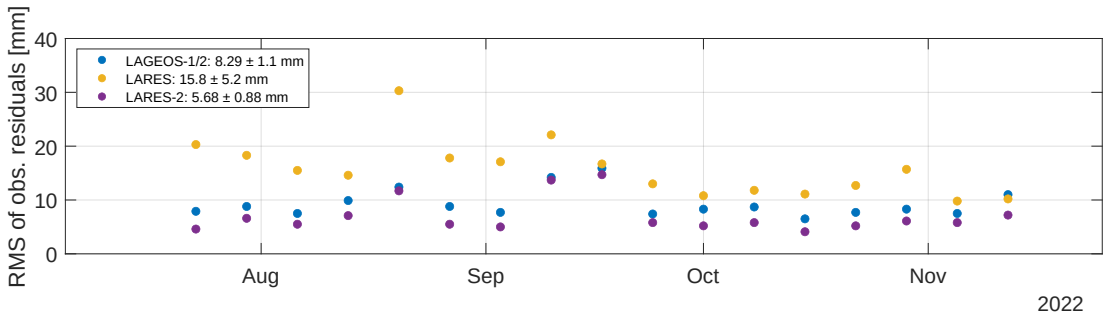

Figure 7.29: RMS of LAGEOS-1/2 (blue), LARES (yellow) and LARES-2 (violet) observation residuals resulting from LAGEOS-1/2, LARES and LARES-2 SLR combinations from mid-July to mid-November, 2022.

i.e., LAGEOS-1/2, LARES and LARES-2, is compared. The mean RMS of the observation residuals from LARES-2 is 1.5 times smaller than for LAGEOS-1/2. On the contrary, LARES observation residuals are the largest with a mean RMS almost twice that of LAGEOS-1/2. However, this is to be expected, since LARES has a lower altitude (see Table 2.2) and thus the orbit modeling becomes more challenging.

Chapter 8

Summary, Conclusions and Outlook

SLR is a well established geodetic technique with its observations covering over more than half a century and currently reaching a measurement accuracy of a few millimeters (Pearlman et al. 2019). It has an indispensable contribution to the determination of geodetic parameters, e.g., the geocenter and station coordinates, which are essential for realizations of long-term stable terrestrial reference frames. As a result, the origin and the scale of the previous ITRF depend solely on SLR and the combination of SLR and VLBI, respectively (Altamimi et al. 2018). Further on, even though nowadays dedicated satellite gravimetry missions such as GRACE/GRACE-FO are available for the determination of the Earth's time-variable gravity field, some of the low-degree SH geopotential coefficients can still be better determined by SLR.
This thesis is devoted to the improvement of the SLR data generation and processing based on the BSW at the AIUB, in order to further strengthen the SLR contribution to geodetic products.

A simulation of a simplified SLR data compression of full-rate data to NPs leads to the conclusion that the quality of the reconstructed orbit of a 40 min satellite pass depends on the actual observation time span. If the observation time span is less than 60 % of the full pass the reconstructed orbit may show larger differences to the original one. Hence, through the data compression some information about the orbit is lost. Furthermore, it also reveals that shorter NP bin sizes may improve the quality of the data compression slightly. However, a shorter NP bin size will also lead to more NP data, which may also have an impact. Nevertheless, due to its strong simplification of the problem, these results will not directly hold for the real SLR data compression without further investigations.
Nonetheless, this simulation motivates further studies, e.g., about the impact of the SLR data distribution over a satellite fly-by (observing the satellite at the beginning and/or at the end of a fly-by), on the quality of the estimated parameters resulting from SLR processing. Consequently, the performance of SLR stations without weakening the quality of the estimated parameters might be improved.

To perform a SLR data compression at the AIUB, a NP generator was implemented into a development version of the BSW. It allows to generate NPs from full-rate data (given in CRD-format) provided by any SLR station. Additionally, different trend functions (polynomials or adjusted orbit trajectories) and screening methods (RMS-based

and Leading-Edge) can be selected and directly be validated by performing a SLR processing to estimate geodetic parameters. Already from the first results, where only NPs from SwissOGS are formed with the new NP generator, differences occur in the estimates of the geodetic parameters from LAGEOS-1/2 SLR combinations. Although these differences are not yet significant, they indicate a potential impact of a homogeneous generation of SLR NPs from all stations on the parameter estimation.

The analysis of the geodetic parametrization based on LAGEOS-1/2 SLR combinations suggests to represent the ERPs by piece-wise linear functions. This guarantees continuity at day boundaries, and thus, describes the temporal evolution of the ERPs in a more physical way. However, this degrades UT1-UTC, where saw-tooth behaviour is induced, due to the emerging strong correlation with the satellite's ascending node and consequently with OPR-W accelerations. Therefore, SLR combinations, where the polar motion and UT1-UTC are differently parametrized by piece-wise linear and piece-wise constant functions, respectively, are to be analyzed.
Furthermore, it is investigated that the set of selected core stations used for the datum definition has a significant impact on the estimates of the geodetic parameters, e.g., ERPs and geocenter coordinates. The Helmert approach of core station selection ensures that only stable SLR stations are used and, therefore, prevents the usage of pre-defined sets of core stations.

The lower a satellite is orbiting the Earth, the more demanding the orbit modeling, e.g., air drag and the Earth's gravity field, becomes. While the air drag modeling is not used for LAGEOS-1/2 and has only a marginal impact on LARES orbits, it is essential but not sufficient for Starlette. It is able to reduce the magnitude of co-estimated constant dynamic orbit parameters but increased weights derived by VCE when applying pseudo-stochastic pulses twelve times a day in along-track indicate remaining modeling deficiencies.
The comparison of the performance of different a priori time-variable gravity field models provided by the ILRS and COST-G confirms the high quality of the COST-G products, since the majority of the estimated geodetic parameters are improved and the RMS of the observation residuals for LARES and Starlette are reduced.

In this work, it is demonstrated that in the SLR data processing VCE can be used to apply appropriate constraints on pseudo-stochastic pulses, to take the NP data for each station according to their quality into account or to provide reasonable station-specific weights when performing multi-satellite SLR combinations.
It may further allow to study the optimal orbit and geodetic parametrizations by introducing appropriate constraints on dynamic orbit parameters or on correlated SH geopotential coefficients. The idea of the station-specific weighting may be used in the procedure of the SLR data screening. Since the performance and therefore the quality of the NPs may vary over time, the weights should be estimated per station and per satellite pass.

Due to correlations, low-degree SH geopotential coefficients, e.g., C_{20} and C_{30}, can only be reliably estimated if the dynamic orbit parameters OPR-W for all satellites and OPR-

S for the low-flying satellites are neglected. The contribution analysis identified that the zonal and tesseral coefficients of degree 2 are mainly determined based on LAGEOS-1/2 SLR observations, while C_{40}, C_{41} and S_{41} rely on LARES SLR data. Additionally, LARES also strongly contributes to the determination of the sectorial coefficients and Starlette becomes important for the remaining tesseral coefficients and for degree 6 terms. Furthermore, the multi-satellite SLR combinations can still be extended by including further geodetic satellites, e.g., Ajisai (Sośnica et al. 2014) or LARES-2.

Finally, the outstanding performance of LARES-2 is shown, which may offer the opportunity to improve the SLR contribution to further ITRF realizations.

Appendix A

Long-Arc Computations

For day $i \in \{1, 2, ..., n\}$ we denote

$$E_{k,i} : \text{osculating orbital elements (with } k \in \{1, ..., 6\}),$$
$$p_{k,i} : \text{dynamic parameters (with } k \in \{1, ..., d\}),$$

where the dynamic parameters are divided into two groups

$$q_{k,i} : \text{dynamic orbit parameters (with } k \in \{1, ..., m_q\}, \text{ where } m_q < d),$$
$$g_{k,i} : \text{gravity field parameters (with } k \in \{1, ..., m_g\}, \text{ where } m_g \leq d - m_q).$$

Asking for continuity and differentiability at the day boundaries of the daily arcs (for day i and $i + 1$) and a first-order Taylor series expansion lead to

$$\begin{aligned} \Delta\mathbf{E}_{i+1} =& \mathbf{H}_{i+1}^{-1}(\mathbf{x}_{0,i} - \mathbf{x}_{0,i+1}) + \mathbf{H}_{i+1}^{-1}\mathbf{H}_i\Delta\mathbf{E}_i \\ &+ \mathbf{H}_{i+1}^{-1}(\mathbf{Q}_i\Delta\mathbf{q}_i - \mathbf{Q}_{i+1}\Delta\mathbf{q}_{i+1}) \\ &+ \mathbf{H}_{i+1}^{-1}(\mathbf{G}_i - \mathbf{G}_{i+1})\Delta\mathbf{g}_i + \mathbf{H}_{i+1}^{-1}\mathbf{G}_{i+1}(\mathbf{g}_{0,i+1} - \mathbf{g}_{0,i}) \end{aligned} \tag{A.1}$$

and if only one set of gravity field parameters shall be computed for the entire long-arc, the following equation holds

$$\Delta\mathbf{g}_{i+1} = \Delta\mathbf{g}_i + \left(\mathbf{g}_{0,i} - \mathbf{g}_{0,i+1}\right) \tag{A.2}$$

with

$$\begin{aligned} \mathbf{x}_{0,i} &= \begin{pmatrix} \mathbf{r}_{0,i} \\ \dot{\mathbf{r}}_{0,i} \end{pmatrix}, \\ \mathbf{H}_i &= \begin{pmatrix} \frac{\partial \mathbf{x}_{0,i}}{\partial E_{1,i}} & \cdots & \frac{\partial \mathbf{x}_{0,i}}{\partial E_{6,i}} \end{pmatrix}, \\ \mathbf{Q}_i &= \begin{pmatrix} \frac{\partial \mathbf{x}_{0,i}}{\partial q_{1,i}} & \cdots & \frac{\partial \mathbf{x}_{0,i}}{\partial q_{m_q,i}} \end{pmatrix}, \\ \mathbf{G}_i &= \begin{pmatrix} \frac{\partial \mathbf{x}_{0,i}}{\partial g_{1,i}} & \cdots & \frac{\partial \mathbf{x}_{0,i}}{\partial g_{m_g,i}} \end{pmatrix}. \end{aligned} \tag{A.3}$$

$i = 1$:

$$\begin{aligned}\Delta\mathbf{E}_2 =&\mathbf{H}_2^{-1}(\mathbf{x}_{0,1} - \mathbf{x}_{0,2}) + \mathbf{H}_2^{-1}\mathbf{H}_1\Delta\mathbf{E}_1\\ &+ \mathbf{H}_2^{-1}(\mathbf{Q}_1\Delta\mathbf{q}_1 - \mathbf{Q}_2\Delta\mathbf{q}_2)\\ &+ \mathbf{H}_2^{-1}(\mathbf{G}_1 - \mathbf{G}_2)\Delta\mathbf{g}_1 + \mathbf{H}_2^{-1}\mathbf{G}_2(\mathbf{g}_{0,2} - \mathbf{g}_{0,1})\end{aligned} \tag{A.4}$$

$$\Delta\mathbf{g}_2 = \Delta\mathbf{g}_1 + \left(\mathbf{g}_{0,1} - \mathbf{g}_{0,2}\right)$$

$i = 2$:

$$\begin{aligned}\Delta\mathbf{E}_3 =&\mathbf{H}_3^{-1}(\mathbf{x}_{0,2} - \mathbf{x}_{0,3}) + \mathbf{H}_3^{-1}\mathbf{H}_2\Delta\mathbf{E}_2\\ &+ \mathbf{H}_3^{-1}(\mathbf{Q}_2\Delta\mathbf{q}_2 - \mathbf{Q}_3\Delta\mathbf{q}_3)\\ &+ \mathbf{H}_3^{-1}(\mathbf{G}_2 - \mathbf{G}_3)\Delta\mathbf{g}_2 + \mathbf{H}_3^{-1}\mathbf{G}_3(\mathbf{g}_{0,3} - \mathbf{g}_{0,2})\end{aligned} \tag{A.5}$$

$$\Delta\mathbf{g}_3 = \Delta\mathbf{g}_2 + \left(\mathbf{g}_{0,2} - \mathbf{g}_{0,3}\right)$$

Inserting Eq. A.4 in Eq. A.5 yields

$$\begin{aligned}\Delta\mathbf{E}_3 =&\mathbf{H}_3^{-1}(\mathbf{x}_{0,2} - \mathbf{x}_{0,3}) + \mathbf{H}_3^{-1}\mathbf{H}_2\Big[\mathbf{H}_2^{-1}(\mathbf{x}_{0,1} - \mathbf{x}_{0,2}) + \mathbf{H}_2^{-1}\mathbf{H}_1\Delta\mathbf{E}_1\\ &+ \mathbf{H}_2^{-1}(\mathbf{Q}_1\Delta\mathbf{q}_1 - \mathbf{Q}_2\Delta\mathbf{q}_2)\\ &+ \mathbf{H}_2^{-1}(\mathbf{G}_1 - \mathbf{G}_2)\Delta\mathbf{g}_1 + \mathbf{H}_2^{-1}\mathbf{G}_2(\mathbf{g}_{0,2} - \mathbf{g}_{0,1})\Big]\\ &+ \mathbf{H}_3^{-1}(\mathbf{Q}_2\Delta\mathbf{q}_2 - \mathbf{Q}_3\Delta\mathbf{q}_3)\\ &+ \mathbf{H}_3^{-1}(\mathbf{G}_2 - \mathbf{G}_3)\left[\Delta\mathbf{g}_1 + \left(\mathbf{g}_{0,1} - \mathbf{g}_{0,2}\right)\right] + \mathbf{H}_3^{-1}\mathbf{G}_3(\mathbf{g}_{0,3} - \mathbf{g}_{0,2})\\ =&\mathbf{H}_3^{-1}(\mathbf{x}_{0,2} - \mathbf{x}_{0,3}) + \mathbf{H}_3^{-1}(\mathbf{x}_{0,1} - \mathbf{x}_{0,2}) + \mathbf{H}_3^{-1}\mathbf{H}_1\Delta\mathbf{E}_1\\ &+ \mathbf{H}_3^{-1}(\mathbf{Q}_1\Delta\mathbf{q}_1 - \mathbf{Q}_2\Delta\mathbf{q}_2)\\ &+ \mathbf{H}_3^{-1}(\mathbf{G}_1 - \mathbf{G}_2)\Delta\mathbf{g}_1 + \mathbf{H}_3^{-1}\mathbf{G}_2(\mathbf{g}_{0,2} - \mathbf{g}_{0,1})\\ &+ \mathbf{H}_3^{-1}(\mathbf{Q}_2\Delta\mathbf{q}_2 - \mathbf{Q}_3\Delta\mathbf{q}_3)\\ &+ \mathbf{H}_3^{-1}(\mathbf{G}_2 - \mathbf{G}_3)\left[\Delta\mathbf{g}_1 + \left(\mathbf{g}_{0,1} - \mathbf{g}_{0,2}\right)\right] + \mathbf{H}_3^{-1}\mathbf{G}_3(\mathbf{g}_{0,3} - \mathbf{g}_{0,2})\\ =&\mathbf{H}_3^{-1}(\mathbf{x}_{0,1} - \mathbf{x}_{0,3}) + \mathbf{H}_3^{-1}\mathbf{H}_1\Delta\mathbf{E}_1\\ &+ \mathbf{H}_3^{-1}(\mathbf{Q}_1\Delta\mathbf{q}_1 - \mathbf{Q}_3\Delta\mathbf{q}_3)\\ &+ \mathbf{H}_3^{-1}(\mathbf{G}_1 - \mathbf{G}_3)\Delta\mathbf{g}_1 + \mathbf{H}_3^{-1}\mathbf{G}_3(\mathbf{g}_{0,3} - \mathbf{g}_{0,1})\end{aligned} \tag{A.6}$$

$$\begin{aligned}\Delta\mathbf{g}_3 =&\Delta\mathbf{g}_2 + \left(\mathbf{g}_{0,2} - \mathbf{g}_{0,3}\right)\\ =&\Delta\mathbf{g}_1 + \left(\mathbf{g}_{0,1} - \mathbf{g}_{0,2}\right) + \left(\mathbf{g}_{0,2} - \mathbf{g}_{0,3}\right)\\ =&\Delta\mathbf{g}_1 + \left(\mathbf{g}_{0,1} - \mathbf{g}_{0,3}\right)\end{aligned}$$

$i = 3$:

$$
\begin{aligned}
\Delta\mathbf{E}_4 =& \mathbf{H}_4^{-1}(\mathbf{x}_{0,3} - \mathbf{x}_{0,4}) + \mathbf{H}_4^{-1}\mathbf{H}_3\Delta\mathbf{E}_3 \\
&+ \mathbf{H}_4^{-1}(\mathbf{Q}_3\Delta\mathbf{q}_3 - \mathbf{Q}_4\Delta\mathbf{q}_4) \\
&+ \mathbf{H}_4^{-1}(\mathbf{G}_3 - \mathbf{G}_4)\Delta\mathbf{g}_3 + \mathbf{H}_4^{-1}\mathbf{G}_4(\mathbf{g}_{0,4} - \mathbf{g}_{0,3}) \\
\Delta\mathbf{E}_4 =& \mathbf{H}_4^{-1}(\mathbf{x}_{0,3} - \mathbf{x}_{0,4}) + \mathbf{H}_4^{-1}\mathbf{H}_3\Big[\mathbf{H}_3^{-1}(\mathbf{x}_{0,1} - \mathbf{x}_{0,3}) + \mathbf{H}_3^{-1}\mathbf{H}_1\Delta\mathbf{E}_1 \\
&+ \mathbf{H}_3^{-1}(\mathbf{Q}_1\Delta\mathbf{q}_1 - \mathbf{Q}_3\Delta\mathbf{q}_3) \\
&+ \mathbf{H}_3^{-1}(\mathbf{G}_1 - \mathbf{G}_3)\Delta\mathbf{g}_1 + \mathbf{H}_3^{-1}\mathbf{G}_3(\mathbf{g}_{0,3} - \mathbf{g}_{0,1})\Big] \\
&+ \mathbf{H}_4^{-1}(\mathbf{Q}_3\Delta\mathbf{q}_3 - \mathbf{Q}_4\Delta\mathbf{q}_4) \\
&+ \mathbf{H}_4^{-1}(\mathbf{G}_3 - \mathbf{G}_4)\Big[\Delta\mathbf{g}_1 + \Big(\mathbf{g}_{0,1} - \mathbf{g}_{0,3}\Big)\Big] + \mathbf{H}_4^{-1}\mathbf{G}_4(\mathbf{g}_{0,4} - \mathbf{g}_{0,3}) \\
=& \mathbf{H}_4^{-1}(\mathbf{x}_{0,3} - \mathbf{x}_{0,4}) + \mathbf{H}_4^{-1}(\mathbf{x}_{0,1} - \mathbf{x}_{0,3}) + \mathbf{H}_4^{-1}\mathbf{H}_1\Delta\mathbf{E}_1 \\
&+ \mathbf{H}_4^{-1}(\mathbf{Q}_1\Delta\mathbf{q}_1 - \mathbf{Q}_3\Delta\mathbf{q}_3) \\
&+ \mathbf{H}_4^{-1}(\mathbf{G}_1 - \mathbf{G}_3)\Delta\mathbf{g}_1 + \mathbf{H}_4^{-1}\mathbf{G}_3(\mathbf{g}_{0,3} - \mathbf{g}_{0,1}) \\
&+ \mathbf{H}_4^{-1}(\mathbf{Q}_3\Delta\mathbf{q}_3 - \mathbf{Q}_4\Delta\mathbf{q}_4) \\
&+ \mathbf{H}_4^{-1}(\mathbf{G}_3 - \mathbf{G}_4)\Big[\Delta\mathbf{g}_1 + \Big(\mathbf{g}_{0,1} - \mathbf{g}_{0,3}\Big)\Big] + \mathbf{H}_4^{-1}\mathbf{G}_4(\mathbf{g}_{0,4} - \mathbf{g}_{0,3}) \\
=& \mathbf{H}_4^{-1}(\mathbf{x}_{0,1} - \mathbf{x}_{0,4}) + \mathbf{H}_4^{-1}\mathbf{H}_1\Delta\mathbf{E}_1 \\
&+ \mathbf{H}_4^{-1}(\mathbf{Q}_1\Delta\mathbf{q}_1 - \mathbf{Q}_4\Delta\mathbf{q}_4) \\
&+ \mathbf{H}_4^{-1}(\mathbf{G}_1 - \mathbf{G}_4)\Delta\mathbf{g}_1 + \mathbf{H}_4^{-1}\mathbf{G}_4(\mathbf{g}_{0,4} - \mathbf{g}_{0,1})
\end{aligned}
$$

$$
\begin{aligned}
\Delta\mathbf{g}_4 =& \Delta\mathbf{g}_1 + \Big(\mathbf{g}_{0,1} - \mathbf{g}_{0,3}\Big) + \Big(\mathbf{g}_{0,3} - \mathbf{g}_{0,4}\Big) \\
=& \Delta\mathbf{g}_1 + \Big(\mathbf{g}_{0,1} - \mathbf{g}_{0,4}\Big)
\end{aligned}
$$

Hence, the recursive transformations from day $i + 1$ to day i can be expressed as

$$
\begin{aligned}
\Delta\mathbf{E}_{i+1} =& \mathbf{H}_{i+1}^{-1}(\mathbf{x}_{0,1} - \mathbf{x}_{0,i+1}) + \mathbf{H}_{i+1}^{-1}\mathbf{H}_1\Delta\mathbf{E}_1 \\
&+ \mathbf{H}_{i+1}^{-1}(\mathbf{Q}_1\Delta\mathbf{q}_1 - \mathbf{Q}_{i+1}\Delta\mathbf{q}_{i+1}) \\
&+ \mathbf{H}_{i+1}^{-1}(\mathbf{G}_1 - \mathbf{G}_{i+1})\Delta\mathbf{g}_1 + \mathbf{H}_{i+1}^{-1}\mathbf{G}_{i+1}(\mathbf{g}_{0,i+1} - \mathbf{g}_{0,1})
\end{aligned} \tag{A.8}
$$

$$
\Delta\mathbf{g}_{i+1} = \Delta\mathbf{g}_1 + \Big(\mathbf{g}_{0,1} - \mathbf{g}_{0,i+1}\Big)
$$

Appendix B

Accelerations, Expressed in the co-rotating Orbital Frame, Acting on a Satellite Due to Spherical Harmonic Geopotential Coefficients C_{20} and C_{30}

The gravity field potential in spherical harmonic expansion in the Earth-fixed frame using the system of spherical coordinates, i.e., radial distance r, longitude λ and colatitude θ, is given by

$$V(r,\lambda,\theta) = \frac{GM}{r}\sum_{i=0}^{\infty}\left(\frac{a_{\mathrm{E}}}{r}\right)^{i}\sum_{k=0}^{i}P_{ik}(\cos\theta)\left\{C_{ik}\cos(k\lambda)+S_{ik}\sin(k\lambda)\right\} \tag{B.1}$$

with the associated Legendre functions

$$\begin{aligned} P_{ik}(x) &= (1-x^2)^{\frac{k}{2}}\frac{d^k}{dx^k}\left\{P_i(x)\right\}, \\ P_{i0}(x) &= P_i(x) = \frac{1}{2^i i!}\frac{d^i}{dx^i}\left\{(x^2-1)^i\right\}, \end{aligned} \tag{B.2}$$

where P_i are the Legendre polynoms of degree i and the Earth's spherical harmonic coefficients C_{ik}, S_{ik} of degree i and order k. Further, a_{E} defines the equatorial radius of the Earth and GM is the gravitational constant multiplied by the mass of the Earth.

The first terms of the gravity field potential are

$$\begin{aligned} V(r,\lambda,\phi) = \frac{GM}{r}(1 &+ \left(\frac{a_E}{r}\right)^1 P_{10}(\cos\theta)\{C_{10}\cos(0) + S_{10}\sin(0)\} \\ &+ \left(\frac{a_E}{r}\right)^1 P_{11}(\cos\theta)\{C_{11}\cos(\lambda) + S_{11}\sin(\lambda)\} \\ &+ \left(\frac{a_E}{r}\right)^2 P_{20}(\cos\theta)\{C_{20}\cos(0) + S_{20}\sin(0)\} \\ &+ \left(\frac{a_E}{r}\right)^2 P_{21}(\cos\theta)\{C_{21}\cos(\lambda) + S_{21}\sin(\lambda)\} \\ &+ \left(\frac{a_E}{r}\right)^2 P_{22}(\cos\theta)\{C_{22}\cos(2\lambda) + S_{22}\sin(2\lambda)\} \\ &+ \left(\frac{a_E}{r}\right)^3 P_{30}(\cos\theta)\{C_{30}\cos(0) + S_{30}\sin(0)\}) + \ldots \end{aligned} \tag{B.3}$$

The Legendre polynoms for the term C_{20} and C_{30} are

$$\begin{aligned} P_{20}(\cos\theta) &= \frac{1}{2^2 2!}\frac{d^2}{dx^2}\left\{(x^2-1)^2\right\}_{(x=\cos\theta)} \\ &= \frac{1}{2^2 2!}\frac{d}{dx}\left\{2(x^2-1)2x\right\}_{(x=\cos\theta)} \\ &= \frac{1}{2!}\left\{(x^2-1)+2x^2\right\}_{(x=\cos\theta)} \\ &= \frac{1}{2}\left\{3\cos^2\theta - 1\right\} \\ P_{30}(\cos\theta) &= \frac{1}{2^3 3!}\frac{d^3}{dx^3}\left\{(x^2-1)^3\right\}_{(x=\cos\theta)} \\ &= \frac{1}{2^3 3!}\frac{d^2}{dx^2}\left\{3(x^2-1)^2 2x\right\}_{(x=\cos\theta)} \\ &= \frac{1}{2^2 2!}\frac{d}{dx}\left\{(x^2-1)^2 + 2(x^2-1)2x^2\right\}_{(x=\cos\theta)} \\ &= \frac{1}{2^2 2!}\left\{2(x^2-1)2x + 4\cdot 2x^3 + 4(x^2-1)2x\right\}_{(x=\cos\theta)} \\ &= \frac{1}{2!}\left\{(x^2-1)x + 2x^3 + (x^2-1)2x\right\}_{(x=\cos\theta)} \\ &= \frac{1}{2!}\left\{x^3 - x + 2x^3 + 2x^3 - 2x\right\}_{(x=\cos\theta)} \\ &= \frac{1}{2}\left\{5\cos^3\theta - 3\cos\theta\right\}. \end{aligned} \tag{B.4}$$

To change the reference frame to the co-rotating orbital frame, the rotation matrix $\mathbf{R} = \mathbf{R}_3(u)\mathbf{R}_1(i)\mathbf{R}_3(\Omega)$ has be used as

$$\begin{pmatrix} r_1 \\ r_2 \\ r_3 \end{pmatrix} = r\mathbf{R}^{-1}\begin{pmatrix} 1 \\ 0 \\ 0 \end{pmatrix} \tag{B.5}$$

with

$$\begin{aligned}\mathbf{R} &= \begin{pmatrix} \cos(u) & \sin(u) & 0 \\ -\sin(u) & \cos(u) & 0 \\ 0 & 0 & 1 \end{pmatrix} \begin{pmatrix} 1 & 0 & 0 \\ 0 & \cos(i) & \sin(i) \\ 0 & -\sin(i) & \cos(i) \end{pmatrix} \begin{pmatrix} \cos(\Omega) & \sin(\Omega) & 0 \\ -\sin(\Omega) & \cos(\Omega) & 0 \\ 0 & 0 & 1 \end{pmatrix} \\ &= \begin{pmatrix} \cos(u) & \sin(u) & 0 \\ -\sin(u) & \cos(u) & 0 \\ 0 & 0 & 1 \end{pmatrix} \begin{pmatrix} \cos(\Omega) & \sin(\Omega) & 0 \\ -\sin(\Omega)\cos(i) & \cos(i)\cos(\Omega) & \sin(i) \\ \sin(i)\sin(\Omega) & -\sin(i)\cos(\Omega) & \cos(i) \end{pmatrix} \\ &= \begin{pmatrix} \cos(u)\cos(\Omega) - \sin(u)\sin(\Omega)\cos(i) & \cos(u)\sin(\Omega) + \sin(u)\cos(i)\cos(\Omega) & \sin(u)\sin(i) \\ -\sin(u)\cos(\Omega) - \cos(u)\sin(\Omega)\cos(i) & -\sin(u)\sin(\Omega) + \cos(u)\cos(i)\cos(\Omega) & \cos(u)\sin(i) \\ \sin(i)\sin(\Omega) & -\sin(i)\cos(\Omega) & \cos(i) \end{pmatrix}. \end{aligned} \tag{B.6}$$

B.1 Acceleration Due to C_{20}

The gravity field potential term containing C_{20} reads as

$$V(r,\lambda,\theta)_{C_{20}} = \frac{GM}{r}\left(\frac{a_\mathrm{E}}{r}\right)^2 \frac{1}{2}\left\{3\cos^2\theta - 1\right\} C_{20}. \tag{B.7}$$

Now, take the gradient of the gravity field potential (with $r_3 = r\cos\theta$)

$$\boldsymbol{\nabla} V(r,\lambda,\theta)_{C_{20}} = \boldsymbol{\nabla}\left[GMa_\mathrm{E}^2 C_{20}\left(\frac{1}{r}\right)^3 \left\{\frac{3}{2}\frac{r_3^2}{r^2} - \frac{1}{2}\right\}\right]. \tag{B.8}$$

With

$$\boldsymbol{\nabla}\left(\frac{1}{r^3}\right) = -3\mathbf{r}\frac{1}{r^5} \tag{B.9}$$

$$\boldsymbol{\nabla}\left(\frac{r_3^2}{r^5}\right) = \begin{pmatrix} \frac{-5r_3^2 r_1}{r^7} \\ \frac{-5r_3^2 r_2}{r^7} \\ \frac{2r_3 r^5 - 5r_3^3 r^3}{r^{10}} \end{pmatrix} = \frac{-5r_3^2}{r^7}\begin{pmatrix} r_1 \\ r_2 \\ r_3 \end{pmatrix} + \begin{pmatrix} 0 \\ 0 \\ \frac{2r_3}{r^5} \end{pmatrix} \tag{B.10}$$

it follows that

$$\begin{aligned} \ddot{\mathbf{r}}_{C_{20}} = \boldsymbol{\nabla} V(r,\lambda,\theta)_{C_{20}} &= GMa_\mathrm{E}^2 C_{20}\left\{\frac{3}{2}\frac{r_3^2}{r^2} - \frac{1}{2}\right\} \\ &= GMa_\mathrm{E}^2 C_{20}\left\{\frac{3}{2}\frac{-5r_3^2}{r^7}\begin{pmatrix} r_1 \\ r_2 \\ r_3 \end{pmatrix} + \frac{3}{2}\begin{pmatrix} 0 \\ 0 \\ \frac{2r_3}{r^5} \end{pmatrix} + \frac{3}{2}\frac{1}{r^5}\begin{pmatrix} r_1 \\ r_2 \\ r_3 \end{pmatrix}\right\} \\ &= GMa_\mathrm{E}^2 C_{20}\frac{3}{2}\frac{1}{r^5}\begin{pmatrix} r_1(1 - 5\frac{r_3^2}{r^2}) \\ r_2(1 - 5\frac{r_3^2}{r^2}) \\ r_3(3 - 5\frac{r_3^2}{r^2}) \end{pmatrix}. \end{aligned} \tag{B.11}$$

In the co-rotating orbital frame (use $r_3 = r\sin(i)\sin(u)$)

$$
\begin{aligned}
\begin{pmatrix} R' \\ S' \\ W' \end{pmatrix}_{C_{20}} =& \mathbf{R}\ddot{\mathbf{r}}_{C_{20}} \qquad \text{(B.12)}\\
=& GMa_{\mathrm{E}}^2 C_{20}\frac{3}{2}\frac{1}{r^5}(1-5\frac{r_3^2}{r^2})\mathbf{R}\mathbf{R}^{-1}r\begin{pmatrix}1\\0\\0\end{pmatrix} + GMa_{\mathrm{E}}^2 C_{20}\frac{3}{2}\frac{1}{r^5}2r_3\mathbf{R}\begin{pmatrix}0\\0\\1\end{pmatrix}\\
=& GMa_{\mathrm{E}}^2 C_{20}\frac{3}{2}\frac{1}{r^4}(1-5\frac{r_3^2}{r^2})\begin{pmatrix}1\\0\\0\end{pmatrix} + GMa_{\mathrm{E}}^2 C_{20}\frac{3}{2}\frac{1}{r^5}2r_3\begin{pmatrix}\sin(u)\sin(i)\\ \cos(u)\sin(i)\\ \cos(i)\end{pmatrix}\\
=& GMa_{\mathrm{E}}^2 C_{20}\frac{3}{2}\frac{1}{r^4}\begin{pmatrix}1-5\sin^2(i)\sin^2(u)+2\sin(u)\sin(i)\sin(u)\sin(i)\\ 2\sin(u)\sin(i)\cos(u)\sin(i)\\ 2\sin(u)\sin(i)\cos(i)\end{pmatrix}\\
=& GMa_{\mathrm{E}}^2 C_{20}\frac{3}{2}\frac{1}{r^4}\begin{pmatrix}1-3\sin^2(i)\sin^2(u)\\ 2\sin^2(i)\sin(u)\cos(u)\\ 2\sin(u)\sin(i)\cos(i)\end{pmatrix}\\
=& GMa_{\mathrm{E}}^2 C_{20}\frac{3}{2}\frac{1}{r^4}\begin{pmatrix}1-3\sin^2(i)\frac{1-\cos(2u)}{2}\\ \sin^2(i)\sin(2u)\\ \sin(u)\sin(2i)\end{pmatrix}\\
=& GMa_{\mathrm{E}}^2 C_{20}\frac{3}{2}\frac{1}{r^4}\begin{pmatrix}1-\frac{3}{2}\sin^2(i)+\frac{3}{2}\sin^2(i)\cos(2u)\\ \sin^2(i)\sin(2u)\\ \sin(2i)\sin(u)\end{pmatrix}
\end{aligned}
$$

B.2 Acceleration Due to C_{30}

The gravity field potential term containing C_{30} reads as

$$V(r,\lambda,\theta)_{C_{30}} = \frac{GM}{r}\left(\frac{a_{\mathrm{E}}}{r}\right)^3\frac{1}{2}\left\{5\cos^3\theta - 3\cos\theta\right\}C_{30} \qquad \text{(B.13)}$$

Now, take the gradient of the gravity field potential (with $r_3 = r\cos\theta$)

$$\boldsymbol{\nabla}V(r,\lambda,\theta)_{C_{30}} = \boldsymbol{\nabla}\left[GMa_{\mathrm{E}}^3 C_{30}\left(\frac{1}{r}\right)^4\left\{\frac{5}{2}\frac{r_3^3}{r^3} - \frac{3}{2}\frac{r_3}{r}\right\}\right]. \qquad \text{(B.14)}$$

With

$$\boldsymbol{\nabla}\left(\frac{r_3^3}{r^7}\right) = \begin{pmatrix}\frac{-7r_3^3 r_1}{r^9}\\ \frac{-7r_3^3 r_1}{r^9}\\ \frac{3r_3^2 r^7 - 7r_3^4 r^5}{r^{14}}\end{pmatrix} = \frac{-7r_3^3}{r^9}\begin{pmatrix}r_1\\r_2\\r_3\end{pmatrix} + \begin{pmatrix}0\\0\\\frac{3r_3^2}{r^7}\end{pmatrix} \qquad \text{(B.15)}$$

$$\boldsymbol{\nabla}\left(\frac{r_3}{r^5}\right) = \begin{pmatrix} \frac{-5r_3r_1}{r^7} \\ \frac{-5r_3r_2}{r^7} \\ \frac{r^5-5r_3^2r^3}{r^{10}} \end{pmatrix} = \frac{-5r_3}{r^7}\begin{pmatrix} r_1 \\ r_2 \\ r_3 \end{pmatrix} + \begin{pmatrix} 0 \\ 0 \\ \frac{1}{r^5} \end{pmatrix} \tag{B.16}$$

it follows that

$$\begin{aligned} \ddot{\mathbf{r}}_{C_{30}} = \boldsymbol{\nabla} V(r,\lambda,\theta)_{C_{30}} &= GMa_{\mathrm{E}}^3 C_{30}\left\{\frac{5}{2}\frac{-7r_3^3}{r^9}\begin{pmatrix} r_1 \\ r_2 \\ r_3 \end{pmatrix} + \frac{5}{2}\begin{pmatrix} 0 \\ 0 \\ \frac{3r_3^2}{r^7} \end{pmatrix} - \frac{3}{2}\frac{-5r_3}{r^7}\begin{pmatrix} r_1 \\ r_2 \\ r_3 \end{pmatrix} - \frac{3}{2}\begin{pmatrix} 0 \\ 0 \\ \frac{1}{r^5} \end{pmatrix}\right\} \\ &= GMa_{\mathrm{E}}^3 C_{30}\left\{\frac{5}{2}\frac{r_3}{r^7}\begin{pmatrix} r_1(3-7\frac{r_3^2}{r^2}) \\ r_2(3-7\frac{r_3^2}{r^2}) \\ r_3(6-7\frac{r_3^2}{r^2}) \end{pmatrix} - \frac{3}{2}\begin{pmatrix} 0 \\ 0 \\ \frac{1}{r^5} \end{pmatrix}\right\}. \end{aligned} \tag{B.17}$$

In the co-rotating orbital frame (use $r_3 = r\sin(i)\sin(u)$)

$$\begin{aligned} \begin{pmatrix} R' \\ S' \\ W' \end{pmatrix}_{C_{30}} &= \mathbf{R}\ddot{\mathbf{r}}_{C_{30}} \qquad\qquad (B.18) \\ &= GMa_{\mathrm{E}}^3 C_{30}\frac{5}{2}\frac{r_3}{r^7}(3-7\frac{r_3^2}{r^2})\mathbf{R}\mathbf{R}^{-1}r\begin{pmatrix} 1 \\ 0 \\ 0 \end{pmatrix} + GMa_{\mathrm{E}}^3 C_{30}\left(\frac{5}{2}\frac{3r_3^2}{r^7} - \frac{3}{2}\frac{1}{r^5}\right)\mathbf{R}\begin{pmatrix} 0 \\ 0 \\ 1 \end{pmatrix} \\ &= GMa_{\mathrm{E}}^3 C_{30}\frac{5}{2}\frac{r_3}{r^6}(3-7\frac{r_3^2}{r^2})\begin{pmatrix} 1 \\ 0 \\ 0 \end{pmatrix} + GMa_{\mathrm{E}}^3 C_{30}\left(\frac{5}{2}\frac{3r_3^2}{r^7} - \frac{3}{2}\frac{1}{r^5}\right)\begin{pmatrix} \sin(u)\sin(i) \\ \cos(u)\sin(i) \\ \cos(i) \end{pmatrix} \\ &= GMa_{\mathrm{E}}^3 C_{30}\frac{5}{2}\frac{1}{r^5}\cdot \\ &\quad \begin{pmatrix} 3\sin(i)\sin(u) - 7\sin^3(i)\sin^3(u) + 3\sin^2(i)\sin^2(u)\sin(u)\sin(i) - \frac{3}{5}\sin(u)\sin(i) \\ 3\sin^2(i)\sin^2(u)\cos(u)\sin(i) - \frac{3}{5}\cos(u)\sin(i) \\ 3\sin^2(i)\sin^2(u)\cos(i) - \frac{3}{5}\cos(i) \end{pmatrix} \\ &= GMa_{\mathrm{E}}^3 C_{30}\frac{5}{2}\frac{1}{r^5}\begin{pmatrix} \frac{12}{5}\sin(i)\sin(u) - 4\sin^3(i)\sin^3(u) \\ \frac{3}{2}\sin^3(i)\sin(u)\sin(2u) - \frac{3}{5}\sin(i)\cos(u) \\ \frac{3}{2}\sin^2(i)\cos(i)(1-\cos(2u)) - \frac{3}{5}\cos(i) \end{pmatrix} \\ &= GMa_{\mathrm{E}}^3 C_{30}\frac{5}{2}\frac{1}{r^5}\begin{pmatrix} \frac{12}{5}\sin(i)\sin(u) - 4\sin^3(i)\sin^3(u) \\ \frac{3}{4}\sin^3(i)\cos(u) - \frac{3}{4}\sin^3(i)\cos(2u) - \frac{3}{5}\sin(i)\cos(u) \\ \frac{3}{2}\sin^2(i)\cos(i)(1-\cos(2u)) - \frac{3}{5}\cos(i) \end{pmatrix}. \end{aligned}$$

Scientific Environment and Publications

The research within the framework of this thesis was carried out at the Astronomical Institute of the University of Bern (AIUB). It has been supported by the European Research Council under the grant agreement no. 817919 (project SPACE TIE). Calculations were performed on UBELIX (http://www.id.unibe.ch/hpc), the HPC cluster at the University of Bern.

The main results of this work have been presented at various international conferences and published in the following conference papers:

Contribution of LARES SLR Data to Co-estimated Earth Geopotential Coefficients (2023). Linda Geisser, Ulrich Meyer, Daniel Arnold and Adrian Jäggi. In: *International Association of Geodesy Symposia*. Springer, Berlin, Heidelberg.
https://doi.org/10.1007/1345_2022_185

Linda Geisser, Ulrich Meyer, Daniel Arnold and Adrian Jäggi, **Multi-satellite SLR analysis including LARES/LARES-2 SLR data**, S01-06. Presented at the 22nd International Workshop on Laser Ranging, Guadalajara, Spain, November 07-11, 2022.

Linda Geisser, Thomas Schildknecht, Ulrich Meyer, Daniel Arnold and Adrian Jäggi, **Homogeneous formation of SLR Normal Point data at AIUB**, S04-02. Presented at the 22nd International Workshop on Laser Ranging, Guadalajara, Spain, November 07-11, 2022.

Bibliography

Altamimi, Z., X. Collilieux, J. Legrand, B. Garayt, and C. Boucher (2007). "ITRF2005: A New Release of the International Terrestrial Reference Frame Based on Time Series of Station Positions and Earth Orientation Parameters". In: *Journal of Geophysical Research* 112.B9, B09401. ISSN: 0148-0227. DOI: 10.1029/2007JB004949.

Altamimi, Z. and X. Collilieux (2009). "IGS Contribution to the ITRF". In: *Journal of Geodesy* 83, pp. 375–383. ISSN: 0949-7714, 1432-1394. DOI: 10.1007/s00190-008-0294-x.

Altamimi, Z., X. Collilieux, and L. Métivier (2011). "ITRF2008: An Improved Solution of the International Terrestrial Reference Frame". In: *Journal of Geodesy* 85.8, pp. 457–473. ISSN: 0949-7714, 1432-1394. DOI: 10.1007/s00190-011-0444-4.

Altamimi, Z., P. Rebischung, L. Métivier, and X. Collilieux (2016). "ITRF2014: A New Release of the International Terrestrial Reference Frame Modeling Nonlinear Station Motions". In: *Journal of Geophysical Research: Solid Earth* 121.8, pp. 6109–6131. ISSN: 21699313. DOI: 10.1002/2016JB013098.

Altamimi, Z., P. Rebischung, X. Collilieux, L. Metivier, and K. Chanard (2018). "Roadmap toward ITRF2020". In: *AGU Fall Meeting Abstracts* 2018, G42A–08.

Angermann, D. and H. Müller (2009). "On the Strength of SLR Observations to Realize the Scale and Origin of the Terrestrial Reference System". In: *Observing our Changing Earth*. Ed. by Michael G. Sideris. Berlin, Heidelberg: Springer Berlin Heidelberg, pp. 21–29. ISBN: 978-3-540-85426-5.

Aoki, S., B. Guinot, G. H. Kaplan, H. Kinoshita, D. D. McCarthy, and P. K. Seidelmann (1981). "The New Definition of Universal Time". In: *Astronomy & Astrophysics* 105, pp. 359–361.

Appleby, G. (1993). "Satellite Signatures in SLR Observations". In: 8th International Workshop on Laser Ranging Instrumentation. Annapolis, MD, USA.

Bähr, H., Z. Altamimi, and B. Heck (2007). *Variance Component Estimation for Combination of Terrestrial Reference Frames*. DOI: 10.5445/KSP/1000007363. preprint.

Beutler, G., E. Brockmann, W. Gurtner, U. Hugentobler, L. Mervart, M. Rothacher, and A. Verdun (1994). "Extended Orbit Modeling Techniques at the CODE Processing Center of the International GPS Service for Geodynamics (IGS): Theory and Initial Results". In: *manuscripta geodaetica*, pp. 367–386. ISSN: 0340-8825.

Beutler, G., E. Brockmann, U. Hugentobler, L. Mervart, M. Rothacher, and R. Weber (1996). "Combining Consecutive Short Arcs into Long Arcs for Precise and Efficient GPS Orbit Determination". In: *Journal of Geodesy* 70, pp. 287–299. DOI: 10.1007/BF00867349.

Beutler, G., L. Mervart, and A. Verdun (2005a). *Methods of Celestial Mechanics Volume I: Physical, Mathematical, and Numerical Principles*. Astronomy and Astrophysics Library. Berlin ; New York: Springer. ISBN: 978-3-540-40749-2 978-3-540-40750-8.

Beutler, G., L. Mervart, and A. Verdun (2005b). *Methods of Celestial Mechanics Volume II: Application to Planetary System, Geodynamics and Satellite Geodesy*. Astronomy and Astrophysics Library. Berlin ; New York: Springer. ISBN: 978-3-540-40749-2 978-3-540-40750-8.

Bizouard, C., S. Lambert, C. Gattano, O. Becker, and J.-Y. Richard (2019). "The IERS EOP 14C04 Solution for Earth Orientation Parameters Consistent with ITRF 2014". In: *Journal of Geodesy* 93.5, pp. 621–633. ISSN: 0949-7714, 1432-1394. DOI: 10.1007/s00190-018-1186-3.

Bloßfeld, M., M. Gerstl, U. Hugentobler, D. Angermann, and H. Müller (2014). "Systematic Effects in LOD from SLR Observations". In: *Advances in Space Research* 54.6, pp. 1049–1063. ISSN: 02731177. DOI: 10.1016/j.asr.2014.06.009.

Bloßfeld, M., S. Rudenko, A. Kehm, N. Panafidina, H. Müller, D. Angermann, U. Hugentobler, and M. Seitz (2018). "Consistent Estimation of Geodetic Parameters from SLR Satellite Constellation Measurements". In: *Journal of Geodesy* 92.9, pp. 1003–1021. ISSN: 0949-7714, 1432-1394. DOI: 10.1007/s00190-018-1166-7.

Böckmann, S., T. Artz, and A. Nothnagel (2010). "VLBI Terrestrial Reference Frame Contributions to ITRF2008". In: *Journal of Geodesy* 84.3, pp. 201–219. ISSN: 0949-7714, 1432-1394. DOI: 10.1007/s00190-009-0357-7.

Brockmann, E. (1997). *Combination of Solutions for Geodetic and Geodynamic Applications of the Global Positioning System (GPS)*. (PhD Thesis) Geodätisch-geophysikalische Arbeiten in Der Schweiz 55. Eidg. Technische Hochschule Zürich, Schweiz: Schweizerische Geodätische Kommission.

Carabajal, C. C. (2023). *Request to stations related to Full Rate (FR) data*. E-mail.

Chandler, S. C. (1891). "On the Variation of Latitude". In: *The Astronomical Journal* 248.

Charlot, P., C. S. Jacobs, D. Gordon, S. Lambert, A. de Witt, J. Böhm, A. L. Fey, R. Heinkelmann, E. Skurikhina, O. Titov, E. F. Arias, S. Bolotin, G. Bourda, C. Ma, Z. Malkin, A. Nothnagel, D. Mayer, D. S. MacMillan, T. Nilsson, and R. Gaume (2020). "The Third Realization of the International Celestial Reference Frame by Very Long Baseline Interferometry". In: *Astronomy & Astrophysics* 644, A159. ISSN: 0004-6361, 1432-0746. DOI: 10.1051/0004-6361/202038368.

Cheng, M., J. C. Ries, and B. D. Tapley (2011). "Variations of the Earth's Figure Axis from Satellite Laser Ranging and GRACE". In: *Journal of Geophysical Research* 116, B01409. ISSN: 0148-0227. DOI: 10.1029/2010JB000850.

Cheng, M. and J. Ries (2017). "The Unexpected Signal in GRACE Estimates of C20". In: *Journal of Geodesy* 91.8, pp. 897–914. ISSN: 0949-7714, 1432-1394. DOI: 10.1007/s00190-016-0995-5.

Chin, G., S. Brylow, M. Foote, J. Garvin, J. Kasper, J. Keller, M. Litvak, I. Mitrofanov, D. Paige, K. Raney, M. Robinson, A. Sanin, D. Smith, H. Spence, P. Spudis, S. A. Stern, and M. Zuber (2007). "Lunar Reconnaissance Orbiter Overview: The Instrument Suite and Mission". In: *Space Science Reviews* 129.4, pp. 391–419. ISSN: 0038-6308, 1572-9672. DOI: 10.1007/s11214-007-9153-y.

Christodoulidis, D. C., D. E. Smith, R. Kolenkiewicz, S. M. Klosko, M. H. Torrence, and P. J. Dunn (1985). "Observing Tectonic Plate Motions and Deformations from Satel-

lite Laser Ranging". In: *Journal of Geophysical Research* 90.B11, p. 9249. ISSN: 0148-0227. DOI: 10.1029/JB090iB11p09249.

Ciufolini, I., D. Lucchesi, F. Vespe, and A. Mandiello (1996). "Measurement of Dragging of Inertial Frames and Gravitomagnetic Field Using Laser-Ranged Satellites". In: *Il Nuovo Cimento A* 109.5, pp. 575–590. ISSN: 0369-3546, 1826-9869. DOI: 10.1007/BF02731140.

Ciufolini, I., E. C. Pavlis, F. Chieppa, E. Fernandes-Vieira, and J. Pérez-Mercader (1998). "Test of General Relativity and Measurement of the Lense- Thirring Effect with Two Earth Satellites". In: *Science* 279.5359, pp. 2100–2103. DOI: doi:10.1126/science.279.5359.2100.

Ciufolini, I. and E. C. Pavlis (2004). "A Confirmation of the General Relativistic Prediction of the Lense–Thirring Effect". In: *Nature* 431, pp. 958–960. DOI: 10.1038/nature03007.

Ciufolini, I., A. Paolozzi, E. Pavlis, R. Koenig, J. Ries, R. Matzner, R. Neubert, D. Rubincam, D. Arnold, G. Sindoni, C. Paris, M. Ramiconi, D. Spano, C. Vendittozzi, and H. Neumayer (2011a). "LARES Laser Relativity Satellite". In: Proceedings of 17th International Workshop on Laser Ranging. Bad Koetzting, Germany.

Ciufolini, I., A. Paolozzi, E. C. Pavlis, J. Ries, R. Koenig, R. Matzner, G. Sindoni, and H. Neumayer (2011b). "Testing Gravitational Physics with Satellite Laser Ranging". In: *The European Physical Journal Plus* 126.8, p. 72. ISSN: 2190-5444. DOI: 10.1140/epjp/i2011-11072-2.

Ciufolini, I., A. Paolozzi, E. C. Pavlis, R. Koenig, J. Ries, V. Gurzadyan, R. Matzner, R. Penrose, G. Sindoni, C. Paris, H. Khachatryan, and S. Mirzoyan (2016). "A Test of General Relativity Using the LARES and LAGEOS Satellites and a GRACE Earth Gravity Model: Measurement of Earth's Dragging of Inertial Frames". In: *The European Physical Journal C* 76.3, p. 120. ISSN: 1434-6044, 1434-6052. DOI: 10.1140/epjc/s10052-016-3961-8.

Combrinck, L. (2010). "Satellite Laser Ranging". In: *Sciences of Geodesy - I*. Ed. by G. Xu. Springer Berlin Heidelberg, pp. 301–338. ISBN: 978-3-642-11740-4 978-3-642-11741-1. DOI: 10.1007/978-3-642-11741-1_9.

Combrinck, L. (2013). "General Relativity and Space Geodesy". In: *Sciences of Geodesy - II*. Ed. by G. Xu. Springer Berlin Heidelberg, pp. 53–96. ISBN: 978-3-642-28000-9. DOI: 10.1007/978-3-642-28000-9_2.

Coulot, D., A. Pollet, X. Collilieux, and Ph. Berio (2010). "Global Optimization of Core Station Networks for Space Geodesy: Application to the Referencing of the SLR EOP with Respect to ITRF". In: *Journal of Geodesy* 84.1, pp. 31–50. ISSN: 0949-7714, 1432-1394. DOI: 10.1007/s00190-009-0342-1.

Dach, R., E. Brockmann, S. Schaer, G. Beutler, M. Meindl, L. Prange, H. Bock, A. Jäggi, and L. Ostini (2009). "GNSS Processing at CODE: Status Report". In: *Journal of Geodesy* 83.3, pp. 353–365. ISSN: 1432-1394. DOI: 10.1007/s00190-008-0281-2.

Dach, R., S. Lutz, P. Walser, and P. Fridez (2015). *Bernese GNSS Software Version 5.2*. DOI: 10.7892/BORIS.72297. URL: https://boris.unibe.ch/72297/ (visited on 09/21/2022). preprint.

Degnan, J. J. (1993). "Millimeter Accuracy Satellite Laser Ranging: A Review". In: *Geodynamics Series*. Ed. by David E. Smith and Donald L. Turcotte. Vol. 25. Washing-

ton, D. C.: American Geophysical Union, pp. 133–162. ISBN: 978-0-87590-526-6. DOI: 10.1029/GD025p0133.

Degnan, John (1985). "Satellite Laser Ranging: Current Status and Future Prospects". In: *IEEE Transactions on Geoscience and Remote Sensing* GE-23.4, pp. 398–413. ISSN: 0196-2892. DOI: 10.1109/TGRS.1985.289430.

Desai, S. D. and A. E. Sibois (2016). "Evaluating Predicted Diurnal and Semidiurnal Tidal Variations in Polar Motion with GPS-based Observations". In: *Journal of Geophysical Research: Solid Earth* 121.7, pp. 5237–5256. ISSN: 2169-9356. DOI: 10.1002/2016JB013125.

De Sitter, W. (1916). "On Einstein's Theory of Gravitation and Its Astronomical Consequences. Second Paper." In: *Monthly Notices of the Royal Astronomical Society* 77.2, pp. 155–184. ISSN: 0035-8711. DOI: 10.1093/mnras/77.2.155. eprint: https://academic.oup.com/mnras/article-pdf/77/2/155/3019882/mnras77-0155.pdf.

Dick, G., G. Gendt, H. Montag, Th. Nischan, and W. Sommerfeld (1993). "Results of ETALON Data Analysis". In: *Geodesy and Physics of the Earth*. Ed. by H. Montag and Ch. Reigber. Red. by W. Torge. Vol. 112. Springer Berlin Heidelberg, pp. 315–318. ISBN: 978-3-540-56572-7 978-3-642-78149-0. DOI: 10.1007/978-3-642-78149-0_73.

Dobslaw, H., I. Bergmann-Wolf, R. Dill, L. Poropat, M. Thomas, C. Dahle, S. Esselborn, R. König, and F. Flechtner (2017). "A New High-Resolution Model of Non-Tidal Atmosphere and Ocean Mass Variability for de-Aliasing of Satellite Gravity Observations: AOD1B RL06". In: *Geophysical Journal International* 211.1, pp. 263–269. ISSN: 0956-540X, 1365-246X. DOI: 10.1093/gji/ggx302.

Einstein, A. (1915). "Die Feldgleichungen Der Gravitation". In: *Sitzungsberichte der Königlich Preussischen Akademie der Wissenschaften*, pp. 844–847.

Fitzmaurice, M. W., B. Abshire, and H. E. Rowe (1977). "Prelaunch Testing of the Laser GeodynamicSatellite (LAGEOS)". In: *NASA Technical Paper 1062*.

Förstner, W. (1979). "Ein Verfahren Zur Schätzung von Varianz- Und Kovarianzkomponenten". In: *Allgemeine Vermessungs-Nachrichten* 11-12, pp. 446–453.

Hampf, D., E. Schafer, F. Sproll, T. Otsubo, P. Wagner, and W. Riede (2019). "Satellite Laser Ranging at 100 kHz Pulse Repetition Rate". In: *CEAS Space Journal* 11.4, pp. 363–370. ISSN: 1868-2502, 1868-2510. DOI: 10.1007/s12567-019-00247-x.

Helmert, F. R. (1893). "Die Euopäische Längengradmessung in 52 Grad Breite von Greenwich Bis Warschau". In: *Des Königl. Preussischen Geodätischen Institutes und Centralbureaus der Internatonalen Erdmessung*.

Helmert, F. R. (1907). *Die Ausgleichungsrechnung Nach Der Methode Der Kleinsten Quadrate: Mit Anwendungen Auf Die Geodäsie Und Die Theorie Der Messinstrumente*. 2nd ed. Leibzig.

Iorio, L. (2010). "On the Impact of the Atmospheric Drag on the LARES Mission". In: *Acta Physica Polonica B* 41. DOI: 10.48550/arXiv.0809.3564.

Jäggi, A., K. Sośnica, D. Thaller, and G. Beutler (2012). "Validation and Estimation of Low-Degree Gravity Field Coefficients Using LAGEOS". In: *Proceedings of the 17th International Workshop on Laser Ranging* 48, pp. 302–304. ISSN: 1436-3445.

Jäggi, A., U. Meyer, M. Lasser, B. Jenny, T. Lopez, F. Flechtner, Ch. Dahle, Ch. Förste, T. Mayer-Gürr, A. Kvas, J.-M. Lemoine, St. Bourgogne, M. Weigelt, and A. Groh (2020). "International Combination Service for Time-Variable Gravity Fields (COST-

G): Start of Operational Phase and Future Perspectives". In: *Beyond 100: The Next Century in Geodesy*. Ed. by J. T. Freymueller and L. Sánchez. Vol. 152. Cham: Springer International Publishing, pp. 57–65. ISBN: 978-3-031-09856-7 978-3-031-09857-4. DOI: 10.1007/1345_2020_109.

Kirchner, G. and F. Koidl (1993). "Work at Graz on Satellite Signatures". In: Proceedings of 8th International Workshop on Laser Ranging Instrumentation. Annapolis, MD, USA.

Kirchner, G. and F. Koidl (1999). "Compensation of SPAD Time-Walk Effects". In: *Journal of Optics A: Pure and Applied Optics* 1.2, pp. 163–167. ISSN: 1464-4258, 1741-3567. DOI: 10.1088/1464-4258/1/2/008.

Kirchner, G. and F. Koidl (2004). "Graz KHz SLR System: Design, Experiences and Results". In: Proceedings of 14th International Workshop on Laser Ranging. San Fernando, Spain.

Koch, K.-R. (2007). *Introduction to Bayesian Statistics*. 2nd, updated and en. ed. Berlin ; New York: Springer. ISBN: 978-3-540-72723-1.

König, R., P. Schreiner, and Ch. Dahle (2019). *Monthly Estimates of C(2,0) Generated by GFZ from SLR Satellites Based on GFZ GRACE/GRACE-FO RL06 Background Models*. application/octet-stream. Version 1.0. GFZ Data Services. DOI: 10.5880/GFZ.GRAVIS_06_C20_SLR.

Lambeck, K. (1971). "Determination of the Earth's Pole of Rotation from Laser Range Observations to Satellites". In: *Bulletin géodésique* 101.1, pp. 263–281. ISSN: 0007-4632. DOI: 10.1007/BF02521878.

Landerer, F. W. et al. (2020). "Extending the Global Mass Change Data Record: GRACE Follow-On Instrument and Science Data Performance". In: *Geophysical Research Letters* 47.12. ISSN: 0094-8276, 1944-8007. DOI: 10.1029/2020GL088306.

Lasser, M., U. Meyer, A. Jäggi, T. Mayer-Gürr, A. Kvas, K. H. Neumayer, Ch. Dahle, F. Flechtner, J.-M. Lemoine, I. Koch, M. Weigelt, and J. Flury (2020). "Benchmark Data for Verifying Background Model Implementations in Orbit and Gravity Field Determination Software". In: *Advances in Geosciences* 55, pp. 1–11. ISSN: 1680-7359. DOI: 10.5194/adgeo-55-1-2020.

Lasser, M. (2022). "Noise Modelling for GRACE Follow-On Observables in the Celestial Mechanics Approach". PhD thesis. Switzerland: Universität Bern. DOI: 10.48549/4127.

Lauber, P. (2023). *Calibration Measurement for SLR at Zimmerwald*. E-mail.

Lense, J. and H. Thirring (1918). "On the Influence of the Proper Rotation of a Central Body on the Motion of the Planets and the Moon, According to Einstein's Theory of Gravitation". In: *Physikalische Zeitschrift* 19, pp. 156–163.

Loomis, B. D., K. E. Rachlin, D. N. Wiese, F. W. Landerer, and S. B. Luthcke (2020). "Replacing GRACE/GRACE-FO With Satellite Laser Ranging: Impacts on Antarctic Ice Sheet Mass Change". In: *Geophysical Research Letters* 47.3. ISSN: 0094-8276, 1944-8007. DOI: 10.1029/2019GL085488.

Lucchesi, D., L. Anselmo, M. Bassan, M. Lucente, C. Magnafico, C. Pardini, R. Peron, G. Pucacco, and M. Visco (2020). "Thermal Thrust Accelerations on LAGEOS Satellites". EGU General Assembly. DOI: 10.5194/egusphere-egu2020-18560.

Lucchesi, D. M. (2003a). "LAGEOS II Perigee Shift and Schwarzschild Gravitoelectric Field". In: *Physics Letters A* 318.3, pp. 234–240. ISSN: 03759601. DOI: 10.1016/j.physleta.2003.07.015.

Lucchesi, D. M. (2003b). "The Asymmetric Reflectivity Effect on the LAGEOS Satellites and the Germanium Retroreflectors". In: *Geophysical Research Letters* 30.18. ISSN: 00948276. DOI: 10.1029/2003GL017741.

Lucchesi, D. M., E. C. Pavlis, I. Ciufolini, and R. Peron (2003). "The Yarkovsky–Schach Thermal Effect on LAGEOS Satellites and Its Modelling". In: EGS–AGU–EUG Joint Assembly. Nice, France.

Lutz, S., G. Beutler, S. Schaer, R. Dach, and A. Jäggi (2016). "CODE's New Ultra-Rapid Orbit and ERP Products for the IGS". In: *GPS Solutions* 20.2, pp. 239–250. ISSN: 1521-1886. DOI: 10.1007/s10291-014-0432-2.

Lyard, F. H., D. J. Allain, M. Cancet, L. Carrère, and N. Picot (2021). "FES2014 Global Ocean Tide Atlas: Design and Performance". In: *Ocean Science* 17.3, pp. 615–649. ISSN: 1812-0792. DOI: 10.5194/os-17-615-2021.

Mao, D., J. F. McGarry, E. Mazarico, G. A. Neumann, X. Sun, M. H. Torrence, Th. W. Zagwodzki, D. D. Rowlands, E. D. Hoffman, J. E. Horvath, James E. Golder, M. K. Barker, D. E. Smith, and M. T. Zuber (2017). "The Laser Ranging Experiment of the Lunar Reconnaissance Orbiter: Five Years of Operations and Data Analysis". In: *Icarus* 283, pp. 55–69. ISSN: 00191035. DOI: 10.1016/j.icarus.2016.07.003.

Mao, X., D. Arnold, V. Girardin, A. Villiger, and A. Jäggi (2021). "Dynamic GPS-based LEO Orbit Determination with 1 Cm Precision Using the Bernese GNSS Software". In: *Advances in Space Research* 67.2, pp. 788–805. ISSN: 02731177. DOI: 10.1016/j.asr.2020.10.012.

Marini, J. W. and C. W. Murray (1973). "Correction of Laser Range Tracking Data for Atmospheric Refraction at Elevations above 10 Degrees". In: *NASA-TM-X- 70555* (Goddard Space Flight Center, Greenbelt, MD).

Mathews, P. M., T. A. Herring, and B. A. Buffett (2002). "Modeling of Nutation and Precession: New Nutation Series for Nonrigid Earth and Insights into the Earth's Interior: New Nutation Series and the Earth's Interior". In: *Journal of Geophysical Research: Solid Earth* 107.B4, ETG 3-1-ETG 3–26. ISSN: 01480227. DOI: 10.1029/2001JB000390.

Mendes, V. B. and E.C. Pavlis (2004). "High-Accuracy Zenith Delay Prediction at Optical Wavelengths". In: *Geophysical Research Letters*. L14602 31. DOI: 10.1029/2004GL020308.

Meyer, U., M. Lasser, A. Jaeggi, Ch. Dahle, F. Flechtner, A. Kvas, S. Behzadpour, T. Mayer-Gürr, J.-M. Lemoine, I. Koch, J. Flury, and St. Bourgogne (2020). *International Combination Service for Time-variable Gravity Fields (COST-G) Monthly GRACE-FO Series*. Version 01. GFZ Data Services. DOI: 10.5880/ICGEM.COST-G.002.

Minott, O. (1974). "Design of Retrodirector Arrays for Laser Ranging of Satellites". In: *NASA Technical Reports Server (NTRS) 19740018193*, p. 21.

Minott, P. O., T. W. Zagwodzki, T. Varghese, and M. Seldon (1993). "Prelaunch Optical Characterization of the Laser Geodynamic Satellite (LAGEOS 2)". In: *NASA Technical Paper 3400* N94-15193.

Montenbruck, O, E Gill, and Fh Lutze (2002). "*Satellite Orbits: Models, Methods, and Applications*". In: *Applied Mechanics Reviews* 55.2, B27–B28. ISSN: 0003-6900, 2379-0407. DOI: 10.1115/1.1451162.

Nelder, J. A. and R. Mead (1965). "A Simplex Method for Function Minimization". In: *The Computer Journal* 7.4, pp. 308–313. ISSN: 0010-4620, 1460-2067. DOI: 10.1093/comjnl/7.4.308.

Noll, C. E. (2010). "The Crustal Dynamics Data Information System: A Resource to Support Scientific Analysis Using Space Geodesy". In: *Advances in Space Research* 45.12, pp. 1421–1440. ISSN: 02731177. DOI: 10.1016/j.asr.2010.01.018.

Noll, C. E. and M. Pearlman (2018). *Request for Full-Rate Data Transmission*. E-mail.

O'Neill, R. (1971). "Algorithm AS 47: Function Minimization Using a Simplex Procedure". In: *Journal of the Royal Statistical Society. Series C (Applied Statistics)* 20.3, pp. 338–345. ISSN: 0035-9254. DOI: 10.2307/2346772. JSTOR: 2346772.

Otsubo, T., J. Amagai, and H. Kunimori (1999). "The Center-of-Mass Correction of the Geodetic Satellite AJISAI for Single-Photon Laser Ranging". In: *IEEE Transactions on Geoscience and Remote Sensing* 37.4, pp. 2011–2018. ISSN: 01962892. DOI: 10.1109/36.774712.

Otsubo, T. and G. M. Appleby (2003). "System-Dependent Center-of-Mass Correction for Spherical Geodetic Satellites". In: *Journal of Geophysical Research: Solid Earth* 108.B4. ISSN: 01480227. DOI: 10.1029/2002JB002209.

Otsubo, T., R. A. Sherwood, Graham M. Appleby, and R. Neubert (2015). "Center-of-Mass Corrections for Sub-Cm-Precision Laser-Ranging Targets: Starlette, Stella and LARES". In: *Journal of Geodesy* 89.4, pp. 303–312. ISSN: 0949-7714, 1432-1394. DOI: 10.1007/s00190-014-0776-y.

Otsubo, T., K. Matsuo, Y. Aoyama, K. Yamamoto, Th. Hobiger, T. Kubo-oka, and M. Sekido (2016). "Effective Expansion of Satellite Laser Ranging Network to Improve Global Geodetic Parameters". In: *Earth, Planets and Space* 68.1, p. 65. ISSN: 1880-5981. DOI: 10.1186/s40623-016-0447-8.

Paolozzi, A., I. Ciufolini, C. Paris, and G. Sindoni (2015). "LARES: A New Satellite Specifically Designed for Testing General Relativity". In: *International Journal of Aerospace Engineering* 2015, pp. 1–9. ISSN: 1687-5966, 1687-5974. DOI: 10.1155/2015/341384.

Pavlis, E. C. (1999). "Fortnightly Resolution Geocenter Series: A Combined Analysis of Lageos 1 and 2 SLR Data". In: *IERS Technical Note* 25, pp. 75–84.

Pavlis, E. C. (2021). *Updated/Extended Gravity Coefficients Series for OPERATIONAL Series ONLY*. E-mail.

Pearlman, M. R., J. J. Degnan, and J.M. Bosworth (2002). "The International Laser Ranging Service". In: *Advances in Space Research* 30.2, pp. 135–143. DOI: 10.1016/S0273-1177(02)00277-6.

Pearlman, M. R., C. E. Noll, E. C. Pavlis, F. G. Lemoine, L. Combrink, J. J. Degnan, G. Kirchner, and U. Schreiber (2019). "The ILRS: Approaching 20 Years and Planning for the Future". In: *Journal of Geodesy* 93.11, pp. 2161–2180. ISSN: 0949-7714, 1432-1394. DOI: 10.1007/s00190-019-01241-1.

Peter, H., U. Meyer, M. Lasser, and A. Jäggi (2022). "COST-G Gravity Field Models for Precise Orbit Determination of Low Earth Orbiting Satellites". In: *Advances in Space Research* 69.12, pp. 4155–4168. ISSN: 02731177. DOI: 10.1016/j.asr.2022.04.005.

Petit, G. and B. Luzum (2010). "IERS Conventions (2010)". In: *IERS Technical Note* 36, p. 179.

Picone, J. M., A. E. Hedin, D. P. Drob, and A. C. Aikin (2002). "NRLMSISE-00 Empirical Model of the Atmosphere: Statistical Comparisons and Scientific Issues: TECH-

NIQUES". In: *Journal of Geophysical Research: Space Physics* 107.A12, SIA 15-1-SIA 15–16. ISSN: 01480227. DOI: 10.1029/2002JA009430.

Plotkin, H. H., Th. S. Johnson, P. L. Spadin, and J. E. Moye (1965). "Reflection of Ruby Laser Radiation From Explorer XXII". In: *Proceedings IEEE* 53, pp. 301–302.

Ray, R. D. and R. M. Ponte (2003). "Barometric Tides from ECMWF Operational Analyses". In: *Annales Geophysicae* 21.8, pp. 1897–1910. ISSN: 1432-0576. DOI: 10.5194/angeo-21-1897-2003.

Ries, J., S. Bettadpur, R. Eanes, Z. Kang, U. Ko, C. McCullough, P. Nagel, N. Pie, S. Poole, T. Richter, H. Save, and B. Tapley (2016). *The Development and Evaluation of the Global Gravity Model GGM05*. preprint.

Rodríguez, J., G. Appleby, and T. Otsubo (2019). "Upgraded Modelling for the Determination of Centre of Mass Corrections of Geodetic SLR Satellites: Impact on Key Parameters of the Terrestrial Reference Frame". In: *Journal of Geodesy* 93.12, pp. 2553–2568. ISSN: 0949-7714, 1432-1394. DOI: 10.1007/s00190-019-01315-0.

Rothacher, M., G. Beutler, Thomas A. Herring, and R. Weber (1999). "Estimation of Nutation Using the Global Positioning System". In: *Journal of Geophysical Research: Solid Earth* 104.B3, pp. 4835–4859. ISSN: 01480227. DOI: 10.1029/1998JB900078.

Rothacher, M. (2003). "Towards a Rigorous Combination of Space Geodetic Techniques". In: *Proceedings of the IERS Workshop on Combination Research and Global Geophysical Fluids*. Ed. by B. Richter, W. Schwegmann, and W. R. Dick. Bavarian Academy of Sciences, Munich, Germany: Verlag des Bundesamts für Kartographie und Geodäsie, pp. 7–18.

Rubincam, D. P. (1987). "LAGEOS Orbit Decay Due to Infrared Radiation from Earth". In: *Journal of Geophysical Research* 92.B2, p. 1287. ISSN: 0148-0227. DOI: 10.1029/JB092iB02p01287.

Rubincam, D. P. (1988). "Yarkovsky Thermal Drag on LAGEOS". In: *Journal of Geophysical Research: Solid Earth* 93.B11, pp. 13805–13810. ISSN: 01480227. DOI: 10.1029/JB093iB11p13805.

Rummel, R. (2000). "Global Integrated Geodetic and Geodynamic Observing System (GIGGOS)". In: *Towards an Integrated Global Geodetic Observing System (IGGOS)*. Ed. by R. Rummel, H. Drewes, W. Bosch, and H. Hornik. Berlin, Heidelberg: Springer Berlin Heidelberg, pp. 253–260. ISBN: 978-3-642-59745-9.

Sasaki, M. and H. Hashimoto (1987). "Launch and Observation Program of the Experimental Geodetic Satellite of Japan". In: *IEEE Transactions on Geoscience and Remote Sensing* GE-25.5, pp. 526–533. ISSN: 0196-2892. DOI: 10.1109/TGRS.1987.289830.

Schildknecht, T., A. Jäggi, M. Ploner, and E. Brockmann (2015). "The Swiss Optical Ground Station and Geodynamics Observatory Zimmerwald". In: *Swiss National Report on the GEODETIC ACTIVITIES in the Years 2011 to 2015*. XXVI General Assembly of the International Union of Geodesy and Geophysics. Prague, Czech Republic: Swiss Geodetic Commission, ETH Zurich, pp. 25–26.

Schwarzschild, K. (1916). "Über Das Gravitationsfeld Eines Massenpunktes Nach Der EINSTEINschen Theorie". In: *Sitzungsberichte der Königlich Preussischen Akademie der Wissenschaften*, pp. 189–196.

Seeber, G. (2003). *Satellite Geodesy*. 2nd completely rev. and extended ed. Berlin ; New York: Walter de Gruyter. 589 pp. ISBN: 978-3-11-017549-3.

Seitz, M., D. Angermann, M. Bloßfeld, H. Drewes, and M. Gerstl (2012). "The 2008 DGFI Realization of the ITRS: DTRF2008". In: *Journal of Geodesy* 86.12, pp. 1097–1123. ISSN: 0949-7714, 1432-1394. DOI: 10.1007/s00190-012-0567-2.

Shapiro, I. I. (1964). "Fourth Test of General Relativity". In: *Physical Review Letters* 13.26, pp. 789–791. ISSN: 0031-9007. DOI: 10.1103/PhysRevLett.13.789.

Smith, D. E., D. C. Christodoulidis, R. Kolenkiewicz, P. J. Dunn, S. M. Klosko, M. H. Torrence, S. Fricke, and S. Blackwell (1985). "A Global Geodetic Reference Frame from LAGEOS Ranging (SL5.1AP)". In: *Journal of Geophysical Research* 90.B11, p. 9221. ISSN: 0148-0227. DOI: 10.1029/JB090iB11p09221.

Smith, D. E., R. Kolenkiewicz, P. J. Dunn, J. W. Robbins, M. H. Torrence, S. M. Klosko, R. G. Williamson, E. C. Pavlis, N. B. Douglas, and S. K. Fricke (1990). "Tectonic Motion and Deformation from Satellite Laser Ranging to LAGEOS". In: *Journal of Geophysical Research* 95.B13, p. 22013. ISSN: 0148-0227. DOI: 10.1029/JB095iB13p22013.

Sneeuw, N. (2000). "A Semi-Analytical Approach to Gravity Field Analysis from Satellite Observations". Technical University of Munich, Germany.

Sośnica, K., A. Jäggi, D. Thaller, G. Beutler, and R. Dach (2014). "Contribution of Starlette, Stella, and AJISAI to the SLR-derived Global Reference Frame". In: *Journal of Geodesy* 88.8, pp. 789–804. ISSN: 0949-7714, 1432-1394. DOI: 10.1007/s00190-014-0722-z.

Sośnica, K. J. (2015). *Determination of Precise Satellite Orbits and Geodetic Parameters Using Satellite Laser Ranging*. (PhD Thesis) Geodätisch-geophysikalische Arbeiten in Der Schweiz 93. Eidg. Technische Hochschule Zürich, Schweiz: Schweizerische Geodätische Kommission. 236 pp. ISBN: 978-3-908440-38-3.

Standish, E. M. (1998). "JPL Planetary and Lunar Ephemerides, DE405/LE405". In: *JPL IOM 312.F-98-048*.

Tapley, B. D., F. Flechtner, S. V. Bettadpur, and M. M. Watkins (2013). "The Status and Future Prospect for GRACE After the First Decade". In: *AGU Fall Meeting Abstracts* 2013, G32A–01.

Thaller, D. (2008). "Inter-Technique Combination Based on Homogeneous Normal Equation Systems Including Station Coordinates, Earth Orientation and Troposphere Parameters". PhD thesis. Germany: Technical University of Munich.

Thaller, D., M. Mareyen, R. Dach, G. Beutler, W. Gurtner, B. Richter, and J Ihde (2008). "Preparing the Bernese GPS Software for the Analysis of SLR Observations to Geodetic Satellites". In: *Proceedings of the 16th International Workshop on Laser Ranging*.

Torge, W. and J. Müller (2012). *Geodesy*. 4th ed. De Gruyter Textbook. Berlin ; Boston: De Gruyter. 433 pp. ISBN: 978-3-11-020718-7 978-3-11-025000-8.

Welsch, W. (1978). "A Posteriori Varianzschätzung Nach Helmert". In: *AVN* (85(2)), pp. 55–63.

Wielicki, Bruce A., B. R. Barkstrom, E. F. Harrison, R. B. Lee, L. G. Smith, and J. E. Cooper (1996). "Clouds and the Earth's Radiant Energy System (CERES): An Earth Observing System Experiment". In: *Bulletin of the American Meteorological Society* 77.5, pp. 853–868. ISSN: 0003-0007, 1520-0477. DOI: 10.1175/1520-0477(1996)077<0853:CATERE>2.0.CO;2.

Wilkinson, M., U. Schreiber, I. Procházka, C. Moore, J. Degnan, G. Kirchner, Zhang Zhongping, Peter Dunn, V. Shargorodskiy, M. Sadovnikov, C. Courde, and H. Kunimori (2019). "The next Generation of Satellite Laser Ranging Systems". In: *Journal*

of Geodesy 93.11, pp. 2227–2247. ISSN: 0949-7714, 1432-1394. DOI: 10.1007/s00190-018-1196-1.

Williams, D. R. (2023). *NASA - NSSDCA - Spacecraft - Details*. URL: https://nssdc.gsfc.nasa.gov/nmc/spacecraft/display.action?id=EXS-66A (visited on 02/17/2023).

Williamson, R. G. and J. G. Marsh (1985). "Starlette Geodynamics: The Earth's Tidal Response". In: *Journal of Geophysical Research* 90.B11. ISSN: 0148-0227. DOI: 10.1029/JB090iB11p09346.

Zajdel, R., K. Sośnica, M. Drożdżewski, G. Bury, and D. Strugarek (2019). "Impact of Network Constraining on the Terrestrial Reference Frame Realization Based on SLR Observations to LAGEOS". In: *Journal of Geodesy* 93.11, pp. 2293–2313. ISSN: 0949-7714, 1432-1394. DOI: 10.1007/s00190-019-01307-0.

Zuber, M. T., D. E. Smith, R. S. Zellar, G. Neumann, X. Sun, R. B. Katz, I. Kleyner, A. Matuszeski, J. F. McGarry, M. N. Ott, L. A. Ramos-Izquierdo, D. D. Rowlands, M. H. Torrence, and T. W. Zagwodzki (2010). "The Lunar Reconnaissance Orbiter Laser Ranging Investigation". In: *Space Science Reviews* 150.1-4, pp. 63–80. ISSN: 0038-6308, 1572-9672. DOI: 10.1007/s11214-009-9511-z.

Declaration

I declare herewith that this thesis is my own work and that I have not used any sources other than those stated. I have indicated the adoption of quotations as well as thoughts taken from other authors as such in the thesis. I am aware that the Senate pursuant to Article 36 paragraph 1 literar of the University Act of September 5th, 1996 and Article 69 of the University Statute of June 7th, 2011 is authorized to revoke the doctoral degree awarded on the basis of this thesis. For the purposes of evaluation and verification of compliance with the declaration of originality and the regulations governing plagiarism, I hereby grant the University of Bern the right to process my personal data and to perform the acts of use this requires, in particular, to reproduce the written thesis and to store it permanently in a database, and to use said database, or to make said database available, to enable comparison with theses submitted by others.